

Fluid-chemical studies of gold systems: Case studies of an Archean greenstone belt, Nunavut, and a Paleozoic slate belt, Meguma terrane, Nova Scotia.

By

Mitchell James Kerr

A thesis submitted in partial fulfillment of the requirements  
for the degree of Doctor of Philosophy (PhD)  
in Mineral Deposits and Precambrian Geology

The Faculty of Graduate Studies  
Laurentian University  
Sudbury, Ontario, Canada

© Mitchell James Kerr, 2020

**THESIS DEFENCE COMMITTEE/COMITÉ DE SOUTENANCE DE THÈSE**  
**Laurentian Université/Université Laurentienne**  
Faculty of Graduate Studies/Faculté des études supérieures

Title of Thesis

Titre de la thèse Fluid-chemical studies of gold systems: Case studies of an Archean greenstone belt, Nunavut, and a Paleozoic slate belt, Meguma terrane, Nova Scotia.

Name of Candidate

Nom du candidat Kerr, Mitchell

Degree

Diplôme Doctor of Philosophy Mineral Deposits and Precambrian Geology

Department/Program

Département/Programme Geology

Date of Defence

Date de la soutenance December 16, 2019

**APPROVED/APPROUVÉ**

Thesis Examiners/Examineurs de thèse:

Dr. Daniel Kontak

(Supervisor/Directeur de thèse)

Dr. Jacob Hanley

(Co-supervisor/Co-directeur de thèse)

Dr. Doug Tinkham

(Committee member/Membre du comité)

Dr. Gena Olivo

(External Examiner/Examineur externe)

Dr. Jeff Shepherd

(Internal Examiner/Examineur interne)

Approved for the Faculty of Graduate Studies  
Approuvé pour la Faculté des études supérieures

Dr. David Lesbarrères

Monsieur David Lesbarrères

Dean, Faculty of Graduate Studies

Doyen, Faculté des études supérieures

**ACCESSIBILITY CLAUSE AND PERMISSION TO USE**

I, **Mitchell Kerr**, hereby grant to Laurentian University and/or its agents the non-exclusive license to archive and make accessible my thesis, dissertation, or project report in whole or in part in all forms of media, now or for the duration of my copyright ownership. I retain all other ownership rights to the copyright of the thesis, dissertation or project report. I also reserve the right to use in future works (such as articles or books) all or part of this thesis, dissertation, or project report. I further agree that permission for copying of this thesis in any manner, in whole or in part, for scholarly purposes may be granted by the professor or professors who supervised my thesis work or, in their absence, by the Head of the Department in which my thesis work was done. It is understood that any copying or publication or use of this thesis or parts thereof for financial gain shall not be allowed without my written permission. It is also understood that this copy is being made available in this form by the authority of the copyright owner solely for the purpose of private study and research and may not be copied or reproduced except as permitted by the copyright laws without written authority from the copyright owner.

## Abstract

Despite several decades of study, the source(s) of gold and mineralizing fluids, and the mechanisms responsible for gold precipitation remain controversial. In particular, there is a need to improve: (i) the identification of secondary gold upgrading processes that lead to very high-grade gold zones; (ii) the understanding of precipitation mechanisms in carbonaceous material (CM)-bearing metasedimentary systems (i.e., slate belts); and (iii) the exploration criteria for the cryptic, finely disseminated gold mineralization in CM-bearing metamudstone lithologies.

The combined results of an extensive in situ microanalytical protocol (SEM, confocal Raman microspectroscopy, microthermometry, decrepitate mound analysis, LA-ICP-MS, cathodoluminescence, SIMS) has identified evidence of secondary gold enrichment at the Madrid deposit, Hope Bay Greenstone Belt, NU, Canada, resulting from the addition of new gold onto an earlier orogenic quartz-carbonate vein deposit by magmatic-hydrothermal fluids. This conclusion is based on robust textural, mineralogical, and fluid inclusion evidence. The geological setting and mineral-chemical features suggest an intrusion-related (i.e., porphyry), or intermediate-sulfidation epithermal mineralization style for the later event. This work provides another example of the importance of compositionally distinct cumulative hydrothermal events in the development of high-grade gold deposits in orogenic settings.

The Dufferin deposit, NS, Canada, is a vein-type system hosted in CM-bearing metasedimentary rocks. A detailed fluid inclusion study strongly suggests that Au mineralization occurred through coupled fluid  $fO_2$  reduction (via interaction with CM) and pH increase, leading to efficient Au precipitation from an Au-undersaturated aqueous-carbonic fluid. This study presents one of the few examples of measured Au concentrations in ore fluids in an economic orogenic Au deposit

and reports direct evidence for the genetic relationship between Au and CM in metasedimentary lithologies. The results of this study show that, despite mineralizing fluids being Au-undersaturated, they may still produce economic deposits through highly efficient precipitation processes.

The Moose Rive anticline, NS, Canada, hosts a number of, commonly inconspicuous, metasediment-hosted disseminated Au deposits. An initial study using an on-line, rock-crushing gas chromatographic technique identified bulk fluid differences (CO<sub>2</sub> and hydrocarbon abundances) between gold-bearing and gold-barren parcels of metasedimentary rock. This work suggests that bulk fluid characteristics may be a viable exploration vector for disseminated gold systems.

**Keywords:** gold; orogenic; magmatic-hydrothermal; upgrading; fluid inclusion; mineralization; decrepitate mound; Hope Bay Greenstone Belt; Dufferin gold deposit; gas chromatography; carbonaceous material; disseminated gold; Meguma terrane; Archean; Phanerozoic

## Statement of co-authorship

This thesis consists of three separate manuscripts prepared for publication in peer-reviewed journals. Chapters two, three and four have been co-authored by the candidate and additional collaborators. Chapter two has been published in *Geochimica et Cosmochimica Acta* (2018, v.241, p.180-218). Chapter three is intended for submission to *Geochimica et Cosmochimica Acta* in Dec 2019. Chapter four is intended for submission to *Journal of Geochemical Exploration* or *The Canadian Journal of Earth Science* in Feb 2020. The thesis was designed by Dr. Jacob Hanley, Dr. Daniel Kontak and the candidate, with financial and/or logistical support provided by strategic industry and government supporters (Chapter two – TMAC Resources Inc.; Chapter three – Maritime Dufferin Gold Corp.; Chapter four – Nova Scotia Department of Energy and Mines & Atlantic Gold Corp.). All fieldwork, sample collection, sample preparation, petrography, and interpretation of analytical results were completed by the candidate with guidance by Drs. Jacob Hanley and Daniel Kontak. Additional collaboration by provided by co-authors listed herein, including technical support, expertise and constructive criticism.

Chapter two is co-authored by Jacob Hanley, Daniel Kontak, Gordon Morrison, Joseph Petrus, Mostafa Fayek, and Zoltán Zajacz. Fieldwork, sample selection and sample preparation were completed by the candidate. Financial and logistical support for sample collection was coordinated by Gordon Morrison and provided by TMAC Resources Inc.

Chapter three is co-authored by Jacob Hanley, Daniel Kontak, Preetysa Ramlochund and Zoltán Zajacz. Fieldwork, sample selection and sample preparation were completed by the candidate. Analytical work was performed by the candidate or by Preetysa Ramlochund with supervision

from the candidate. Logistical support for sample collection was coordinated by Mr. Rick Horne and Maritime Dufferin Gold Corp.

Chapter four is co-authored by Daniel Kontak and Jacob Hanley. Fieldwork, sample selection and sample preparation were completed by the candidate. Access to select diamond drill cores for sampling was provided by the Nova Scotia Department of Energy and Mines.

All manuscripts were edited by Jacob Hanley and Daniel Kontak. Drs. Mostafa Fayek (coauthor) and Iain Samson (reviewer) provided insight that helped improve the manuscript in Chapter two.

## **Acknowledgements**

I would like abundantly thank my supervisors Jacob Hanley, and Daniel Kontak for their phenomenal mentorship and support throughout my PhD. Their thoughtful input and guidance have helped me develop into an effective geoscientist. I would like to thank Dr. Jeffrey Shepherd for acting as my internal examiner and Dr. Gema Olivo for acting as external examiner and providing thoughtful feedback that improved this thesis manuscript.

I would like to recognize the support from TMAC Resources Inc. for getting me up to the Hope Bay Greenstone Belt for three weeks to complete sample collection. Specifically, I would like to thank Gordon Morrision, Dave King, and Matt Lapointe. I would also like to thank the Orix Geoscience team that worked with me at Hope Bay, including Ashley Kirwan, Craig Fitchett, Justin Bernard, Alexa Dettman, Sam Long and Paige Giddy.

Thank you to those with Maritime Dufferin Gold Corp. who provided logistical support to collect samples from the underground workings at the Dufferin Mine, including Rick Horne (now former employee) and Aaron Hoyle.

Having completed my PhD primarily based out of Saint Mary's University in Halifax, NS, I would like to warmly thank the SMU faculty and staff that have provided advice and technical support, including Randy Corney, Tara Inman, Fergus Tweedale and Xiang Yang. I would like to thank my colleagues and friends in the Mineral Exploration and Ore Fluids Laboratory at SMU. I can always count on them to share in an engaging chat or cold beer.

Where I am today is largely a result of the encouragement and support of my family and good friends. I would like to thank my mother Bonnie and my late father Rob for their unwavering support throughout my academic career. I am extremely grateful to both of you for everything.

I would like to thank my wife Erin for her continual love and support throughout this process. She is my best friend, closest ally and academic colleague, and I am very grateful to have her in my life.

## Table of Contents

Abstract .....	iii
Statement of co-authorship .....	v
Acknowledgements .....	vii
Table of Contents .....	ix
List of Figures .....	xiv
List of Tables .....	xvii
List of Electronic Appendices .....	xviii
Chapter 1 .....	1
1 Introduction to thesis.....	1
1.1 Background .....	1
1.2 Research problems .....	4
1.3 Thesis objectives .....	5
1.4 Structure of thesis .....	6
1.5 Statement of original contributions.....	8
1.6 References.....	9
Chapter 2.....	16
2 Evidence of upgrading of gold tenor in an orogenic quartz-carbonate vein system by late magmatic-hydrothermal fluids at the Madrid Deposit, Hope Bay Greenstone Belt, Nunavut, Canada.....	16
2.1 Abstract .....	16
2.2 Introduction.....	17
2.3 Regional geology, Madrid deposit geology and vein mineralization .....	20
2.3.1 Regional geological setting of the Hope Bay Greenstone Belt and Madrid deposit ...	20
2.3.2 Mineralization, vein and alteration characteristics at Madrid.....	23

2.4 Methods.....	26
2.4.1 Sample collection and vein characterization.....	27
2.4.2 SEM-EDS analysis.....	28
2.4.3 Fluid inclusion microthermometry .....	28
2.4.4 Fluid inclusion decrepitate mound analysis.....	29
2.4.5 Confocal Laser Raman microspectroscopy (LRM) .....	30
2.4.6 Fluid inclusion laser ablation inductively coupled plasma mass spectrometry (LA-ICP-MS) .....	31
2.4.7 Secondary Ion Mass Spectrometry (SIMS) .....	32
2.4.8 Hot cathodoluminescence (HCL) imaging of quartz .....	32
2.4.9 Laser ablation inductively coupled plasma mass spectrometry (LA-ICP-MS) trace element mapping of pyrite .....	33
2.5 Results.....	33
2.5.1 High- and low-grade veins of the Madrid Deposit .....	33
2.5.1.1 <i>Textural comparison of high- and low-grade veins</i> .....	35
2.5.1.2 <i>Comparison of the ore mineralogy of the high- and low-grade veins</i> .....	36
2.5.1.3 <i>Wall-rock alteration mineralogy</i> .....	38
2.5.2 Ore fluid characteristics .....	39
2.5.2.1 <i>Fluid inclusion types</i> .....	39
2.5.2.2 <i>Fluid inclusion microthermometry and laser Raman microspectroscopy</i> .....	42
2.5.2.3 <i>Fluid inclusion decrepitate mound analysis</i> .....	44
2.5.2.4 <i>Fluid inclusion LA-ICP-MS</i> .....	45
2.5.2.5 <i>Oxygen isotopes by SIMS</i> .....	45
2.5.3 Trace element abundances as correlations in vein-hosted pyrite.....	45
2.6 Discussion.....	47

2.6.1 Evidence for secondary magmatic-hydrothermal upgrading of gold grades in Madrid	47
.....	
2.6.1.1 Sulfosalt mineralization and quartz vein textures.....	48
2.6.1.2 Pyrite trace element chemistry.....	53
2.6.1.3 Ore fluid geochemistry and isotopic evidence.....	54
2.6.1.3.1 Significance and textural relationship of fluid inclusion types.....	54
2.6.1.3.2 Compositional differences between hydrothermal fluid generations.....	58
2.6.1.3.3 $\delta^{18}\text{O}$ of vein-forming fluids.....	61
2.6.2 Overprinting of orogenic gold mineralization by magmatic-hydrothermal fluid assemblages.....	62
2.6.3 Potential fluid sources and implications for orogenic vein upgrading by magmatic-hydrothermal fluids at Hope Bay.....	66
2.7 Conclusions.....	68
2.8 Acknowledgements.....	70
2.9 References.....	71
Chapter 3.....	132
3 Fluid inclusion and microtextural evidence for efficient gold precipitation from Au-undersaturated fluids through coupled redox-pH change, Meguma terrane, Nova Scotia, Canada.	132
.....	
3.1 Abstract.....	132
3.2 Introduction.....	133
3.3 Geologic setting of the Dufferin gold deposit.....	136
3.4 Methods.....	139
3.4.1 Sampling.....	139
3.4.2 Analytical techniques.....	139
3.5 Results.....	142

3.5.1 Vein mineralogy, nature of CM and C isotopic compositions.....	142
3.5.2 Fluid inclusion systematics .....	143
3.5.2.1 <i>Fluid inclusion petrography and microthermometry</i> .....	143
3.5.2.2 <i>Fluid inclusion chemistry: LRM and LA-ICP-MS</i> .....	145
3.6 Discussion.....	147
3.6.1 A fluid chemical model for gold precipitation at the Dufferin deposit.....	147
3.6.2 Fluid evolution during fluid/rock interaction.....	153
3.6.3 Potential origins of auriferous vein-forming fluids .....	155
3.7 Conclusions.....	158
3.8 References.....	160
Chapter 4.....	194
4 An initial study on the use of bulk fluid volatile chemistry for exploration of metasedimentary-hosted orogenic gold deposits: An example from the Meguma terrane, Nova Scotia, Canada..	194
4.1 Abstract.....	194
4.2 Introduction.....	196
4.3 Geological Setting.....	199
4.3.1 Regional geology of the Meguma terrane.....	199
4.3.2 Stratigraphy of the Meguma metasedimentary rocks .....	200
4.3.3 Summary of metasedimentary rock-hosted disseminated gold mineralization .....	201
4.3.4 Nature and origin of Meguma gold deposits.....	202
4.3.5 Geology of the Moose River anticline and Touquoy gold mineralization.....	204
4.4 Methods.....	207
4.4.1 Sample selection and preparation .....	207
4.4.2 Confocal laser Raman microspectroscopy (LRM) .....	209
4.4.3 On-line rock-crushing gas chromatography.....	210

4.5 Results.....	212
4.5.1 Petrography of mineralized metamudstones from Touquoy.....	212
4.5.2 Fluid inclusion petrography .....	213
4.5.3 Fluid inclusion laser Raman microspectroscopic (LRM) analysis .....	215
4.5.4 On-line rock-crushing gas chromatography of metamudstones .....	216
4.5.4.1 <i>Evaluation of sample reproducibility</i> .....	216
4.5.4.2 <i>Gas chromatographic analysis of metamudstones</i> .....	217
4.6 Discussion.....	218
4.6.1 Limitations and advantages of GC-based exploration methods .....	219
4.6.2 Origin of volatiles in metamudstones of the Moose River anticline .....	219
4.6.2.1 <i>Origin of the N<sub>2</sub>-CH<sub>4</sub> fluids</i> .....	220
4.6.2.2 <i>Origin of the CO<sub>2</sub>-bearing fluids</i> .....	224
4.6.3 Bulk volatile systematics – Comparison between mineralized and barren metamudstones.....	225
4.6.4 Implications for disseminated gold mineralization and exploration.....	228
4.6.5 Methodological refinements and future work.....	229
4.7 Conclusions.....	231
4.8 References.....	232
Chapter 5.....	270
5.1 Conclusions.....	270
5.2 Future Work .....	272

## List of Figures

Figure 2-1: Geological map of the Hope Bay Greenstone Belt .....	99
Figure 2-2: Geological map of the Madrid region of the Hope Bay Greenstone Belt.....	101
Figure 2-3: Drill core images .....	102
Figure 2-4: Estimated mineral abundances in drill core vein intercepts.....	104
Figure 2-5: Histogram displaying average gold grades .....	105
Figure 2-6: Photomicrographs showing representative textures seen in the high-grade vein ....	107
Figure 2-7: SEM-BSE and reflected light images .....	109
Figure 2-8: Photomicrographs of fluid inclusion types and subtypes.....	111
Figure 2-9: Schematic sketch summarizing the textural relationships .....	112
Figure 2-10: A summary of microthermometric data for fluid inclusions.....	114
Figure 2-11: Analysis of evaporate mounds .....	116
Figure 2-12: LA-ICP-MS results from analyses of type 3b fluid inclusions.....	117
Figure 2-13: Ranges in $\delta^{18}\text{O}$ for quartz-1 (n=10) and quartz-2 (n=13) from high-grade vein samples.....	118
Figure 2-14: LA-ICP-MS trace element laser maps of a pyrite grain from high-grade vein.....	119
Figure 2-15: LA-ICP-MS trace element laser maps of a pyrite grain from high-grade vein.....	120
Figure 2-16: LA-ICP-MS trace element laser maps of a pyrite grain from low-grade vein.....	121
Figure 2-17: Elemental bivariate plots of pyrite LA-ICP-MS trace element data.....	123
Figure 2-18: Hot cathodoluminescence images of vein quartz.....	125
Figure 2-19: Fluid inclusion isochores temperature versus pressure plot.....	127
Figure 2-20: Simplified deposit model .....	129
Figure 3-1: Macroscopic features of Dufferin saddle veins.....	180

Figure 3-2: Microscopic and Raman spectroscopic features of Au-mineralized septa in vein laminations .....	182
Figure 3-3: Petrographic characteristics of quartz-hosted fluid inclusions .....	183
Figure 3-4: Raman spectra and molecular maps.....	185
Figure 3-5: Isochoric fields for all inclusion types .....	186
Figure 3-6: LA-ICP-MS quantified elemental concentrations and signal .....	188
Figure 3-7: Microthermometric and bulk compositional data for fluid inclusion types.....	190
Figure 3-8: Log $fO_2$ - pH diagram.....	191
Figure 3-9: Geological model for gold precipitation at Dufferin .....	192
Figure 4-1: Geological maps of the Meguma terrane and Moose River anticline.....	249
Figure 4-2: Hand samples and rock chips.....	250
Figure 4-3: Schematic of the online rock-crushing apparatus used for gas chromatographic analysis.....	251
Figure 4-4: Petrography of Touquoy metamudstones .....	253
Figure 4-5: Fluid inclusions hosted in non-vein quartz samples from the Touquoy metamudstone. ....	255
Figure 4-6: Quartz vein-hosted fluid inclusions .....	257
Figure 4-7: Representative LRM spectra of fluid inclusion vapour-phase analysis.....	259
Figure 4-8: Fluid inclusion vapor phase compositions.....	260
Figure 4-9: Evaluation of the reproducibility of gas chromatographic analysis.....	261
Figure 4-10: Representative chromatograms of crushed metamudstones .....	262
Figure 4-11: Box-and-whisker plots .....	264
Figure 4-12: Saturated hydrocarbon abundances versus carbon number .....	265

Figure 4-13: Ternary plots of bulk volatile ratios in metamudstones ..... 267

## **List of Tables**

Table 2-1: Ore minerals and their associated elemental compositions.....	130
Table 2-2: Summary table of the fluid inclusion types.....	131
Table 3-1: Fluid inclusion types and corresponding compositional data. ....	193
Table 4-1: Sampled metamudstones from Au-mineralized and -barren settings.....	268

## **List of Electronic Appendices**

### Chapter 2

Table EA 2-1: Microthermometry data

Table EA 2-2: Fluid inclusion LRM data

Table EA 2-3: Decrepitate mound SEM analyses

Table EA 2-4: Fluid inclusion LA-ICP-MS data

Table EA 2-5: Quartz SIMS analyses

### Chapter 3

Table EA 3-1: Microthermometry data

Table EA 3-2: Fluid inclusion LRM data

Table EA 3-3: Fluid inclusion LA-ICP-MS data

Figure EA 3-1: SEM-EDS elemental map of CM and Au

### Chapter 4

Table EA 4-1: Fluid inclusion LRM data

Table EA 4-2: Bulk rock GC data – Method 1

Table EA 4-3: Bulk rock GC data – Method 2

## Chapter 1

### Introduction to thesis

#### 1.1 Background

Orogenic gold deposits can be defined as hypozonal to epizonal ore systems spatially (and commonly temporally) associated with compressional and transpressional deformation processes at convergent plate margins (e.g., collisional orogens; Groves et al., 1998). Despite extensive research on the nature of orogenic gold deposits (OGD) around the world (Goldfarb et al., 2005; Goldfarb and Groves, 2015), there is still much debate regarding (i) the source and relative contribution of metamorphic and magmatic fluids to gold mineralization in OGD, (ii) the identification of late fluid overprinting and subsequent gold enrichment, and (iii) the mechanistic factors controlling gold mineralization in these settings. The continuous demand for gold and the diminishing recovery of large-tonnage lode deposits necessitate better constraints on the genetic factors controlling gold precipitation in a variety of geologic settings to better inform exploration strategies. Two topics of particular importance (and addressed in this thesis) with regards to understanding the genetic models controlling gold mineralization include: (i) the relative importance, contribution, and identification of overprinting of pre-existing auriferous vein systems by magmatic-hydrothermal fluids leading to secondary gold enrichment (e.g., Mao et al., 2003; Oberthür and Weiser, 2008); and (ii) the role of carbonaceous material (CM) in gold complex destabilization and subsequent precipitation in, or in contact with, organic-rich lithologies (e.g., Bierlein et al., 2001; Hu et al., 2017).

Although extensive research has been performed on the composition and occurrence of ore fluids associated with OGD, conclusions regarding the geochemical nature of these fluids remains equivocal (Goldfarb and Groves, 2015). An aqueous-carbonic fluid with an  $X_{\text{CO}_2} \approx 0.1 - 0.15$ ,

low- to intermediate salinity (3 – 13 wt.% NaCl equiv.), P-T conditions of ~250 - 350°C and 1 -3 kbar,  $\delta^{18}\text{O} = 6 - 13\text{‰}$ , and diverse metal associations (Au  $\pm$  As, Ag, Bi, Cu, Pb, Zn, Sb, Te, W) equally describe causative fluids in both OGD and intrusion-related gold (IRG) systems (McCuaig and Kerrich, 1998; Ridley and Diamond, 2000; Goldfarb et al., 2005; Bodnar et al., 2014; Thompson et al., 1999; Lang and Baker, 2001; Hart, 2007). Moreover, styles of mineralization (e.g., disseminated, replacement, vein, etc.) and ore mineralogy (e.g., sulfides and sulfosalts) may be shared by both deposit types. Therefore, geochemical similarities between deposits types with dissimilar origins creates the potential for misclassification without comprehensive supporting evidence. The identification of gold grade upgrading in established orogenic vein systems by late magmatic-hydrothermal fluid overprinting is limited in the literature (Mao et al., 2003; Oberthür and Weiser, 2008), and identification and appropriate classification is made even more challenging in systems that have been affected by protracted magmatic-hydrothermal overprinting via fluid ingress through re-activated structures (e.g., Helt et al., 2014; de Souza et al., 2015; Wang et al., 1998; Goldfarb et al., 2004). In the Madrid Deposit in the Hope Bay Greenstone Belt (HBGB), Nunavut, Canada, hydrothermal activity was protracted and complex in nature, suggested by the overprinting of veining events with distinct alteration assemblages (Clow et al., 2013, 2015). Although a considerable amount of research has been conducted in the HBGB documenting regional geology, alteration, veining, mineralization, and structure (Thompson, 1997; Hebel, 1999; Sherlock et al., 2003; Shannon, 2005; Therriault, 2006; Madsen et al., 2007; Sherlock et al., 2012), there has been no detailed account of the influence of late magmatic-hydrothermal processes at the Madrid Deposit, determined through an investigation of the fluid inclusion record, late Au-Ag-telluride and sulfosalt mineralization, and associated textural information.

The association of variably metamorphosed or thermally degraded carbonaceous material (e.g., pyrobitumen, bitumen, graphite) and gold in flysch-hosted gold deposits is not uncommon. The spatial association of gold mineralization and CM has been known of for over a century (e.g., Brooks, 1912), and has been well documented in the gold deposit literature (e.g., Carlin gold Deposit: Joralemon, 1951; Radtke and Scheiner, 1970; Con and Giant gold deposits, Yellowknife district, Canada: Padgham, 1986; the Kupferschiefer, Poland: Kucha, 1993; Western Lachlan Orogen, Victoria, Australia: Bierlein et al., 2001; Macraes Gold Mine, Otago Schist, New Zealand: Craw, 2002; Pitcairn et al., 2006; Hoyle Pond Deposit, Abitibi Greenstone Belt, Canada: Diné et al., 2008; Ashanti Gold Belt, Ghana: Berge, 2011), and industrial gold processing literature alike (e.g., “preg-robbing” phenomena: Breerwood, 1938; Scheiner, 1971; Miller et al., 2005). Despite this, the physicochemical mechanisms controlling gold precipitation through mineralizing fluid  $fO_2$  reduction via interaction with CM is still poorly understood, with mechanistic models only expressed in a few publications (e.g., Matthäi et al., 1995; Hu et al., 2017).

Disseminated gold deposits present significant challenges with regard to exploration. Gold in these settings is not hosted in obvious quartz-carbonate lode veins, and the commonly micron-scale (< 150  $\mu\text{m}$ ; Ryan and Smith, 1998; Bierlein and Smith, 2003) gold grains in metamudstone sequences is unidentifiable during routine core logging. Mineralization of this nature is currently being actively mined (e.g., Touquoy), or drilled to improve resource estimates (e.g., Beaver Dam, Fifteen Mile Stream). Apart from the strong focus on lithological and lithochemical (e.g., whole rock assay) analysis used in contemporary exploration programs, little is known of fluid geochemical variations in Au-mineralized and –barren parcels of metasedimentary rocks within broader structural settings (e.g., Moose River Anticline)

## 1.2 Research problems

Little work has been done documenting the nature of gold mineralization in the Madrid Deposit of the Hope Bay Greenstone Belt, NU, and in the Dufferin Deposit, NS. Additionally, to date, no comprehensive studies investigating the fluid inclusion records preserved in these two deposits have been performed. Previous work on these two deposits is limited to open file reports documenting the general geology, alteration and structure (e.g., Madrid: Sherlock et al., 2002. Dufferin: Horne and Jodrey, 2002), industry reports (e.g., Hope Bay and Madrid: Clow et al., 2013, 2015. Dufferin: Hannon et al., 2017), and a small number of peer-reviewed journal articles (Kontak et al., 2011; Morelli et al., 2005; Sherlock et al., 2012). Therefore, the variety, composition and timing of mineralizing fluids in these hydrothermal systems is under-documented.

Mineralization in the Madrid Deposit is diverse in nature, ranging from free gold in laminated to brecciated quartz-carbonate vein arrays to pyrite-associated gold (e.g., as invisible gold or inclusions) in pyritized Fe-rich volcanic country rocks (Madsen et al., 2007, Sherlock et al., 2012). It has been reported that at least two gold mineralizing events are evident at Madrid, suggested by the overprinting of veining events with distinct alteration assemblages (Clow et al., 2013, 2015). However, the role of late gold mineralizing fluids of magmatic-hydrothermal origin has not been reported in the literature. Therefore, an integrated study applying a variety of microanalytical techniques was used to address the nature, distribution and timing of mineralizing fluids at Madrid in order to better understand gold distribution and inform exploration programs. Additionally, this work provides important insight into a potentially unrecognized, but perhaps relatively common, process of gold upgrading and enrichment in orogenic ore systems elsewhere.

The role of carbonaceous material (CM) in the precipitation of gold has not been directly reported in the Nova Scotian gold deposit literature. In the Dufferin Deposit in particular, the spatial association of CM-bearing black slates with auriferous saddle veins warrants a careful investigation of the influence on organic material on gold precipitation via mineralizing fluid  $fO_2$  reduction. Previous work has documented the geometry, structure and age relationships of saddle veins at Dufferin (Horne and Jodrey, 2001; Morelli et al., 2005) and Kontak et al., (2011) made inferences as to the nature of vein-forming fluid based on the oxygen isotopic compositions of quartz vein material from Dufferin. However, no detailed fluid inclusion study has been performed to date, and thus the nature and composition of ore fluids hosted as fluid inclusion in quartz saddle veins at Dufferin remains unresolved.

Furthermore, unlike vein-type deposits hosted throughout the Meguma Terrane (e.g., Dufferin, Goldboro, Tangier), disseminated gold mineralization in carbonaceous flysch country rocks constitute economically-viable ore bodies that are currently being mined. In particular, the Touquoy, Beaver Dam, and Fifteen Mile Stream gold deposits hosted along the Moose River anticline are currently in production or being developed. Therefore, mineralizing fluids must have permeated country rocks precipitating gold in, or in contact with, favorable lithologies. Thus far, exploration for these “invisible” gold occurrences is limited to diamond drilling and whole rock assaying, warranting the investigation of more unconventional exploration techniques. As a result, an initial study employing an on-line rock-crushing, bulk fluid gas chromatographic technique has been performed to evaluate its efficacy for the exploration of disseminated gold mineralization in the Meguma Terrane.

### **1.3 Thesis objectives**

The primary objective of this thesis is to document and characterize gold mineralization in “orogenic”-style greenstone-hosted and metasedimentary rock-hosted gold deposits in order to better understand the nature of gold-mineralizing fluid events, and improve genetic and mechanistic models for mineralization in these settings. The following research questions will be addressed herein:

- 1) How can we recognize the overprinting, and subsequent gold upgrading, of pre-existing orogenic veins by late auriferous magmatic-hydrothermal fluid ingress?
  - a. What mineralogical, textural, and fluid geochemical evidence suggests the influence of late magmatic-hydrothermal fluids in the Madrid Deposit, Hope Bay Greenstone Belt?
  - b. What implications does this have on current genetic models for orogenic gold deposits in greenstone terranes?
- 2) What is the influence of carbonaceous material on the destabilization of soluble gold species, and what are the mechanistic controls for gold precipitation via local fluid reduction?
- 3) Can a bulk volatile gas chromatographic technique be effectively used for the exploration of metasedimentary rock-hosted disseminated gold deposits?
  - a. Do the bulk fluid signatures of mineralized metasedimentary units, hosting disseminated gold, differ from those of gold-barren metasedimentary units of analogous composition?
  - b. What does the bulk fluid signatures in these settings suggest about the nature of mineralizing fluids in disseminated gold deposits?

#### **1.4 Structure of thesis**

This PhD dissertation is organized into five chapters. Chapters two to four are written as stand-alone manuscripts intended for submission, or already submitted, to peer-reviewed academic

journals. Therefore, some repetition may be present between chapters with respect to methodology and geological background.

Chapter two is a manuscript entitled “**Evidence of upgrading of gold tenor in an orogenic quartz-carbonate vein system by late magmatic-hydrothermal fluids at the Madrid Deposit, Hope Bay Greenstone Belt, Nunavut, Canada**”. This manuscript has been published in *Geochimica et Cosmochimica Acta* (2018, v.241, p.180-218; see Kerr et al., 2019) and presents a detailed account of the upgrading of gold tenor in early orogenic laminated quartz-carbonate veins of the Madrid Deposit, Hope Bay Greenstone Belt, by late magmatic-hydrothermal fluids. Evidence for late magmatic-hydrothermal overprinting and subsequent gold upgrading is provided through an exhaustive microanalytical protocol performed on strategic vein samples (i.e., high-grade versus low-grade veins).

Chapter three is a manuscript entitled “**Fluid inclusion and microtextural evidence for efficient gold precipitation from Au-undersaturated fluids through coupled redox-pH change, Meguma terrane, Nova Scotia, Canada**”. This manuscript is intended for submission to *Earth and Planetary Science Letters* (anticipated submission in Sept. 2019). This manuscript investigates the nature of gold-bearing fluids and gold mineralization in the saddle reef-style veins of the Dufferin deposit, Nova Scotia, Canada. This study provides evidence for gold mineralization through an efficient fluid reduction mechanism via interaction of an auriferous ore fluid with carbonaceous material (i.e., organic matter) in black slate wall rocks, within vein-hosted wall rock fragments, and in early laminated vein fragments.

Chapter four is written as a manuscript entitled “**An initial study on the use of bulk fluid volatile chemistry for exploration of metasedimentary-hosted orogenic gold deposits: An example**”

**from the Meguma terrane, Nova Scotia, Canada.”** This manuscript has been written for submission to the *Journal of Geochemical Exploration* or the *Canadian Journal of Earth Sciences* (anticipated submission in Sept 2019). This manuscript describes the use of bulk rock volatile signatures, determined by on-line rock-crushing gas chromatography, as a potential tool for the exploration of disseminated gold deposits in the Meguma Terrane. This study is a pilot project and represents a preliminary investigation of this unconventional technique.

### **1.5 Statement of original contributions**

A summary of the original contributions by the candidate to this study is as follows:

- First detailed, integrated fluid inclusion investigation of the Madrid Deposit in the Hope Bay Greenstone Belt, Nunavut, Canada.
  - First to document evidence for the upgrading of gold tenor at Madrid via overprinting by late magmatic-hydrothermal fluids through the use of ore mineral petrography, fluid inclusion microthermometry, laser Raman microspectroscopy, fluid inclusion LA-ICP-MS, elemental mapping of pyrite by LA-ICP-MS and associated principle component analysis of data, cathodoluminescence imaging, decrepitate mound analysis, and oxygen isotopic analysis.
- First detailed fluid inclusion investigation of gold-bearing fluids in the Dufferin gold deposit, NS, Canada.
  - Documented evidence of the relationship between carbonaceous material and gold precipitation in this setting.
  - First report gold concentrations in secondary fluid inclusions from an economic gold deposit in a Phanerozoic slate belt.

- Improved genetic models for gold mineralization by means of fluid reduction in metasedimentary rock-hosted “orogenic” gold systems (Dufferin and analogous systems).
- First preliminary investigation of the bulk rock volatile signatures of Au-mineralized and Au-barren metasedimentary units (slate/argillite) along the Moose River Anticline, NS, Canada.
- Proposed a gas chromatography-based exploration technique to supplement traditional gold exploration programs in NS gold deposits and analogous systems.

## **1.6 References**

- Berge, J. (2011). Paleoproterozoic, turbidite-hosted, gold deposits of the Ashanti gold belt (Ghana, West Africa): Comparative analysis of turbidite-hosted gold deposits and an updated genetic model. *Ore Geology Reviews* 39, 91-100.
- Bierlein, F.P., Cartwright, I., and McKnight, S., (2001). The role of carbonaceous “indicator” slates in the genesis of lode gold mineralization in the Western Lachlan orogen, Victoria, Southeastern Australia. *Economic Geology* 96, 431–451.
- Bierlein, F.P., and Smith, P.K., (2003). The Touquoy Zone deposit: an example of “unusual” orogenic gold mineralization in the Meguma Terrane, Nova Scotia, Canada. *Canadian Journal of Earth Science* 40, 447-466.
- Bodnar, R.J., Lecumberri-Sanchez, P., Moncada, D., and Steele-MacInnis, M. (2014). Fluid inclusions in hydrothermal ore deposits. In *Reference Module in Earth Systems and Environmental Sciences, Treatise on Geochemistry (Second Edition)*, 13, 119-142.
- Breerwood, C.H. (1938). US Patent No. 2130574. Flotation of Carbonaceous Ore.
- Brooks, A.H. (1912). Gold Deposits Near Valdez. U.S. Geology Surv. Bull. 520-D, pp. 108-130.

- Clow, G.G., Lecuyer, N.L., Horan, S., Krutzelmann, H., Chubb, D., and Rykaart, M. (2015). Technical Report on the Hope Bay Project, Nunavut, Canada, NI 43-101 Report. March 2015.
- Clow, G.G., Lecuyer, N.L., Valliant, W.W., Krutzelmann, H., Chubb, D., and Rykaart, M. (2013). Preliminary Economic Assessment Study on the Hope Bay Project, Nunavut, Canada, NI 43-101 Report. December 2013.
- Craw, D., (2002). Geochemistry of late metamorphic hydrothermal alteration and graphitization of host rock, Macraes gold mine, Otago Schist, New Zealand. *Chemical Geology* 191, 257–275.
- De Souza, S., Dubé, B., McNicoll, V.J., Dupuis, C., Mercier-Langevin, P., Creaser, R.A., and Kjarsgaard, I.M. (2015). Geology, hydrothermal alteration, and genesis of the world-class Canadian Malartic stockwork-disseminated Archean gold deposit, Abitibi, Quebec. In Dubé, B. and Mercier-Langevin (eds.), *Targeted Geoscience Initiative 4: Contributions to the Understanding of Precambrian Lode Gold Deposits and Implications for Exploration*. Geological Survey of Canada, Open File 7852.
- Dinel, E., Fowler, A.D., Ayer, J., Still, A., Tylee, K., and Barr, E. (2008). Lithogeochemical and Stratigraphic Controls on Gold Mineralization within the Metavolcanic Rocks of the Hoyle Pond Mine, Timmins, Ontario. *Economic Geology* 103, 1341-1363.
- Goldfarb, R.J., Baker, T., Dubé, B., Groves, D.I., Hart, C.J.R., and Gosselin, P. (2005). Distribution, character, and genesis of gold deposits in metamorphic terranes. *Economic Geology* 100<sup>th</sup> Anniversary Volume, p. 407-450.
- Goldfarb, R.J. and Groves, D.J. (2015). Orogenic gold: Common or evolving fluid and metal sources. *Lithos* 2, 2-26.

- Goldfarb, R.J., Ayuso, R., Miller, M.L., Ebert, S. W., Marsh, E.E., Petsel, S.A., Miller, L.D., Bradley, D., Johnson, C., and McClelland, W. (2004). The late Cretaceous Donlin Creek gold deposit, Southwestern Alaska: Controls on epizonal ore formation. *Economic Geology* 99(4), 643-671.
- Groves, D.I., Goldfarb, R.J., Gebre-Mariam, M., Hagemann, S.G., and Robert, F. (1998) Orogenic gold deposits: a proposed classification in the context of their crustal distribution and relationship to other gold deposit types. *Ore Geology Reviews* 13, 7-27.
- Hannon, P., Roy, D., Mosher, G. (2017). Revised Preliminary Economic Assessment of the Dufferin Gold Deposit. Resource Capital Gold Corp. April 2017.
- Hart, C.J.R. (2007). Reduced intrusion-related gold systems. In Goodfellow, W.D., (ed.), *Mineral deposits of Canada: A Synthesis of Major Deposit Types, District Metallogeny, the Evolution of Geological Provinces, and Exploration Methods: Geological Association of Canada, Mineral Deposits Division, Special Publication No. 5*, 95-112.
- Hebel, M.U. (1999). U-Pb geochronology and lithogeochemistry of the Hope Bay greenstone belt, Slave Structural Province, Northwest Territories, Canada: M.Sc. thesis, Vancouver, Canada, University of British Columbia, 96 p.
- Helt, K.A., Williams-Jones, A.E., Clark, J.R., Wing, B.A., and Wares, R.P. (2014). Constraints on the genesis of the Archean oxidized intrusion-related Canadian Malartic gold deposit, Quebec, Canada. *Economic Geology* 109, 713-735.
- Horne, R.J., Jodrey, M. (2002). Geology of the Dufferin gold deposit (NTS 11D/16), Halifax County. In: MacDonald DR (ed) *Mineral Res Branch, Rpt Act 2001, Nova Scotia Dept Nat Res, Rpt 2002-1*, pp. 51–68

- Hu, Si-Yu, Evans, K., Craw, D., Rempel, K., and Grice, K. (2017). Resolving the role of carbonaceous material in gold precipitation in metasediment-hosted orogenic gold deposits. *Geology* 45, 167-170.
- Joralemon, P. (1951). The occurrence of gold at the Getchell Mine, Nevada. *Economic Geology* 46, 267-310.
- Kerr, M.J., Hanley, J.J., Kontak, D.J., Morrison, G.G., Petrus, J., Fayek, M., and Zajacz, Z. (2018). Evidence of upgrading of gold tenor in an orogenic quartz-carbonate vein system by late magmatic-hydrothermal fluids at the Madrid Deposit, Hope Bay Greenstone Belt, Nunavut, Canada. *Geochimica et Cosmochimica Acta* 241, 180-218.
- Kontak, D.J., Horne, R.J., and Kyser, K., (2011). An oxygen isotope study of two contrasting orogenic vein gold systems in the Meguma Terrane, Nova Scotia, Canada, with implications for fluid sources and genetic models: *Mineralium Deposita* 46, 289-304.
- Kucha, H. (1993). Noble metals associated with organic matter, Kupferschiefer, Poland. In *Bitumens in Ore Deposits* (pp. 153-170). Springer, Berlin, Heidelberg.
- Lang, J.R. and Baker, T. (2001). Intrusion-related gold systems: the present level of understanding. *Mineralium Deposita* 36, 477-489.
- Madsen, J.K., Sherlock, R., and Lindsay, D. (2007). The geology, geochemistry and mineralization of the Naartok gold deposit: Hope Bay belt, Nunavut Territory [abs.]: *Geology Association Canadian Abstract*, p. 52.
- Mao, W., Rusk, B., Yang, F., and Zhang, M. (2017). Physical and chemical evolution of the Dabaoshan porphyry Mo deposit, South China: Insights from fluid inclusions, cathodoluminescence, and trace elements in quartz. *Economic Geology* 112, 889-918.

- Matthäi, S.K., Henley, R.W., and Heinrich, C.A. (1995). Gold precipitation by fluid mixing in bedding-parallel fractures near carbonaceous slates at the Cosmopolitan Howley gold deposit, northern Australia. *Economic Geology* 90(8), 2123-2142.
- McCuaig, T.C., and Kerrich, R. (1998). P-T-t-deformation-fluid characteristics of lode gold deposits: evidence from alteration systematics. *Ore Geology Reviews* 12, 381-453.
- Miller, J.D., Wan, R.Y., and Diaz, X. (2005). Preg-robbing gold ores. *Developments in Mineral Processing* 15, 937-972.
- Morelli, R.M., Creaser, R., Selby, D., Kontak, D.J., Horne, R.J. (2005). Rhenium-Osmium geochronology of arsenopyrite in Meguma Group gold deposits, Meguma Terrane, Nova Scotia, Canada: evidence for multiple gold-mineralizing events. *Economic Geology* 100, 1229–1242
- Oberthür, T. and Weiser, T.W. (2008). Gold-bismuth-telluride-sulphide assemblages at the Viceroy Mine, Harare-Bindura-Shamva greenstone belt, Zimbabwe. *Mineral. Magazine* 72(4), 953-970.
- Padgham, W.A. (1986). Turbidite-Hosted Gold–Quartz Veins in the Slave structural Province, NWT. In: Keppie, J.D., Boyle, R.W., Haynes, S.J. (Eds.), *Turbidite-Hosted Gold Deposits: Geologic Association of Canada, Special Paper*, 32, 119–134.
- Pitcairn, I.K., Teagle, D.A., Craw, D., Olivo, G.R., Kerrich, R., and Brewer, T.S. (2006). Sources of metals and fluids in orogenic gold deposits: insights from the Otago and Alpine Schists, New Zealand. *Economic Geology* 101(8), 1525-1546.
- Radtko, A.S., and Scheiner, B.J. (1970). *Studies of Hydrothermal Gold Deposition (I). Carlin Gold Deposit, Nevada: The Role of Carbonaceous Materials in Gold Deposition*. *Economic Geology* 65, 87-102.

- Ridley, J.B., and Diamond, L.W. (2000). Fluid chemistry of orogenic lode gold deposits and implications for genetic models. *Soc. Economic Geology Reviews* 13, 141-162.
- Ryan, R.J., and Smith, P.K. (1998). A review of the mesothermal gold deposits of the Meguma Group, Nova Scotia, Canada. *Ore Geology Reviews* 13, 153-183.
- Scheiner, B.J. (1971). Processing refractory carbonaceous ores for gold recovery. *The Journal of The Minerals, Metals & Materials Society* 23(3), 37-40.
- Shannon, A.J. (2005). Volcanic framework and geochemical evolution of the Archean Hope Bay Greenstone Belt, Nunavut, Canada: M.Sc. thesis, Vancouver, BC, The University of British Columbia, 200 p.
- Sherlock, R.L., Carpenter, R.L., and Quang, C. (2003). Volcanic stratigraphy, structural geology and gold mineralization in the Doris-Wolverine corridor, northern Hope Bay volcanic belt, Nunavut. Geological Survey of Canada Open File 1553.
- Sherlock, R.L., Shannon, A., Hebel, M., Lindsay, D., Madsen, J., Sandeman, H., Hrabi, B., Mortensen, J.K., Tosdal, R.M., and Friedman, R. (2012). Volcanic Stratigraphy, Geochronology, and Gold Deposits of the Archean Hope Bay Greenstone Belt, Nunavut, Canada. *Economic Geology* 107, 991-1042.
- Therriault, R. (2006). Geology, geochemistry and gold mineralization in the Madrid Corridor, Hope Bay Volcanic Belt, Nunavut, Canada: M.Sc. thesis, London, Ontario, The University of Western Ontario, 216 p.
- Thompson, P.H. (1997). Regional geology of Archean granitoid rocks adjacent to the Hope Bay and Elu Inlet volcanic belts, northeastern Slave structural province, Canadian Shield: BHP Minerals Canada Ltd. Internal Report, 56 p.

Thompson, J.F.H., Sillitoe, R.H., Baker, T., Lang, J.R., and Mortensen, J. K. (1999). Intrusion-related gold deposits associated with tungsten-tin provinces. *Mineralium Deposita* 34(4), 323-334.

Wang, L.G., Qiu, Y.M., McNaughton, N.J., Groves, D. I., Luo, Z.K., Huang, J.Z., and Liu, Y.K. (1998). Constraints on crustal evolution and gold metallogeny in the Northwestern Jiaodong Peninsula, China, from SHRIMP U–Pb zircon studies of granitoids. *Ore Geology Reviews* 13(1-5), 275-291.

## Chapter 2

### **Evidence of upgrading of gold tenor in an orogenic quartz-carbonate vein system by late magmatic-hydrothermal fluids at the Madrid Deposit, Hope Bay Greenstone Belt, Nunavut, Canada**

#### **2.1 Abstract**

Evidence of secondary gold enrichment due to the addition of new gold onto an earlier orogenic quartz-carbonate vein deposit by magmatic-hydrothermal fluids is strongly suggested for the Madrid Deposit, hosted in the Hope Bay Greenstone Belt in Nunavut, Canada. The conclusion is based on an extensive in situ microanalytical protocol (SEM, confocal Raman microspectroscopy, microthermometry, decrepitate mound analysis, LA-ICP-MS, cathodoluminescence, SIMS) not previously applied to gold systems. This approach was used to characterize the mineralogy and fluid inclusion systematics associated with the upgrading event.

Mineralization comprised of only Ag-bearing gold (“electrum”; 89.8 at. % Au avg.; n = 8) is present throughout all investigated laminated and brecciated orogenic quartz veins. However, in high-grade vein intersections where gold grades are locally elevated (up to 122 g/t), assemblages containing tennantite-tetrahedrite + chalcopyrite + electrum (80.7 at. % Au avg.; n = 15) ± Ag-Pb-Au tellurides occur that are texturally late-stage relative to electrum-only mineralization. Subdomains of quartz coeval with this later assemblage are optically- and texturally-distinct from earlier orogenic quartz. This late mineral assemblage is absent in all low-grade vein intersections (~1 g/t Au avg.) examined where only electrum is identified. Quartz-hosted fluid inclusions (H<sub>2</sub>O-NaCl±CO<sub>2</sub>) of intermediate salinity (16.7 ± 1.2 wt. % NaCl equiv.; n = 93) were identified only in the high-grade vein samples and are present along healed planes associated with tennantite-tetrahedrite + chalcopyrite + electrum ± Ag-Pb-Au telluride assemblages. In situ SIMS δ<sup>18</sup>O

analyses of quartz, combined with temperature constraints from mineral equilibria, show that early orogenic vein quartz and late quartz subdomains associated with gold upgrading precipitated from fluids with similar  $\delta^{18}\text{O}$  values of 4.5 to 12.4‰ (n = 10) and -5.5 to 11.8‰ (n = 13), respectively. Isotopic data suggests that meteoric water was a negligible component in fluids responsible for gold precipitation. Microthermometry and Raman spectroscopy show that upgrading fluids were distinct in composition compared to the earlier metamorphic fluids ( $\text{H}_2\text{O-NaCl-CO}_2\pm\text{CH}_4\pm\text{N}_2$ ;  $4.6 \pm 1.6$  wt. % NaCl equiv., n = 33) and later Canadian Shield basement brines ( $\text{H}_2\text{O-NaCl}$ ;  $22.4 \pm 1.2$  wt. % NaCl equiv., n = 12) which have also been identified in the fluid inclusion record at Madrid. Laser ablation ICP-MS analyses indicate the gold upgrading fluids are enriched in As-Sb-Zn-Pb and LILE (Cs-Ba-Rb-Sr); these data are consistent with late fluids derived from an evolved magmatic-hydrothermal system. Trace element mapping of pyrite, coupled with principle component analysis of the data, confirms a strong correlation between Au and Ag-Te-Sb-Bi-W(-As) in upgraded veins, whereas only Au and As strongly correlate in low-grade veins.

The study suggests that gold upgrading, either involving newly introduced gold or remobilization of existing gold, can be linked to the incursion of a late magmatic-hydrothermal fluid that post-dated formation of the main orogenic-type auriferous quartz vein system. The geological setting and mineral-chemical features suggest an intrusion-related (i.e., porphyry), or intermediate-sulfidation epithermal mineralization style for the later event. This work provides another example of the importance of compositionally distinct cumulative hydrothermal events in the development of high-grade gold deposits in orogenic settings.

## **2.2 Introduction**

The origin of orogenic gold deposits and source of the mineralizing fluids remains a subject of debate (e.g., Goldfarb et al., 2005; Goldfarb and Groves, 2015). With the continuous demand for gold combined with the diminishing discovery of large tonnage lode gold deposits, it is necessary to better constrain the genetic factors that contribute to ore-deposit models to refine exploration strategies. In particular, there is a need to better understand the origin of very high-grade gold zones in orogenic gold deposit settings, which considerably enhance bulk gold grades.

There are several factors that lead to secondary gold enrichment (i.e., subsequent to the first gold-mineralizing event), such as: (i) exsolution of metal-rich volatiles from magmatic sources synchronous with or post-dating the primary orogenic gold enrichment (Mao et al., 2003; Oberthür and Weiser, 2008); (ii) superposition of orogenic gold mineralization on earlier gold-bearing magmatic-hydrothermal proto-ore systems (McFarlane et al., 2011; Helt et al., 2014; de Souza et al., 2015; Molnár et al., 2016); or (iii) remobilization, by either magmatic or metamorphic fluids/melts, of pre-existing magmatic-hydrothermal-diagenetic metal concentrations spatially related to orogenic gold deposits (Tomkins and Mavrogenes, 2002; Tomkins et al., 2004; Buchholz et al., 2007; Large et al., 2009, 2016; Mériaud and Jébrak, 2017). In order to address these varied interpretations and models for secondary gold enrichment, detailed mineralogical and geochemical studies using a variety of complimentary analytical and field approaches are required that collectively aim to “fingerprint” the nature and timing of upgrading processes. Such studies, while rare, have the potential to improve exploration strategies in existing gold mining camps by broadening the focus of exploration to include not only the sites of gold deposition, but to also establish the role of causative intrusions (i.e., heat, fluid and/or metal sources) or other potential sources/processes related to secondary gold enrichment. We test these hypotheses for upgrading in an Archean orogenic deposit setting in the Nunavut Territory of northern Canada, which lies in

an emerging gold district that is known to have highly variable gold grades and anomalous high-grade veins.

The Hope Bay Greenstone Belt (HBGB), Nunavut, Canada, is located in the northeastern region of the Archean Slave Province. This belt is host to several orogenic gold deposits, including the Doris, Madrid and Boston deposits. Gold occurs in veins and disseminations associated with fold and/or fault structures (Sherlock et al., 2012 and references therein), as is common in orogenic gold settings (Poulsen et al., 2000; Goldfarb et al., 2005). To the best of our knowledge, only one previous fluid inclusion study on the auriferous veins of the Boston deposit exists (Stemler et al., 2006) where the authors show, not unlike other well-documented orogenic gold deposits (cf., Bodnar et al., 2014), that H<sub>2</sub>O-CO<sub>2</sub>-bearing, low-salinity fluids occur in the host quartz. Such fluids are generally considered as the main gold-mineralizing fluid in orogenic systems; however, it is well documented that cooling intrusions, as in reduced intrusion-related gold deposit (RIRGD) settings, can also yield metalliferous aqueous fluids having both variable salinities and CO<sub>2</sub> contents (e.g., White et al., 1995; Thompson et al., 1999; Lang et al., 2000; Lang and Baker, 2001; Marsh et al., 2003; Hart, 2007; Taylor 2007). Therefore, in orogenic gold deposits displaying evidence of multiple mineralizing events, as is the case in the Madrid deposit, a comprehensive investigation exploiting a wide variety of analytical techniques is needed to address the nature and origin of the mineralizing fluids, and the cumulative effects of hydrothermal events on gold grade and distribution. In particular, mineralized sub-regions of the Madrid Deposit, delineated by recent drilling, show marked differences in gold grade range and distribution. These differences are considered to reflect variations in mineralization style and fluid origin.

This study is the first integrated mineralogical and fluid inclusion investigation of the giant HBGB orogenic gold system. Based on the integration of a variety of in situ microanalytical techniques (Raman microspectroscopy, microthermometry, SEM-EDS decrepitate mound analysis, LA-ICP-MS, hot cathodoluminescence, SIMS  $\delta^{18}\text{O}_{\text{quartz}}$ ), which are rarely presented in a single study, we provide the following to address the origin of the gold mineralization in the Madrid Deposit: (i) textural, mineralogical, and fluid inclusion evidence for secondary gold upgrading in an orogenic-type, laminated quartz-carbonate vein system, and (ii) evidence that the increase in gold concentrations (upgrading) is associated with the introduction of later stage hydrothermal fluids sourced from protracted magmatic-hydrothermal activity in the region. Therefore, this work provides insights into a generally unrecognized but perhaps common process of gold enrichment and upgrading that is present in orogenic ore systems.

## **2.3 Regional geology, Madrid deposit geology and vein mineralization**

### **2.3.1 Regional geological setting of the Hope Bay Greenstone Belt and Madrid deposit**

The HBGB is an 82 km-long, north-south striking Archean granite-greenstone-metasedimentary terrane (2.72 – 2.66 Ga; Hebel, 1999; Sherlock et al., 2012) located in the northeastern region of the Slave Province in the Bathurst Block; its general setting has been well described by previous workers (Hebel, 1999; Carpenter et al., 2003; Sherlock et al., 2003, 2012). This belt hosts several closely spaced and likely geologically-related, large orogenic gold deposits (Fig. 1), including the Doris, Madrid, and Boston deposits (i.e., Doris: 1.47 Moz Au, Madrid: 7.66 Moz Au, Boston: 1.56 Moz Au; Sherlock et al., 2012).

The HBGB is dominated by mafic volcanic rocks, with lesser occurrences of ultramafic volcanic and metasedimentary rock units; the presence of rare felsic volcanic rocks in the succession are interpreted as products of arc volcanism (Sherlock et al., 2012). Metamorphism in the belt has not been well documented, although throughout most of the belt rocks display a greenschist-facies mineral assemblage characterized by albite-actinolite-chlorite-epidote-calcite in mafic volcanic rocks (Sherlock et al., 2012). Locally (e.g., near belt margins), metamorphic grade increases to an amphibolite-facies mineral assemblage (Thompson, 1997; Sherlock et al., 2012). At least three episodes of deformation have affected the HBGB, with the second episode ( $D_2$ ) corresponding to the main episode of compressional deformation in the Slave Province constrained to between 2.63 and 2.60 Ga (van Breeman et al., 1992; Sherlock et al., 2012). Throughout the HBGB, pervasive ankerite-ferroan dolomite-sericite-pyrite alteration assemblage is commonly associated with penetrative  $S_2$  fabrics, interpreted to have developed during  $D_2$  deformation. In the Madrid area, iron-bearing carbonate alteration assemblages are overprinted by  $S_2$  fabrics, suggesting an earlier Fe-bearing alteration event occurred in this area (Sherlock et al., 2012). During the third episode of deformation ( $D_3$ ), which is associated with retrograde metamorphism between 2.61 and 2.58 Ga, a transition from purely compressive to more oblique compression occurred, which was responsible for the generation of shear zones ( $< 1$  to 10 m) that display well developed fabrics (Sherlock and Sandeman, 2004; Stemler et al., 2006).

Roughly contemporaneous with the  $D_3$  deformation event, medium-grained, calc-alkaline granitoids (e.g., diorite-tonalite-granodiorite) intruded the western part of the greenstone belt (Padgham and Fyson, 1992; Bleeker and Villeneuve, 1995; Sherlock et al., 2012). Dating constrains these marginal granitoids to between 2.68 Ga (U-Pb zircon crystallization) and 2.56 Ga (K-Ar biotite closure,  $\sim 280^\circ\text{C}$ ; Sherlock et al., 2012). More broadly, in the Slave Province,

including the Bathurst Block, abundant granitoid intrusions (e.g., tonalite-trondhjemite-granodiorite and potassium feldspar granite) occur, with approximately 60% of the area underlain by intrusions < 2.7 Ga old (Pettijohn, 1970; Padgham and Fyson, 1992, van Breeman et al., 1991, 1992; Thompson, 1997). Detailed geochronological studies of these rocks indicate an initial syn-volcanic period from 2695 to 2650 Ma followed by a subsequent period of plutonism that was responsible for ~80% of the presently exposed granitoid intrusions, between 2625 to 2580 Ma (van Breemen et al., 1992). The emplacement of post-deformational intrusions (i.e., post-D<sub>3</sub>; < 2.61 Ga) between approximately 2599 to 2580 Ma, consist of more silicic and meta- to peraluminous granitoids, and are inferred to have a dominantly crustal derivation. These granitoids include muscovite-biotite granites, biotite granites and granodiorites, K-feldspar-rich porphyritic granodiorites, syenogranites, and pegmatitic granite dikes (Davis et al., 1990; van Breemen et al., 1992).

Gold mineralization in the HBGB is generally associated with the contacts between mafic volcanic rock units. This contact-controlled fluid focusing and related alteration, and the formation of auriferous quartz + carbonate ± sulfide veins are inferred to be related to D<sub>2</sub> deformation (Sherlock et al., 2012). In the Boston deposit area of the HBGB, the gold-bearing veins and their associated alteration record the effects of later D<sub>3</sub> deformation, thereby suggesting auriferous vein emplacement occurred at some point between D<sub>2</sub> and D<sub>3</sub> deformation events (Stemler et al., 2006; Sherlock et al., 2012).

The Madrid Deposit (the focus of this detailed study) comprises a group of sub-regions (i.e., mineralized zones; Fig. 2), including Naartok, Rand, Spur, Suluk and Patch. These mineralized zones are hosted in a north-south-striking package of Fe-Ti-rich mafic tholeiitic volcanic rocks

(2.69 Ga; Sherock et al., 2012) intercalated with fine-grained mudstone (i.e., argillites) that display peperitic textures. Bodies of massive quartz-feldspar porphyry containing up to 60 ppb gold (e.g., the 2.686 Ga Wolverine intrusive porphyry; TMAC Resources Core Log Reports, 2014) crosscut and inter-finger with local mafic volcanic rocks and are common in the Patch sub-region (Hebel, 1999; Sherlock et al., 2002). These felsic bodies are interpreted to represent small sub-volcanic intrusions that were likely sourced from a main felsic intrusive stock centered under Wolverine Lake, south-west of Patch Lake (Clow et al., 2013, 2015). The gold mineralization at the Madrid Deposit is described in the following section.

### **2.3.2 Mineralization, vein and alteration characteristics at Madrid**

Gold mineralization in the Madrid Deposit is associated with an array of quartz veins that display laminated to multi-stage brecciation textures (Fig. 3). Depending on the zone, veins cut a variety of lithologies including mafic volcanics, mudstones, and felsic dike rocks. In general, the veins have selvages of sericite-carbonate (ankerite, ferroan dolomite) and, where stockwork-type veins are present, the host rocks are intensely altered to an assemblage of quartz-carbonate-chlorite-albite-sericite-rutile-pyrite. At least two distinct gold mineralization events are present, as suggested by the overprinting of veining events with distinct alteration assemblages (Clow et al., 2013, 2015). For example, in the Naartok sub-region of Madrid, secondary quartz-dolomite veins with a brecciated texture overprint mm- to cm-scale quartz veins that display strong sericite (muscovite-paragonite) and iron-carbonate alteration; gold is observed in both vein styles. Variations in vein density, composition, sulfide content, textures, host rock type, and alteration intensity create a diversity of mineralization styles (Therriault, 2006). In general, the gold mineralization at Madrid is associated with Fe-Ti-rich tholeiitic volcanic rocks and/or intercalated

mudstone units, and is controlled by a large-scale deformation zone, the Madrid Deformation Zone (MDZ), that is implicated as the main fluid “conduit” promoting gold mineralization (Clow et al., 2013; Sherlock et al., 2012).

The MDZ is largely composed of intensely altered and deformed quartz-feldspar phyrlic porphyry, with lesser amounts of mafic volcanics and mudstones recognized (Therriault, 2006). In the MDZ, the intensely altered porphyry is characterized by strongly foliated alternating bands of quartz + ankerite + phyllosilicates (sericite ± chlorite) with ubiquitous disseminated pyrite (Fig. 3A). Geochemical analysis has identified the parent lithology of the MDZ in the south Madrid area as the Wolverine Porphyry, in addition to recognizable lozenge-shaped segments of pink coloured porphyry and mylonitized quartz phenocrysts (Therriault, 2006). The MDZ is interpreted to have been developed as a pre-D<sub>2</sub> fault system that was reactivated at later times during syn- and post-Au mineralization (Sherlock et al., 2003, 2012).

Hydrothermal alteration is complex and is characterized by at least two distinct alteration events. The earlier alteration consists of sericite-carbonate (ankerite, magnesite, ferroan dolomite) assemblages with stockwork quartz-carbonate veinlets (Sherlock et al., 2012), with the most intense alteration characterized by albite-carbonate-quartz-chlorite-rutile-sericite-hematite-pyrite (Therriault, 2006; Shannon, 2008). The later, main auriferous alteration assemblage is characterized by secondary albite and paragonite, with quartz-ankerite stockwork veinlets (Sherlock et al., 2012). Tourmaline is a common alteration mineral in the septa of laminated quartz-carbonate veins in the Patch sub-regions (Sherlock et al., 2002).

Protracted hydrothermal activity is evident by the presence of multiple veining events. Crosscutting relationships and mineralogical variations suggest at least three generations of quartz

veins (e.g., after Therriault, 2006): (i) type 1 veins are the earliest and form as abundant, thin (2-4 mm) quartz-dolomite veins and stockworks that are pre- to syn-D<sub>2</sub> deformation. Pyrite is common in these veins or in their alteration selvages. Fine-grained gold is present in both the veins and as inclusions in pyrite; (ii) type 2 veins occur as pink quartz + ankerite + albite ± hematite veins and stockworks that crosscut, hence post-date, type 1 veins. Type 2 veins contain wall-rock fragments of sericite-ankerite-altered basalt and mudstone. Pyrite and gold are associated with thin vein septa parallel to vein margins; and (iii) type 3 veins are the latest vein stage and consist of white quartz + ankerite veins that crosscut all other vein types and post-date D<sub>2</sub> deformation. In type 3 veins, hematite is common and chalcopyrite and gersdorffite are the main sulfides, with rare pyrite and arsenopyrite. Gold in type 3 veins mainly occurs as inclusions in pyrite and less commonly in late intergrowths with chalcopyrite + gersdorffite that replace or crosscuts pyrite, suggesting gold has been remobilized or additional gold has been introduced into the system (Therriault, 2006).

In the north Madrid sub-regions, which include Naartok, Suluk and Rand, auriferous veins are localized as second and third order splays in the hanging wall of the MDZ. In these zones, type 1 veins are present as stockworks, or less commonly as laminated (Fig. 3B, C) to locally brecciated (Fig. 3D, E) vein types, that are locally overprinted by albitic type 2 veins (Therriault, 2006). These veins are hosted in altered mafic volcanics rocks of the Patch Group (Fe-Ti-rich tholeiitic rocks). Strong silicification, albitization, and brecciation of the host rocks is commonly associated with auriferous veins in the north Madrid sub-regions, and variable degrees of hematite alteration give these veins a salmon-pink colouration. Gold mineralization is typically associated with pyrite such that the highest Au tenors are in units containing over 10 vol % of fine-grained pyrite (Therriault, 2006; Madsen, 2007; Shannon, 2008; Sherlock et al., 2012). Thus, the degree of sulfidation and related replacement of favorable units (e.g., Fe-rich volcanic rocks) appears to correlate with gold

tenor (Sherlock et al., 2012). This gold occurs as: (i) inclusions in sulfide grains (pyrite, chalcopyrite and gersdorffite); (ii) fine grains in type 1 veins; (iii) aggregates in type 2 veins; and (iv) fine grains in altered basalt adjacent to vein margins (Therriault, 2006). In addition, one significant zone of polymetallic Ag-Au-Bi-Te mineralization (Kanosak showing) was located at Naartok East (Fig. 2), proximal to granitic bodies (TMAC Resources Inc., 2014).

In the more sparsely drilled Patch and Wolverine sub-regions of Madrid (Fig. 2), mineralization is contained in narrow, discrete structures. Mineralized veins are hosted in deformed and altered mafic volcanic rocks bounded by steeply dipping porphyry dikes. These mineralized zones lack the sulfidation aspect present elsewhere, and whereas pyrite is the most common sulfide mineral present in the laminated parts of veins, the Au-rich veins are generally pyrite-poor with approximately 2 vol% pyrite (Sherlock et al., 2002). These mineralized veins are characterized by having both laminated and partly brecciated textures. More rarely, mineralized zones also contain narrow (< 1-3 cm wide) stockwork-type veins (Sherlock et al., 2002). Thus, the gold-bearing veins were formed by a combination of crack-seal processes and, where stockwork vein are present, replacement of the host rock adjacent to vein margins. In the Patch 14 sub-region, veins bifurcate and truncate one another, and display boudinaged and open-space infilling textures (TMAC Resources Inc., 2014). High-grade gold mineralization in these zones forms a narrow ore shoot that plunges to the south. In the Patch sub-regions in particular, the presence of overprinting foliation, small-scale folding and multiple generations of crosscutting quartz veins suggests a dynamic history of deformation and fluid infiltration that remains poorly understood (Sherlock et al., 2002; TMAC Resources Inc., 2014).

## **2.4 Methods**

### 2.4.1 Sample collection and vein characterization

From a collection of more than 50 laminated and brecciated vein samples from the exploration drill program of the Madrid deposit (TMAC Resources Incorporated), a subset of 19 samples were selected as being representative of the range in mineralogical, textural, and grade characteristics. These samples were selected from two separate, spatially-related (~17-20 metres apart downhole in drillhole TM00115), sub-parallel quartz-carbonate veins from the South Madrid deposit (Patch 14 sub-region; Sherlock et al., 2002; Sherlock et al., 2012) for detailed comparison. The characteristics of the veins and corresponding samples investigated are as follows: (1) *High-grade vein 115-03*: eight samples (03A to 03H; Fig. 4) were collected from across the 1.75 metre width of a single vein intersected between 408.51 – 410.27 metres in drillhole TM00115. Vein 115-03 displays a bimodal Au-grade distribution across the vein, with reported grades of 1.85 g/t Au (between 408.51 – 409.35 m) and 122 g/t Au (between 409.35 – 410.51 m) with an average of 62 g/t Au across the entire vein (TMAC Resources fire assay data). Importantly, abundant tennantite-tetrahedrite + chalcopyrite + electrum ± Ag-Pb-Au telluride mineralization (abbreviated tn+td+ccp+el±tell) is present in the 409.35 – 410.51 metre interval of this vein; (2) *Low-grade vein 115-02*: 11 samples (02A to 02K; Fig. 4) were collected from across a 2.2 metre vein intersected ~17 metres down the same drill hole as vein 115-03 and was sampled for comparison. This vein was intersected between 427.9 – 430.11 metres and returned assays of 0.76 g/t Au (between 427.9 – 429.01 m) and 1.43 g/t Au (between 429.01 – 430.11 m) with an average of 1 g/t Au (TMAC Resources Inc. fire assay data). This interval had *no* evidence of tn+td+ccp+el±tell mineralization that was identified in the high-grade vein 115-03 noted above. Selected vein material from these intervals were made into polished thin sections and fluid inclusion sections for analysis.

### 2.4.2 SEM-EDS analysis

Ore mineral identification and major element quantification was performed using a TESCAN MIRA 3 LMU Variable Pressure Schottky Field Emission Scanning Electron Microscope (SEM) at Saint Mary's University, Halifax, Nova Scotia, Canada. The SEM is equipped with a back-scattered electron detector coupled with EDS functionality. For the latter, a solid-state, 80 mm<sup>2</sup> X-max Oxford Instruments EDS detector was used. A beam voltage of 20 kV and an approximate working distance of 17 mm was used for all analyses.

### 2.4.3 Fluid inclusion microthermometry

Fluid inclusion microthermometry was performed using a Linkham FTIR600 heating-freezing stage mounted on an Olympus BX51 microscope at Saint Mary's University, Halifax, Nova Scotia, Canada. Calibration of the heating-freezing stage was done using synthetic fluid inclusion standards of pure H<sub>2</sub>O (melting at 0°C and homogenization at the critical point of 374.1°C), and pure CO<sub>2</sub> (melting at -56.6°C; T<sub>mCO<sub>2</sub></sub>). Total uncertainties associated with microthermometric measurements, based on the reproducibility of measurements conducted on reference standards and the measurement precision of the instrumentation, range from ±2 to 3°C for temperatures recorded near the extremes of working conditions for the heating-freezing stage (-190 and 560°C) to ±0.1°C for temperatures near 0°C. In CO<sub>2</sub>-rich inclusions (H<sub>2</sub>O<sub>L</sub>+CO<sub>2L</sub>+CO<sub>2V</sub>), clathrate melting (T<sub>mCLA</sub>) was used to determine salinity based on the methods of Darling (1991) and Diamond (1992). The software packages BULK and ISOC (Bakker, 2003) were used to calculate molar volumes (cm<sup>3</sup>/mol) and isochores, utilizing the calculated salinities, temperatures and modes of total homogenization (Th<sub>TOT</sub>), the homogenization of the CO<sub>2</sub> phase (Th<sub>CO<sub>2</sub></sub>), and the estimated volumetric proportion of the CO<sub>2</sub> phase at Th<sub>CO<sub>2</sub></sub>. In H<sub>2</sub>O-rich inclusions lacking clathrate

nucleation, final ice melting temperatures ( $T_{mICE}$ ) were used to calculate salinities (Bodnar and Vityk, 1994) and isochores were determined using the ISOC software package (Bakker, 2003).

#### **2.4.4 Fluid inclusion decrepitate mound analysis**

Decrepitate mound analysis (evaporate salt mounds liberated from the over-heating of fluid inclusions; e.g., Haynes and Kesler, 1987; Haynes, 1988; Kontak, 1995, 2004) was performed on quartz wafers selected from both high-grade (115-03) and low-grade (115-02) veins. Whether the decrepitate mounds originated from fluid inclusions hosted in quartz-1 or -2 could not be determined using this technique. Seven samples across the high-grade vein (samples 03A, 03B, 03C, 03E, 03F, 03G, 03H) and four samples from across the low-grade vein (samples 02A, 02F, 02H, 02K) were selected for analysis. A total of 247 individual mounds from high-grade vein samples, and a total of 83 individual mounds from low-grade vein samples were analyzed. Quartz wafer preparation was performed by cutting (dental saw) and liberating (solvent bath) quartz chips (approx. 0.5 cm by 0.5 cm) from fluid inclusion sections. The surface of the wafers were cleaned thoroughly using sterile cotton swabs and methanol, and heated to 450°C in a Linkham FTIR600 heating-freezing stage at a rate of 40°C/min to ensure decrepitation of fluid inclusions. After heating, quartz wafers were removed, placed on double-sided carbon tape mounted to a glass slide, and carbon coated for SEM-EDS analysis. The mounds were analysed using either spot (< 5 µm) or raster (> 5 µm) mode depending on size, with count times of 40 seconds. The composition of decrepitate mounds are expressed in atomic % of solute species, determined using a standardless analytical routine with analyses normalized to 100%. Analytical precision is estimated to be within 5-10 atomic % (Haynes and Kesler, 1987; Haynes, 1988). Silicon and O (from quartz substrate) were excluded during normalization. Decrepitated wafers were stored in a desiccation chamber

when not in use. All analyses were performed at Saint Mary's University, Halifax, Nova Scotia, Canada.

#### **2.4.5 Confocal Laser Raman microspectroscopy (LRM)**

Laser Raman microspectroscopy (LRM) was performed to determine the volatile composition of selected fluid inclusions. LRM can identify the presence of trace amounts of gas phases (CO<sub>2</sub>, N<sub>2</sub>, CH<sub>4</sub>, etc.) which are otherwise unidentifiable using microthermometry. LRM analysis was performed using a Horiba Jobin-Yvon LabRam HR confocal instrument at Saint Mary's University, Halifax, Nova Scotia, Canada. The instrument is equipped with a 100mW 532 nm Nd-YAG diode laser (Toptica Photonics) and a Synapse charge-coupled device (CCD; Horiba Jobin-Yvon) detector. Pure silicon was used as a frequency calibration standard. Analyses were performed using a 20-40 micron confocal hole diameter to maximize resolution at depth. A 600 grooves/mm grating (spectral resolution of approximately  $\pm 2 \text{ cm}^{-1}$ ) was used for identification of fluid inclusion-hosted volatile phases. An 1800 grooves/mm grating (spectral resolution of approximately  $\pm 0.5 \text{ cm}^{-1}$ ) was used to accurately determine the fermi diad spacing between the  $\nu_1$  and  $\nu_2$  Raman peaks of CO<sub>2</sub>. The fermi diad spacing was used to determine the density of CO<sub>2</sub> in the vapor phase (e.g., Rosso and Bodnar, 1995; Yamamoto et al., 2003; Yamamoto and Kagi, 2006; Fall et al., 2011 Wang et al., 2011). Spectra were collected using an accumulation of three, 50-60 second acquisitions with a laser spot size of ~1-2 micron at 100% laser power (~2.15 mW at sample surface). Semi-quantitative determination of the relative abundance of inclusion-hosted gas species (in mol %) was performed using the methodology and empirical quantification parameters described by Wopenka and Pasteris (1986, 1987), Dubessy et al. (1989), Burke (2001), and Beeskow et al. (2005). The instrument efficiency factors ( $z$ ) for

CO<sub>2</sub> and CH<sub>4</sub> were determined by comparing CO<sub>2</sub> and CH<sub>4</sub> contents determined by Raman spectroscopy to the results obtained via microthermometric analysis for quartz-hosted CO<sub>2</sub>-CH<sub>4</sub> standard inclusions from the South Wales Coal Field (Beeskov et al., 2005). Instrument efficiencies for other gas species were assumed to be unity in the absence of standards, and results in a slight overestimation of the mole fraction (e.g., N<sub>2</sub>). Uncertainties in the mole fractions of dissolved species in the carbonic phase of the inclusions are estimated to be within 20% relative.

#### **2.4.6 Fluid inclusion laser ablation inductively coupled plasma mass spectrometry (LA-ICP-MS)**

The trace element compositions of fluid inclusions were determined by LA-ICP-MS at the University of Toronto, Department of Earth Sciences. The instrument used was a NWR 193 UC laser ablation system coupled to an Agilent 7900 inductively coupled plasma quadrupole mass spectrometer. Gas flow rates of 1.0l/min (He) and 0.85l/min (Ar) were used, and tuning of the ICP-MS was done by monitoring mass-21/mass-42, ThO/Th, and U/Th ratios in order to maintain an ThO production rate of <0.3% and U/Th ~ 1. Dwell times were set to 10 ms for all masses measured, except for Ag (30 ms) and Au (50 ms). Ablation pit diameter was set to ~5-10 μm wider than the inclusion being ablated. Trace element quantification of fluid inclusions was performed using the software platform SILLIS (Guillong et al. 2008). This involved deconvoluting the mixed inclusion+host signal from the host-only signal after calculation of background corrected count rates for each isotope and quantification of inclusion and host compositions. Analyte sensitivities were calibrated using the reference standard NIST610, ablated at the beginning and end of each block of inclusions. The salinity of the inclusions (in NaCl wt. % equiv.) determined by microthermometry was used for internal standardization.

### **2.4.7 Secondary Ion Mass Spectrometry (SIMS)**

Oxygen isotope ratios ( $^{18}\text{O}/^{16}\text{O}$ ) of quartz were collected using a CAMECA IMS 7f SIMS at the University of Manitoba, Winnipeg, Canada. Analyzed quartz grains were selected from samples 03A and 03G from the high-grade vein (115-03). Analysis was performed on two generations of quartz identified based on their textures and association with mineralization: (i) quartz-1: strained and turbid vein quartz that is of inferred syn-orogenic origin ( $n = 10$ ); and (ii) quartz-2: optically clearer quartz (due to the apparent absence of fluid inclusions) texturally-associated with tectonic mineralization and interpreted as the product of post-orogenic magmatic-hydrothermal activity responsible for vein upgrading ( $n = 13$ ). A cesium ( $\text{Cs}^+$ ) primary beam with a 6.5 nA current was accelerated (+10 kV) onto the sample surface with a sputtering diameter of approximately 25  $\mu\text{m}$ . The instrument employed a 200 V offset voltage, -9 kV secondary accelerating voltage, and a mass resolving factor of 350. For a more detailed description of operating parameters and the techniques used to correct mass fractionation and matrix effects, see Fayek et al. (2002). Grains of University of Wisconsin rose quartz (UWQ-1) with a  $\delta^{18}\text{O}$  value of  $12.3 \pm 0.1 \text{ ‰}$  (Kelley et al., 2007) were used as the standard. Spot-to-spot reproducibility on this quartz standard was consistently between 0.5 to 0.8 ‰. Precision between analyses was 1.2 for  $\delta^{18}\text{O}$ , yielding a  $2\sigma$  error of 1.2 ‰. All isotopic data are presented using  $\delta$ -notation relative to the appropriate standards (V-SMOW for  $^{18}\text{O}/^{16}\text{O}$ ).

### **2.4.8 Hot cathodoluminescence (HCL) imaging of quartz**

Hot cathodoluminescence emission imaging was performed on a polished thin section of selected quartz vein material (samples 03H, 03G, and 02F) in order to provide textural information for discrete quartz generations and quartz growth zones. HCL analysis was performed using a Lumic

HC4-LM hot-cathode cathodoluminescence microscope at Saint Mary's University, Halifax, Nova Scotia, Canada. The cathodoluminescence microscope is coupled to an Olympus BXFM focusing mount with images captured by a Kappa DX40C peltier cooled camera operated using the DX40C-285FW software package. An acceleration voltage between 9.5-11.5 kV, a beam current of 0.25 mA, a filament current of 2.3 A, a deflection of 10 V and a focus of 5.5 V were used during analysis.

#### **2.4.9 Laser ablation inductively coupled plasma mass spectrometry (LA-ICP-MS) trace element mapping of pyrite**

Quantitative elemental distribution maps of pyrite grains were generated by LA-ICP-MS in the Geochemical Fingerprinting Lab at Laurentian University, Sudbury, Ontario, Canada. Maps were acquired using a Resonetics (now Australian Scientific Instruments) RESolution M-50, pulsed (20 s) 193-nm ArF excimer laser ablation microprobe coupled to a Thermo X-Series II Ar plasma quadrupole ICP-MS. A two-volume Laurin Technic sample cell was used, which has very fast washout characteristics (Müller et al., 2009). Elemental maps were acquired by rastering selected pyrite grains with a laser spot size between 8 and 14  $\mu\text{m}$  (depending on the size of the pyrite) at 5  $\mu\text{m}/\text{s}$  with 13  $\mu\text{m}$  offsets between each raster line. Analyses were performed using 10 ms dwell times for each analyte, a laser fluence of 6  $\text{J}/\text{cm}^2$ , and gas flow rates of 0.8 L/min, 0.65 L/min and 6 mL/min for Ar, He and  $\text{N}_2$ , respectively. The calibrations employed NIST SRM 610 external and Fe internal standards.

## **2.5 Results**

### **2.5.1 High- and low-grade veins of the Madrid Deposit**

The style of mineralization at Madrid is different from that of the Doris or Boston deposits. In the northern sub-regions of Madrid (e.g., Rand, Suluk, Naartok; Fig. 2), mineralization is generally characterized by the products of sulfidation reactions (e.g., pyritization) showing replacement of favourable stratigraphic units (e.g., Fe-rich units). In the southern sub-regions of Madrid (e.g., Patch, Wolverine; Fig. 2), mineralization is restricted primarily to sub-parallel quartz-carbonate veins hosted in a zone of intensely altered (carbonatized-sericitized) mafic volcanic rocks and narrow porphyry dikes (Clow et al., 2015). The average gold grades in drilled and assayed “domains” associated with the Madrid deposit are different between northern and southern sub-regions (Fig. 5). Within sub-regions of the deposit, domains refer to individual mineralized bodies or structures defined using a variety of geological data types including surface mapping, cross-section interpretation, structural measurements, core photos, grade continuity in core, and 3D geological modelling. Typically, a domain refers to a specific geological body or structure expressed in industry wireframe models of grade distribution (e.g., fault zone, shear zone, vein, breccia pipe, etc.; Clow et al., 2015). Interpretation of assayed domains shows that the northern Madrid sub-regions contain domains in which average gold grades are < 6 g/t, with only one domain averaging 8.1 g/t Au (n = 93,956 assays in northern sub-regions Suluk, Rand and Naartok). In contrast, domains in the southern Madrid sub-regions display more widely distributed average gold grades, ranging between 1.1 and 26.7 g/t Au (n = 625 assays in southern sub-regions Patch and Wolverine; Fig. 5; Clow et al., 2015).

Quartz-carbonate veins in the Patch sub-regions of Madrid are variable in terms of vein density, sulfide content, texture, and gold grade (< 1 g/t to > 120 g/t). Although diamond drilling operations in the Patch sub-regions of the Madrid deposit remain limited, veins are interpreted to bifurcate and truncate one another and appear to have been formed through a combination of repeated vein

dilation and sealing (i.e., crack-seal) and carbonate-sericite replacement of wall rock (Clow et al., 2015). Drill hole TM00115, which cuts part of this mineralized zone, yielded the best vein intersections available in terms of full vein width recovery and representative gold grade distribution. Veins 115-03 and 115-02, which were intersected in drill hole TM00115, were sampled as representative for the purpose of understanding gold mineralization in these quartz-carbonate-dominated veins. The sampled veins, 115-03 and 115-02, are spatially-related (~17 meters apart in same drill hole) yet display contrasting gold grades (~1 g/t vs. ~62 g/t average Au, respectively, over vein width). Veins were selected primarily on grade contrast and not on the basis of other features in order to eliminate any bias toward geological characteristics (e.g., texture, composition, structure) that may be related to the primary gold mineralization or subsequent upgrading.

#### *2.5.1.1 Textural comparison of high- and low-grade veins*

The high-grade (115-03) and low-grade (115-02) veins showed no apparent textural differences in drill core. However, contrasting textural features are evident when observed using a petrographic microscope with the high-grade vein showing distinct domains of secondary quartz (quartz-2) associated with intergrowths of tennantite-tetrahedrite + chalcopyrite + electrum ± Ag-Pb-Au telluride mineralization (Fig. 6A); in addition, veinlets of secondary quartz commonly crosscut turbid primary vein quartz (quartz-1) (Fig. 6B). The turbidity of quartz-1 is due to the abundance of fluid inclusions and fluid inclusion decrepitate textures. In contrast, the clarity of quartz-2 is attributed to the relative absence of fluid inclusions relative to quartz-1. Quartz-1 from both high- and low-grade veins shows evidence of strain (i.e., undulose extinction) and is locally recrystallized. In the high-grade vein, fibrous to comb-textured grains (cf., Dong et al., 1995;

Moncada et al., 2012) of quartz-1 terminate at the margins of carbonate-filled and tnd+ccp+el±tell-mineralized cavities. The termini of quartz-1 grains are overgrown by euhedral crystals of quartz-2 that protrude into the cavities (Fig. 6C). The carbonate-filled cavities appear to represent variably continuous ‘veinlets’ that crosscut quartz and carbonate grains (i.e., yellow dashed lines in Fig. 6C). Fibrous-textured quartz and euhedral quartz-lined cavities were not identified in the low-grade vein. In the high-grade vein, fractures extending away from carbonate-filled veinlets crosscut carbonate and quartz grains (Fig. 6D); this textural feature was not observed in samples from the low-grade part of the vein.

#### *2.5.1.2 Comparison of the ore mineralogy of the high- and low-grade veins*

High-grade and low-grade veins both contain gold mineralization consisting of Ag-bearing gold (electrum) inclusions in the cores of pyrite grains (Fig. 7A), in fractures within early quartz-1 (Fig. 7B, C), along quartz-carbonate grain boundaries, along carbonate + sericite + rutile ± chlorite septa margins, and in alteration haloes in wall rocks at vein margins. The abundance of electrum in these textural associations is similar in high- and low-grade veins. However, high-grade and low-grade veins have significantly different gold grades due to contrasting abundances of electrum (much higher in high-grade veins) and Au-bearing tellurides (auriferous-hessite  $[Au_xAg_{2-x}Te]$ , petzite  $[Ag_3AuTe_2]$ ) intergrown with tennantite-tetrahedrite + chalcopyrite (only present in high-grade veins; Fig. 7D, E, F). The relative abundances of these minerals, as determined by semi-quantitative SEM observation (i.e., grain counting and grain size to produce an approximate modal abundance), is shown in Figure 4 and a list of ore minerals and their elemental compositions, determined by SEM-EDS, is shown in Table 1.

The high-grade vein displays a bimodal gold distribution across the vein, with 1.85 g/t Au between 408.51 – 409.35 m and 122 g/t Au between 409.35 – 410.51 m; the overall average of this intersection is 62 g/t Au. In the high-grade vein interval between 409.35 and 410.51 m, the ore mineralogy is significantly more complex than in the gold-poorer interval between 408.51 – 409.35 m. Aggregates of anhedral to subhedral grains of chalcopyrite and scheelite are abundant in quartz and in pyrite-apatite-bearing septa and their margins. In the high-grade vein, the following mineral intergrowths were observed: (i) abundant fracture/cavity-infilling intergrowths of sulfosalts (tennantite-tetrahedrite  $\pm$  gersdorffite) + chalcopyrite + electrum  $\pm$  Ag-Pb-Au tellurides  $\pm$  clausthalite (PbSe), that are associated with secondary domains of optically-clearer quartz-2 enclosed within primary quartz-1 (Figs. 6A, 7D, E, F); (ii) telluride-dominated intergrowths of hessite (Ag<sub>2</sub>Te) + altaite (PbTe)  $\pm$  petzite  $\pm$  auriferous-hessite intergrown with quartz-2 or as inclusions or fracture-infillings in pyrite (Fig. 7G, H); and (iii) minor occurrences of Fe-poor sphalerite (< 1 at. % Fe) + galena  $\pm$  chalcopyrite  $\pm$  tennantite-tetrahedrite that occur as cavity-infilling intergrowths (Fig. 7I), with sphalerite displaying sporadic chalcopyrite disease. Additionally, fractures extending away from carbonate-filled veinlets (Fig. 6D) are common in the high-grade vein and contain pyrite and barite, with trace native silver.

The low-grade vein displays more uniform gold grades across the vein with values of 0.76 g/t Au between 427.9 – 429.01 m and 1.43 g/t Au between 429.01 – 430.11 m, with an overall average of 1 g/t Au. Across the *entire* low-grade vein, and in the high-grade vein interval between 408.51 and 409.35 metres (grading 1.85 g/t), gold grade is controlled mainly by electrum abundance. In the Au-poor region of the high-grade vein, minor chalcopyrite, pyrite, gersdorffite, and subordinate arsenopyrite, galena, Fe-poor sphalerite, and tennantite-tetrahedrite occur along septa margins and quartz-carbonate grain boundaries; telluride and selenide minerals are absent in this interval of the

high-grade vein. In all low-grade vein samples, arsenopyrite, tennantite-tetrahedrite, and selenide minerals were not observed. Trace amounts of tellurides (altaite and hessite) and chalcopyrite occur in the low-grade vein as small inclusions ( $< 10 \mu\text{m}$ ) in pyrite.

Pyrite is significantly more abundant in the low-grade vein than in the high-grade vein. It occurs in the low-grade vein as disseminations or grain aggregates in wall rock fragments and in septa or septa margins. The As content of pyrite in the low-grade vein varies between 0.73 and 1.64 wt. %. In the high-grade vein, pyrite grains are subhedral and commonly zoned with sieve-textured cores (py-1) and clear, sieve-free As-rich rims (py-2) containing between 0.69 and 2.45 wt. % As (Fig. 7G). Sieve-textured pyrite is rarer in the low-grade versus the high-grade vein samples. In addition, pyrite in the low-grade vein contains mineral inclusions of quartz, sericite and ferroan dolomite, and subordinate rutile and chlorite. Chlorite inclusions are absent from pyrite in the high-grade vein but quartz, sericite and rutile inclusions are common.

The atomic percent of Au in electrum varies depending on its occurrence. For example, electrum in quartz-1 averages 89.8 at. % Au (87.4 – 99.0 at. %; Ag-balance;  $n = 8$ ), whereas where it occurs with the assemblage  $\text{tn}+\text{td}+\text{ccp}+\text{el}+\text{tell}$  associated with quartz-2 in the high-grade vein, it averages 80.7 at. % Au (43.4 – 88.5 at. %; Ag-balance;  $n = 15$ ). In contrast, electrum present as inclusions in pyrite in both vein types, although more common in the high-grade vein, averages 77.7 at. % Au (67.2 – 88.2 at. %; Ag-balance;  $n = 12$ ).

### *2.5.1.3 Wall-rock alteration mineralogy*

In both the high- and low-grade veins, vein septa and wall-rock fragments display a similar alteration mineralogy dominated by sericite (muscovite-paragonite), carbonate (ankerite, ferroan

dolomite), pyrite and rutile, with trace to minor monazite and minor apatite in septa of the high-grade vein. SEM-EDS analysis of very fine-grained areas in septa from the low-grade vein shows elevated Mg and Fe contents, in addition to Si, K and Al, and is therefore interpreted as fine-grained sericite-chlorite-quartz intergrowths. Alteration halos around quartz-carbonate veins display intense foliation that is characterized by alternating mm- to cm-scale bands of sericite ± chlorite and quartz + carbonate ± albite, and which extend up to 3 metres into the country rocks. The mafic volcanic host rock displays a propylitic-like alteration, characterized by the assemblage albite + chlorite + carbonate + pyrite + rutile.

## **2.5.2 Ore fluid characteristics**

### *2.5.2.1 Fluid inclusion types*

In high- and low-grade veins, six fluid inclusion types are recognized based on petrographic and microthermometric characteristics. The features of the inclusions are summarized in Table 2, representative images shown in Figures 8 and a summary of the different inclusion types presented in Figure 9. Fluid inclusion types have been designated as distinct from one another based on composition and phases present at room temperature (21°C). Note that use of the subscript CO<sub>2</sub> for the carbonic phase does not preclude the presence of minor CH<sub>4</sub> and N<sub>2</sub>. Using the criteria of Goldstein and Reynolds (1994) and Bodnar (2003), the fluid inclusions are classified in the context of fluid inclusion assemblages (FIA) by establishing the relative timing of entrapment (i.e., primary versus secondary) for small groups of texturally coeval inclusions. The microthermometric data is presented in Table EA 2-1 (Electronic Appendix).

The fluid inclusion types identified, with compositional information described in the following section, are as follows:

(i) Type 1: Three-phase aqueous-carbonic ( $L_{\text{aq}} + L_{\text{CO}_2} + V_{\text{CO}_2}$ )  $\text{H}_2\text{O-NaCl-CO}_2 \pm \text{CH}_4 \pm \text{N}_2$  inclusions with a carbonic phase volume % between 10 and 30 (i.e., vapor  $\pm$  liquid  $\text{CO}_2$ ), salinity between 2.8 and 7.5 wt. % NaCl equiv., and  $X_{\text{CO}_2}$  of  $0.076 \pm 0.026$ . These inclusions are present in both the high- and low-grade veins.

(ii) Type 2a: Two-phase carbonic-dominated ( $L_{\text{aq}} + L_{\text{CO}_2}$ )  $\text{CO}_2 \pm \text{CH}_4 \pm \text{N}_2 + \text{H}_2\text{O-NaCl}$  inclusions with a carbonic phase volume % between 70 and 90, salinity between 2.1 and 7.2 wt. % NaCl equiv., and  $X_{\text{CO}_2}$  of  $0.52 \pm 0.14$ . These inclusions are present in both the high- and low-grade veins.

(iii) Type 2b: Mono-phase carbonic-dominated ( $L_{\text{CO}_2} \pm V_{\text{CO}_2}$ )  $\text{CO}_2 \pm \text{CH}_4 \pm \text{N}_2$  inclusions lacking a visible  $\text{H}_2\text{O}$  phase at  $21^\circ\text{C}$  (i.e.,  $X_{\text{CO}_2} \sim 1$ ). These inclusions are present in both the high- and low-grade veins, but microthermometric data are not available.

(iv) Type 3a: Two-phase aqueous-dominated ( $L_{\text{aq}} + V_{\text{CO}_2}$ )  $\text{H}_2\text{O-NaCl} + \text{CO}_2 \pm \text{CH}_4 \pm \text{N}_2$  inclusions with a vapor phase volume % between 5 and 10, salinity between 3.0 and 9.7 wt. % NaCl equiv., and  $X_{\text{CO}_2}$  of  $0.041 \pm 0.009$ . These inclusions are present in both the high- and low-grade veins.

(v) Type 3b: Two-phase aqueous-dominated ( $L_{\text{aq}} + V_{\text{CO}_2}$ )  $\text{H}_2\text{O-NaCl} + \text{CO}_2$  inclusions with a vapor phase volume % between 5 and 15, and salinity between 13.8 and 19.6 wt. % NaCl equiv. Only trace amounts of low density  $\text{CO}_2$  is present in the vapor phase and could not be quantified by microthermometric or LRM techniques. These inclusions are present in *only* the high-grade vein.

(vi) Type 3c: Two-phase aqueous-dominated ( $L_{aq} + V_{aq}$ )  $H_2O$ -NaCl inclusions with a vapor phase volume % between 2 and 5, salinity between 19.6 and 24.2 wt. % NaCl equiv., and  $X_{CO_2} = 0$ . These inclusions are present in both the high- and low-grade veins.

In general, types 1, 2 and 3a inclusions are more abundant and better preserved (i.e., lower extent of decrepitation) in the low-grade vein samples than in high-grade samples. Type 1 inclusions most often occur as FIA of indeterminate origin in the cores of quartz grains (Fig. 8A, B, C) or less commonly on secondary planes, which are more frequent in the low-grade vein relative to the high-grade vein. Type 2a inclusions are present as FIA in secondary planes or in clusters of indeterminate origin (Figs. 8D, E). Type 2b inclusions are present in both low- and high-grade veins as FIA of indeterminate origin along quartz grain boundaries, in decrepitate halos and clusters, and rarely in secondary planes. Whereas types 3a and 3b inclusions are common, type 3c are rare. Type 3a and 3c inclusions are present in *both* the low-grade and high-grade vein as FIA in secondary planes, or as clusters of indeterminate origin in quartz-1 (Fig. 8F, G). Type 3b inclusions are common in secondary planes in quartz-2, and as inclusions in the cores of euhedral quartz crystals interpreted as having a primary origin (cf., Roedder; 1984). The host quartz crystals line the walls/margins of carbonate-filled cavities and veinlets (Fig. 8H, I) in high-grade veins. Planes of secondary origin host type 3b inclusions in quartz-1 (Fig. 8J), but are less abundant than type 3a inclusions in quartz-1. Type 3c inclusions are a late-stage inclusion type, and are present along secondary planes crosscutting quartz grain boundaries within both high- and low-grade veins (Fig. 8K). Their relationship to other inclusion types are unknown.

### 2.5.2.2 Fluid inclusion microthermometry and laser Raman microspectroscopy

Type 1 aqueous-carbonic inclusions (n = 50; 11 FIA) yielded the following data: (1) The melting point of the carbonic phase ( $T_{mCO_2}$ ) is between -57.2 to -56.1°C. Values lower than -56.6°C may be the result of a combination of cumulative measurement uncertainties or the presence of minor concentrations of other compounds that depress the CO<sub>2</sub> melting temperature. Values above -56.6°C are the result of cumulative measurement uncertainty. Measurement uncertainty for measurements around -56.6°C is  $\pm 0.4^\circ\text{C}$ ; (2) homogenization of CO<sub>2</sub> ( $T_{hCO_2}$ ) occurs via vapor bubble disappearance ( $L_{aq} + L_{CO_2} + V_{CO_2} \rightarrow L_{aq} + L_{CO_2}$ ), or by a transition to a critical phase, between 18.7 and 31.1°C; and (3) total homogenization ( $T_{hTOT}$ ;  $L_{aq} + L_{CO_2} \rightarrow L$ ) is between 194 and 318°C with the maximum variability within single FIA of 36°C. It is noted that 20 of the 50 inclusions measured decrepitated before total homogenization. The salinity of the inclusions, based on clathrate melting between 5.9 and 8.9°C, is between 2.8 and 7.5 wt. % NaCl equivalent. The calculated bulk densities of type 1 inclusions ranged from 0.84 to 1.00 g/cc and the average  $X_{CO_2}$  is  $0.076 \pm 0.026$  ( $1\sigma$ ; n = 38). The presence of trace to minor CH<sub>4</sub> and N<sub>2</sub> was confirmed by LRM.

Type 2 CO<sub>2</sub>-rich inclusions are classified into subtypes 2a and 2b based on the presence or absence of H<sub>2</sub>O at room temperature, respectively; whereas type 2a inclusions are rare, type 2b are common. Similar to type 1 inclusions, microthermometry of type 2a inclusions indicate near pure CO<sub>2</sub> based on  $T_{mCO_2}$  values between -56.8 to -56.1°C. Homogenization of CO<sub>2</sub> occurs via vapor bubble disappearance between 11.3 and 29.7°C, and total homogenization between 238 and 319°C, with the maximum variation within a single FIA of 27°C. The salinity of the aqueous phase in type 2a inclusions, based on clathrate melting between 7.3 and 8.5°C, corresponds to between 2.1 and 7.2 wt. % NaCl equiv. Calculated bulk densities of type 2a inclusions range from 0.72 to 0.89 g/cc,

and their average  $X_{\text{CO}_2}$  is  $0.52 \pm 0.14$  ( $1\sigma$ ;  $n = 12$ ). Similar to type 1 inclusions, the presence of trace to minor  $\text{CH}_4$  and  $\text{N}_2$  in the vapor phase was confirmed by LRM.

Type 3  $\text{H}_2\text{O}$ -rich inclusions are classified into three subtypes. Type 3 inclusion subtypes are petrographically similar and are further distinguished using compositional data from microthermometric and LRM analyses. Specifically, type 3 inclusion subtypes are differentiated in part based on the presence of dissolved gases, as determined by LRM, the vol. % of the phases present at  $21^\circ\text{C}$ , and measured  $\text{Th}_{\text{TOT}}$  and salinity (Fig. 10). Type 3a inclusions were too small to observe final  $\text{CO}_2$  melting accurately, however LRM data confirms the vapor phase in these inclusions is dominated by  $\text{CO}_2$  with a density between 0.18 and 0.58 g/cc; in addition,  $< 0.8$  mol %  $\text{N}_2$  and  $< 0.5$  mol %  $\text{CH}_4$  ( $n = 3$ ) are present in the vapor phase. The salinity of these inclusions, as determined by final ice melting ( $\text{T}_{\text{MICE}}$ ), is 3.0 to 9.7 wt. % NaCl equiv. ( $n = 56$ ; Fig. 10A). Total homogenization occurred between  $156$  and  $291^\circ\text{C}$ , with the maximum variation for a single FIA of  $\sim 25^\circ\text{C}$  (Fig. 10B). Type 3b inclusions lack  $\text{N}_2$  based on LRM and the  $\text{CO}_2$  component is low density ( $\leq 0.18$  g/cc;  $n = 15$ ). In the vapor phase of five type 3b inclusions, trace  $\text{N}_2$  was also detected using LRM with an additional two outliers having anomalous  $\text{N}_2$  (1.8 mol %) and  $\text{CH}_4$  (4.1 mol %) values. The salinity of these inclusions is between 13.8 and 19.6 wt. % NaCl equiv. ( $n = 119$ ; Fig. 10A) and their total homogenization occurred between  $84$  and  $200^\circ\text{C}$ , with the maximum variation in a single FIA of  $\sim 25^\circ\text{C}$  (Fig. 10B). Type 3c inclusions are aqueous-only and, based on LRM, lack volatile species ( $\text{CO}_2$ ,  $\text{CH}_4$ ,  $\text{N}_2$ ;  $n = 2$ ). The salinity of these inclusions is between 19.6 and 24.2 wt. % NaCl equiv ( $n = 16$ ; Fig. 10A) and total homogenization occurred between  $93$  and  $136^\circ\text{C}$ , with the maximum variation in a single FIA of  $\sim 13^\circ\text{C}$  (Fig. 10B). A complete data set of all microthermometric and LRM analyses can be found in Tables EA 2-1 and EA 2-2 (Electronic Appendix), respectively.

### 2.5.2.3 Fluid inclusion decrepitate mound analysis

Analysis of decrepitate mounds (i.e., mounds of fluid inclusion solute salts remaining after decrepitation and devolatilization), present as discrete clusters or defining trails (Fig. 11A, B), from selected samples across high- and low-grade veins indicates the presence of three fluid types based on their chemistry (Fig. 11C, D): (i) a Na+Cl - rich endmember lacking F; (ii) a Na+Ca+Mg+Cl type also lacking F but with variable contents of Ca+Mg (up to 59 at. %); and (iii) a Na+K+Cl+F - bearing fluid with elevated F values (expressed as at. % F/Cl; Table EA 2-3; Fig. 4). The maximum F/Cl values in mounds from the high- and low-grade veins are 4 and 0.3, respectively. In the high-grade vein, decrepitate mounds with elevated F/Cl values have only low amounts of Ca ( $3.1 \pm 2$  at. %;  $n = 18$ ) and no Mg (Fig. 11E, F). However, in the low-grade vein the mounds with elevated F/Cl ratios are significantly more enriched in Ca and Mg and average  $10.6 \pm 4.6$  and  $1.8 \pm 1.5$  at. % ( $n = 12$ ), respectively (Fig. 11G, H). Also, more F-bearing mounds were identified in high-grade vein samples ( $n = 45$ ; 18% of total) compared to the low-grade vein ( $n = 10$ ; 12% of total). In addition, all except one of the identified F-bearing decrepitate mounds were found in those parts of the high-grade vein hosting the assemblage  $tn\text{-}td\text{+}ccp\text{+}el\pm tell$  and type 3b inclusions. Some mounds from the high-grade ( $n = 18$ ) and low-grade vein ( $n = 12$ ) also contain minor S, with values up to 3.5 at. % and 1 at. %, respectively. Potassium was identified in 17 mounds from the high-grade vein ( $< 12.6$  at. % K; ~7% of total mounds analyzed) and in only 2 mounds from the low-grade vein ( $< 2.5$  at. % K; ~2% of total mounds analyzed). Potassium was detected in approximately 50% of the F-bearing mounds from the high-grade vein. Iron was detected ( $< 1.4$  at. %) in only four mounds from the low-grade vein. No instances of transition metals (e.g., Ni, Co, Cr) were noted. A complete data set of all decrepitate mound analyses can be found in Table EA 2-3.

#### 2.5.2.4 Fluid inclusion LA-ICP-MS

Preliminary LA-ICP-MS analyses of type 3b inclusions were obtained; type 1 and 3a inclusions from the high-grade vein were too small, or their salinity too low, to provide sufficient fluid mass to analyze. Analysis of type 3b fluid inclusions detected As-Sb-Zn-Pb-Cs-Ba-Sr-Rb in the fluid (Fig. 12; Table EA 2-4 in Electronic Appendix). In type 3b inclusions, As, Sb, Zn, and Pb concentrations average 519, 38, 294, and 76 ppm, respectively, whereas Sr, Cs, Ba, and Rb contents average 1090, 35, 343, and 6.7 ppm, respectively. The concentration of Ca and Mg average 13200 and 720 ppm, respectively. The ore metals Au, Ag, Cu, Bi, and Te were not detected in any of the analyzed inclusions (average detection limits of 10, 21, 74, 10 and 172 for Au, Ag, Cu, Bi and Te, respectively).

#### 2.5.2.5 Oxygen isotopes by SIMS

Oxygen isotope compositions were obtained on orogenic quartz-1 and secondary quartz-2 (Fig. 13) and the complete data set is presented in Table EA 2-5. Quartz-1 has  $\delta^{18}\text{O}_{\text{qtz}}$  values ranging from +14.9 to +19.6‰ (n = 10), which compare to quartz-2  $\delta^{18}\text{O}$  values of +12.8 to +17.7‰ (n = 13), hence overlap in their  $\delta^{18}\text{O}$  values. Both quartz types displayed considerable heterogeneity at the sample scale, with quartz-2  $\delta^{18}\text{O}$  values varying by as much as 5‰ in the same sample, and quartz-1  $\delta^{18}\text{O}$  values varying by as much as 4‰.

### 2.5.3 Trace element abundances as correlations in vein-hosted pyrite

Three hydrothermal pyrite grains were mapped using LA-ICP-MS: two grains from a high-grade vein (samples 03D and 03F; Figs. 14, 15), and one grain from a low-grade vein (sample 02F; Fig.

16). Trace element zonation in pyrite is variable with both oscillatory and complex patterns present but, regardless of the type of zoning, consistent elemental associations are present.

The pyrite from the high-grade vein show variable enrichment of As-Ni-Co in the core and rim zones. Elements such as Au-Ag-Te-Bi-Pb occur in the core zones, but shows a very irregular and variable distribution relative to As-Ni-Co. The rim zones are enriched in Au-Ag-Te-Sb-Bi-Pb-Cu-W, and late fractures are enriched in Bi-Pb-Te-Sb-Ag relative to the core zones (e.g., in sample 03D; Fig. 14).

The core zone in pyrite from the low-grade vein is enriched in As-Au relative to the rim zones, with a more variable enrichment of Te-Pb-Se present. Growth zones outside of the core are depleted in both Au and As relative to the core zone. The rim zones of the pyrite show variable enrichment of Te-Pb-Sb-Ag-Ni-Co with elevated Ag-Cu-W in late fractures.

The chemical data shown in pyrite maps were extracted as a large series of ablation time-series data points with each ablation pit and associated measurement representing a single pyrite quantitative analysis (see Gourcerol et al. [2018] for detailed discussion). This allowed a direct comparison of trace elements to be made via bivariate plots (Fig. 17). Several key relationships between Au and other trace elements are recognized. It is evident that Au in pyrite from the high-grade vein increases in abundance with increasing Bi+Te+W (Fig. 17A), but with no clear correlation between Au and As (As vs Au  $r^2 = 0.0005$ ; Fig. 17B). In contrast, Au in pyrite from the low-grade vein correlates well with As rather than Bi+Te+W (As vs Au  $r^2 = 0.482$ ; Fig. 17C, D). Also, maximum Au and Bi+Te+W abundances (in ppm) in pyrite from the high-grade vein samples are up to an order of magnitude higher than Au and Bi+Te+W abundances in pyrite from the low-grade vein (e.g., high-grade vein pyrite [sample 03F]:  $Au_{\max} = 6771$  ppm,  $[Bi+Te+W]_{\max} = 14520$

ppm; low-grade vein pyrite [sample 02F]:  $Au_{\max} = 354$  ppm,  $[Bi+Te+W]_{\max} = 1387$  ppm). In pyrite from the high-grade vein, micro- to nano-scale inclusions of Au, and Au-Ag-tellurides are inferred to be abundant as suggested by numerous data points at or above the Au saturation line in the As versus Au bivariate plot (~70 out of 3678 total analysis points in pyrite; Fig. 17B; see Reich et al., 2005). In contrast, significantly fewer data points plot above the Au saturation line in low-grade vein pyrite (7 out of 9865 total analysis points in pyrite).

Principle components analysis (PCA) was performed on all time-series data points from pyrite laser maps from both veins in order to determine elemental correlations. Principle component analysis allows for the visualization of multi-dimensional (multi-elemental) data onto particularly useful planes by identifying orthogonal directions in the data that produce maximum variance (i.e., linear combinations; see Winderbaum et al., 2012). Each PCA plot (using PAST Software: Hammer, Ø., Natural History Museum, University of Oslo; Figs. 14, 15, 16) was generated using principle components two and three (out of 16 components; i.e., the number of elements considered for statistical treatment). Principle component two accounted for 10 to 13.9% of the total variance, and principle component three accounted for 8 to 11% of the total variance observed in the trace element data. Principal component analysis confirms a strong correlation between Au and As in the low-grade vein pyrite, whereas Au is strongly correlated with Ag-Te-(±Sb) rather than with As in the high-grade vein pyrite grains. Principal component analysis confirms a Bi-Pb-Zn(±As-Cu) correlation, and the decoupling of Ni-Co from As-Au-Ag-Te-Sb-Bi-Pb-Cu in both veins.

## **2.6 Discussion**

### **2.6.1 Evidence for secondary magmatic-hydrothermal upgrading of gold grades in Madrid**

### *2.6.1.1 Sulfosalt mineralization and quartz vein textures*

It is well documented that orogenic gold deposits (OGD) host diverse metal (i.e. Au-Ag ± As ± Bi ± Sb ± Te ± W ± Sn) and ore mineral assemblages, which has led to considerable confusion in distinguishing OGD from intrusion-related gold deposits (IRGD; Sillitoe and Thompson, 1998; Goldfarb et al., 2000, 2005; Hart et al., 2002; Groves et al., 2003; Hart and Goldfarb, 2005; Hart, 2007). Archean OGD and younger (typically Phanerozoic) IRGD share common characteristics, including a commonly post-peak metamorphic timing of hydrothermal gold enrichment, thermal equilibrium with wallrocks, an aqueous-carbonic ore-fluid bulk composition of low- to moderate salinity, and depths of formation ranging widely between 3 and 20 km (Colvine et al., 1988; Groves et al., 1998; Goldfarb et al., 2001, 2005; Hart, 2007; Mériaud and Jébrak, 2017). Prograde metamorphism of crustal rocks in orogenic settings produces aqueous-carbonic fluids with variable metal tenors that reflect the composition of the crustal rocks metamorphosed/devolatilized (Pitcairn et al., 2006; Goldfarb and Groves, 2015). Therefore, classifying such gold deposits using mineralogical data in isolation may be misleading. Interpretation in a broader, vein-scale context utilizing a range of data types is required in order to identify the commonly cryptic evidence for upgrading by late-stage magmatic-hydrothermal processes.

Veins in the Patch 14 sub-region of the Madrid deposit show evidence of primary gold enrichment by orogenic aqueous-carbonic ore fluids (e.g., free gold inclusions in type 1 fluid inclusion-bearing quartz-1). However, secondary gold enrichment (upgrading) by late-stage hydrothermal fluids is also evident, which has resulting in the bimodality of gold grades observed in high-grade veins (Fig. 4), an observation that may be extrapolated to explain contrasting grade distributions in the north and south Madrid domains. Primary orogenic gold mineralization is characterized by the

occurrence of electrum with an average Au content of ~90 at. %. This style of mineralization is observed in the studied low-grade vein and a portion of the high-grade vein (1.85 g/t). The occurrence of primary electrum as inclusions in pyrite (Fig. 7A), in quartz-1 (Fig. 7B, C), and along quartz-carbonate grain boundaries and septa margins is consistent with observations from other auriferous OGD (e.g., Neyedley et al., 2017). In the region of the high-grade vein with grades  $\leq 122$  g/t Au, texturally-late (secondary relative to primary electrum) sulfosalt-bearing assemblages of tennantite-tetrahedrite + chalcopyrite + electrum [~80 at. % Au] + Ag-Pb-Au tellurides  $\pm$  clausthalite in quartz (Fig. 7D, E, F), as well as assemblages of Fe-poor sphalerite + galena  $\pm$  chalcopyrite are observed. These secondary gold-bearing assemblages represent the products of an upgrading event. Although scarce, observations of sulfosalt mineralization have been reported in orogenic settings with equivocal origins (e.g., Kerrich and Watson, 1984; Bateman and Hagemann, 2004; Tomkins et al., 2004; Lawrence et al., 2013). However, similar sulfosalt-bearing assemblages to those identified in the high-grade vein share similarities with mineralization characteristic of 'transitional' Cu-Au-porphyry (Maydagan et al., 2013; LeFort et al., 2014), intermediate- to high-sulfidation epithermal (Hedenquist et al., 2000; Ruano et al., 2000; Taylor, 2007), and reduced IRG systems (Pantleyev, 1986, 1991; Lang and Baker, 2001; Hart, 2007). For instance, intermediate-sulfidation epithermal-style mineralization is characterized by the association of chalcopyrite, tennantite-tetrahedrite and Fe-poor sphalerite, with a lack of appreciable quantities of arsenopyrite and pyrrhotite (Hart, 2007). Additionally, in many ORG settings, Pb and Zn mineralization is generally absent, with Pb and Zn enrichment commonly not exceeding average crustal values (Kerrich and Fryer, 1981; Phillips and Powell, 2010; Goldfarb and Groves, 2015; Fusswinkel et al., 2017). Conversely, Pb and Zn mineralization is common in magmatic-hydrothermal systems and is often associated with late hydrothermal activity that has

generated Ag-rich galena- and sphalerite-bearing quartz-carbonate veins (Lang and Baker, 2001; Hart, 2007). Assemblages of scheelite + chalcopyrite, tn+td+ccp+el±tell, and sphalerite + galena ± chalcopyrite in the same vein setting may represent a ‘telescoping’ of intrusion-related mineralization, that is common to evolving systems associated with cooling source intrusions (e.g., RIRGS in the Tintina Gold Belt; Lang and Baker, 2001; Hart et al., 2002; Hart, 2007).

At the Madrid deposit, telluride minerals are abundant in high-grade veins as telluride inclusions (mainly altaite and hessite) in sieve-textured pyrite (pyrite-1) which suggests an initial cogenetic deposition. However, tellurides and electrum precipitation must have continued after pyrite mineralization since they occur as fracture-infillings in pyrite in addition to occurring along growth zones that rim sieve-textured cores (e.g., associated with pyrite-2; Fig. 7G). Telluride minerals are commonly considered to be associated with magmatic settings (Afifi et al., 1988, Bowell and Foster, 1990; Spooner, 1993), such as intermediate- to high-sulfidation epithermal systems (Fulignati and Sbrana, 1998; Pals et al., 2003) and IRG deposits in both Phanerozoic (e.g., Mao et al., 2003; Hart, 2007; Cook et al., 2009) and Archean (e.g., Robert 2001; de Sousa et al., 2015; Mériaud and Jébrak, 2017) settings. However, telluride minerals are also common in OGD (Kontak and Smith, 1993; Large et al., 2009, 2011; Ciobanu et al., 2010; Neyedley et al., 2017); hence, their presence is not necessarily discriminatory. In the latter setting, their presence is often attributed to: (i) primary enrichment by a metamorphic ore fluid, (ii) concentration by remobilized low-temperature polymetallic melts (Tomkins and Mavrogenes, 2002; Tomkins et al., 2004; Ciobanu et al., 2006; Cook et al., 2009), or (iii) release of Te (with Au, Pb, Cu, and Zn) into a hydrothermal fluid during pyrite recrystallization (Large et al., 2009). Despite this, the occurrence of a tn+td+ccp+el±tell assemblage, such as that identified in the high-grade vein at Madrid, has not

been reported in an unequivocal OGD, to the best of our knowledge, and thus may suggest that a metalliferous hydrothermal fluid overprint was responsible for gold upgrading at Madrid.

Following on the above interpretation, the temperature of the associated hydrothermal event responsible for late-stage gold enrichment can be approximated from the ore mineral assemblages (Fig. 19). In telluride-dominated intergrowths of altaite (PbTe) + hessite (Ag<sub>2</sub>Te) + electrum + chalcopyrite + gersdorffite ± petzite (Ag<sub>3</sub>AuTe<sub>2</sub>) ± auriferous-hessite associated with quartz-2 (Fig. 7H), the assemblage of petzite + β-hessite + gold has been shown through X-ray power diffraction of experimental run products (Legendre et al., 1980) to be stable below ~313°C, confirmed through observations in natural assemblages (Bortnikov et al., 1988). Above ~313°C, petzite is absent from the assemblage. Furthermore, the Ag content of gold/electrum (~20 at. % Ag) in petzite constrains an equilibrium assemblage to ~250°C (Legendre et al., 1980; Bortnikov et al., 1988), whereas end-member gersdorffite constrains formation to < 300°C, as the Fe-Ni-Co content of hydrothermal glaucodot-gersdorffite is temperature sensitive (Klemm, 1965).

Distinct textural and paragenetic evidence should be preserved in the vein quartz if pre-existing orogenic veins were subsequently cut and upgraded by a later hydrothermal fluid event. Quartz-carbonate veins in the Patch sub-regions locally display hydrothermal breccias and open-space textures (Sherlock et al., 2002; Madsen et al., 2007; Shannon, 2008), but such features are not exclusively observed in vein systems formed at shallow crustal levels (e.g., epizonal settings; Bateman and Hagemann, 2004; Moncada et al., 2012). Albeit controversial, similar vein textures are reported in systems interpreted to have formed at mesozonal crustal levels (e.g., Campbell and Dickenson mines, Red Lake: MacGeehan and Hodgson, 1982; Hodgson, 1989, Golden Mile: Bateman and Hagemann, 2004, Pampalo: Fusswinkel et al., 2017). However, the origin of fluids

in these systems, their exact crustal level of formation, and the questionable magmatic contributions remains equivocal. That such open-space textures are particularly abundant in the high-grade vein studied is therefore of significance. Comb-textured quartz, characteristic of growth into open space (e.g., Adams, 1920; Moncada et al., 2012), is abundant and shows quartz fibers often terminating as euhedral crystals at the margins of variably mineralized, carbonate-filled cavities (Fig. 6C).

The application of hot cathodoluminescence (CL) imaging suggests that multiple overprinting processes affected veins in the Patch 14 sub-region of Madrid. The images reveal that the majority of quartz displays a consistent dull brown-red to brown-purple luminescence with no evidence of zoning (Fig. 18). Although data for such veins is sparse, this luminescence is apparently more characteristic of orogenic-type vein quartz at  $> 300^{\circ}\text{C}$  (e.g. Rice Lake orogenic gold setting; Neyedley et al., 2017; see Fig. 18A, B). In addition, the uniform nature of the CL images suggests a non-fluctuating fluid composition and temperature during the orogenic stage of vein crystallization (cf., Ioannou et al., 2004). In areas where the high-grade vein displays the  $\text{tn}+\text{td}+\text{ccp}+\text{el}\pm\text{tell}$  assemblage, and in some cases where it is lacking, quartz displays distinctly different luminescence colours including deep purples, light blues and pale yellow-greens, and is often marked by short lived ( $< 30$  s) blue CL (Fig. 18C, D). In certain areas, the CL variation seems to delineate quartz growth zones, which are not evident in either polarized or cross-polarized light (Fig. 18E, F). Magmatic-hydrothermal quartz displays a variety of CL colors with distinct zonation. Studies of the CL characteristics of quartz from a variety of settings have concluded that the CL color may reflect the temperature of precipitation; quartz formed at  $> 400^{\circ}\text{C}$  tends to result in a homogenous blue CL color, whereas at temperatures  $< 300^{\circ}\text{C}$ , CL zoning is commonly observed with zones displaying blue to yellow CL colors (Boggs et al., 2002; Ioannou et al., 2003;

Rusk et al., 2008; Götze, 2009). The short-lived blue CL, noted in both synthetic and natural hydrothermal quartz (Götze, 2001, 2009), has also been attributed to local hydrothermal overprinting (Ioannou et al., 2004). Therefore, based on CL characteristics, it is evident a distinct quartz-precipitating hydrothermal event is recorded in veins at the Patch 14 sub-region of Madrid. Furthermore, it is unlikely that the blue to yellow CL colors reflect deformation/recrystallization processes as quartz growth zones are preserved (Fig. 18F) and CL zonation does not appear to correspond with recrystallization textures.

#### *2.6.1.2 Pyrite trace element chemistry*

Grain-scale trace element variability between hydrothermal pyrite grains from the low- and high-grade veins has been characterized and their patterns and enrichments are distinctly different. Comparing the chemistry of pyrite from both veins, a number of contrasting features are identified:

1. The rims of pyrite hosted in the high-grade vein are enriched in Au-Ag-Te-Sb-Bi-Pb-Cu-W, whereas fractures have elevated Bi-Pb-Te-Sb-Ag (Figs. 14, 15). In contrast, pyrite from the low-grade vein are Au-depleted and show a different metal enrichment compared to pyrite hosted by the high-grade vein (Fig. 16).
2. The time-series data (Fig. 17) confirms a positive correlation between As and Au ( $r^2 = 0.482$ ) in pyrite from the low-grade vein, which is a common elemental coupling in orogenic systems (Reich et al., 2005; Large et al., 2009; Gourcerol et al., 2018a, 2018b). Pyrite from the high-grade vein does not show any As-Au correlation ( $r^2 = 0.0005$ ).
3. Pyrite from the high-grade vein contains an order of magnitude more Te and electrum micro-inclusions, as represented by many data points located above the Au saturation line (after Reich et al., 2005), than the low-grade vein.

4. Gold in pyrite from the high-grade vein shows a correlation with Bi+Te+W, with the highest Au values corresponding to elevated  $\Sigma\text{Bi+Te+W}$ . The correlation between Au with  $\Sigma\text{Bi+Te+W}\pm\text{As}$  is a common feature of many RIRG systems that often contain low- to intermediate-sulfidation quartz veins (Hart, 2007). For instance, in the Fort Knox and Clear Creek deposits, Au is poorly correlated with As, but strongly correlated with Bi and Te and with W-Mo-Sb to a lesser degree (Marsh et al., 1999; Hart, 2007).

5. The PCA confirms that Au is strongly coupled with As and decoupled from Te-Ag-Bi-W-Pb-Cu-Zn in pyrite from the low-grade vein. Conversely, in pyrite from the high-grade vein, Au is strongly coupled with Te-Ag-(Sb) and is weakly associated with, or decoupled from, As.

Pyrite trace element data provide further evidence of an overprinting hydrothermal event involving secondary Au-Ag-Te-Sb-Bi-Pb-(Cu-W) enrichment in high-grade veins. This enrichment is lacking in pyrite from low-grade veins, suggesting: (i) upgrading fluids could not structurally access all parts of the deposit resulting in uneven secondary gold enrichment; or (ii) upgrading fluids accessed low-grade veins, but did not modify pyrite composition or precipitate secondary electrum and other accessory minerals.

### *2.6.1.3 Ore fluid geochemistry and isotopic evidence*

#### *2.6.1.3.1 Significance and textural relationship of fluid inclusion types*

Several fluid types are identified in the mineralized veins studied, as summarized in Table 2 and Figure 9. Discussed in sequence below are the PTX conditions attributed to the entrapment of these fluids and their order of entrapment. In order to constrain the latter, we integrate the timing of fluid entrapment, as constrained from petrographic observations, and their respective P-T conditions, as

in some cases the fluids may represent complementary pairs due to fluid unmixing. In this context, the order of fluid entrapment is: 1) type 1 as part of orogenic vein formation, with lesser types 2a and 3a due to unmixing of the type 1 fluid evidenced by consistent vapour phase composition, aqueous phase salinity and total homogenization temperatures between type 3a and 2a inclusions; 2) type 3b during formation of the high-grade gold assemblage, which reflects ingress of a later fluid; and 3) type 3c, which represents a much later stage barren fluid event. Note that the type 2b fluid, while ubiquitous, is not discussed as its occurrence is highly variable in both veins (e.g., in indeterminate clusters, secondary trails, along grain boundaries, and as neonates in decrepitate haloes), and they often show evidence of significant post-entrapment modification (e.g., highly misshapen, variable CO<sub>2</sub> density).

Low-salinity (2.8 to 7.5 wt. % equiv. NaCl), aqueous-carbonic fluids ( $X_{\text{CO}_2} = 0.076 \pm 0.026$ ) trapped in type 1 inclusions in the high-grade and low-grade veins from the Patch 14 sub-region of Madrid are the earliest preserved fluids and are consistent with those identified in many orogenic gold systems (cf., summary by Bodnar et al., 2014). The textural associations of gold with quartz-1 and along the margins of laminations/septa are consistent with gold precipitation during repeated faulting and hydrothermal vein resealing (Robert and Kelly, 1987; Sibson et al., 1988; Robert et al., 1995; Wilson et al., 2009). Transient fluid pressure fluctuations, which contribute to vein formation (i.e., “fault valve” model; Sibson et al., 1988; Robert et al., 1995), may also result in the unmixing of a primary H<sub>2</sub>O-NaCl-CO<sub>2</sub> ± CH<sub>4</sub> hydrothermal fluid, depending on appropriate PTX conditions, which yields aqueous- and carbonic-dominated fluid endmembers (Naden and Caulfield, 1989; Diamond, 2003). The latter process is important, as, during unmixing, soluble gold bisulfide complexes (e.g., AuHS<sup>0</sup><sub>(aq)</sub> and Au(HS)<sub>2</sub><sup>-</sup><sub>(aq)</sub>) are destabilized, which promotes gold

precipitation (Huang et al., 1985; Naden and Shepherd, 1989; Stefánsson and Seward, 2004; Williams-Jones et al., 2009).

Petrographic evidence documenting the coeval entrapment of unmixed aqueous and carbonic fluid endmembers in single FIA is rare in the literature (e.g., Robert et al., 1995). The low probability of aqueous and carbonic fluid co-entrapment is likely a result of the different wetting properties of aqueous- and carbonic-dominant fluids (e.g., Neyedley et al., 2017), as well as post-entrapment modification of the host quartz and fluid inclusions. However, evidence for the entrapment of fluid endmembers in coevally healed fractures has been identified (cf., Shelton et al., 2004). In high- and low-grade veins, type 2a and 3a inclusion types are interpreted to represent the carbonic- and aqueous-dominant endmembers, respectively, of fluid unmixing from a parental  $\text{H}_2\text{O-NaCl-CO}_2 \pm \text{CH}_4$  fluid. Comparison of the bulk salinity and aqueous phase salinity of type 1 and type 3a fluid inclusions show that, although type 3a inclusions have a higher bulk salinity than type 1 inclusions ( $0.04 \pm 0.02$  and  $0.027 \pm 0.008 X_{\text{NaCl}}$ , respectively), these inclusion types share identical aqueous phase salinity ( $4.6 \pm 1.6$  and  $4.6 \pm 1.3$  wt. % NaCl equiv., respectively) (Table 2). This can be explained by fluid unmixing resulting from pressure fluctuations during vein formation. Upon unmixing of a single phase  $\text{H}_2\text{O-NaCl-CO}_2$  fluid (i.e., type 1) to produce immiscible  $\text{CO}_2\text{-(H}_2\text{O-NaCl)}$  (i.e., type 2a) and  $\text{H}_2\text{O-NaCl-(CO}_2)$  (i.e., type 3a) end-members, the aqueous-dominant end-member should have a higher bulk salinity than the parental fluid owing to the differential partitioning of  $\text{H}_2\text{O}$  and  $\text{NaCl}$  between these end-members (with  $\text{NaCl}$  preferentially partitioned into the aqueous phase; Takenouchi and Kennedy, 1965; Gehrig et al., 1980; Schmidt and Bodnar, 2000; Diamond, 2003). This compositional data, together with the petrographic relations observed between type 1, type 2a and type 3a inclusions, suggests that type 2a and type 3a could be the unmixed products from a parental type 1 fluid.

In addition, H<sub>2</sub>O-NaCl inclusions with salinities up to 15 wt. % NaCl equivalent with very low CO<sub>2</sub> contents have been reported in orogenic deposits and are interpreted to represent the product of boiling of a low-salinity, low-CO<sub>2</sub> aqueous fluid (Bodnar et al., 2014). Petrographically, type 1 inclusions occur as clusters in quartz-1 (Fig. 8B, C; Fig. 9) and more rarely in secondary planes with carbonic phase volume % ranging between 10 to 30. However, the volume % can vary significantly and is interpreted to be the result of post-entrapment modification of type 1 inclusions through preferential water leakage (e.g., Bakker and Jansen, 1991). This interpretation is consistent with the presence of locally intense deformation of the host quartz, as evidenced by undulose extinction and recrystallization textures in both high- and low-grade veins. Thus, despite some post-entrapment modification, these inclusions are interpreted to represent the primary auriferous orogenic ore fluid that provided the original gold mineralization in both the low- and high-grade veins (Fig. 7A, B, C). Combining the H<sub>2</sub>O-NaCl-CO<sub>2</sub> solvi of Gehring (1980) with isochores for type 1 inclusions (Fig. 19), minimum P-T conditions of > 260°C at > 1 kbar for entrapment are suggested. That the isochores for type 1 inclusions show a ~3 kbar range at constant temperature of entrapment suggests the orogenic quartz veins in the Patch 14 sub-region were emplaced under widely fluctuating fluid pressure (cf., Kontak and Tuba, 2017).

Petrographic and microthermometric evidence for boiling is absent from the high-grade parts of the high-grade vein and a fluid of intermediate-salinity (16.7 ± 1.2 wt. % NaCl equiv.) is present, as represented by type 3b inclusions. This fluid is compositionally distinct and temporally late compared to the earlier fluid, represented by type 1 inclusions and its unmixed counterparts. Importantly, type 3b inclusions are only present in the high-grade vein in secondary planes that extend from texturally-late sulfosalt-bearing assemblages (Fig. 8H), and in the cores of euhedral quartz crystals that post-date orogenic-type vein deformation (Fig. 8I). Isochores for type 3b

inclusions overlap with the isochores for type 1 inclusions above  $\sim 300^{\circ}\text{C}$ , however, mineralogy constrains type 3b fluids to  $\leq 250$  to  $300^{\circ}\text{C}$  and therefore types 1 and 3b fluids cannot have coexisted in P-T space.

The low-temperature, high-salinity fluid trapped in type 3c fluid inclusions along secondary planes (Fig. 8K) is interpreted to represent the late infiltration of basement brine that is unrelated to mineralization and postdates all other fluid inclusion types (e.g., Robert et al., 1995). The consistently low  $T_{h(\text{final})}$  ( $109 \pm 13^{\circ}\text{C}$ ) and moderate salinities (20.9 to 24.2 wt. % NaCl equiv.) suggest it is distinct from the fluid trapped in type 3b inclusions. This fluid is similar to Canadian Shield basement brines identified at several other Archean deposits in Canada (Frape et al., 1984; Frape and Fritz, 1987; Kyser and Kerrich, 1990; Boullier et al., 1998; Neyedley et al., 2017; Rezeau et al., 2017). Similarly, in the Boston deposit of the HBGB, approximately 70 km south of Madrid, moderate- to high-salinity aqueous fluids ( $> 20.8$  wt. % NaCl equiv.) were identified and interpreted as representing the infiltration of late barren basement brines unrelated to gold mineralization (Stemler et al., 2006).

#### 2.6.1.3.2 Compositional differences between hydrothermal fluid generations

Fluid inclusion-specific compositional differences have been identified based on microthermometry, LRM, decrepitate mound chemistry, and LA-ICP-MS analysis. These data indicate very distinct fluid events and implicate a late metalliferous magmatic-hydrothermal fluid that is responsible for upgrading of gold in the Patch 14 sub-region of the Madrid deposit. These different methods and their implications are discussed below.

While type 1 and 2 inclusions can be distinguished using a variety of petrographic and microthermometric criteria alone, the aqueous-dominated type 3a, 3b, and 3c inclusions appear similar at room temperature in terms of their phase ratios and require careful microthermometric determination of salinities and LRM analysis of vapor compositions to differentiate them from one another. Fluid inclusion-specific LRM confirms the vapor phases of types 3a, 3b and 3c inclusions are compositionally distinct (Table EA 2-2). The H<sub>2</sub>O-dominated type 3a inclusions have a vapor phase rich in CO<sub>2</sub> ( $\pm$ CH<sub>4</sub> $\pm$ N<sub>2</sub>) and intermediate CO<sub>2</sub> density (0.18 to 0.58 g/cm<sup>3</sup>); it is interpreted to originate from unmixing of a parental aqueous-carbonic orogenic fluid (see above). Although showing similar phase ratios as type 3a inclusions, the vapor phase in type 3b inclusions is significantly different with only minor low-density CO<sub>2</sub> (0.17 to 0.18 g/cm<sup>3</sup>), if present at all, and generally devoid of CH<sub>4</sub> and N<sub>2</sub>. The presence of CO<sub>2</sub> is often interpreted as evidence of an orogenic origin for fluids and host veins, with a source related to metamorphism of deep crustal rocks (e.g., Ridley and Diamond, 2000; Goldfarb et al., 2005). However, it is also possible to produce magmatic fluids with appreciable levels of CO<sub>2</sub> in a variety of settings, such as IRG deposits (e.g., Burrows and Spooner, 1984, 1987; McCoy et al., 1997; Sillitoe and Thompson, 1998) porphyry Cu-Mo deposits (Rusk et al., 2008, Mao et al. 2017), W skarns (Mathieson and Clark 1984), and LCT-type pegmatites (Thomas and Spooner, 1992). There is therefore confusion between ORG fluids and fluids generated via magmatic processes, such as in IRG systems. The presence of CO<sub>2</sub> in early type 1 inclusions, and its unmixed counterpart (type 3a), does not therefore differentiate between a metamorphic or magmatic origin. In contrast, type 3b inclusions contain a vapor phase lacking appreciable CO<sub>2</sub>, and devoid of CH<sub>4</sub>, and N<sub>2</sub>. To further differentiate the origins of these fluids, additional geochemical data are explored and integrated below.

The presence of at least three distinct fluids is supported by the chemistry of the decrepitate mounds produced from across the widths of the high-grade and low-grade veins. Decrepitate mounds rich in F are abundant in the high-grade vein, particularly in the vein interval displaying significant tn-td+ccp+el±tell mineralization (Fig. 11F). Although F-enriched mounds were also identified in low-grade vein samples, they are both less abundant and relatively depleted in F, and instead have more Ca+Mg than mounds in the high-grade vein samples (Fig. 11C). This may be a result of type 3b and 3c fluids sharing common fracture planes and co-precipitating their solute load on the quartz surface during decrepitation, or may represent a non-mineralizing Na+Ca+Mg+F+Cl-bearing fluid not identified in the high-grade vein. The former argument is favored due to the lack of fluid inclusion data to support the presence of a unique fluid in the low-grade vein samples. The detection of K in high-grade vein samples is coincident with F-enrichment in approximately 50% of analyzed mounds, and suggests that a fluid variably enriched in Na+Ca+K+Cl+F infiltrated the vein system. Fluorine- and K-enriched fluids are a common feature in evolving magmatic-hydrothermal ore systems, including Cu±Au porphyry (Munoz and Swenson, 1981; Selby and Nesbitt, 2000), IRG (Coulson et al., 2001) and epithermal systems (Richards and Kerrich, 1993; Fulignati and Sbrana, 1998).

Laser ablation ICP-MS analysis of type 3b fluid inclusions indicate enrichment in As-Sb-Fe-Zn-Pb-Cs-Ba-Sr-Rb (Fig. 12A). By comparison, ore fluids associated with OGD are typically depleted in base metals, including Fe, Zn and Pb (Fusswinkel et al., 2017), resulting in the absence of Pb and Zn sulfide mineralization often noted in these settings (Kerrich and Fryer, 1981; Phillips and Powell, 2010; Goldfarb and Groves, 2015). Type 3b inclusions contain Zn and Pb concentrations (294 and 76 ppm, respectively) that are 4-5 orders of magnitude higher than those reported in Au-rich OGD fluids (e.g., Pampalo OGD: 0.17 ppm Au; Fusswinkel et al., 2017). Lead and Zn-

enrichment in the high-grade veins at Madrid is therefore consistent with the presence of galena and sphalerite mineralization (Fig. 7I). Furthermore, the Pb-Zn-As-Sb concentrations are similar to those measured in porphyry-epithermal magmatic-hydrothermal fluids (e.g., 100s to 1000s ppm; Heinrich et al., 1999; Ulrich et al., 1999; Rusk et al., 2004; Yardley, 2005, 2013; Audétat et al., 2008; Williams-Jones et al., 2010), and the high concentrations of Sr, Cs, Ba and Rb in type 3b fluids similarly suggest a magmatic origin (cf., Audétat et al., 1998; Heinrich et al., 1999; Landtwing et al., 2010; Large et al., 2016).

#### 2.6.1.3.3 $\delta^{18}\text{O}$ of vein-forming fluids

The temperature of quartz-1 formation, based on type 1 fluid inclusion microthermometric constraints, was estimated to be between  $\sim 230\text{-}290^\circ\text{C}$  (i.e.,  $\pm 1\sigma$  from average  $T_{\text{TOT}}$  of  $258^\circ\text{C}$ ) and infers a  $\delta^{18}\text{O}_{\text{H}_2\text{O}}$  value for the vein fluid of between 4.5 to 12.4‰, calculated using the equation of Matsuhisa et al. (1979). However, the temperature range determined using the final homogenization temperatures of fluid inclusions represents a minimum, and thus a fluid possessing  $\delta^{18}\text{O}_{\text{H}_2\text{O}}$  values  $> 12.4\text{‰}$  is possible (Fig. 13). This range is slightly lower than that of orogenic lode gold systems of all ages (i.e., 12 to 18‰; Kerrich, 1987; McCuaig and Kerrich, 1998; Jia et al., 2001). In contrast, using a temperature range of  $\sim 120\text{-}310^\circ\text{C}$  for the later quartz-2 that is associated with high-grade gold mineralization, constrained by type 3b fluid inclusion microthermometry and mineral equilibria, the range in  $\delta^{18}\text{O}_{\text{H}_2\text{O}}$  for this fluid is between -5.5 and 11.8‰. The ranges in  $\delta^{18}\text{O}_{\text{H}_2\text{O}}$  for fluids crystallizing both quartz-1 and -2 overlap considerably within the magmatic field, with quartz-2 extending into the meteoric field at lower temperatures (Fig. 13). Previous  $\delta^{18}\text{O}$  work at the Boston deposit, 70 km south of Madrid, by Stemler et al. (2006) indicate that orogenic vein quartz and carbonate from the orogenic-type veins were co-

precipitated from a fluid with  $\delta^{18}\text{O}_{\text{H}_2\text{O}}$  between 6 and 9‰ at 320°C, based on fluid inclusion microthermometry of aqueous-carbonic inclusions analogous to the type 1 inclusions identified in this study. However, this work was performed on vein separates (not in situ) and may represent a bulk  $\delta^{18}\text{O}$  value from multiple quartz generations.

Although a magmatic source is proposed for the fluid associated with late upgrading and the precipitation of quartz-2, its O-isotopic composition could have been modified by re-equilibration with country rock and during fluid-vein interactions, especially during periods marked by low water-rock ratios. Mixing of an initially heavy,  $^{18}\text{O}$ -rich fluid with a lighter,  $^{18}\text{O}$ -depleted fluid (e.g., meteoric or sea water) would satisfactorily account for the range in  $\delta^{18}\text{O}$  observed in quartz-2 (cf., Hagemann et al., 1994). Furthermore, the mixing of a magmatic-hydrothermal fluid with cooler meteoric waters may represent a viable precipitation mechanism for tn+td+ccp+el±tell mineralization in textural equilibrium with quartz-2. However, the absence of evidence for fluid mixing in the fluid inclusion record (e.g., mixing trends in fluid inclusion temperature-salinity plots and highly variable  $X_{\text{CO}_2}$ ; Wilkinson, 2001; Kontak et al., 2011; Marsala et al., 2015) precludes this scenario. Additionally, despite the overlap between quartz-1 and quartz-2  $\delta^{18}\text{O}$  values, there is no evidence for a significant component of meteoric water involved in the formation of quartz-1 or 2 ( $\leq 0\%$ ; Craig, 1961; Emsbo et al., 2003; Menzies et al., 2014) in the Patch 14 sub-region of the Madrid Deposit.

## **2.6.2 Overprinting of orogenic gold mineralization by magmatic-hydrothermal fluid assemblages**

It has been widely suggested (cf., review by Groves and Goldfarb, 2015) that OGD fluids are most commonly the product of devolatilization of crustal rocks via prograde metamorphism. Associated

mobilization of Au and other metals (e.g., Ag, Te, Sb, As, W) likely occurs during either devolatilization of metal-enriched source rocks or during subsequent scavenging of metals elsewhere in the crust through which metamorphic fluids migrate. Whereas mineralizing fluids are most often generated due to large-scale collisional tectonic processes, deeper sources, such as the metasomatized sublithospheric mantle (Bierlein et al., 2006; Groves and Santosh, 2016), have also been considered as potential fluid and metal reservoirs. The fluids forming OGD are composed of S-bearing, low-salinity, aqueous-carbonic fluids with the related gold mineralization forming over a large range in pressure, ranging from deep in the crust in ductile shear settings to shallower and more brittle regions. The latter has been encapsulated as the crustal continuum model first proposed by Groves (1993) and Groves et al. (1998) and subsequently widely promoted (Ridley and Diamond, 2000; Goldfarb et al., 2005; Elmer et al., 2006; Pitcairn et al., 2006; Phillips and Powell, 2010; Kolb et al., 2015). However, significant deficiencies remain in the context of the crustal continuum framework. For example, for deposits hosted in high metamorphic grade domains, such as at Hemlo, Canada (Phillips, 1985; Kuhns et al., 1994; Lin, 2001) and Challenger, Australia (Tomkins and Mavrogenes, 2002), it has been noted that this model does not adequately account for the nature and origin of the fluid, gold transportation, and metal deposition (Phillips and Powell, 2009). In addition, unusual ore mineral assemblages, some textures, fluid inclusion characteristics, and zones of metal enrichment, have all been cited as evidence for either multiple gold events or gold remobilization (Hughes et al., 1997; Ridley and Diamond, 2000; Morey et al., 2008; Oberthur and Weiser, 2008; Ciobanu et al., 2009; Lawrence et al., 2011; MacFarlane et al., 2011; Molnar et al., 2016; Rezeau et al., 2017).

Despite extensive research on OGD, including a profusion of fluid inclusion and stable isotope (S, O, C, D) data, conclusions regarding the geochemical nature of the mineralizing fluid remain

equivocal (Goldfarb and Groves, 2015). The aqueous-carbonic bulk composition of the ore fluid with an  $X_{\text{CO}_2} = 0.1 - 0.15$ , a  $\delta^{18}\text{O}$  composition of 6 to 13‰, a low- to moderately salinity (3 to 13 wt. % NaCl equiv.), P-T conditions of ~250-350°C and 1-3 kbar, and a diversity of observed metal associations (Au ± As, Ag, Bi, Cu, Pb, Zn, Sb, Te, and W) equally describe causative fluids in both OGD (McCuaig and Kerrich, 1998; Ridley and Diamond, 2000; Goldfarb et al., 2005; Bodnar et al., 2014) and IRG (Thompson et al., 1999; Lang and Baker, 2001; Hart, 2007) systems. Similarly, in many cases, the styles of the gold mineralization (e.g., disseminated, replacement, and/or as structurally-controlled vein arrays) are shared by both deposit types. At shallow crustal levels ( $\leq 1.5$  km), epithermal deposits form vein and disseminated ore that is dominated by precious metals (Au, Ag), with variable amounts of Cu, As, Sb, Pb, Zn, Bi, Hg, W, Te, and Se that are sourced from, and/or mobilized by, magmatic fluids with variable salinities and  $\text{CO}_2$  contents (Taylor 2007; White et al., 1995). There are sufficient geochemical similarities among gold deposits with dissimilar origins that broad generalizations regarding their origins, without supporting evidence, can potentially lead to misclassification. Deposit classification is made more complex where overprinting due to either protracted magmatic-hydrothermal activity or where reactivation of structures occurs, resulting in the ingress of later fluids. Such scenarios have been suggested for many gold deposits including Malartic, Canada (Helt et al., 2014; de Sousa et al., 2017), Jiaodong Peninsula deposits, China (Wang et al., 1998), Donlin Creek, Alaska (Goldfarb et al., 2004), and Hemlo, Canada (Tomkins and Mavrogenes, 2002).

Not unlike the aforementioned gold deposits, the hydrothermal activity in the Madrid region was protracted and complex, as evidenced by several generations of auriferous veins that display textural and fluid characteristics of both OGD and IRG systems. Early orogenic gold mineralization in the Patch 14 sub-region of Madrid is characterized by electrum mineralization in

quartz-1 that is hosted in laminated quartz-carbonate veins that were emplaced approximately during D<sub>2</sub> deformation. Low-salinity, aqueous-carbonic fluid (type 1 inclusions) and the unmixed aqueous- and carbonic-rich endmembers thereof (type 3a and 2a inclusions) are inferred to have been associated with primary orogenic gold precipitation that resulted from fluid unmixing during transient fluid pressure fluctuations. Later re-activation of pre-existing orogenic vein structures allowed for the infiltration of an aqueous-dominant, magmatic-hydrothermal fluid of intermediate salinity (type 3b inclusions), enriched in Au-Ag-As-Sb-Te-Pb-Zn-Cu-Bi-Se into the Patch 14 sub-region of the Madrid deposit (Fig. 20). Although several lines of evidence for a late hydrothermal gold upgrading event are presented, it is still unclear whether the metals have a direct (e.g., concentrated in fluid exsolved from a cooling intrusion), or indirect origin (e.g., leaching and remobilization of metals from ‘proto-ore’ from deeper in the crust).

The role of early-stage magmatic-hydrothermal processes in the generation of pre-orogenic proto-ores have been reported in the Yilgarn Craton (Boddington deposit: Mole et al., 2013; The Golden Mile: Bateman and Hagemann, 2004), the West African Craton (Morila deposit: MacFarlane et al., 2011), the Fennoscandian Shield (Pampalo deposit: Molnár et al., 2016) and the Abitibi Greenstone Belt (Wasamac deposit: Mériaud and Jébrak, 2017), and lend evidence to the importance of early intrusion-related processes in enhancing later orogenic gold endowment. Conversely, evidence of syn- to post-orogenic upgrading/overprinting by magmatic-hydrothermal processes has also been identified in various deposits of the Abitibi Greenstone Belt (Lac Herbin deposit; Rezeau et al., 2017), the Harare-Bindura-Shamva greenstone belt (Viceroy Deposit; Oberthür and Weiser, 2008), the Loulo Mining District of Mali (Lawrence et al., 2011), and in the Yilgarn Craton (Boorara and Bardoc shear system deposits; Morey et al., 2008). Thus, the overprinting of earlier auriferous mineralized systems by a later fluid event at Madrid is not

without precedent in the geological record. Therefore, the relevant question is perhaps not how, but in fact, how often does this process of magmatic-hydrothermal upgrading occur?

### **2.6.3 Potential fluid sources and implications for orogenic vein upgrading by magmatic-hydrothermal fluids at Hope Bay**

Aqueous, variably CO<sub>2</sub>-bearing fluids of intermediate- to high salinity, similar to type 3b inclusion fluids, have been documented in porphyry-epithermal and intrusion-related deposits. It has also been noted that gold concentrations in warm (i.e., ~150°C), S-bearing, low- to intermediate salinity magmatic fluids can be orders of magnitude higher than those found in active geothermal waters of meteoric origin (Brown, 1986; Heinrich et al., 2004). It is possible that secondary gold-bearing assemblages at Madrid were formed from a low-temperature sulfosalt melt or metal-enriched fluid formed through syn- to post-orogenic dissolution-recrystallization processes or the breakdown of pre-existing sulfide minerals (e.g., pyrite, arsenopyrite; Tomkins and Mavrogenes, 2002; Large et al., 2011; Meriaud and Jebrak, 2017). Gold remobilization at Madrid by circulating meteoric fluids in zones of high heat flow (e.g., Carlin-type: Ilchik and Barton, 1997; Emsbo et al., 2003) is not supported by oxygen isotope or fluid inclusion evidence from vein quartz.

Speculating on the source of type 3b fluid, it is necessary to consider the plutonic environment surrounding the HBGB and of the Slave Province, in which the HBGB is hosted. A proximal source for magmatic-hydrothermal fluid in the Madrid region would be a homogenous quartz-feldspar porphyritic dacite intrusion (Wolverine porphyry) that cross-cuts pillowed basalts in the region and is identical in age to the north-south trending epiclastic volcanic rocks of the Windy felsic suite (age of  $2684.2 \pm 3.6$  Ma; Sherlock et al., 2012). Relative to the surrounding tholeiitic host rocks, the Windy felsic suite (and the contemporaneous Wolverine porphyry) is

approximately an order of magnitude more enriched in Sr, Ba, Cs, and Rb (bulk rock assay: Windy Felsic Suite [median, ppm] – Sr = 210, Ba = 329, Cs = 1.2, Rb = 37.1; Patch tholeiitic rocks [median, ppm] – Sr = 88.4, Ba = 31, Cs = 0.1, Rb = 3; Sherlock et al., 2012) and contains anomalous whole rock gold values (5 to 60 ppb; Clow et al., 2013, 2015). Thus, the Wolverine Porphyry seems like a plausible source of the LILE-rich fluid considered responsible for secondary gold upgrading, and represented by the type 3b fluid inclusions in high-grade veins. However, the mineralized structures at Madrid are mainly D<sub>2</sub>-related and formed between 2.63 to 2.58 Ga (i.e., constrained by D<sub>2</sub> and D<sub>3</sub> episodes; Sherlock et al., 2012). Mineralized veins at Madrid are hosted by second and third order splays off the Madrid Deformation Zone (MDZ), which apparently truncates the Wolverine porphyry on its west-most margin (Fig. 2). Therefore, considering crosscutting relationships and absolute age constraints, it would seem that overprinting/upgrading by magmatic-hydrothermal fluids sourced from the Wolverine porphyry is unlikely. The HBGB is host to a variety of other marginal granitoid intrusions and felsic volcanics of dacitic composition with calc-alkaline geochemical affinities that were emplaced during the D<sub>3</sub> deformation event between 2.679 – 2.560 Ga, and that may be suitable causative intrusions for late fluids (Sherlock et al., 2012). Alternatively, granitoid intrusion(s) from which the upgrading metalliferous fluids were sourced may not be expressed at surface.

A more distal late fluid source must also be considered. It has been noted that basement rocks and volcanic-turbiditic assemblages in the Slave Province are heavily intruded and crosscut by various late-orogenic granitic plutonic complexes (Henderson, 1985; King et al., 1992; van Breeman et al., 1992; Bleeker and Hall, 2007; Ernst and Bleeker, 2010). A period of plutonism between 2.65 – 2.58 Ga, broadly contemporaneous with the D<sub>3</sub> deformation episode affecting the HBGB, involved the widespread emplacement of granitoid intrusions (i.e., granite “blooms”) that, at

present erosional levels, underlie approximately 60% of the Province (Padgham and Fyson, 1992; van Breeman et al., 1991, 1992). This period of active plutonism is concurrent with the Pan-Slave tectono-thermal event, which was responsible for widespread calc-alkaline magmatism that has been attributed to zones of underthrusting during basin closure in the eastern Slave Province, and is responsible for pluton emplacement along crustal basement fracture systems (i.e., Andino-type tectonic regime; Pitcher, 1979; Fyson and Helmstaedt, 1988; Abraham et al., 1994). After basin closure, the locus of subduction and its associated calc-alkaline magmatism, shifted westward across the Slave Province (Fyson and Helmstaedt, 1988). A variety of granitoid bodies have been identified in the Slave Province with ages that correspond to the Pan-Slave tectono-thermal event, including but not limited to: (i) unfoliated K-feldspar megacrystic granodiorite and granite and two-mica granites of the Healey Lake, Artillery Lake and Tinney Hills regions of the Slave Province (ages between 2.61 – 2.59 Ga; van Breeman et al., 1992; Culshaw and van Breeman, 1990); (ii) quartz-feldspar porphyry dikes cross-cutting underlying mafic volcanic rocks of the Yellowknife Greenstone Belt region (Fyson and Helmstaedt, 1988); and (iii) late, cross-cutting granites of the Anialik River region (ages of 2601 ±6/-4 Ma; Fyson and Helmstaedt, 1988). The active plutonism within the Slave Province during the Pan-Slave tectono-thermal event is broadly contemporaneous with the estimated timing of auriferous orogenic vein formation at Hope Bay. Therefore, it is not unreasonable to consider an intrusion-derived fluid contribution to the ore systems at Hope Bay.

## **2.7 Conclusions**

Evidence of secondary Au upgrading in an orogenic quartz-carbonate vein system by late magmatic-hydrothermal fluids has been identified in the Patch 14 sub-region of the Madrid deposit

in the HBGB. Two spatially-associated veins were investigated using a number of analytical approaches. A high-grade vein (115-03) with a strongly bimodal distribution of gold grade (62 g/t average) and shows evidence of late-stage upgrading and subsequent gold enrichment by metalliferous fluids of inferred magmatic origin. In contrast, a low-grade vein (115-02) has more uniform gold grades (1 g/t average) and does not show evidence of upgrading. The results of this study may be extrapolated to explain the contrasting gold tenors of mineralized domains in the south (upgraded) versus north Madrid sub-regions. A two-stage model for mineralization involved a typical H<sub>2</sub>O-NaCl-CO<sub>2</sub> fluid for the primary orogenic Au stage and a later H<sub>2</sub>O-NaCl±CO<sub>2</sub> fluid responsible for the upgrading stage. Evidence in support of a late upgrading event by a magmatic-hydrothermal fluid in the high-grade vein are as follows:

- Texturally-late assemblages of tennantite-tetrahedrite + chalcopyrite + electrum ± Au-Ag-Pb tellurides, scheelite + chalcopyrite, and sphalerite + galena ± chalcopyrite in high-grade veins overprinting pre-existing auriferous orogenic gold mineralization. The overprinting mineral assemblage (and metal association) is consistent with intermediate-sulfidation settings observed in intrusion-related and epithermal systems.
- Hot cathodoluminescence imaging of quartz veins show that both high-grade and low-grade veins contain multiple generations of hydrothermal quartz precipitated from compositionally distinct fluids identified by different quartz luminescence colors (e.g., homogeneous red for quartz-1 versus deep blue-purple, light blue and/or yellow for secondary quartz-2).
- Decrepitate mound analysis from both veins show the presence of a distinct F±K-enriched fluid in the overprinted high-grade vein that is absent in the low-grade vein.
- Pyrite in the high-grade vein shows a positive correlation between Au and ΣBi+Te+W, and principle component analysis verifies a correlation between Au, Ag, Te, ± Sb. This correlation is

most evident in rim growth zones and fractures within pyrite. This geochemical signature is characteristic of gold systems with a magmatic signature (e.g., intrusion-related, epithermal), and contrasts with simpler Au-As signature of pyrite in the low-grade orogenic veins.

- Type 3b fluid inclusions in the high-grade vein contain elevated As-Sb-Zn-Pb-Cs-Ba-Sr-Rb, similar to magmatic-hydrothermal fluids.

Upgraded veins in the Madrid region represent a volumetrically minor feature related to intermediate-sulfidation, epithermal-like magmatic-hydrothermal processes; however, the potential magnitude of secondary gold enrichment makes overprinted and upgraded veins important targets to consider. Magmatic-hydrothermal overprinting and local upgrading of pre-existing orogenic veins is likely more common than previously thought.

## **2.8 Acknowledgements**

The authors would like to acknowledge TMAC Resources Incorporated for funding travel expenses, drill core access, and logistical support associated with travel related to this project. We would like to thank Dave King, Scott Parsons, and Matt Lapointe with TMAC Resources Inc. Orix Geoscience is acknowledged for their assistance with drill core sampling and geological interpretation, and the authors would like to thank Ashley Kirwan, Craig Fitchett, Justin Bernard, Alexa Dettman, Sam Long and Paige Giddy for their assistance. Thank you to Kevin Neyedley and Ryan Sharpe for assistance with SIMS analysis and to Dr. Zoltán Zajacz for assistance with fluid inclusion LA-ICP-MS work. The authors would also like to acknowledge Dr. Iain Samson for constructive reviews that improved the manuscript. This project was partially funded from NSERC DG grants to JH and DK.

## 2.9 References

- Abraham, A.P.G., Davis, D.W., Kamo, S.L., and Spooner, E.T.C. (1994). Geochronological constraints on late Archean magmatism deformation and gold–quartz vein mineralization in the northwestern Anialik River greenstone belt and igneous complex, Slave Province, NWT. *Canadian Journal of Earth Science* 31(8), 1365-1383.
- Adams, S.F. (1920). A microscopic study of vein quartz. Stanford University, Stanford.
- Afifi, A.M., Kelly, W.C., Essene, E.J. (1988). Phase relations among tellurides, sulfides, and oxides: part II: applications to telluride-bearing ore deposits. *Economic Geology* 83, p. 395–404.
- Audetat, A., Günther, D., and Heinrich, C.A. (1998). Formation of a magmatic-hydrothermal ore deposit: Insights with LA-ICP-MS analysis of fluid inclusions. *Science* 279(5359), 2091-2094.
- Baker, T. (2002). Emplacement depth and carbon dioxide-rich fluid inclusions in intrusion-related gold deposits. *Economic Geology* 97, 1111-1117.
- Baker, T., and Lang, J.R. (2001). Fluid inclusion characteristics of intrusion-related gold mineralization, Tombstone–Tungsten magmatic belt, Yukon Territory, Canada. *Mineralium Deposita* 36(6), 563-582.
- Bakker, R.J. (1999). Adaption of Bowers and Helgeson (1983) equation of state to isochore and fugacity coefficient calculation in the H<sub>2</sub>O-CO<sub>2</sub>-CH<sub>4</sub>-N<sub>2</sub>-NaCl fluid system. *Chemical Geology* 154, 225-236.
- Bakker, R.J. (2003). Package FLUIDS 1. Computer programs for analysis of fluid inclusion data and for modeling bulk fluid properties. *Chemical Geology* 194, 3-23.

- Bakker, R.J., and Jansen, J.B.H. (1991). Experimental post-entrapment water loss from synthetic CO<sub>2</sub>-H<sub>2</sub>O inclusions in natural quartz. *Geochimica et Cosmochimica Acta* 55(8), 2215-2230.
- Bateman, R., and Hagemann, S. (2004). Gold mineralisation throughout about 45 Ma of Archean orogenesis: protracted flux of gold in the Golden Mile, Yilgarn craton, Western Australia. *Mineralium Deposita* 39, 536-559.
- Beaudoin, G. (2011). The stable isotope geochemistry of orogenic gold deposits. Oral presentation at the Society for Geology Applied to Mineral Deposits conference, Antofagasta, Chile.
- Beeskow, B., Rankin, A. H., Murphy, P. J., and Treloar, P. J. (2005). Mixed CH<sub>4</sub>-CO<sub>2</sub> fluid inclusions in quartz from the South Wales Coalfield as suitable natural calibration standards for microthermometry and Raman spectroscopy. *Chemical Geology* 223, 3-15.
- Bierlein, F.P., Arne, D.C., Foster, D.A., Reynolds, P. (2001). A geochronological framework for orogenic gold mineralization in central Victoria, Australia. *Mineralium Deposita* 36, 741-767.
- Bierlein, F.P., Groves, D.I., Goldfarb, R.J., and Dubé, B. (2006). Lithospheric controls on the formation of giant orogenic gold deposits. *Mineralium Deposita* 40, 874-886.
- Bleeker, W., and Hall, B. (2007). The Slave Craton: geology and metallogenic evolution. In Goodfellow, W.D., (ed.). *Mineral deposits of Canada: a synthesis of major deposit-types, district metallogeny, the evolution of geological provinces, and exploration methods.* Geological Association of Canada MDD Special Publication 5, 849-879.
- Bleeker, W., Villeneuve, M., and Bethune, K. (1996). Thematic structural studies in the Slave Province, Northwest Territories: contrasting basement-cover relationships on the western

- and southwestern flanks of the Sleepy Dragon Complex. Geological Survey of Canada Paper, Current Research Part C, p. 27-37.
- Bodnar, R.J. (2003). Introduction to fluid inclusions. In, Samson, I., Anderson, A., and Marshall, M., (eds.) Fluid Inclusions: Analysis and Interpretation: Mineralogical Association of Canada Short Course 32, 1-8.
- Bodnar, R.J., Lecumberri-Sanchez, P., Moncada, D., Steele-MacInnis, M. (2014). Fluid inclusions in hydrothermal ore deposits. In Reference Module in Earth Systems and Environmental Sciences, Treatise on Geochemistry (Second Edition), 13, 119-142.
- Bodnar, R.J., and Vityk, M.O. (1994). Interpretation of microthermometric data for H<sub>2</sub>O-NaCl fluid inclusions. In De Vivo, B., and Frezzotti, M.L., (eds.), Fluid Inclusions in Minerals, Methods, and Applications: Virginia Tech, 117-130.
- Boggs, S., Kwon, Y-I., Goles, G.G., Rusk, B.G., Krinsley, D., and Seyedolali, A. (2002). Is quartz cathodoluminescence color a reliable provenance tool? A quantitative examination. Journal of Sedimentary Research 72, 408-415.
- Bortnikov, N.S., Kramer, Kh., Genkin, A.D., Krapiva, L.Ya., and Santa Cruz, M. (1988). Paragenesis of gold and silver tellurides in the Florencia deposit, Cuba. International Geology Review 30, 294-306.
- Boullier, A-M., Firdaous, K., and Robert, F. (1998). On the significance of aqueous fluid inclusions in gold-bearing quartz vein deposits from the southeastern Abitibi Subprovince (Quebec, Canada): Economic Geology 93, 216-223.
- Bowell, R.J., Foster, R.P. (1990). Telluride mineralisation at Ashanti gold mine, Ghana: Mineralogical Magazine 54, 617-627.

- Brookins, D.G. (1989). Aqueous geochemistry of rare earth elements. In Lipin, B.R., McKay, G.A. (eds.), *Geochemistry and mineralogy of rare earth elements*. *Rev Mineral, Mineralogical Society of America* 21, 201-225.
- Brown, K.L. (1986). Gold deposition from geothermal discharges in New Zealand. *Economic Geology* 81, 979–983.
- Buchholz, P., Oberthür, T., Lüders, V., and Wilkinson, J. (2007). Multistage Au-As-Sb mineralization and crustal-scale fluid evolution in the Kwekwe District, Midlands Greenstone Belt, Zimbabwe: A combined geochemical, mineralogical, stable isotope, and fluid inclusion study. *Economic Geology* 102, 347-378.
- Burke, E.A. (2001). Raman microspectrometry of fluid inclusions. *Lithos* 55, 139–158.
- Burrows, D.R. and Spooner, E.T.C. (1987). Generation of a magmatic H<sub>2</sub>O-CO<sub>2</sub> fluid enriched in Au, Mo, and W within an Archean sodic granodiorite stock, Mink Lake, northwestern Ontario. *Economic Geology* 82, 1931–1957.
- Burrows, D. R., Wood, P.C., and Spooner, E.T.C. (1986). Carbon isotope evidence for a magmatic origin for Archaean gold-quartz vein ore deposits. *Nature* 321(6073), 851.
- Carpernter, R.L., Sherlock, R.L., Quang, C., Kleespies, P., and McLeod, R. (2003). Geology of the Doris North gold deposit, northern Hope Bay volcanic belt, Slave Structural Province, Nunavut. *Geological Survey of Canada Current Research*, p. 10
- Cassidy, K.F., Barley, M.E., Groves, D.I., Perring, C.S., and Hallberg, J.A. (1991). An overview of the nature, distribution and inferred tectonic setting of granitoids in the late-Archaean Norseman-Wiluna Belt. *Precambrian Research* 51(1-4), 51-83.

- Ciobanu, C.L., Birch, W.D., Cook, N.J., Pring, A., and Grundler, P. V. (2010). Petrogenetic significance of Au–Bi–Te–S associations: the example of Maldon, Central Victorian gold province, Australia. *Lithos* 116(1-2), 1-17.
- Ciobanu, C.L., Cook, N.J., and Spry, P.G. (2006). Preface–Special Issue: telluride and selenide minerals in gold deposits–how and why? *Mineralogy and Petrology* 87(3-4), 163-169.
- Ciobanu, C.L., Cook, N.J., Utsunomiya, S., Kogagwa, M., Green, L., Gilbert, S., and Wade, B. (2012). Gold-telluride nanoparticles revealed in arsenic-free pyrite. *American Mineralogist* 97(8-9), 1515-1518.
- Claoué, J.C., King, R.W., and Kerrich, R. (1990). Archaean hydrothermal zircon in the Abitibi greenstone belt: constraints on the timing of gold mineralisation. *Earth and Planetary Science Letters* 98(1), 109-128.
- Clow, G.G., Lecuyer, N.L., Horan, S., Krutzmann, H., Chubb, D., and Rykaart, M. (2015). Technical Report on the Hope Bay Project, Nunavut, Canada, NI 43-101 Report. March 2015.
- Clow, G.G., Lecuyer, N.L., Valliant, W.W., Krutzmann, H., Chubb, D., and Rykaart, M. (2013). Preliminary Economic Assessment Study on the Hope Bay Project, Nunavut, Canada, NI 43-101 Report. December 2013.
- Colvine, A.C. (1988). Archean lode gold deposits in Ontario. In Ontario Ministry of Northern Development and Mines, Ont. Geology Survey Miscellaneous Paper 139, 136 p.
- Cook, N.J., Ciobanu, C.L., and Mao, J. (2009). Textural control on gold distribution in As-free pyrite from the Dongping, Huangtuliang and Hougou gold deposits, North China Craton (Hebei Province, China). *Chemical Geology* 264, 101-121.

- Coulson, I.M., Dipple, G.M., and Raudsepp, M. (2001). Evolution of HF and HCl in magmatic volatiles of the gold-mineralized Emerald Lake pluton, Yukon Territory, Canada. *Mineralium Deposita* 36, 594-606.
- Craig, H. (1961). Isotopic variations in meteoric waters. *Science* 133, 1702–1703.
- Culshaw, N., and van Breemen, O. (1990). A zoned low P-high T complex at the level of anatexis—structural and plutonic patterns in metasediments of the Archean Yellowknife Supergroup, near Bathurst Inlet, NWT, Canada. *Precambrian Research* 48(1-2), 1-20.
- Darling, R.S. (1991). An extended equation to calculate NaCl contents from final clathrate melting temperatures in H<sub>2</sub>O-CO<sub>2</sub>-NaCl fluid inclusions: Implications for P-T isochores location. *Geochimica et Cosmochimica Acta* 55, 3869–3871.
- Davis, W.J., King, J., Fryer, B.J., and van Breemen, O. (1990). Petrogenesis and evolution of Late-Archean granitoids in the central Slave Province: implications for the tectonic development of the Slave Province, Canada [abs.]. 3rd International Archean Symposium, Perth, Australia, p. 185-187.
- De Ronde, C.E.J., Spooner, E.T.C., de Wit, M.J., and Bray, C.J. (1992). Shear zone-related, Au quartz vein deposits in the Barberton greenstone belt, South Africa; field and petrographic characteristics, fluid properties, and light stable isotope geochemistry. *Economic Geology* 87(2), 366-402.
- De Souza, S., Dubé, B., McNicoll, V.J., Dupuis, C., Mercier-Langevin, P., Creaser, R.A., and Kjarsgaard, I.M. (2015). Geology, hydrothermal alteration, and genesis of the world-class Canadian Malartic stockwork-disseminated Archean gold deposit, Abitibi, Quebec. In Dubé, B. and Mercier-Langevin (eds.), Targeted Geoscience Initiative 4: Contributions to

- the Understanding of Precambrian Lode Gold Deposits and Implications for Exploration. Geological Survey of Canada, Open File 7852.
- Diamond, L. (1992). Stability of CO<sub>2</sub> clathrate hydrate + CO<sub>2</sub> liquid + CO<sub>2</sub> vapour + aqueous KCl-NaCl solutions: Experimental determination and application to salinity estimates of fluid inclusions. *Geochimica et Cosmochimica Acta* 56, 273-280.
- Diamond, L.W. (2003). Introduction to gas-bearing, aqueous fluid inclusions. In Samson, I., Anderson, A., and Marshall, M., (eds.), *Fluid Inclusions: Analysis and Interpretation: Mineralogical Association of Canada Short Course 32*, 101-158.
- Diamond, L.W., and Tarantola, A. (2015). Interpretation of fluid inclusions in quartz deformed by weak ductile shearing: Reconstruction of differential stress magnitudes and pre-deformation fluid properties. *Earth and Planetary Science Letters* 417, 107-119.
- Dong, G., Morrison, G., and Jaireth, S. (1995). Quartz textures in epithermal veins, Queensland; classification, origin and implication. *Economic Geology* 90(6), 1841-1856
- Dubé, B., Williamson, K., McNicoll, V., Malo, M., Skulski, T., Twomey, T., Sanborn-Barrie, M. (2004). Timing of gold mineralization at Red lake, northwestern Ontario, Canada: new constraints from U-Pb geochronology at the Goldcorp high-grade zone, Red Lake Mine, and the Madsen Mine. *Economic Geology* 99, 1611-1641.
- Dubessy, J., Poty, B., and Ramboz, C. (1989). Advances in C-O-H-N-S fluid geochemistry based on micro-Raman spectrometric analysis of fluid inclusions. *European Journal of Mineralogy* 1, 517 - 534.
- Elmer, F.L., White, R.W., and Powell, R. (2006). Devolatilization of metabasic rocks during greenschist-amphibolite facies metamorphism. *Journal of Metamorphic Geology* 24, 497-513.

- Emsbo, P., Hofstra, A.H., Lauha, E.A., Griffin, G.L., Hutchinson, R.W. (2003). Origin of High-Grade Gold Ore, Source of Ore Fluid Components, and Genesis of the Meikle and Neighboring Carlin-Type Deposits, Northern Carlin Trend, Nevada. *Economic Geology* 96, 1069-1105.
- Ernst, R., and Bleeker, W. (2010). Large igneous provinces (LIPs), giant dyke swarms, and mantle plumes: significance for breakup events within Canada and adjacent regions from 2.5 Ga to the Present. *Canadian Journal of Earth Science* 47(5), 695-739.
- Fall, A., Tattitch, B., and Bodnar, R.J. (2011). Combined microthermometric and Raman spectroscopic technique to determine the salinity of H<sub>2</sub>O–CO<sub>2</sub>–NaCl fluid inclusions based on clathrate melting. *Geochimica et Cosmochimica Acta* 75(4), 951-964.
- Fayek, M., Harrison, T.M., Ewing, R.C., Grove, M., and Coath, C.D. (2002). O and Pb isotopic analyses of uranium minerals by ion microprobe and U-Pb ages from the Cigar Lake deposit. *Chemical Geology* 185, 205-225.
- Frape, S.K., and Fritz, P. (1987). Geochemical trends for groundwaters from the Canadian Shield. In, *Saline water and gases in crystalline rocks*. Geological Association of Canada 33, 19-38.
- Frape, S. K., Fritz, P., and McNutt, R. T. (1984). Water-rock interaction and chemistry of groundwaters from the Canadian Shield. *Geochimica et Cosmochimica Acta* 48(8), 1617-1627.
- Faure, G., and Mensing, T.M. (2005). *Isotopes: principles and applications*. John Wiley and Sons Inc, p. 897.

- Fulignati, P., and Sbrana, A. (1998). Presence of native gold and tellurium in the active high-sulfidation hydrothermal system of the La Fossa volcano (Vulcano, Italy). *Journal of Volcanology and Geothermal Research* 86, 187-198.
- Fusswinkel, T., Wagner, T., and Sakellaris, G. (2017). Fluid evolution of the Neoproterozoic Pampalo orogenic gold deposit (E Finland): Constraints from LA-ICPMS fluid inclusion microanalysis. *Chemical Geology* 450, 96-121.
- Fyson, W.K., and Helmstaedt, H. (1988). Structural patterns and tectonic evolution of supracrustal domains in the Archean Slave Province, Canada. *Canadian Journal of Earth Science* 25, 301-315.
- Gebre-Mariam, M., Hagemann, S.G., and Groves, D.I. (1995). A classification for epigenetic Archean lode-gold deposits. *Mineralium Deposita* 30, 408-410.
- Gehrig, M. (1980). Phasengleichgewichte und pVT-Daten ternärer Mischungen aus Wasser, Kohlendioxid und Natriumchlorid bis 3 kbar und 550°C. Doctoral dissertation, Univ. Karlsruhe.
- Goldfarb, R.J., Baker, T., Dubé, B., Groves, D.I., Hart, C.J.R., and Gosselin, P. (2005). Distribution, character, and genesis of gold deposits in metamorphic terranes. *Economic Geology* 100<sup>th</sup> Anniversary Volume, p. 407-450.
- Goldfarb, R.J., Groves, D.I., and Gardoll, S. (2001). Orogenic gold and geologic time: a global synthesis. *Ore Geology Reviews* 18, 1-75.
- Goldfarb, R.J. and Groves, D.J. (2015). Orogenic gold: Common or evolving fluid and metal sources. *Lithos* 2, 2-26.

- Goldstein, R.H., and Reynolds, T.J. (1994). Fluid Inclusion Microthermometry. In Goldstein, R.H., and Reynolds, T.J., Systematics of Fluid Inclusions in Diagenetic Minerals. Society of Sedimentary Geology Short Course 31, 87-122.
- Goldfarb, R.J., Snee, L.W., Miller, L.D., and Newberry, R.J. (1991). Rapid dewatering of the crust deduced from ages of mesothermal gold deposits. *Nature* 354(6351), 296.
- Götze, J. (2009). Chemistry, textures and physical properties of quartz—geological interpretation and technical application. *Mineralogical Magazine* 73(4), 645-671.
- Götze, J., Plötze, M., and Habermann, D. (2001). Origin, spectral characteristics and practical applications of the cathodoluminescence (CL) of quartz—a review. *Mineralogy and Petrology* 71, 225–250.
- Gourcerol, B., Kontak, D.J., Thurston, P.C., and Petrus, J.A. (2018a). Results of LA-ICP-MS sulfide mapping from Algoma-type BIF gold systems with implications for the nature of mineralizing fluids, metal sources, and deposit models. *Mineralium Deposita* 1-24. <https://doi.org/10.1007/s00126-017-0788-7>.
- Gourcerol, B., Kontak, D.J., Thurston, P.C., and Petrus, J.A. (2018b). Application of LA-CP-MS sulfide analysis and methodology for deciphering elemental paragenesis and associations to multi-stage processes in metamorphic gold settings. *Canadian Mineralogist* 56. 1-16.
- Groves, D.I. (1993). The crustal continuum model for late-Archean lode-gold deposits of the Yilgarn Block, Western Australia. *Mineralium Deposita* 28, 366-374.
- Groves, D.I., Goldfarb, R.J., Gebre-Mariam, M., Hagemann, S.G., and Robert, F. (1998). Orogenic gold deposits: a proposed classification in the context of their crustal distribution and relationship to other gold deposit types. *Ore Geology Reviews* 13, 7-27.

- Groves, D.I., Goldfarb, R.J., Robert, F., and Hart, C.J.R. (2003). Gold deposits in metamorphic belts: overview of current understanding, outstanding problems, future research, and exploration significance. *Economic Geology* 98, 1-29.
- Groves, D.I., Phillips, G.N., Ho, S.E., Henderson, C.A., Clark, M.E., and Wood, G.M. (1984). Controls on distribution of Archaean hydrothermal gold deposits in Western Australia, In Foster, R. P., (ed.), *Gold '82 — The geology, geochemistry and genesis of gold deposits*: Rotterdam, Balkema, p. 689–712.
- Groves, D.I., and Phillips, G.N. (1987). The genesis and tectonic control on Archaean gold deposits of the Western Australian Shield—a metamorphic replacement model. *Ore Geology Reviews* 2, 287–322.
- Groves, D.I. and Santosh, M. (2016). The giant Jiaodong gold province: The key to a unified model for orogenic gold deposits? *Geoscience Frontiers* 7, 409-417.
- Guillong, M., Meier, D.L., Allan, M.M., Heinrich, C.A., Yardley, B.W.D. (2008). Appendix A6: SILLS: a Matlab-based program for the reduction of Laser Ablation ICP–MS data of homogeneous materials and inclusions. *Short Course Ser., Mineralogical Association of Canada* 40, 328–333. Vancouver B.C.
- Hagemann, S.G., Gebre-Mariam, M., and Groves, D. I. (1994). Surface-water influx in shallow-level Archean lode-gold deposits in Western, Australia. *Geology* 22(12), 1067-1070.
- Hart, C.J.R., (2007). Reduced intrusion-related gold systems. In, Goodfellow, W.D., (ed.), *Mineral deposits of Canada: A Synthesis of Major Deposit Types, District Metallogeny, the Evolution of Geological Provinces, and Exploration Methods*: Geological Association of Canada, Mineral Deposits Division, Special Publication No. 5, 95-112.

- Hart, C.J.R., and Goldfarb, R.J. (2005). Distinguishing intrusion-related from orogenic gold systems: New Zealand Minerals Conference: Realising New Zealand's Mineral Potential, New Zealand, Proceedings, Australasian Institute of Mining and Metallurgy, p. 125-133.
- Hart, C.J., Goldfarb, R.J., Qiu, Y., Snee, L., Miller, L.D., and Miller, M.L. (2002). Gold deposits of the northern margin of the North China Craton: multiple late Paleozoic–Mesozoic mineralizing events. *Mineralium Deposita* 37(3-4), 326-351.
- Haynes, F.M., and Kesler, S.E. (1987). Chemical evolution of brines during Mississippi valley-type mineralization; evidence from East Tennessee and Pine Point. *Economic Geology* 82(1), 53-71.
- Haynes F.M., Sterner, S.M., and Bodnar, R.J. (1988). Synthetic fluid inclusions in natural quartz. IV. Chemical analyses of fluid inclusions by SEM/EDA: Evaluation of method. *Geochimica et Cosmochimica Acta* 52, 969-977.
- Hebel, M.U. (1999). U-Pb geochronology and lithogeochemistry of the Hope Bay greenstone belt, Slave Structural Province, Northwest Territories, Canada: M.Sc. thesis, Vancouver, Canada, University of British Columbia, 96 p.
- Hedenquist, J.W., Arribas, A., and Gonzalez-Urien, E. (2000). Exploration for epithermal gold deposits. *Reviews in Economic Geology* 13(2), 45-77.
- Heinrich, C.A., Driesner, T., Stefánsson, A., and Seward, T.M. (2004). Magmatic vapor contraction and the transport of gold from the porphyry environment to epithermal ore deposits. *Geology* 32(9), 761-764.
- Heinrich, C.A., Gunther, D., Audétat, A., Ulrich, T., and Frischknecht, R. (1999). Metal fractionation between magmatic brine and vapor, determined by microanalysis of fluid inclusions. *Geology* 27(8), 755-758.

- Helt, K.A., Williams-Jones, A.E., Clark, J.R., Wing, B.A., and Wares, R.P. (2014). Constraints on the genesis of the Archean oxidized intrusion-related Canadian Malartic gold deposit, Quebec, Canada. *Economic Geology* 109, 713-735.
- Henderson, J.B. (1985). Geology of the Yellowknife – Hearne Lake area, District of MacKenzie: a segment across an Archean basin. Geological Survey of Canada, Memoir 414.
- Hodgson, C.J. (1989). The Structure of Shear-Related, Vein-Type Gold Deposits: A Review. *Ore Geology Reviews* 4, 231-273.
- Huang, S.S., Leu, A.D., Ng., H.J., and Robinson, D.B. (1985). The phase behavior of two mixtures of methane, carbon dioxide, hydrogen sulfide and water. *Fluid Phase Equilibria* 19, 21-32.
- Ilchik, R.P. and Barton, M.D. (1997). An Amagmatic Origin for Carlin-Type Gold Deposits. *Economic Geology* 92, 269-288.
- Ioannou, S.E., Götze, J., Weiershäuser, L., Zubowski, S.M., and Spooner, E.T.C. (2004). Cathodoluminescence characteristics of Archean volcanogenic massive sulfide related quartz: Noranda, Ben Nevis and Matagami districts, Abitibi Subprovince, Canada. *Geochem. Geophys. Geosy.* 5(2), 1-24.
- Jia, Y., Li, X., and Kerrich, R. (2001). Stable isotope (O, H, S, C, and N) systematics of quartz vein systems in the turbidite-hosted Central and North Deborah gold deposits of the Bendigo gold field, central Victoria, Australia: Constraints on the origin of ore-forming fluids. *Economic Geology* 96(4), 705-721.
- Jia, Y., Li, X., and Kerrich, R. (2000). A fluid inclusion study of Au-bearing quartz vein systems in the Central and North Deborah deposits of the Bendigo Gold Field, Central Victoria, Australia. *Economic Geology* 95, 467-494.

- Kelly J.L., Fu, B., Kita N.T. and Valley J.W. (2007). Optically continuous silcrete quartz cements of the St. Peter Sandstone: high precision oxygen isotope analysis by ion microprobe. *Geochimica et Cosmochimica Acta* 71, 3812-3832.
- Kerrick, R. (1987). The stable isotope geochemistry of Au-Ag vein deposits in metamorphic rocks. In Kyser, T.K. (ed.), *Mineralogical Association of Canada Short Course 13*, 287-336.
- Kerrick, R., and Cassidy, K.F. (1994). Temporal relationships of lode gold mineralization to accretion, magmatism, metamorphism and deformation – Archean to present: A review. *Ore Geology Reviews* 9, 263-310.
- Kerrick, R., and Fyfe, W.S. (1981). The gold-carbonate association: Source of CO<sub>2</sub>, and CO<sub>2</sub> fixation reactions in Archean lode deposits. *Chemical Geology* 33, 265–294.
- Kerrick, R., Fryer, B.J. (1979). Archean precious-metal hydrothermal systems, Dome mine, Abitibi greenstone belt: II. REE and oxygen isotope relations. *Canadian Journal of Earth Science* 16, 440-458.
- Kerrick, R., and Watson, G.P. (1984). The Macassa Mine Archean lode gold deposit, Kirkland Lake, Ontario; geology, patterns of alteration, and hydrothermal regimes. *Economic Geology* 79(5), 1104-1130.
- King, J.E., Davis, W.J., and Relf, C. (1992). Late Archean tectono-magmatic evolution of the central Slave Province, Northwest Territories. *Canadian Journal of Earth Science* 29(10), 2156-2170.
- Klemm, D.D. (1965). Synthesen und Analysen in den Dreieckdiagrammen FeAsS-CoAsS-NiAsS und FeS<sub>2</sub>-CoS<sub>2</sub>-NiS<sub>2</sub>. *Neues Jahrbuche fuer Mineralogie, Abhandlungen*, 103, 205–255.

- Kolb, J., Dziggel, A., and Bagas, L. (2015). Hypozonal lode gold deposits: A genetic concept based on a review of the New Consort, Renco, Hutti, Hira Buddini, Navachab, Nevoria and The Granites deposits. *Precambrian Research* 262, 20-44.
- Kontak, D.J. (2016). A Rayleigh Distillation model to explain large variations in oxygen isotope data for orogenic gold veins [abs.]. GAC-MAC 2016 Whitehorse abstract volume, p. 46.
- Kontak, D.J. (1995). A study of fluid inclusions in sulfide and nonsulfide mineral phases from a carbonate-hosted Zn-Pb deposit, Gays River, Nova Scotia, Canada. *Economic Geology* 93(6), 793-817.
- Kontak, D.J. (2004). Analysis of evaporate mounds as a complement to fluid-inclusion thermometric data: case studies from granitic environments in Nova Scotia and Peru. *Canadian Mineralogist* 42, 1315-1329.
- Kontak, D.J., Horne, R.J., and Kyser, K. (2011). An oxygen isotope study of two contrasting orogenic vein gold systems in the Meguma Terrane, Nova Scotia, Canada, with implications for fluid sources and genetic models. *Mineralium Deposita* 46, 289-304.
- Kontak, D.J. and Smith, P.K. (1993). A metaturbidite-hosted lode gold deposit; the Beaver Dam Deposit, Nova Scotia; I, Vein paragenesis and mineral chemistry. *Canadian Mineralogist* 31(2), 471-522.
- Kontak, D.J. and Tuba, G. (2017). How can fluid inclusion studies better constrain orogenic gold deposit models: Case studies from the Superior Province and Meguma Terrane, Canada. SGA Meeting, Quebec, Canada, August 2017, Volume Proceedings of Extended Abstracts.
- Kyser, T.K., and Kerrich, R. (1990). Geochemistry of fluids in tectonically active crustal regions. In Nesbitt, B.E. (ed.), *Fluids in Tectonically Active Regimes of the Continental Crust*. Mineralogical Association of Canada Short Course 19, 133-215.

- Landtwing, M.R., Furrer, C., Redmond, P.B., Pettke, T., Guillong, M., and Heinrich, C.A. (2010). The Bingham Canyon porphyry Cu-Mo-Au deposit. III. Zoned copper-gold ore deposition by magmatic vapor expansion. *Economic Geology* 105(1), 91-118.
- Lang, J.R. and Baker, T. (2001). Intrusion-related gold systems: the present level of understanding. *Mineralium Deposita* 36, 477-489.
- Large, R.R., Danyushevsky, L., Hollit, C., Maslennikov, V., Meffre, S., Gilbert, S.B., Scott, R., Emsbo, P., Thomas, H., Singh, B., and Foster, J. (2009). Gold and trace element zonation in pyrite using a laser imaging technique: Implications for the timing of gold in orogenic and Carlin-style sediment-hosted deposits. *Economic Geology* 104, 635-668.
- Large, S.J., Bakker, E.Y., Weis, P., Wälle, M., Ressel, M., and Heinrich, C.A. (2016). Trace elements in fluid inclusions of sediment-hosted gold deposits indicate a magmatic-hydrothermal origin of the Carlin ore trend. *Geology* 44(12), 1015-1018.
- Large, R.R., Bull, S.W., and Maslennikov, V.V. (2011). A carbonaceous sedimentary source-rock model for Carlin-type and orogenic gold deposits. *Economic Geology* 106(3), 331-358.
- Lawrence, D.M., Treloar, P.J., Rankin, A.H., Boyce, A., and Harbidge, P. (2013). A fluid inclusion and stable isotope study at the Loulo mining district, Mali, West Africa: Implications for multifluid sources in the generation of orogenic gold deposits. *Economic Geology* 108(2), 229-257.
- LeFort, D., Hanley, J., and Guillong, M. (2011). Subepithermal Au-Pd Mineralization Associated with an Alkalic Porphyry Cu-Au Deposit, Mount Milligan, Quesnel Terrane, British Columbia, Canada. *Economic Geology* 106(5), 781-808.
- Legendre, B., Saileau, C., and Hancheng, C. (1980). Le système ternaire or-argent-tellure. *Soc. Chim. France Bull.* pt 1, 197-204.

- MacGeehan, P.J., and Hodgson, C.J. (1982). Environments of gold mineralization in the Campbell Red Lake and Dickenson mines, Red Lake district, Ontario. In, *Geology of Canadian gold deposits*. Canadian Institute of Mining and Metallurgy, Special 24, 184-207.
- Madsen, J.K., Sherlock, R., and Lindsay, D. (2007). The geology, geochemistry and mineralization of the Naartok gold deposit: Hope Bay belt, Nunavut Territory [abs.]: Geological Association of Canada Abstract, p. 52.
- Mao, J., Li, Y., Goldfarb, R.J., He, Y., and Zaw, K. (2003). Fluid inclusion and noble gas studies of the Dongping gold deposit, Hebei Province, China: A mantle connection for mineralization? *Economic Geology* 98, 517-534
- Mao, W., Rusk, B., Yang, F., and Zhang, M. (2017). Physical and chemical evolution of the Dabaoshan porphyry Mo deposit, South China: Insights from fluid inclusions, cathodoluminescence, and trace elements in quartz. *Economic Geology* 112, 889-918.
- Marsh, E.E., Goldfarb, R.J., Hart, C.J., and Johnson, C.A. (2003). Geology and geochemistry of the Clear Creek intrusion-related gold occurrences, Tintina Gold Province, Yukon, Canada. *Canadian Journal of Earth Science* 40(5), 681-699.
- Matsuhisa Y., Goldsmith J.R., and Clayton, R.N. (1979). Oxygen isotopic fractionation in the system quartz-albite-anorthite-water. *Geochimica et Cosmochimica Acta* 43, 1131-1140.
- Mathieson, G.A., and Clark, A.H. (1984). The Cantung E Zone scheelite skarn orebody, Tungsten, Northwest Territories; a revised genetic model. *Economic Geology* 79(5), 883-901.
- Maydagán, L., Franchini, M., Lentz, D., Pons, J., and McFarlane, C. (2013). Sulfide composition and isotopic signature of the Altar Cu-Au deposit, Argentina: Constraints on the evolution of the porphyry-epithermal system. *Canadian Mineralogist* 51(6), 813-840.

- McCoy, D., Newberry, R.J., Layer, P., DiMarchi, J.J., Bakke, A., Masterman, S. and Minehane, D.L. (1997). Plutonic-related gold deposits of Interior Alaska. In, Mineral Deposits of Alaska. Goldfarb, R. J. and Miller, L. D., (eds.), Economic Geology Monograph 9, 191–241.
- McCuaig, T.C., and Kerrich, R. (1998). P-T-t-deformation-fluid characteristics of lode gold deposits: evidence from alteration systematics. *Ore Geology Reviews* 12, 381-453.
- Menzies, C.D., Teagle, D.A.H., Craw, D., Cox, S.C., Boyce, A.J., Barrie, C.D., and Roberts, S. (2014). Incursion of meteoric waters into the ductile regime in an active orogen. *Earth and Planetary Science Letters* 399, 1-13.
- Mériaud, N., and Jébrak, M. (2017). From intrusion-related to orogenic mineralization: The Wasamac deposit, Abitibi Greenstone Belt, Canada. *Ore Geology Reviews* 84, 289-308.
- Mole, D.R., Fiorentini, M.L., Cassidy, K.F., Kirkland, C.L., Thebaud, N., McCuaig, T.C., Doublier, M.P., Durning, P., Romano, S.S., Maas, R., Belousova, E. A., Barnes, S.J., and Miller, J. (2013). Crustal evolution, intra-cratonic architecture and the metallogeny of an Archaean craton. Geological Society, London, Special Publications 393, SP393-8.
- Molnár, F., O'Brien, H., Lahaye, Y., Käpyaho, A., Sorjonen-Ward, P., Hyodo, H., and Sakellaris, G. (2016). Signature of multiple mineralization processes in the Archean orogenic gold deposit of the Pampalo Mine, Hattu Schist Belt, eastern Finland. *Economic Geology* 111, 1659-1703.
- Moncada, D., Mutchler, S., Nieto, A., Reynolds, T.J., Rimstidt, J.D., and Bodnar, R.J. (2012). Mineral textures and fluid inclusion petrography of the epithermal Ag–Au deposits at Guanajuato, Mexico: Application to exploration. *Journal of Geochemical Exploration* 114, 20-35.

- Morey, A.A., Tomkins, A.G., Bierlein, F.P., Weinberg, R.F., and Davidson, G.J. (2008). Bimodal distribution of gold in pyrite and arsenopyrite: Examples from the Archean Boorara and Bardoc shear systems, Yilgarn craton, Western Australia. *Economic Geology* 103(3), 599-614.
- McFarlane, C.R.M., Mavrogenes, J., Lentz, D., King, K., Allibone, A., and Holcombe, R. (2011). Geology and intrusion-related affinity of the Morila Gold Mine, southeast Mali. *Economic Geology* 106, 727-750.
- McNeil, A.M., and Kerrich, R. (1986). Archean lamprophyre dykes and gold mineralization, Matheson, Ontario: the conjunction of LILE-enriched mafic magmas, deep crustal structures, and Au concentration. *Canadian Journal of Earth Science* 23(3), 324-343.
- Müller, W., Shelley, M., Miller, P., and Broude, S. (2009). Initial performance metrics of a new custom-designed ArF excimer LA-ICPMS system coupled to a two-volume laser-ablation cell. *Journal of Analytical Atomic Spectrometry* 24, 209-214.
- Munoz, J.L., and Swenson, A. (1981). Chloride-hydroxyl exchange in biotite and estimation of relative HCl/HF activities in hydrothermal fluids. *Economic Geology* 76(8), 2212-2221.
- Naden, J., and Caulfield, J.B.D. (1989). Fluid inclusion and isotopic studies of gold mineralization in the southern upland of Scotland. *Institution of Mining and Metallurgy, Transactions, Section B. Applied Earth Science* 98, 46-48.
- Naden, J., and Shepard, T.J. (1989). Role of methane and carbon dioxide in gold deposition. *Nature* 342, 793-795.
- Neyedley, K., Hanley, J.J., Fayek, M., and Kontak, D.J. (2017). Textural, fluid inclusion, and stable oxygen isotope constraints on vein formation and gold precipitation at the 007

- deposit, Rice Lake Greenstone Belt, Bissett, Manitoba, Canada. *Economic Geology* 112(3), 629-660.
- Oberthür, T. and Weiser, T.W. (2008). Gold-bismuth-telluride-sulphide assemblages at the Viceroy Mine, Harare-Bindura-Shamva greenstone belt, Zimbabwe. *Mineralogical Magazine* 72(4), 953-970.
- Padgham, W.A., and Fyson, W.K. (1992). The Slave province: A distinct Archean craton. *Canadian Journal of Earth Science* 29(10), 2072-2086.
- Pals, D.W., Spry, P.G., and Chryssoulis, S. (2003). Invisible gold and tellurium in arsenic-rich pyrite from the Emperor gold deposit, Fiji: implications for gold distribution and deposition. *Economic Geology* 98(3), 479-493.
- Panteleyev, A. (1986). Ore deposits #10. A Canadian Cordilleran model for epithermal gold-silver deposits. *Geoscience Canada* 13(2).
- Panteleyev, A. (1991). Gold in the Canadian Cordillera-A focus on epithermal and deeper environments. In, McMillian, W.J., Höy, T., MacIntyre, D.G., Nelson, J.L., Nixon, G.T., Hammack, J.L., Panteleyev, A., Ray, G.E., and Webster, I.C.L., *Ore Deposits, Tectonics and Metallogeny in the Canadian Cordillera*, Paper 4, 163-212.
- Pettijohn, F.J. (1970). The Canadian Shield—a status report, 1970. Basins and geosynclines of the Canadian Shield. *Geological Survey of Canada Paper* 70-40.
- Phillips, G.N. (1985). Interpretation of Big Bell/Hemlo-type gold deposits; precursors, metamorphism, melting and genetic constraints. *South Afr. J. Geology* 88(1), 159-173.
- Phillips, G.N., and Powell, R. (2009). Formation of gold deposits: Review and evaluation of the continuum model. *Earth-Science Review* 94, 1-21.

- Phillips, G.N., and Powell, R. (2010). Formation of gold deposits: a metamorphic devolatilization model. *Journal of Metamorphic Geology* 28(6), 689-718
- Pitcairn, I. K., Teagle, D.A., Craw, D., Olivo, G. R., Kerrich, R., and Brewer, T.S. (2006). Sources of metals and fluids in orogenic gold deposits: insights from the Otago and Alpine Schists, New Zealand. *Economic Geology* 101(8), 1525-1546.
- Pitcher, W.S. (1987). Granites and yet more granites forty years on. *Geologische Rundschau*, 76(5), 1 -79.
- Poulsen, K. H., Robert, F., and Dubé, B. (2000). Geological classification of Canadian gold deposits. *Geological Survey of Canada Bulletin* 540, 1-106.
- Reich, M., Kesler, S.E., Utsunomiya, S., Palenik, C.S., Chryssoulis, S.L., and Ewing, R.C. (2005). Solubility of gold in arsenian pyrite. *Geochimica et Cosmochimica Acta* 69, 2781-2796.
- Rezeau, H., Moritz, R., and Beaudoin, G. (2017). Formation of Archean batholith-hosted gold veins at the Lac Herbin deposit, Val-d'Or district, Canada: Mineralogical and fluid inclusion constraints. *Mineralium Deposita* 52(3), 421-442.
- Richards, J.P., and Kerrich, R. (1993). The Porgera gold mine, Papua New Guinea; magmatic hydrothermal to epithermal evolution of an alkalic-type precious metal deposit. *Economic Geology* 88(5), 1017-1052.
- Ridley, J.B., and Diamond, L.W. (2000). Fluid chemistry of orogenic lode gold deposits and implications for genetic models. *Society of Economic Geology Review* 13, 141-162.
- Robert, F. (2001). Syenite-associated disseminated gold deposits in the Abitibi greenstone belt, Canada. *Mineralium Deposita* 36(6), 503-516.

- Robert, F., and Kelly, W.C. (1987). Ore-forming fluids in Archean gold-bearing quartz veins at the Sigma mine, Abitibi greenstone belt, Quebec, Canada. *Economic Geology* 82, 1464-1482.
- Robert, F., Boullier, A.M., and Firdaous, A. (1995). Gold-quartz veins in metamorphic terranes and their bearing on the role of fluids in faulting. *Journal of Geophysical Research* 100, 12861-12879.
- Roedder, E. (1984). Fluid inclusions. *Reviews in Mineralogy and Geochemistry* 12, 644.
- Rosso, K.M., and Bodnar, R.J. (1995). Microthermometric and Raman spectroscopic detection limits of CO<sub>2</sub> in fluid inclusions and the Raman spectroscopic characterization of CO<sub>2</sub>. *Geochimica et Cosmochimica Acta* 59, 3961-3975.
- Ruano, S.M., Rosúa, F.J.C., Hach-Alí, P.F., Chacón, F.D.L.F., and López, E.C. (2000). Epithermal Cu–Au mineralization in the Palai–Islica deposit, Almeria, Southeastern Spain: fluid-inclusion evidence for mixing of fluids as a guide to gold mineralization. *Canadian Mineralogist* 38(3), 553-565.
- Rusk, B., and Reed, M. (2002). Scanning electron microscope-cathodoluminescence analysis of quartz reveals complex growth histories in veins from the Butte porphyry copper deposit, Montana. *Geology* 30, 727-730.
- Rusk, B.G., Reed, M.H., and Dilles, J.H. (2008). Fluid inclusion evidence for magmatic-hydrothermal fluid evolution in the porphyry copper-molybdenum deposit at Butte, Montana. *Economic Geology* 103(2), 307-334.
- Rusk, B.G., Reed, M.H., Dilles, J.H., Klemm, L.M., and Heinrich, C.A. (2004). Compositions of magmatic hydrothermal fluids determined by LA-ICP-MS of fluid inclusions from the

- porphyry copper–molybdenum deposit at Butte, MT. *Chemical Geology* 210(1-4), 173-199.
- Salier, B.P., Groves, D.I., McNaughton, N.J., Fletcher, I.R. (2005). Geochronological and stable isotope evidence for widespread orogenic gold mineralization from a deep-seated fluid source at ca. 2.65 Ga in the Laverton gold province, Western Australia. *Economic Geology* 100, 1363–1388.
- Schmidt, C., and Bodnar, R.J. (2000). Synthetic Fluid Inclusions: XIV. PVTX properties in the System H<sub>2</sub>O-NaCl-CO<sub>2</sub> at elevated temperatures, pressures and salinities. *Geochimica et Cosmochimica Acta*. 64, 3853-3869.
- Selby, D., and Nesbitt, B.E. (2000). Chemical composition of biotite from the Casino porphyry Cu-Au-Mo mineralization, Yukon, Canada: evaluation of magmatic and hydrothermal fluid chemistry. *Chemical Geology* 171, 77-93.
- Shannon, A.J. (2005). Volcanic framework and geochemical evolution of the Archean Hope Bay Greenstone Belt, Nunavut, Canada: M.Sc. thesis, Vancouver, BC, The University of British Columbia, 200 p.
- Shelton, K.L., McMenemy, T.A., Van Hees, E.H.P., and Falck, H. (2004). Deciphering the complex fluid history of a greenstone-hosted gold deposit: fluid inclusion and stable isotope studies of the Giant mine, Yellowknife, Northwest Territories, Canada. *Economic Geology* 99, 1643-1663.
- Sherlock, R.L., Carpenter, R.L., and Quang, C. (2003). Volcanic stratigraphy, structural geology and gold mineralization in the Doris-Wolverine corridor, northern Hope Bay volcanic belt, Nunavut. Geological Survey of Canada Open File 1553.

- Sherlock, R.L., and Sandeman, H.A. (2004). Volcanic stratigraphy and structural geology of the area of the Boston gold deposit, Hope Bay volcanic belt, Nunavut. Geological Survey of Canada Current Research 2004-C2, 11 p.
- Sherlock, R.L., Shannon, A., Hebel, M., Lindsay, D., Madsen, J., Sandeman, H., Hrabi, B., Mortensen, J.K., Tosdal, R.M., and Friedman, R. (2012). Volcanic Stratigraphy, Geochronology, and Gold Deposits of the Archean Hope Bay Greenstone Belt, Nunavut, Canada. *Economic Geology* 107, 991-1042.
- Sibson, R.H., Robert, F., and Poulsen, K.H. (1988). High-angle reverse faults, fluid-pressure cycling, and mesothermal gold-quartz deposits. *Geology* 16(6), 551-555.
- Sillitoe, R.H. (1989). Gold deposition in western Pacific island arcs: The magmatic connection: *Economic Geology* 6, 274-291.
- Sillitoe, R.H., and Hedenquist, J.W. (2003). Linkages between volcanotectonic settings, ore-fluid compositions, and epithermal precious metal deposits, In Simmons, S.F., and Graham, I.J., (eds.), *Volcanic, geothermal, and ore-forming fluids: Rulers and witnesses of processes within the Earth*. Society of Economic Geology Special Publication 10, 315-343.
- Sillitoe, R.H., and Thompson, J.F. (1998). Intrusion-Related Vein Gold Deposits: Types, Tectono-Magmatic Settings and Difficulties of Distinction from Orogenic Gold Deposits. *Resource Geology* 48(4), 237-250.
- Spooner E.T.C. (1993). Magmatic sulphide/volatile interaction as a mechanism for producing chalcophile element enriched, Archean Au-quartz, epithermal Au-Ag and Au skarn hydrothermal ore fluids. *Ore Geology Reviews* 7, 359-379.
- Stefánsson, A., and Seward, T.M. (2004). Gold (I) complexing in aqueous sulphide solutions to 500 C at 500 bar. *Geochimica et Cosmochimica Acta* 68(20), 4121-4143.

- Stemler, J.U., Richards, J.P., Muehlenbachs, K. (2006). A Fluid Inclusion and Stable Isotopic Investigation of the Boston Lode-Gold Deposit, Hope Bay Volcanic Belt, Nunavut. *Explor. Mining Geology* 15, 101-121.
- Takenouchi, S., and Kennedy, G. (1965). The solubility of carbon dioxide in NaCl solutions at high temperatures and pressures. *American Journal of Science* 263, 445-454.
- Tarantola, A., Diamond, L. W., and Stünitz, H. (2010). Modification of fluid inclusions in quartz by deviatoric stress I: experimentally induced changes in inclusion shapes and microstructures. *Contributions to Mineralogy and Petrology* 160(6), 825-843.
- Taylor, B.E. (2007). Epithermal gold deposits. In, Goodfellow, W.D., (ed.), *Mineral Deposits of Canada: A Synthesis of Major Deposit-Types, District Metallogeny, the Evolution of Geological Provinces, and Exploration Methods*. Geological Association of Canada, MDD Spec. Pub. No. 5, 113-139.
- Therriault, R. (2006). *Geology, geochemistry and gold mineralization in the Madrid Corridor, Hope Bay Volcanic Belt, Nunavut, Canada: M.Sc. thesis, London, Ontario, The University of Western Ontario, 216 p.*
- Thomas, A.V., and Spooner, E.T.C. (1992). The volatile geochemistry of magmatic H<sub>2</sub>O-CO<sub>2</sub> fluid inclusions from the Tanco zoned granitic pegmatite, southeastern Manitoba, Canada. *Geochimica et Cosmochimica Acta* 56(1), 49-65.
- Tomkins, A.G. and Mavrogenes, J.A. (2002). Mobilization of gold as a polymetallic melt during pelite anatexis at the Challenger Deposit, South Australia: A metamorphosed Archean gold deposit. *Economic Geology* 97, 1249-1271.

- Tomkins, A.G., Pattison, D.R.M., and Zaleski, E. (2004). The Hemlo Gold Deposit, Ontario: An example of melting and mobilization of a precious metal-sulfosalt assemblage during amphibolite facies metamorphism and deformation. *Economic Geology* 99, 1063-1084.
- Thompson, P.H. (1997). Regional geology of Archean granitoid rocks adjacent to the Hope Bay and Elu Inlet volcanic belts, northeastern Slave structural province, Canadian Shield: BHP Minerals Canada Ltd. Internal Report, 56 p.
- Thompson, J.F.H., Sillitoe, R.H., Baker, T., Lang, J.R., and Mortensen, J.K. (1999). Intrusion-related gold deposits associated with tungsten-tin provinces. *Mineralium Deposita* 34(4), 323-334.
- TMAC Resources Incorporated (2014). Exploration Diamond Drilling on Inuit Owned Land (IOL) Exploration Agreements at Hope Bay, NTI Assessment Report.
- Ulrich, T., Guenther, D., and Heinrich, C.A. (1999). Gold concentrations of magmatic brines and the metal budget of porphyry copper deposits. *Nature* 399(6737), 676.
- van Breemen, O., Davis, W.J., and King, J.E. (1991). Geochronology of granitoid rocks in the Archean Slave Province, N.W.T. Geological Association of Canada Program with Abstracts 16, A127.
- van Breemen, O., Davis, W.J., and King, J.E. (1992). Temporal distribution of granitoid plutonic rocks in the Archean Slave Province, northwest Canadian Shield. *Canadian Journal of Earth Science* 29, 2186-2199.
- Vielreicher, N.M., Groves, D.I., Snee, L.W., Fletcher, I.R., McNaughton, N.J. (2010). Broad synchronicity of three goldmineralization styles in the Kalgoorlie gold field—SHRIMP, U-Pb, and  $^{40}\text{Ar}/^{39}\text{Ar}$  geochronological evidence. *Economic Geology* 105, 187–227.

- Wang, X., Chou, I.M., Hu, W., Burruss, R. C., Sun, Q., and Song, Y. (2011). Raman spectroscopic measurements of CO<sub>2</sub> density: Experimental calibration with high-pressure optical cell (HPOC) and fused silica capillary capsule (FSCC) with application to fluid inclusion observations. *Geochimica et Cosmochimica Acta* 75(14), 4080-4093.
- Wang, L.G., Qiu, Y.M., McNaughton, N.J., Groves, D.I., Luo, Z.K., Huang, J. Z., and Liu, Y.K. (1998) Constraints on crustal evolution and gold metallogeny in the Northwestern Jiaodong Peninsula, China, from SHRIMP U–Pb zircon studies of granitoids. *Ore Geology Reviews* 13(1-5), 275-291.
- White, N.C., and Hedenquist, J. W. (1995). Epithermal gold deposits: styles, characteristics and exploration. *SEG Newsletter* 23(1), 9-13.
- Wilkinson, J.J. (2001). Fluid inclusions in hydrothermal ore deposits. *Lithos* 55(1-4), 229-272.
- Williams-Jones, A.E., Bowell, R.J., and Migdisov, A.A. (2009). Gold in Solution. *Elements* 5, 281-287.
- Wilson, C.J.L., Robinson, J.A., and Dugdale, A.L. (2009). Quartz vein fabrics coupled to elevated fluid pressures in the Stawell gold deposit, south-eastern Australia. *Mineralium Deposita* 44, 245-263.
- Winderbaum, L., Ciobanu, C.L., Cook, N.J., Paul, M., Metcalfe, A., and Gilbert, S. (2012). Multivariate analysis of an LA-ICP-MS trace element dataset for pyrite. *Mathematical Geoscience* 44(7), 823-842.
- Wood, P.C., Thomas, A.V., Burrows, D.R., Macdonald, A.J., Noble, S.R., and Spooner, E. T. C. (1984). CO<sub>2</sub>-bearing lowmoderate salinity fluids in Archean gold-quartz-carbonate-(W-Mo) vein deposits and magmatically derived Mo, W, Ta and Sn mineralization labs. I: *Geological Society of America Abstracts with Programs* 16(6), 700.

- Wopenka, B., and Pasteris, J.D. (1986). Limitations to quantitative analysis of fluid inclusions in geological samples by laser Raman microprobe spectroscopy. *Applied Spectroscopy* 24, 144–151.
- Wopenka, B., and Pasteris, J.D. (1987). Raman intensities and detection limits of geochemically relevant gas mixtures for a laser Raman microprobe. *Anal. Chemical* 59, 2165-2170.
- Yamamoto, J., and Kagi, H. (2006). Extended micro-Raman densimeter for CO<sub>2</sub> applicable to mantle-originated fluid inclusions. *Chemical Letters* 35(6), 610-611
- Yamamoto, J., Kagi, H., Kaneoka, I., Lai, Y., Prikhod'ko, V.S., and Arai, S. (2002). Fossil pressures of fluid inclusions in mantle xenoliths exhibiting rheology of mantle minerals: implications for the geobarometry of mantle minerals using micro-Raman spectroscopy. *Earth and Planetary Science Letters* 198(3-4), 511-519.
- Yardley, B.W. (2005). 100th Anniversary Special Paper: metal concentrations in crustal fluids and their relationship to ore formation. *Economic Geology* 100(4), 613-632.
- Yardley, B.W. (2013). The chemical composition of metamorphic fluids in the crust. In Harlov, D.E., Austrheim, H. (eds.) *Metasomatism and the Chemical Transformation of Rock*. Springer-Verlag, Berlin, Heidelberg, p. 17-51.
- Yardley, B.W., and Bodnar, R.J. (2014). Fluids in the continental crust. *Geochemical Perspectives* 3(1), 1-2.

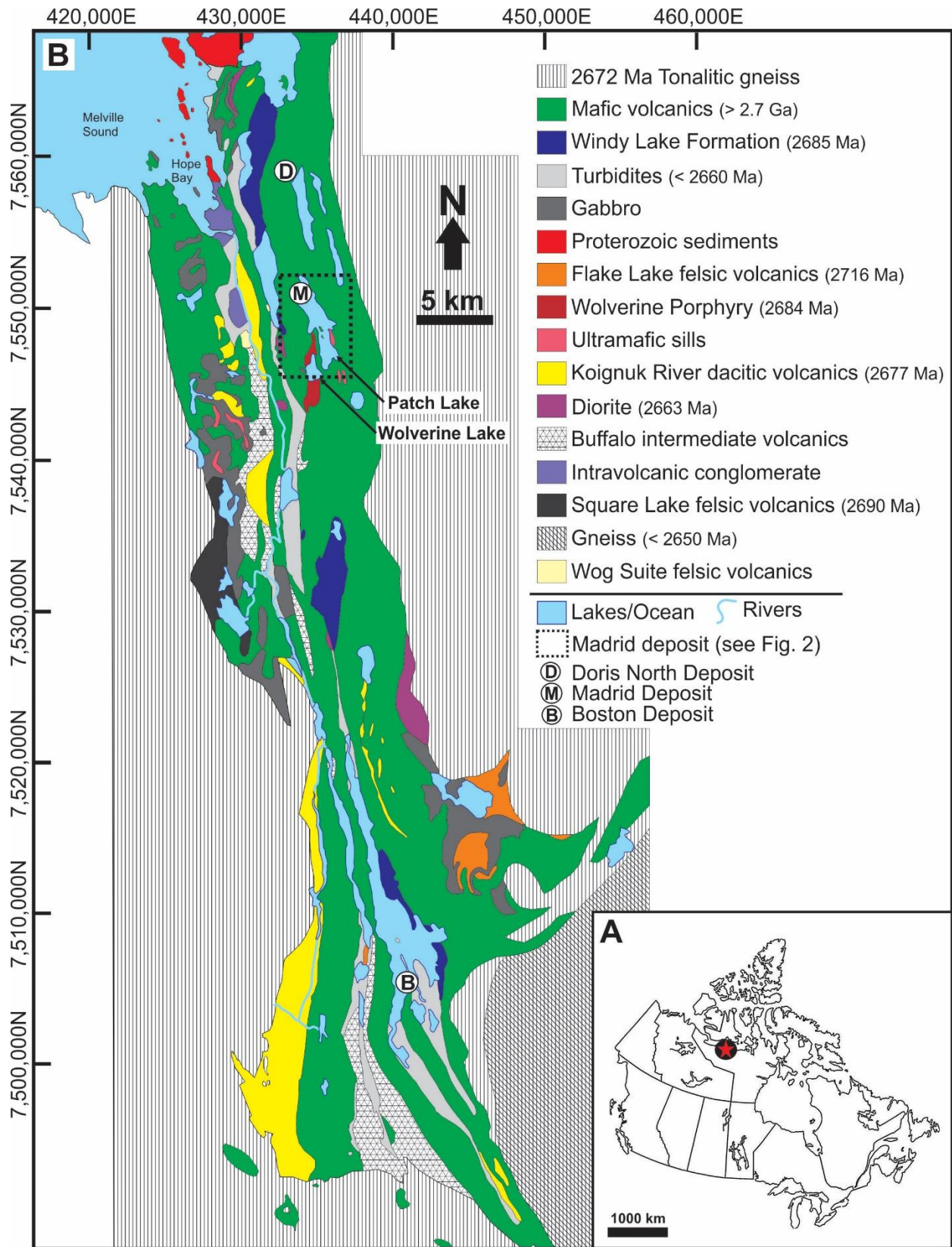


Figure 2-1: A) Map of Canada showing the location of the Hope Bay Greenstone Belt. B) Geological map of the Hope Bay Greenstone Belt with the Doris North (D), Madrid (M) and Boston (B) deposits shown. The region around the Madrid deposit (dashed box) is shown in more detail in Figure 2. UTM coordinates are shown (UTM NAD83 Zone 13). Map adapted from Clow et al. (2013). Geochronology of the rock units is from Sherlock et al., (2012) and Clow et al., (2013).

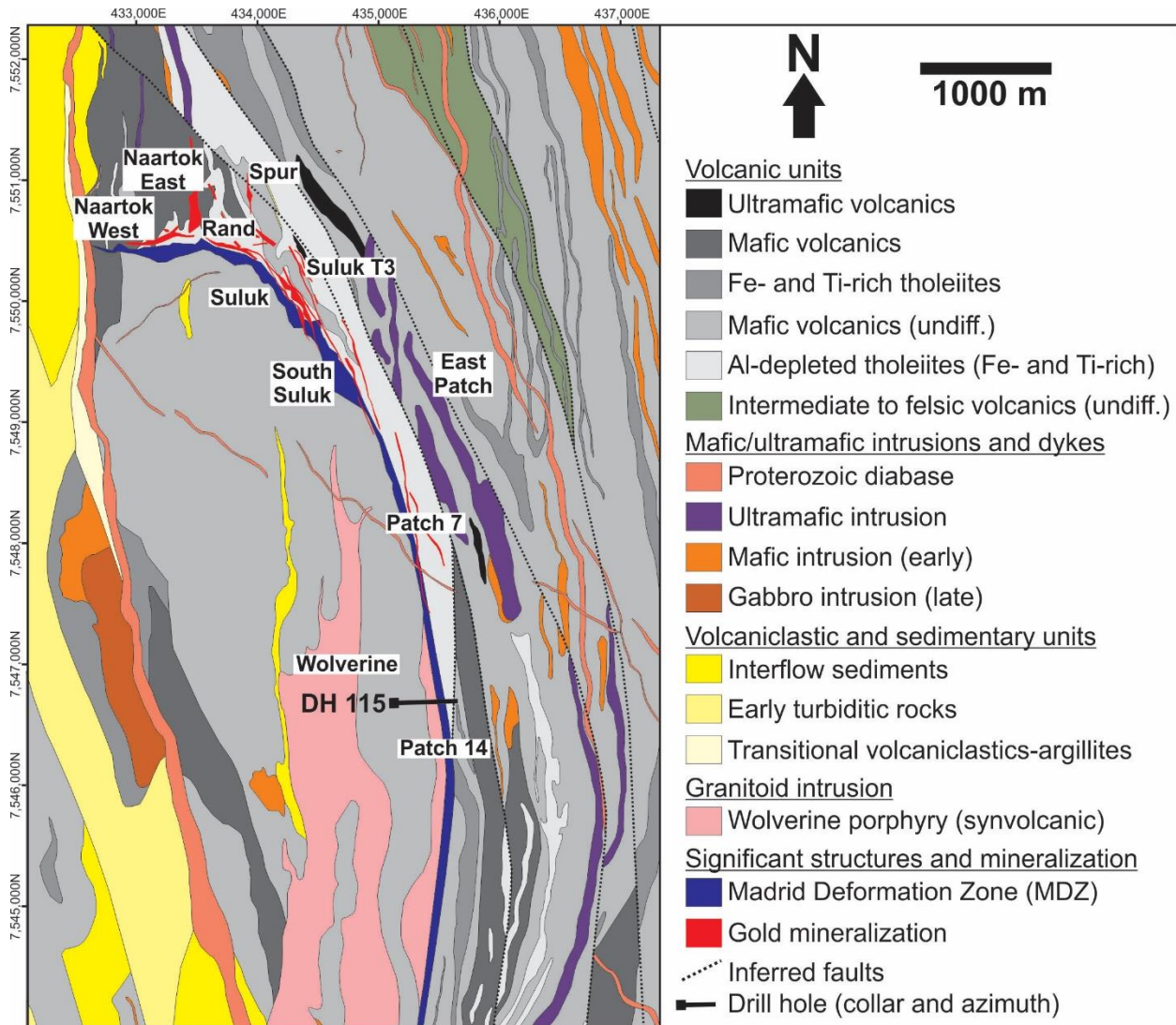


Figure 2-2: Simplified geological map of the Madrid region of the Hope Bay Greenstone Belt; shown in white boxes are sub-regions (e.g., Patch 14) discussed in the text. Samples from high-grade vein 115-03 and low-grade vein 115-02 were taken from drill hole (DH) TM00115 in the Patch 14 sub-region. UTM coordinates are shown (UTM NAD83 Zone 13). Lakes and rivers have been removed for clarity. Map adapted from Clow et al. (2013).

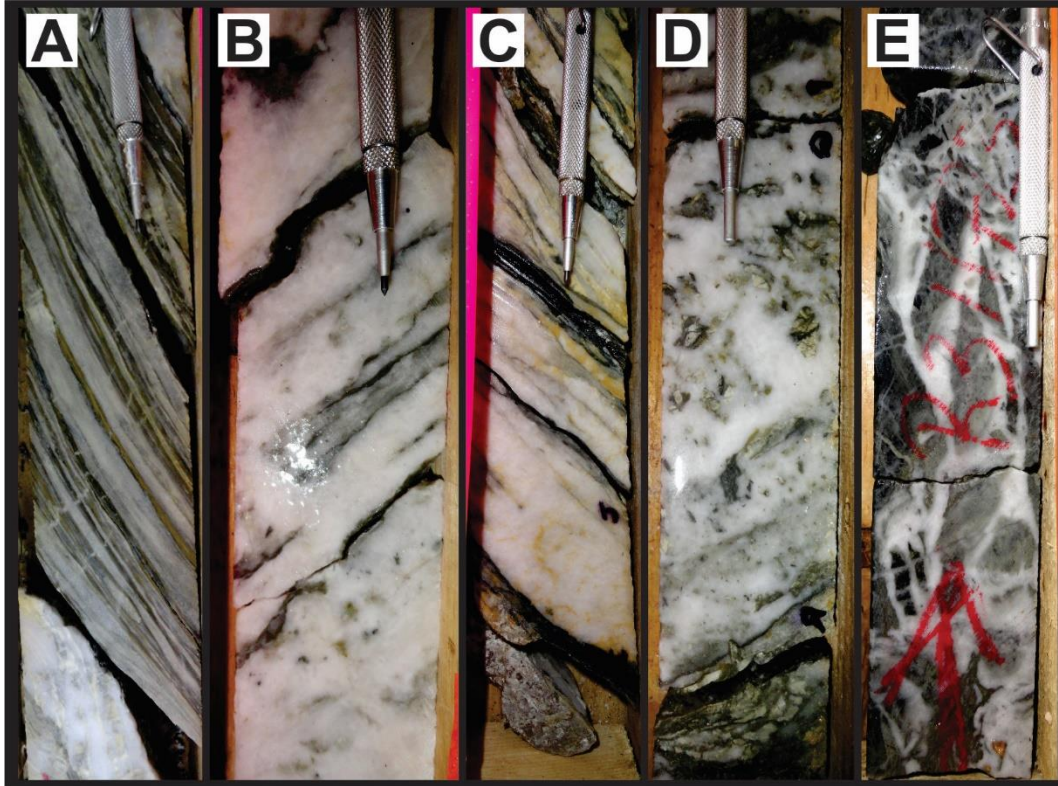


Figure 2-3: Drill core images. A) Strongly foliated and altered quartz-feldspar porphyry (i.e., Wolverine Porphyry) characteristic of the Madrid Deformation Zone. Note the alternating bands of quartz + carbonate  $\pm$  albite (milky white) and sericite  $\pm$  chlorite (dark yellow and green-black laminations). B, C) Laminated quartz-carbonate vein samples in the Madrid Patch 14 sub-region. Laminations are of altered wall rock composed of carbonate + sericite + rutile + pyrite  $\pm$  chlorite. Yellowish ankerite is present in some vein samples. D) An interval of a broadly laminated quartz-carbonate vein in the Madrid Patch 14 sub-region locally displaying brecciation texture. E) Brecciated quartz-carbonate vein sample in the Madrid Naartok sub-region which shows multiple generations of quartz veining.

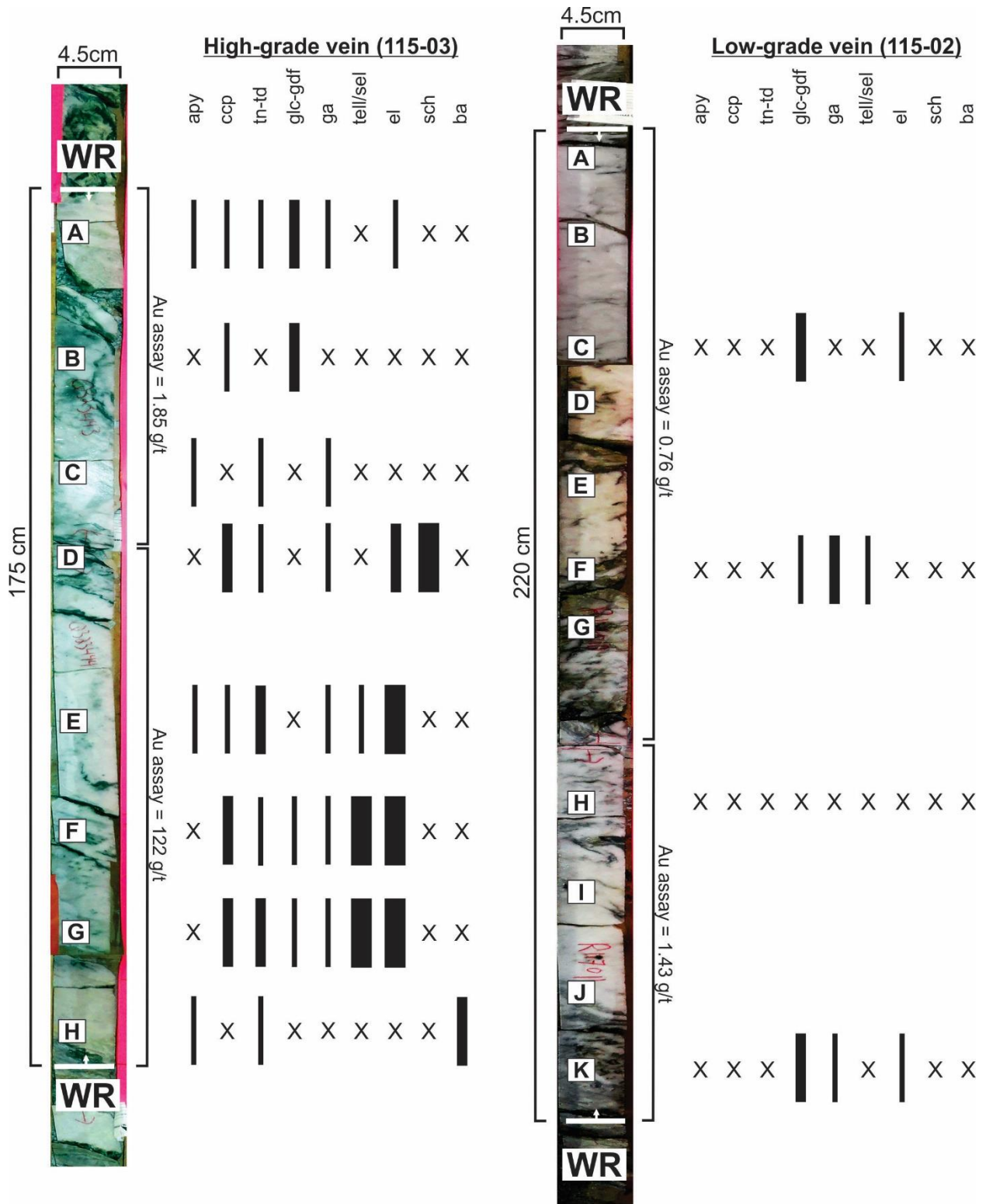


Figure 2-4: Photos of two ore-grade drill core intercepts of vein packages showing the estimated mineral abundances. Locations of prepared polished thin sections used for detailed petrographic and mineralogical studies, as discussed in the text, are shown in lettered boxes. Mineral abundances were estimated qualitatively based on frequency of observation (i.e., grain count) via SEM. Mineral abundances are represented by the thickness of the black lines, with an 'X' indicating that mineral phase was not identified. The high-grade vein 115-03 shows evidence of late upgrading characterized by the presence of the assemblage tn-td+ccp+el±tell/sel. Abbreviations: apy – arsenopyrite, ba – barite, ccp – chalcopyrite, el – electrum, ga – galena, gdf – gersdorffite, sch – scheelite, tell/sel – tellurides/selenides (e.g., altaite, clausthalite, hessite, petzite), tn-td – tennantite-tetrahedrite, g/t – grams per tonne.

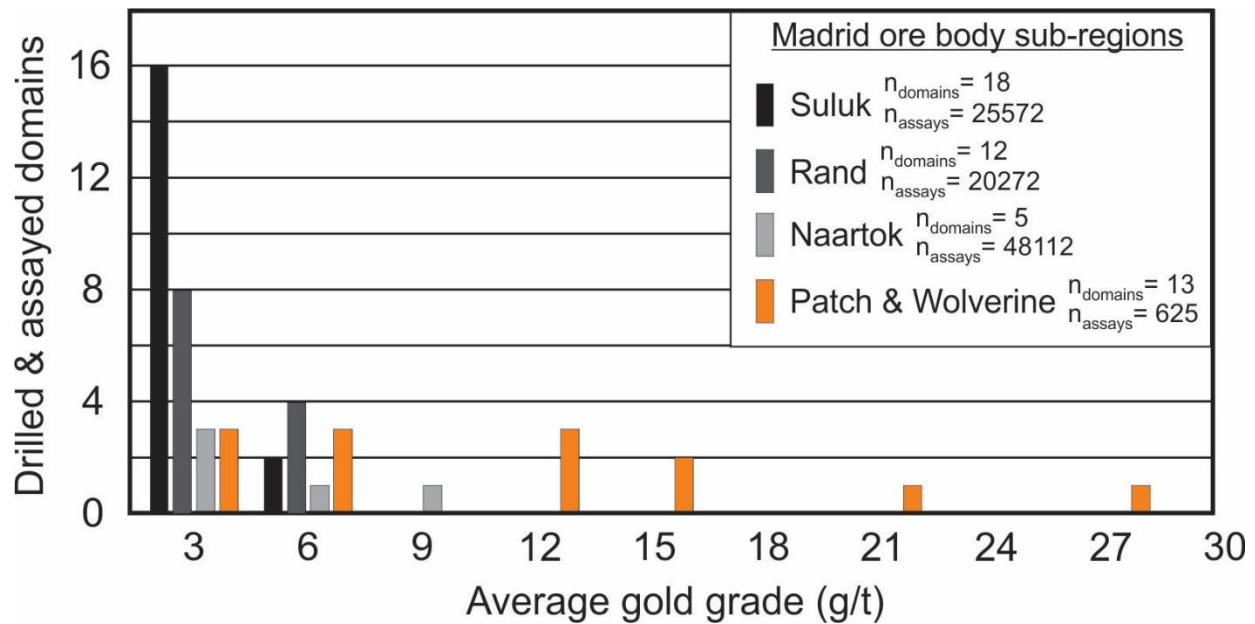


Figure 2-5: Histogram displaying average gold grades in the Rand, Suluk, Naartok, Patch and Wolverine sub-regions of the Madrid deposit based on assays of 0.25 to 1 m drill core intervals. Data is from the TMAC Resources Incorporated NI 43-101 report (Clow et al., 2015). Each Madrid sub-region is divided into a number of domains ( $n_{\text{domains}}$ ) that were drilled and assayed. The total number of assays ( $n_{\text{assays}}$ ) represent the total assays associated with all drilled domains in a given sub-region (e.g., Suluk: total number of drilled domains = 18; total number of assays from all domains = 25572). Northern Madrid sub-regions (Rand, Suluk and Naartok) have average gold grades  $\leq 8.13$  g/t with the highest proportion of domains grading  $< 3$  g/t Au in all assayed domains. Note that in contrast, the Southern Madrid sub-regions (Patch and Wolverine) have more widely distributed average gold grades ranging between 1.05 to 26.68 g/t Au.

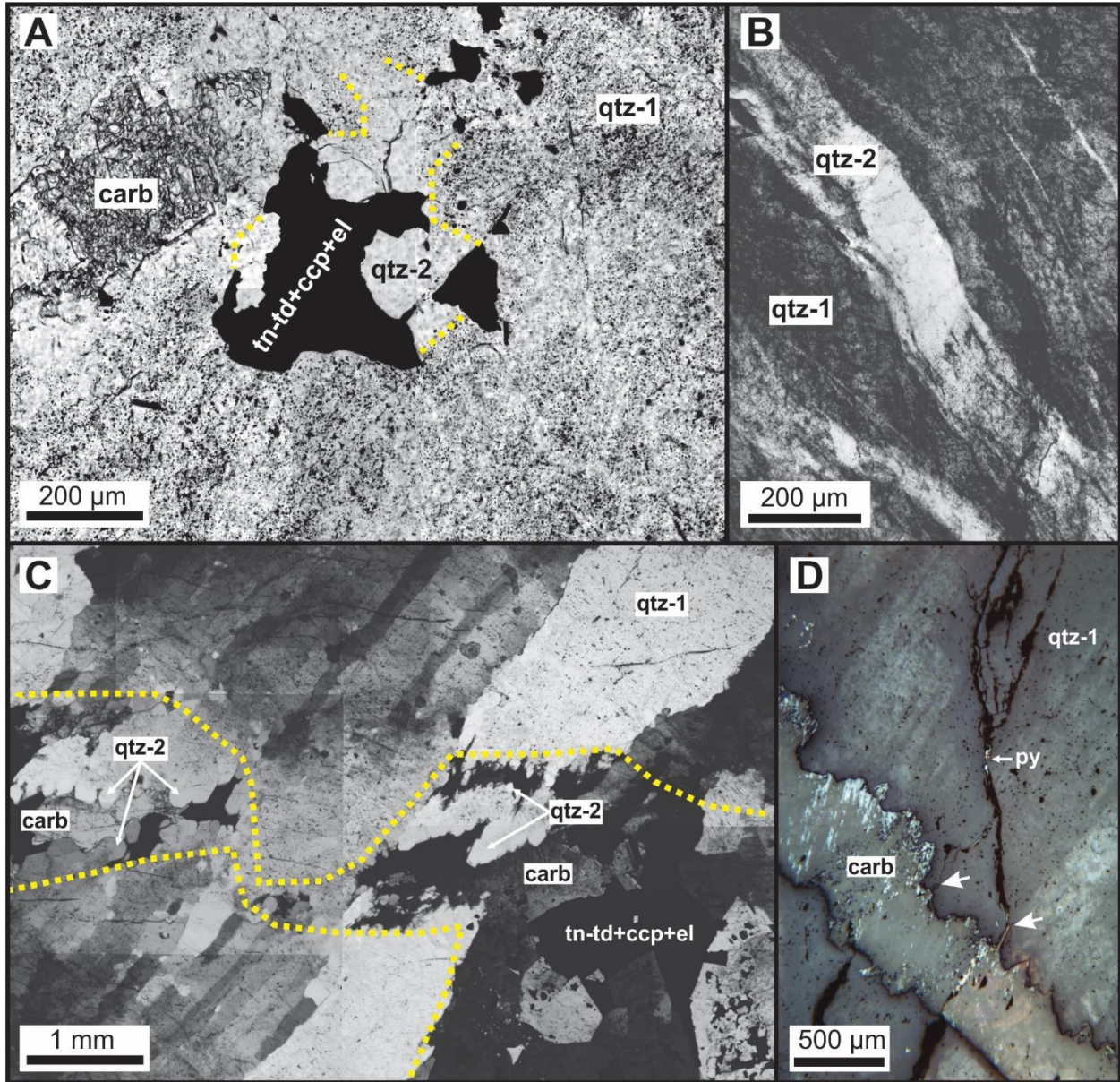


Figure 2-6: Photomicrographs showing representative textures seen in the high-grade vein (115-03) intercept. A) More transparent secondary quartz domain (qtz-2; outlined by dashed yellow lines) associated with an intergrowth of tn-td+ccp+el which post-dates early quartz (qtz-1). B) More transparent veinlets of qtz-2 cutting through the more turbid qtz-1. C) A mosaic illustrating carbonate-filled cavities that appear as broadly continuous veinlets at a thin section scale. Note that these cavities contain the assemblage tn-td+ccp+el and are associated with qtz-2. Also apparent is the fibrous texture of qtz-1 which terminates against the cavities and is subsequently overgrown by euhedral qtz-2 that protrudes into the cavities. D) A reflected light image of a carbonate-filled veinlet cutting qtz-1. Note that the fractures extending away from this veinlet (white arrows) host pyrite, barite and native silver. Abbreviations: carb – carbonate, ccp – chalcopyrite, el – electrum, py – pyrite, qtz – quartz, tn-td – tennantite-tetrahedrite.

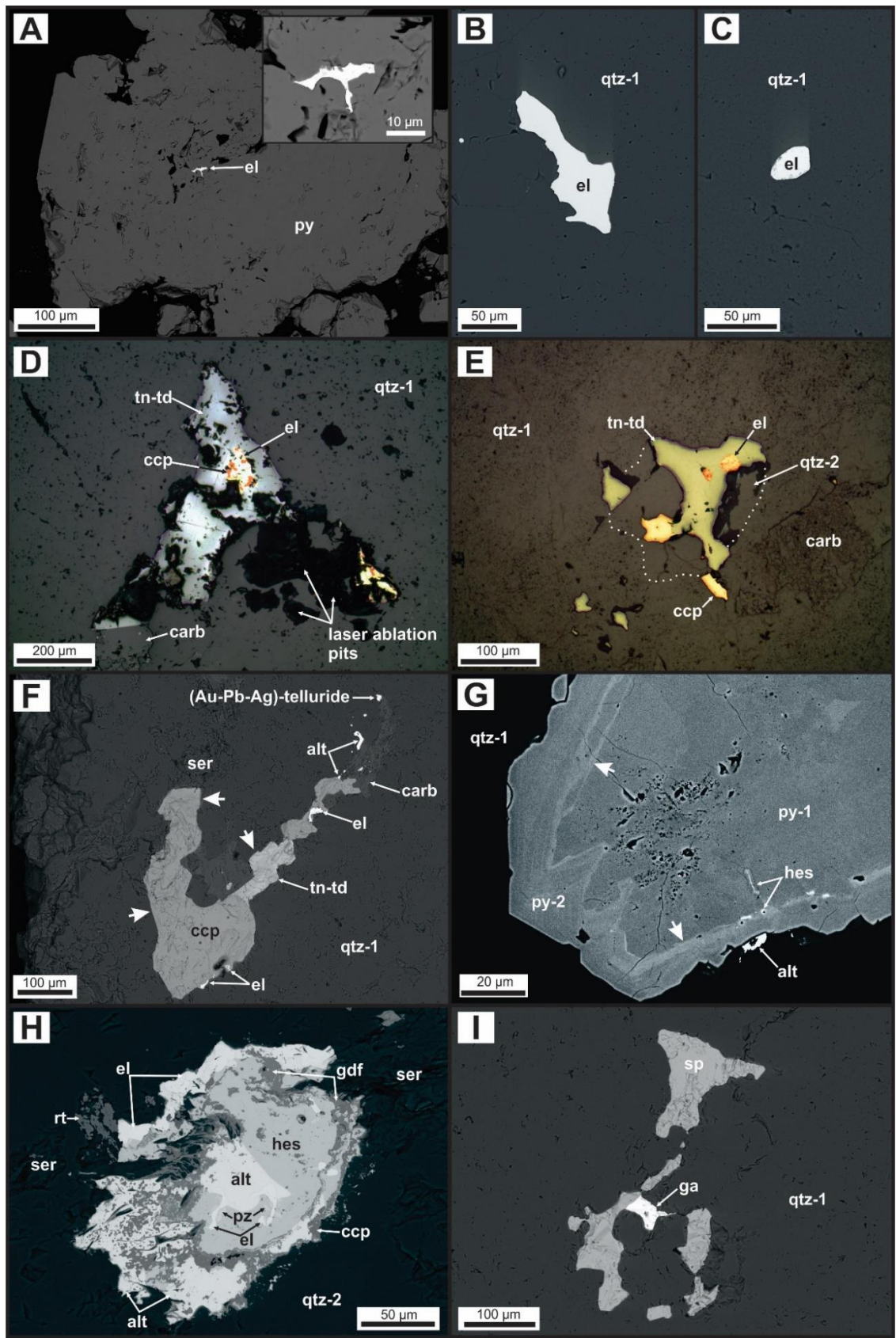


Figure 2-7: Combination of SEM-BSE and reflected light (RL) images showing the ore minerals identified in quartz-carbonate veins. A) An inclusion of electrum in pyrite in the low-grade vein (115-02). See the inset for expansion of electrum inclusion. B, C) Electrum inclusions in quartz (qtz-1) from the high-grade vein (115-03). Electrum in qtz-1, with an average of 89.8 atomic % Au, is the primary control on Au grade in the low-grade vein and in the Au-poor region of the high-grade vein (i.e., between 408.51 – 409.35 m; 1.85 g/t). D) RL image of the assemblage tn+td+ccp+el. Note that fluid inclusions of type 3b were identified along healed planes in the quartz (qtz-2) associated with this mineralization. E) RL image of an occurrence of tn+td+ccp+el associated with secondary quartz (qtz-2). F) SEM-BSE image showing the assemblage of tn+td+ccp+el+tellurides+carb+ser in quartz. Note the planar faces of quartz (small white arrows) which indicate it grew into a cavity. G) SEM-BSE image of a subhedral grain of early pyrite (py-1) displaying a sieve-textured core that is overgrown by a later generation pyrite (py-2) associated with As zoning and the tellurides hessite and altaite. H) SEM-BSE image of an aggregate of tellurides [hes+alt+pz] + el + ccp + gdf in a rutile- and sericite-bearing vein septum and secondary quartz (qtz-2). I) SEM-BSE image of sp and ga infilling a cavity and fractures in quartz. Abbreviations: alt – altaite, carb – carbonate, ccp – chalcopyrite, el – electrum, ga – galena, gdf – gersdorffite, hes – hessite, py – pyrite, pz – petzite, qtz – quartz, rt – rutile, ser – sericite, sp – sphalerite, tn+td – tennantite-tetrahedrite.

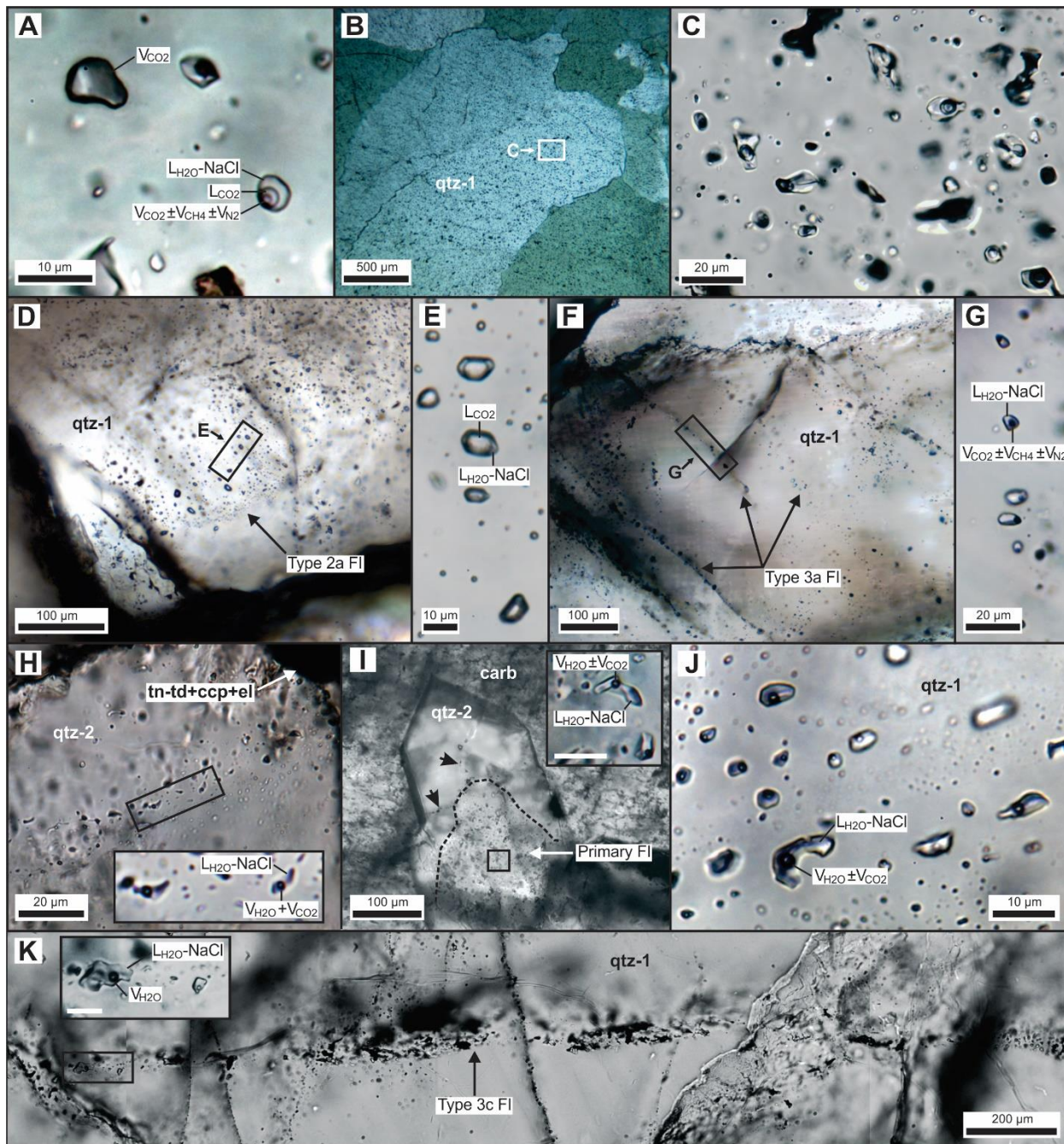


Figure 2-8: Photomicrographs of fluid inclusion types and subtypes. A) Three phase, type 1 -  $\text{H}_2\text{O}$ - $\text{NaCl}$ - $\text{CO}_2 \pm \text{CH}_4 \pm \text{N}_2$  inclusion and a mono phase, type 2b  $\text{CO}_2$ -only inclusion in orogenic vein quartz. B) The early quartz (qtz-1) hosting numerous clusters of type 1 fluid inclusions of indeterminate origin. C) Magnified image of three phase, type 1 inclusions (white box in frame B) and decrepitated fluid inclusions (black inclusions). D) Quartz hosting a plane of type 2a  $\text{CO}_2 \pm \text{CH}_4 \pm \text{N}_2 + \text{H}_2\text{O}$ - $\text{NaCl}$  inclusions. E) Magnified image of type 2a inclusions (black box in frame D). F) A quartz grain hosting multiple planes of type 3a  $\text{H}_2\text{O}$ - $\text{NaCl}$ - $\text{CO}_2 \pm \text{CH}_4 \pm \text{N}_2$  inclusions. G) Magnified image of type 3a inclusions (black box in frame F). H) A plane of type 3b inclusions trapped in a healed fracture physically connected to, and extending away from, an intergrowth of tn-td+ccp+el. I) A euhedral quartz crystal protruding into a carbonate-filled cavity hosting primary type 3b inclusions in the core of the crystal (dashed outline) and along fractures (black arrows). Magnified type 3b inclusions from the core are shown in the inset box. Inset scale bar is 10  $\mu\text{m}$ . J) A secondary plane of type 3b inclusions displaying consistent liquid:vapor phase ratios. K) A secondary plane of type 3c fluid inclusions crosscutting qtz-1 grain boundaries. Magnified type 3c inclusions are shown in the inset box. Inset scale bar is 30  $\mu\text{m}$ .

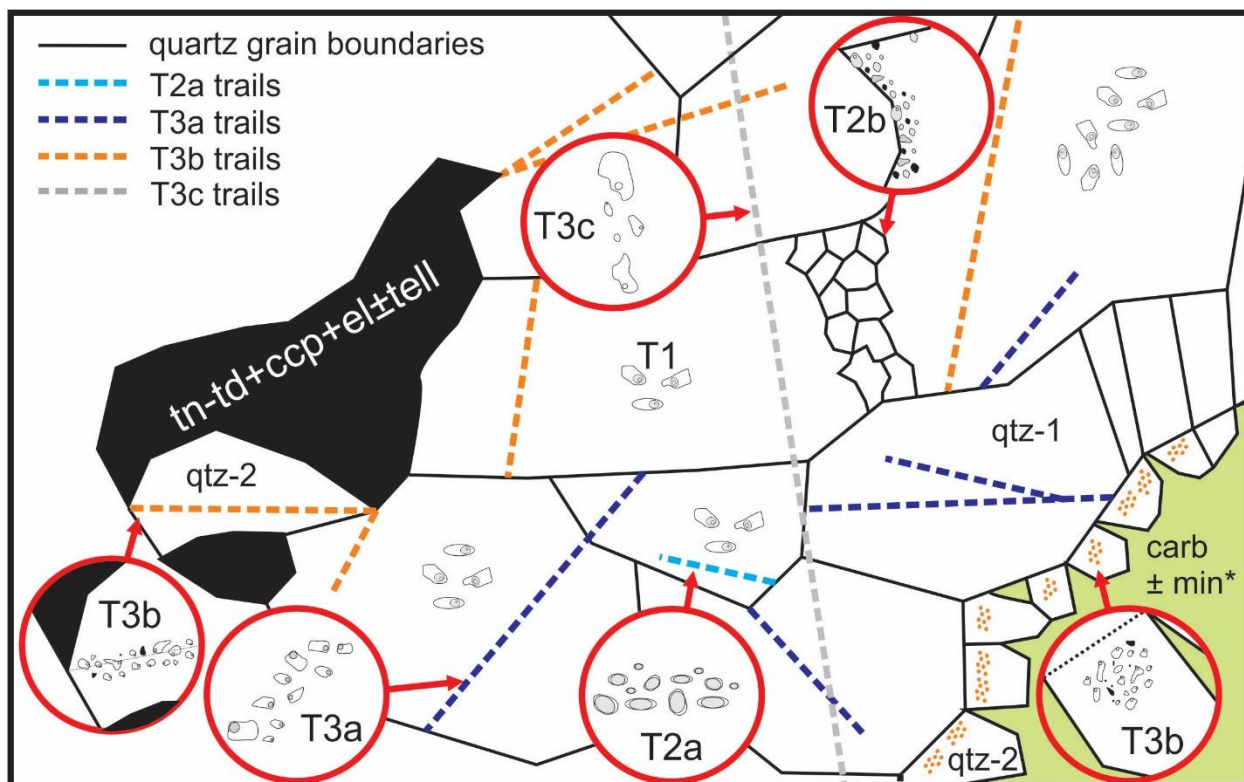


Figure 2-9: Schematic sketch summarizing the textural relationship between the mineral assemblage identified in the high-grade vein (115-03), primary quartz (qtz-1), secondary quartz (qtz-2) associated with  $tn+td+ccp+el\pm tell$  mineralization, carbonate-filled cavities, and fluid inclusion assemblages. Type 1 inclusions occur in clusters of indeterminate origin within qtz-1 grains. Carbonate-filled cavities are lined with euhedral qtz-2 crystals containing type 3b inclusion in the cores. Type 2a, 3a, and 3b inclusions are commonly hosted in secondary trails in quartz. Type 3c inclusions, hosted in secondary trails, crosscut quartz grain boundaries and other inclusion trails. Black inclusions in type 2b and 3b assemblages represent empty inclusions. Abbreviations: carb – carbonate, ccp – chalcopyrite, el – electrum, tell – tellurides, tn+td – tennantite-tetrahedrite. Note: min\* represents the assemblage  $tn+td+el+ccp\pm tell$ .

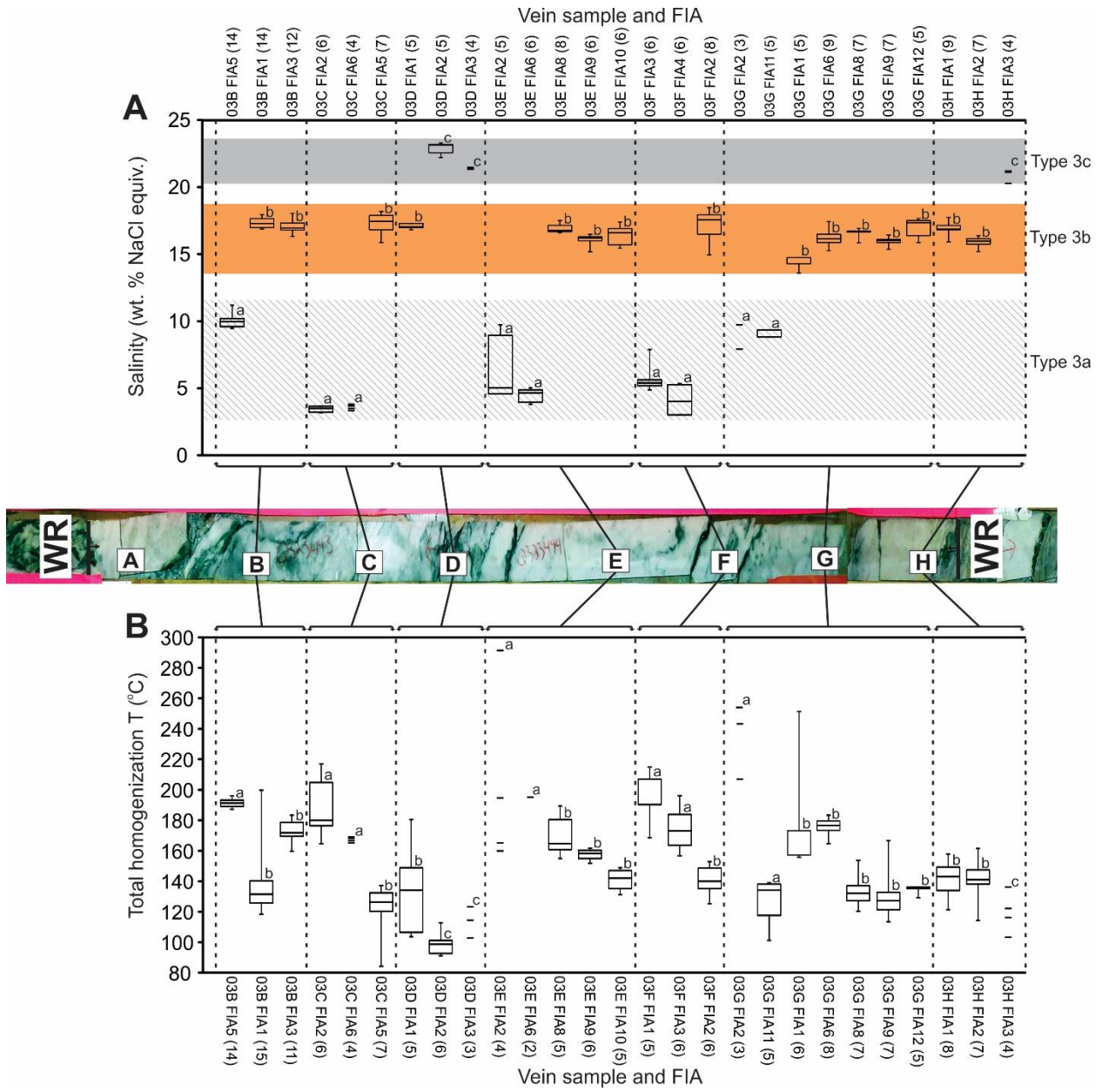


Figure 2-10: A summary of microthermometric data for fluid inclusions showing salinity (frame A) and total homogenization (frame B) data for type 3a, 3b and 3c aqueous fluid inclusion assemblages from the high-grade vein (115-03). The letters 'a', 'b' and 'c' signifies data is from type 3a, 3b, or 3c fluid inclusions, respectively. The number of inclusions (n) analyzed and used in statistical treatment are shown in brackets beside the assemblage ID. Fluid inclusion assemblages with < 5 measurements are expressed as individual data points. Type 1 and 2a inclusions are omitted for clarity of comparison between H<sub>2</sub>O-dominated inclusion types. A complete microthermometric data set for all analyzed FIA can be found in Table EA 2-1.

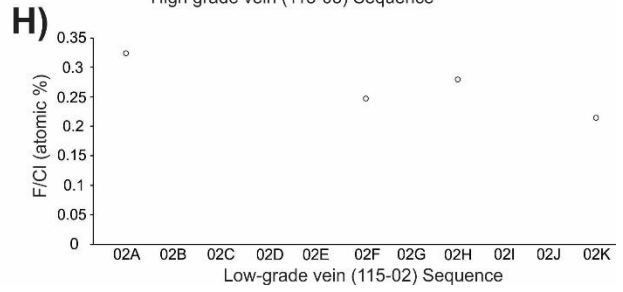
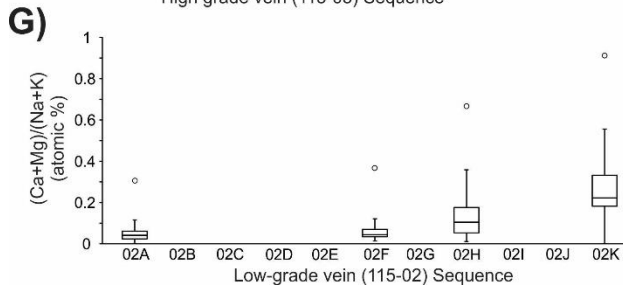
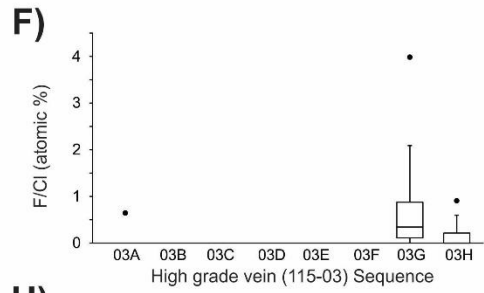
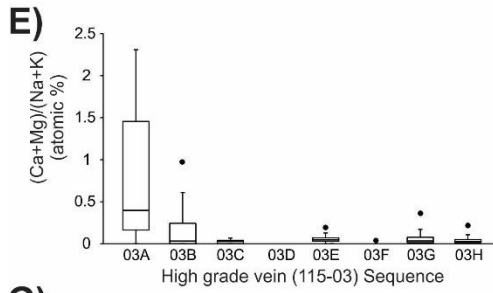
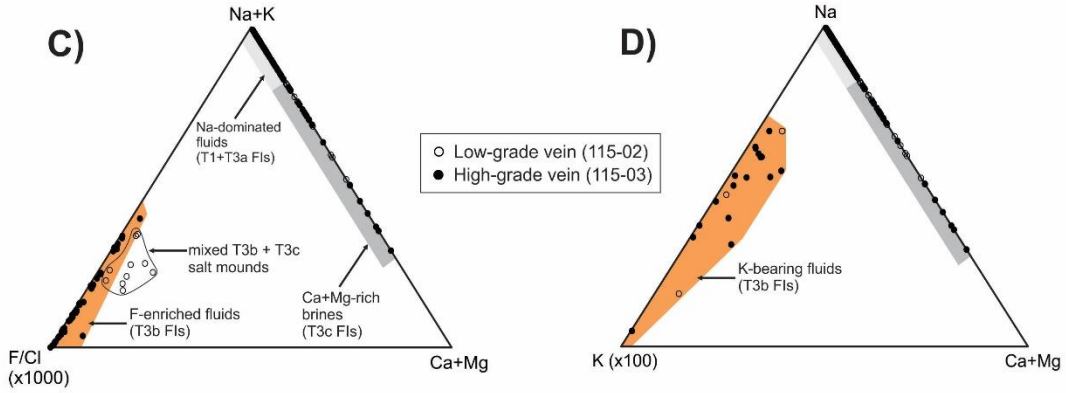
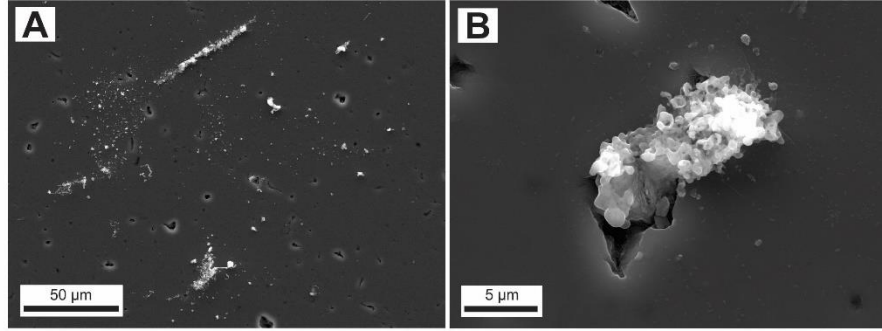


Figure 2-11: Analysis of evaporate mounds generated from decrepitating quartz-hosted fluid inclusions from across the low-grade (115-02) and high-grade (115-03) veins. A) A secondary electron SEM image of trails and clusters of decrepitate mounds on the surface of quartz. B) A secondary electron SEM image of a decrepitate mound in a cavity in quartz. C) Na+K versus Ca+Mg versus F/Cl (x1000) ternary plot (all data from both veins). D) Na versus Ca+Mg versus K (x1000) ternary plot (all data from both veins). Ternary plots show the presence of three distinct fluids: (i) Na-dominated fluid, (ii) a Ca+Mg-rich fluid, and (iii) a F±K-enriched fluid. E) (Ca+Mg)/(Na+K) ratios from across the high-grade vein. F) F/Cl ratios from across the high-grade vein. G) (Ca+Mg)/(Na+K) ratios from across the low-grade vein. H) F/Cl ratios from across the low-grade vein. Note: All ratios and abundances are reported in atomic %. A total of 247 mounds from the high-grade vein and 83 mounds from the low-grade vein were analyzed. Open and closed circles represent mound analyses from the low-grade and high-grade vein, respectively. The ends of the whiskers are set to 1.5 x IQR (interquartile range) above and below the third and first quartiles, respectively. If data points plot outside of these ranges, they are shown as outliers. Decrepitate mounds from sample 03D from the high-grade vein and samples 02B, 02C, 02D, 02E, 02G, 02I, and 02J from the low-grade were not analyzed. A complete decrepitate mound data set can be found in Table EA 2-3.

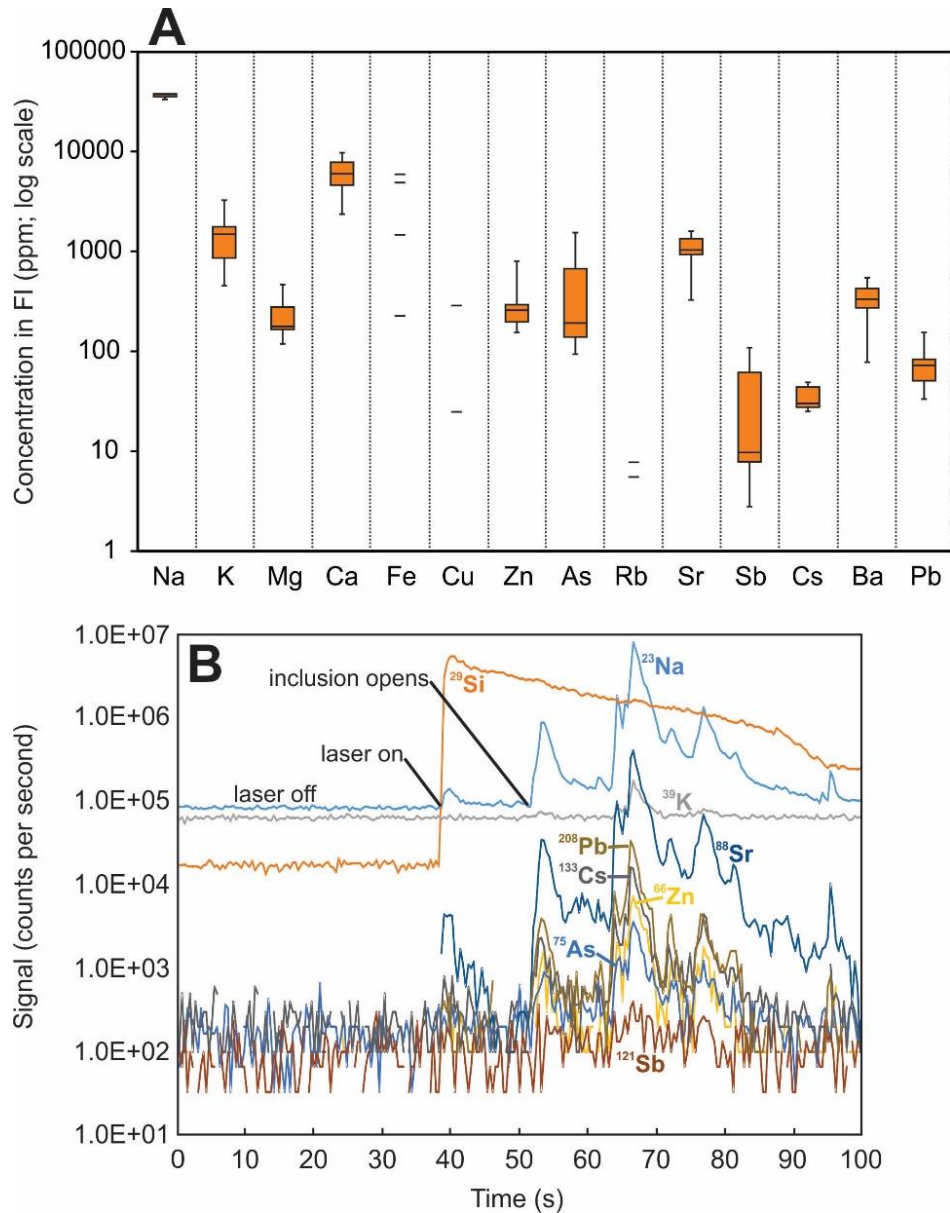


Figure 2-12: A) Laser ablation ICP-MS results from the analyses of type 3b fluid inclusions from high-grade vein samples 03D, 03E, and 03G. Values below detection limits were excluded from statistical treatment rather than set to 0 ppm, hence the number of inclusions considered is different for each element. B) Laser ablation ICP-MS signal (count rate versus time) from a type 3b inclusion hosted in the high-grade vein. A complete LA-ICP-MS data set for all analyzed inclusions can be found in Table EA 2-4.

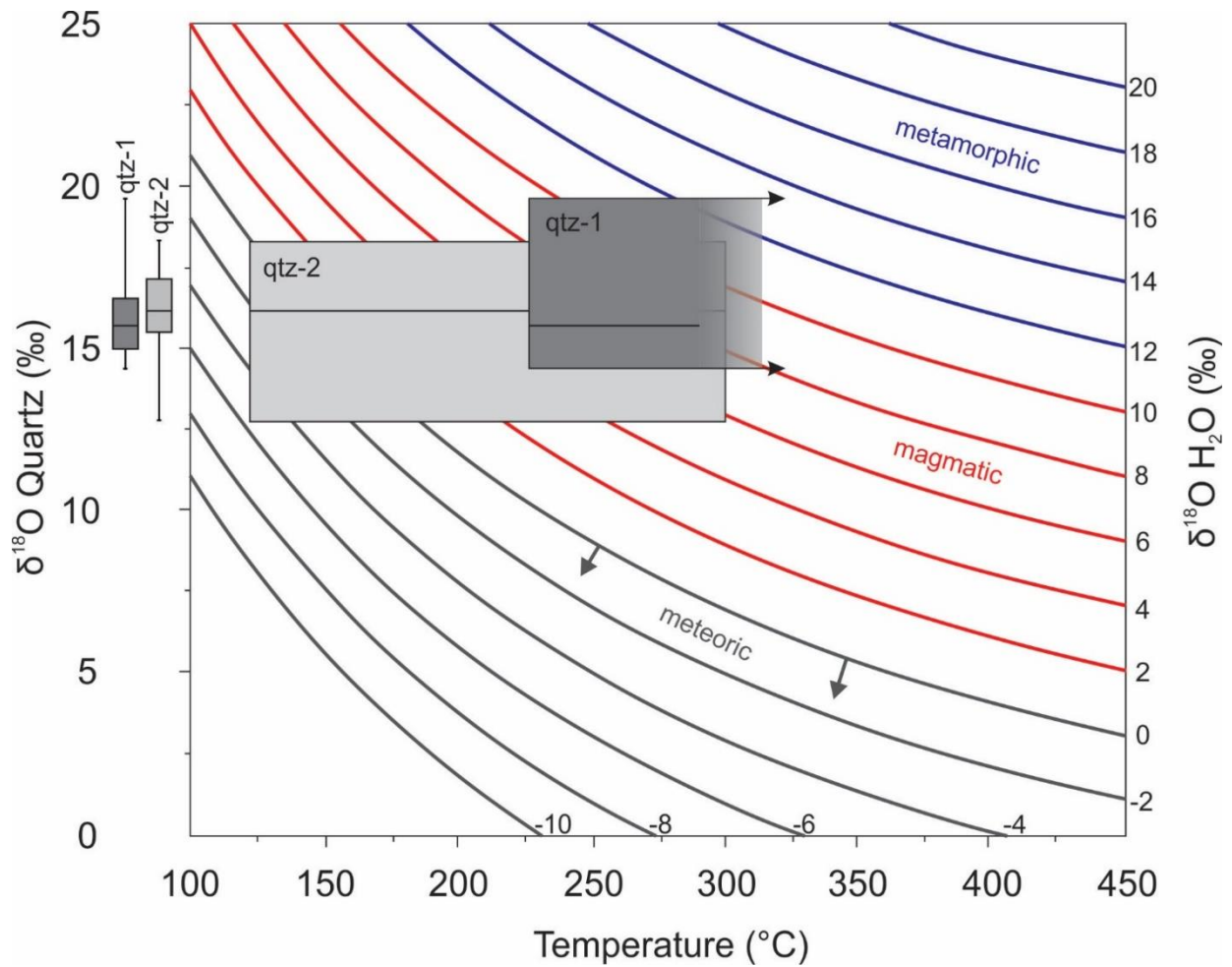


Figure 2-13: Ranges in  $\delta^{18}\text{O}$  for quartz-1 ( $n=10$ ) and quartz-2 ( $n=13$ ) from high-grade vein samples. Box and whisker plots are shown at the left of the plot. Boxes encompassing the total range in data are shown and correspond to the estimated temperature ranges for quartz formation based on mineralogical and microthermometric constraints. The lines through the boxes represent the averages. Isopleths for associated fluid  $\delta^{18}\text{O}$  shown were calculated using the quartz- $\text{H}_2\text{O}$  fractionation equation of Matsushita et al. (1979). A complete SIMS  $\delta^{18}\text{O}$  data set for all analyzed quartz grains can be found in Table EA 2-5.

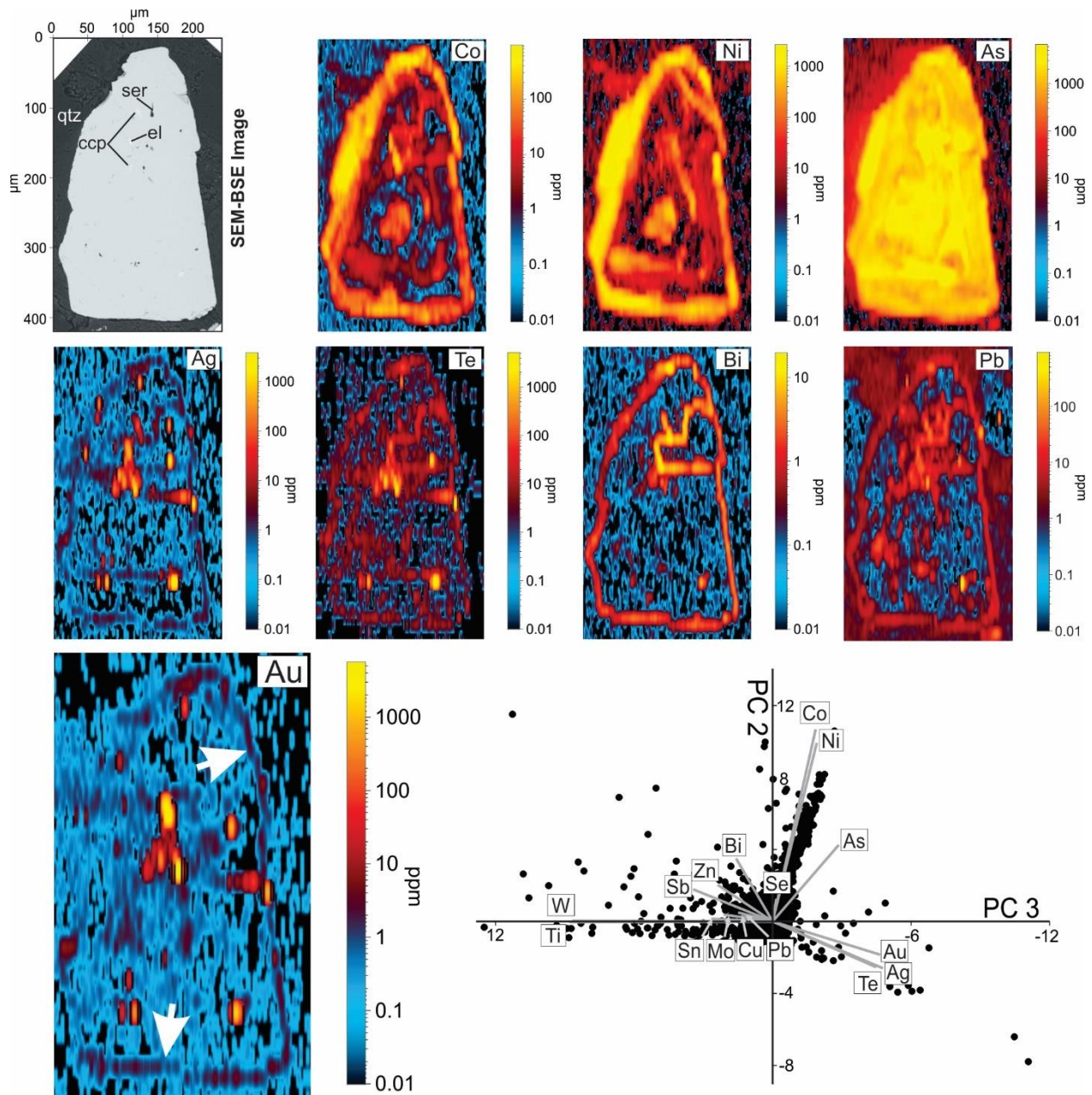


Figure 2-14: LA-ICP-MS trace element laser maps of a hydrothermal pyrite grain from the high-grade vein sample 115-03D contoured using logarithmic values. Also shown is the corresponding SEM-BSE image and principle component analysis (PCA). The PCA plot was generated by using the elemental map data as a collection of time-series data points. Some points from the PCA plots have been deleted for clarity.

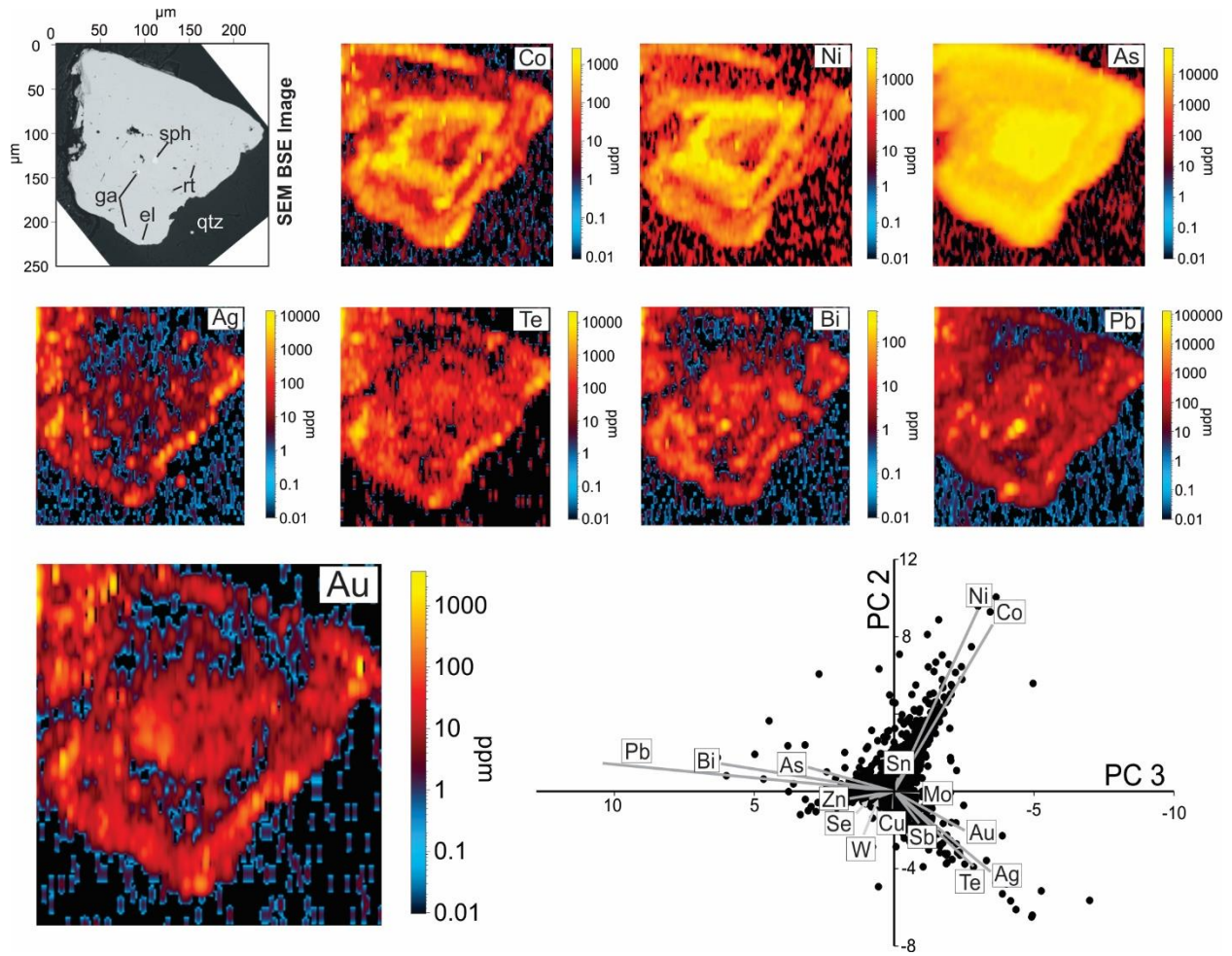


Figure 2-15: LA-ICP-MS trace element laser maps of a hydrothermal pyrite grain from the high-grade vein sample 115-03F contoured using logarithmic values. Also shown is the corresponding SEM-BSE image and principle component analysis (PCA). The PCA plot was generated by using the elemental map data as a collection of time-series data points. Some points from the PCA plots have been deleted for clarity.

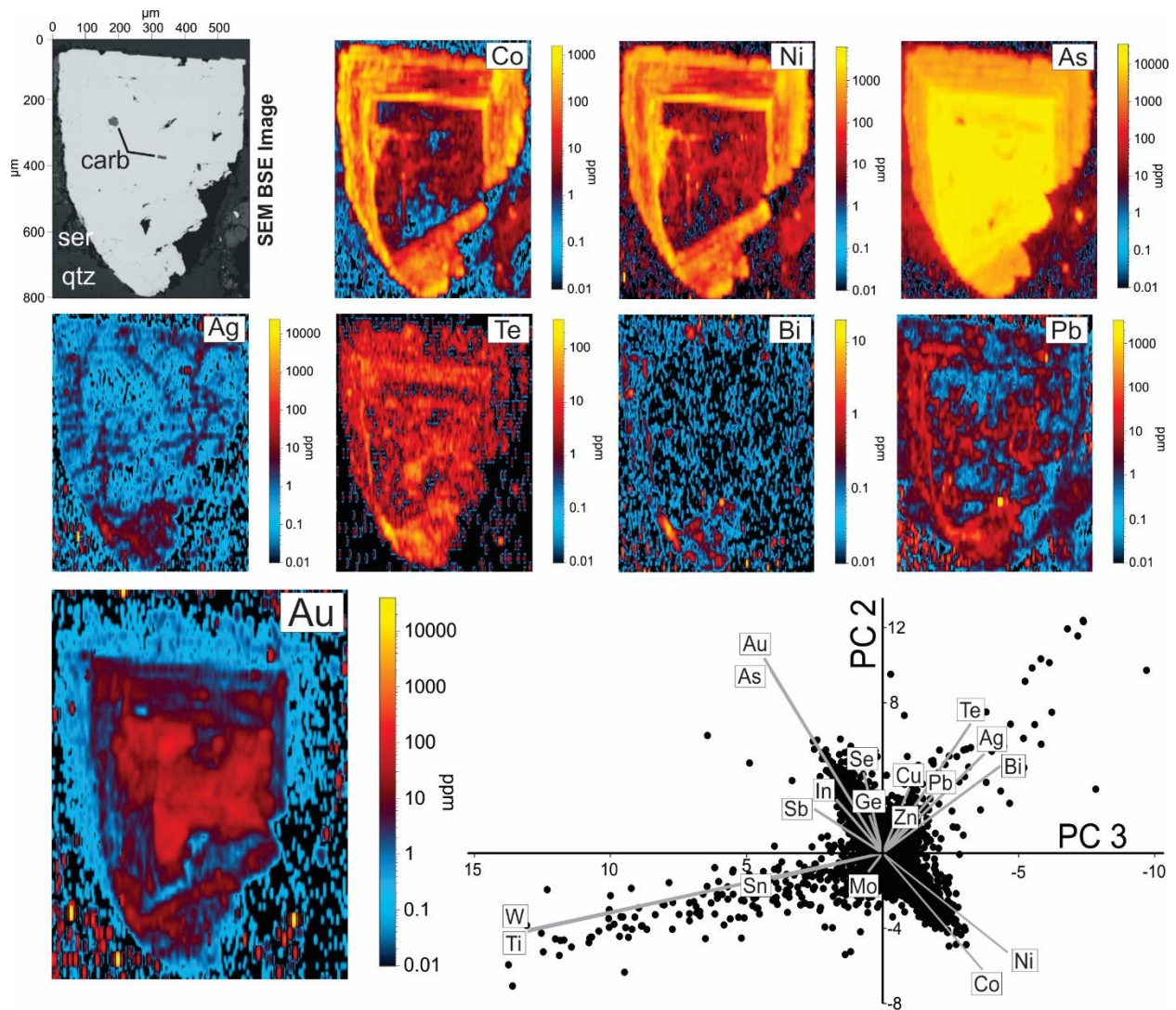


Figure 2-16: LA-ICP-MS trace element laser maps of pyrite grains, contoured using logarithmic values, for material from the low-grade vein sample 115-02F. Also shown are the corresponding SEM-BSE images and principle component analyses (PCA). The PCA plot was generated by using the elemental map data as a collection of time-series data points. Some points from the PCA plots have been deleted for clarity.

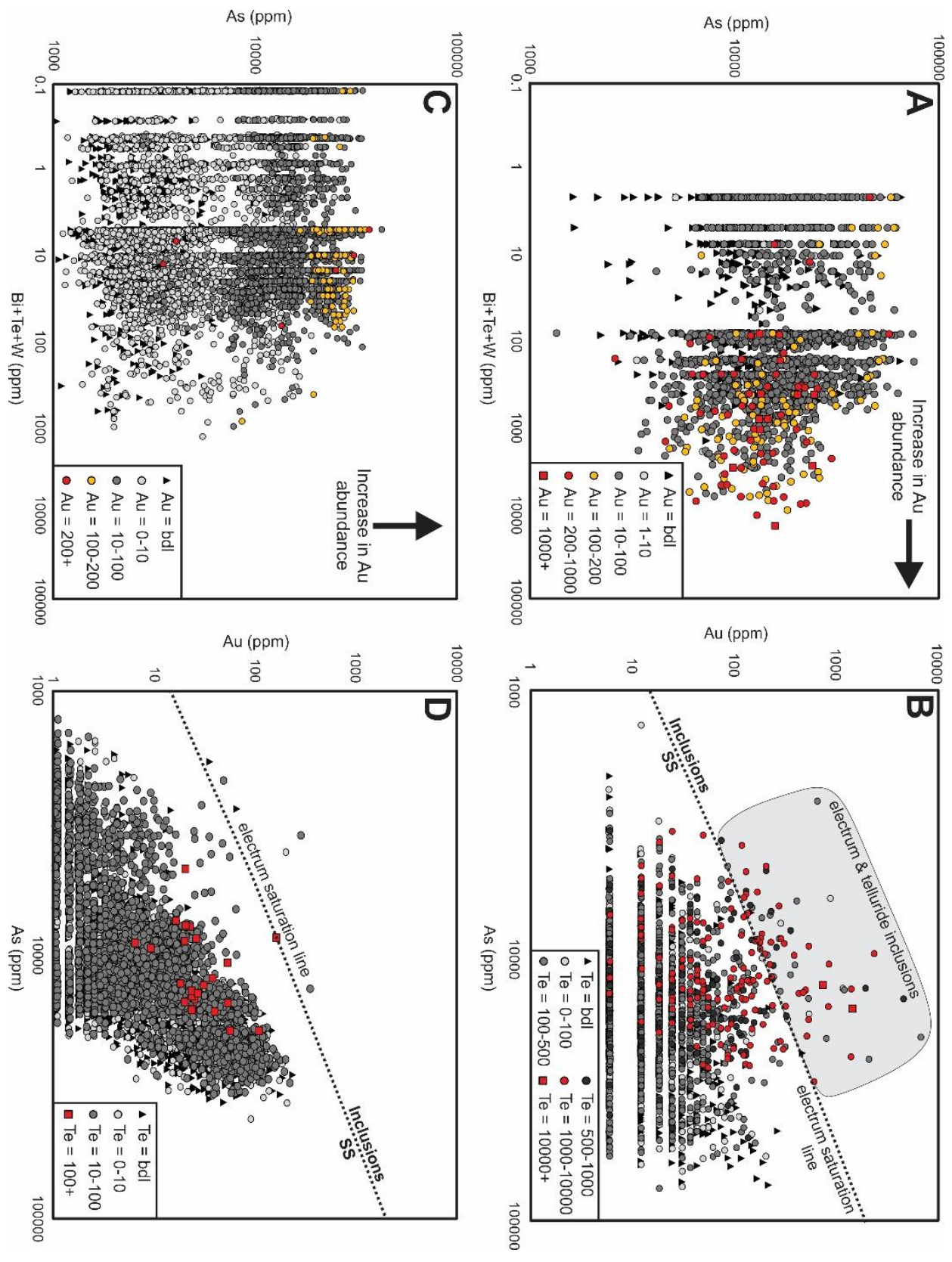


Figure 2-17: Elemental bivariate plots made using the time-series LA-ICP-MS trace element data (log scale) from the analyzed pyrite grains. A) Plot of Bi+Te+W versus As for sample 03F from the high-grade vein. Gold abundance is delineated and shows a trend toward Au enrichment with increasing Bi+Te+W abundance. B) Plot of As versus Au for sample 03F from the high-grade vein with Te delineated. Note that As and Au show no correlation ( $r^2=0.005$ ) and many electrum and Ag-Au-tellurides are present as micro-inclusions in the pyrite, as identified by data points above the electrum saturation line (Reich et al., 2005). C) Plot of Bi+Te+W versus As for sample 02F from the low-grade vein. Note that Au abundance is delineated and shows a strong correlation with As, with no apparent correlation with Bi+Te+W abundance. D) Plot of As versus Au for sample 02F from the low-grade vein with Te delineated. There is a strong correlation between As and Au ( $r^2=0.482$ ) with limited inclusions of electrum and tellurides. Note: bdl – below detection limit, SS – solid solution.

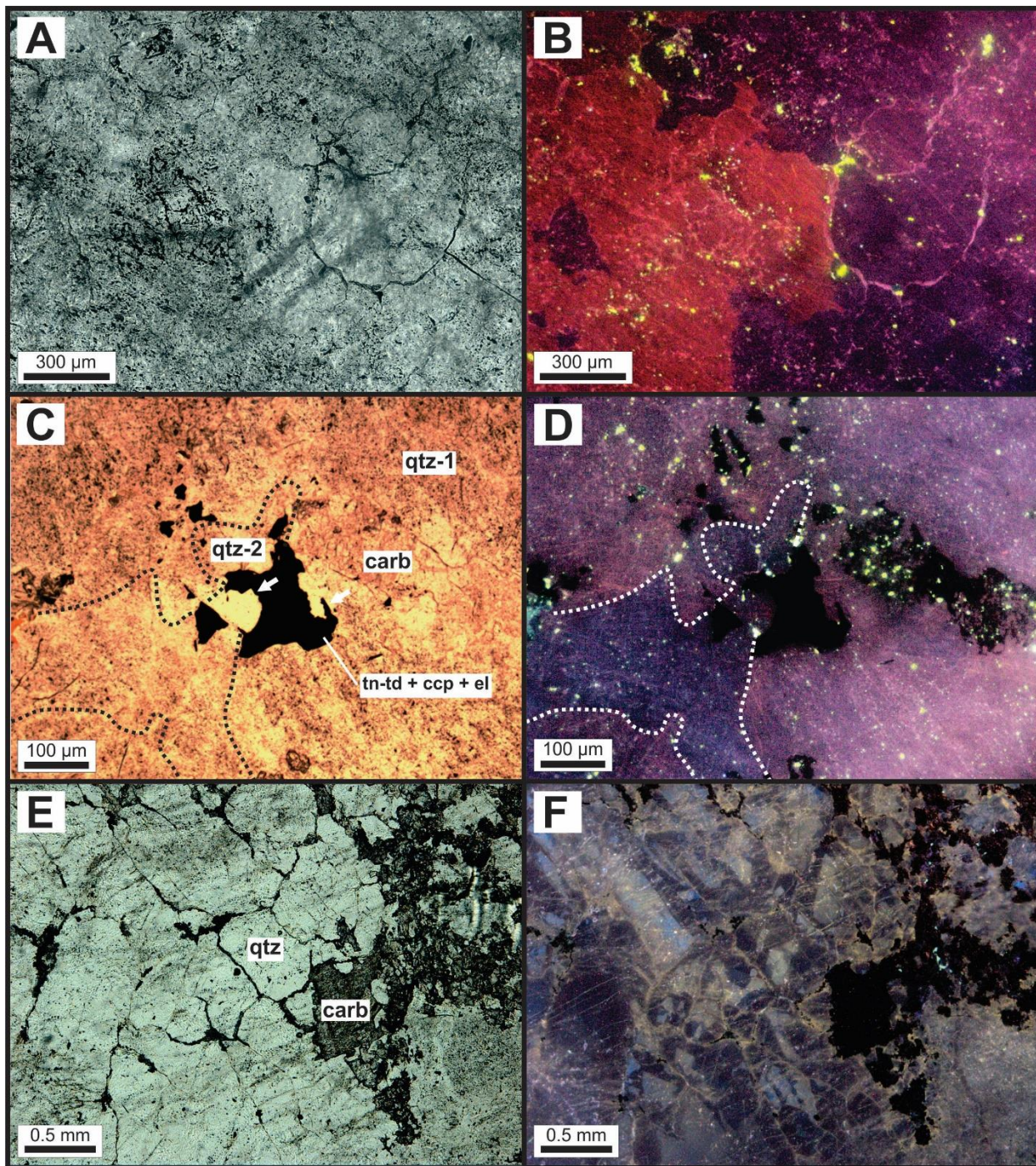
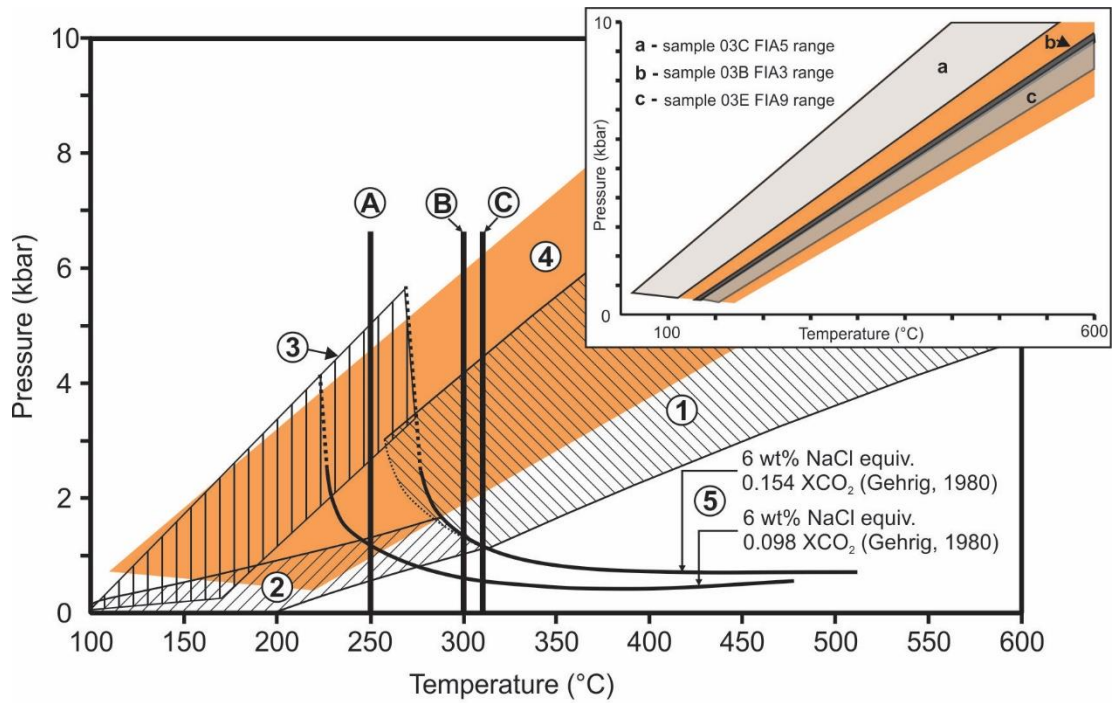


Figure 2-18: Hot cathodoluminescence (CL) images of vein quartz from the low-grade (115-02) and high-grade (115-03) veins. Variation in CL colour suggests multiple generations of quartz have precipitated from distinct fluids. A+B) Transmitted light and CL images from sample 03H from the high-grade vein, respectively. Homogenous red luminescence colours contrast with deep purple colours indicating at least two generations of quartz are present. The quartz generations delineated using CL are not obvious in transmitted light. C+D) Transmitted light and CL images from sample 03G from the high-grade vein, respectively. Deep blue-purple colours, distinct from the pink-purple luminescence characteristic of orogenic vein quartz (Ioannou et al., 2004), is texturally-associated with intergrowths of tennantite-tetrahedrite + chalcopyrite + electrum ± Ag-Pb-Au tellurides. E+F) Transmitted light and CL images from sample 02F from the low-grade vein, respectively. Short-lived blue and yellow (i.e., ~30 seconds), characteristic of  $\alpha$ -quartz crystallized from aqueous solutions, broadly define quartz growth zones (cf., Ioannou et al., 2004; Gotze, 2009).



Mineral thermometers

- Ⓐ Ag content of electrum = ~250°C (20 atomic%; Legendre et al., 1980; Bortnikov et al., 1988)
- Ⓑ Stability of hydrothermal sulfarsenide in quartz = <300°C (i.e., end-member gersdorffite; Klemm, 1965)
- Ⓒ Max. stability of petzite +  $\beta$ -hessite + gold = <313°C (Cabri, 1965; Legendre et al., 1980; Bortnikov et al., 1988)

Isochoric fields and unmixing curves

- ① Type 1 inclusions: 3-phase aqueous-carbonic
- ② Type 2a inclusions: CO<sub>2</sub>-rich
- ③ Type 3a inclusions: H<sub>2</sub>O-rich
- ④ Type 3b inclusions: H<sub>2</sub>O-NaCl  $\pm$  CO<sub>2</sub>
- ⑤ Solvi for H<sub>2</sub>O-NaCl  $\pm$  CO<sub>2</sub> fluids

Figure 2-19: Temperature versus pressure plot showing the inferred trapping conditions for type 1, type 2a, type 3a, and type 3b fluid inclusion assemblages identified in high-grade vein (115-03) of the Patch 14 sub-region of the Madrid deposit. The areas shown represent the calculated isochores for the different types of inclusions indicated: 1) area 1: type 1, 3-phase, aqueous-carbonic inclusions; 2) area 2: type 2a carbonic-dominant inclusions; 3) area 3: type 3a aqueous-dominant inclusions; and 4) area 4: type 3b aqueous inclusion only found in the upgraded high-grade vein. The smaller inset shows the range in isochores from three examples of type 3b fluid inclusion assemblages. Lines 5 show curves separating 2-phase and 1-phase fields (solvi) corresponding to aqueous-carbonic fluids with compositions of 6 wt% NaCl equiv. and 0.154  $X_{CO_2}$  and 0.098  $X_{CO_2}$  (from Gehring, 1980; dashed lines represent extrapolation of the curves to higher pressure); at pressures and temperatures above these curves, the corresponding fluid is homogeneous (i.e., type 1). Note that estimated fields of entrapment for type 2a and 3a inclusions must lie at PT conditions below the solvi (lines 5), however, this does not suggest these fluids were in equilibrium at the time of entrapment. The dashed curve on area 1 approximates the locus of type 1 inclusion isochore termini. Line A represents the temperature at which electrum with ~20 atomic % Ag coexists with petzite in an equilibrium assemblage (~250°C; Bortnikov et al., 1988). Line B represents the maximum stability of the hydrothermal sulfarsenide phase (i.e., end-member gersdorffite) hosted along quartz-septa boundaries (Klemm, 1965). Line C represents the maximum temperature at which petzite +  $\beta$ -hessite + gold can coexist as a stable equilibrium assemblage (< 313°C; Bortnikov et al., 1988; Cabri, 1965).

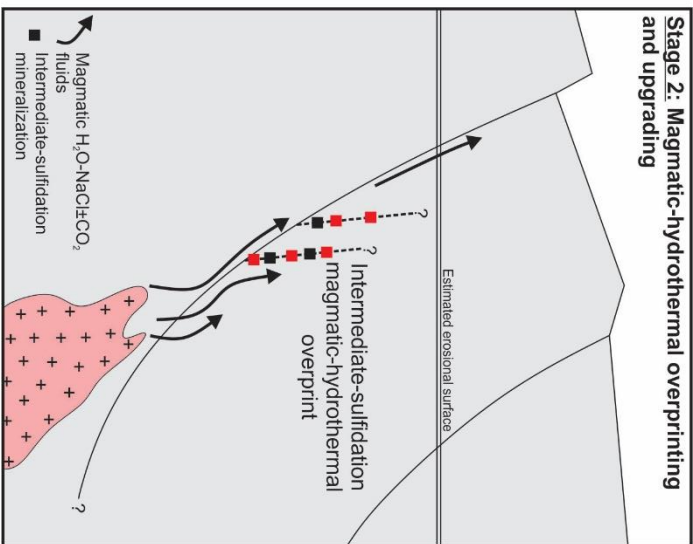
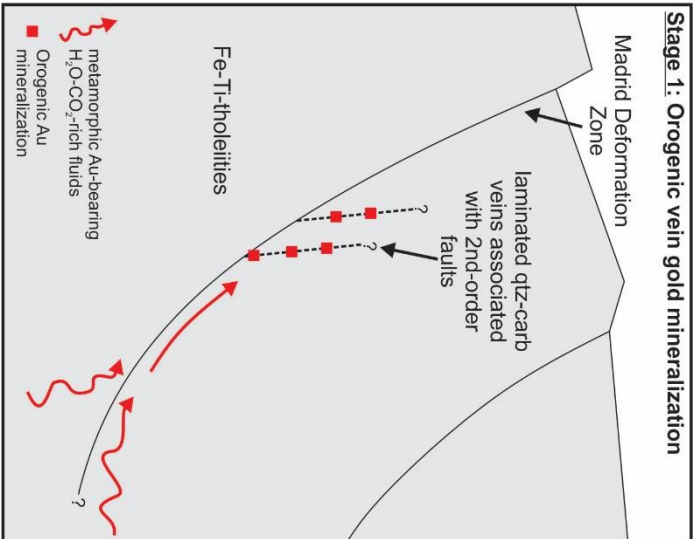
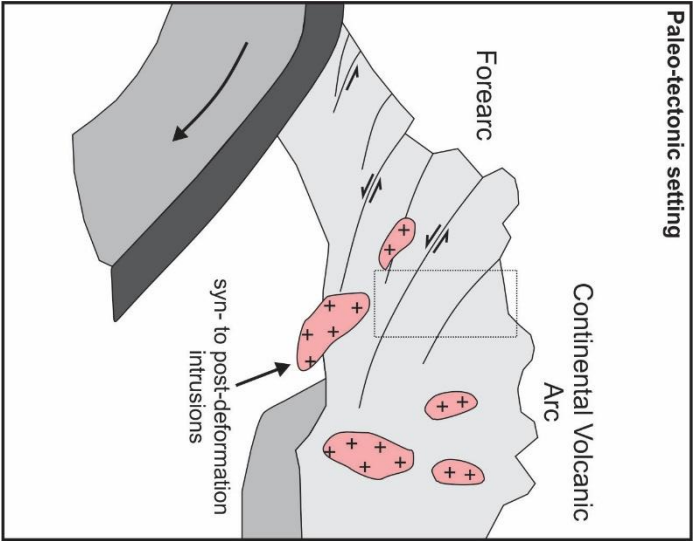


Figure 2-20: Simplified model showing the magmatic-hydrothermal overprinting and gold tenor upgrading of orogenic quartz-carbonate veins. In this model, the earlier auriferous laminated quartz-carbonate vein system (~2.63 – 2.6 Ga) was infiltrated by magmatic-hydrothermal fluids exsolved from an intrusion ( $\leq 2.61$  Ga), which in this case may not be expressed at the surface. These later fluids could have exploited pre-existing fluid conduits (e.g., MDZ) and brittle networks of orogenic quartz-carbonate veins, allowing for the development of the overprinting relationships observed in this study whereby intermediate-sulfidation style mineralization post-dates the orogenic style. Importantly, it remains unclear as to whether metals were sourced directly from a cooling intrusion or have been leached and remobilized from metal enrichment at depth (i.e., proto-ore).

Table 2-1: Ore minerals and their associated elemental compositions as determined by SEM-EDS quantification in high- and low-grade vein samples

High-grade vein 115-03 ore minerals														
Element (at. %)	el	ccp	tn-td	ga	sp	hes	auro-hes	alt	pz	cla	sch	apy	glc-gdf	nk
O	-	-	-	-	-	-	-	-	-	-	67.2	-	-	-
S	-	53.4	47.9	51.5	54.2	-	-	-	-	-	-	37.9	34	3.8
Ca	-	-	-	-	-	-	-	-	-	-	15.59	-	-	-
Fe	-	23.3	1.9	-	0.8	-	-	-	-	-	-	30.6	3.8	-
Co	-	-	-	-	-	-	-	-	-	-	-	-	-	-
Ni	-	-	-	-	-	-	-	-	-	-	-	-	24.3	41
Cu	-	23.3	30.8	-	-	-	-	-	-	-	-	-	-	-
Zn	-	-	4.8	-	44.9	-	-	-	-	-	-	-	-	-
As	-	-	9.1	-	-	-	-	-	-	-	-	31.6	37.9	55.2
Se	-	-	-	-	-	-	-	-	-	40.2	-	-	-	-
Ag	21.6	-	-	-	-	66.4	61.7	-	49.9	-	-	-	-	-
Sb	-	-	5.6	-	-	-	-	-	-	-	-	-	-	-
Te	-	-	-	-	-	33.6	36.8	52	31.9	-	-	-	-	-
W	-	-	-	-	-	-	-	-	-	-	17.2	-	-	-
Au	78.4	-	-	-	-	-	1.5	-	18.3	-	-	-	-	-
Pb	-	-	-	48.5	-	-	-	48	-	59.8	-	-	-	-
<b>TOTAL</b>	<b>100</b>	<b>100</b>	<b>100.1</b>	<b>100</b>	<b>99.9</b>	<b>100</b>	<b>100</b>	<b>100</b>	<b>100.1</b>	<b>100</b>	<b>99.99</b>	<b>100.1</b>	<b>100</b>	<b>100</b>

Low-grade vein 115-02 ore minerals														
Element (at. %)	el	ccp	tn-td	ga	sp	hes	auro-hes	alt	pz	cla	sch	apy	glc-gdf	nk
O	-	-	-	-	-	-	-	-	-	-	-	-	-	-
S	-	56.1	-	59.8	-	-	-	-	-	-	-	37.8	37.4	-
Ca	-	-	-	-	-	-	-	-	-	-	-	-	-	-
Fe	-	23.1	-	-	-	-	-	-	-	-	-	28.1	4.3	-
Co	-	-	-	-	-	-	-	-	-	-	-	-	17.4	-
Ni	-	-	-	-	-	-	-	-	-	-	-	1.8	6.9	-
Cu	-	20.8	-	-	-	-	-	-	-	-	-	-	-	-
Zn	-	-	-	-	-	-	-	-	-	-	-	-	-	-
As	-	-	-	-	-	-	-	-	-	-	-	32.4	33.9	-
Se	-	-	-	-	-	-	-	-	-	-	-	-	-	-
Ag	13.4	-	-	-	-	-	-	-	-	-	-	-	-	-
Sb	-	-	-	-	-	-	-	-	-	-	-	-	-	-
Te	-	-	-	-	-	-	-	47.1	-	-	-	-	-	-
W	-	-	-	-	-	-	-	-	-	-	-	-	-	-
Au	86.6	-	-	-	-	-	-	-	-	-	-	-	-	-
Pb	-	-	-	40.2	-	-	-	52.9	-	-	-	-	-	-
<b>TOTAL</b>	<b>100</b>	<b>100</b>	<b>0</b>	<b>100</b>	<b>0</b>	<b>0</b>	<b>0</b>	<b>100</b>	<b>0</b>	<b>0</b>	<b>0</b>	<b>100.1</b>	<b>99.9</b>	<b>0</b>

Note: Dashes represent 'not present/identified'. Abbreviations: alt - altaite; apy - arsenopyrite; ccp - chalcopyrite; cla - clausenthalite; el - electrum; ga - galena; glc-gdf - glaucodot-gersdorffite; hes - hessite; nk - nickeline; pz - petzite; sch - scheelite; sp - sphalerite; tn-td - tennantite-tetrahedrite

Table 2-2: Summary table of the fluid inclusion types identified in the high- and low-grade veins 115-03 and 115-02, respectively, along with their properties. Note that type 3b inclusions (bolded column), which are associated with late gold upgrading, are only present in the high-grade vein 115-03.

Fl types	Type 1: aqueous-carbonic		Type 2: carbonic-dominated			Type 3: aqueous-dominated		
	Properties	Representative inclusion appearance	2a	2b	3a	3b	3c	
Phases present at 20°C	(H <sub>2</sub> O-NaCl) + (CO <sub>2</sub> ) + (CO <sub>2</sub> ± CH <sub>4</sub> ± N <sub>2</sub> )		(CO <sub>2</sub> ± CH <sub>4</sub> ± N <sub>2</sub> ) + (H <sub>2</sub> O-NaCl)	(CO <sub>2</sub> ± CH <sub>4</sub> ± N <sub>2</sub> )	(H <sub>2</sub> O-NaCl) + (CO <sub>2</sub> ± CH <sub>4</sub> ± N <sub>2</sub> )	(H <sub>2</sub> O-NaCl) ± (CO <sub>2</sub> ) <sup>v</sup>	(H <sub>2</sub> O-NaCl) + (H <sub>2</sub> O) <sup>v</sup>	
Present in vein:	115-03 and 115-02		115-03 and 115-02	115-03 and 115-02	115-03 and 115-02	<b>Only 115-03</b>	115-03 and 115-02	
Occurrence and origin	Common; clusters of indeterminate origin. Rarely in S planes		Rare; clusters of indeterminate origin. Rarely in S planes. Often very small (~5 µm)	Common; often in clusters of indeterminate origin, S planes; decapitate halos or along GBS	Common; often in clusters of indeterminate origin or in S planes	Common; in S planes and as P inclusions in the cores of euhedral qtz crystals. Associated with late mineralization	Uncommon; hosted in partially healed S planes crosscutting GBS.	
Total # of inclusions measured (n)	50 (11 FIA)	17 (3 FIA)	-	-	60 (10 FIA)	<b>123 (15 FIA)</b>	17 (4 FIA)	
Size (µm)	< 10	< 12	< 12	< 12	< 10	< 20	< 25	
% Vapor (or carbonic) phase	10 to 30 (variable when modified)	70 to 90	100	100	5 to 10	5 to 15	variable from modification)	
Tmice	ND	ND	-	-	-7.6 to -1.8; n=56	<b>-16.2 to -9.8; n=118</b>	-22.8 to -16.2; n=16	
Tmcla	5.9 - 8.9; n=63	7.3 - 8.5; n=15	-	-	ND	ND	ND	
Salinity of aq phase (wt% NaCl equiv)	2.8 - 7.5 (4.6 ± 1.3); n=63	2.1 - 7.2 (4.2 ± 1.3); n=15	-	-	3.0 - 9.7 (4.6 ± 1.6); n=56	<b>13.8 - 19.6 (16.8 ± 1.2); n=118</b>	19.6 - 24.2 (22 ± 1.3); n=16	
X <sub>mci</sub>	0.017 - 0.068 (0.027 ± 0.008); n=38	0.008 - 0.017 (0.012 ± 0.003); n=12	-	-	0.019 - 0.067 (0.04 ± 0.02); n=9	<b>0.073 - 0.131 (0.109 ± 0.01); n=104</b>	0.131 - 0.165 (0.148 ± 0.01); n=11	
Tmcoz	-57.2 to -56.1 (-56.6 ± 0.34); n=42	-56.8 to -56.1 (-56.6 ± 0.11); n=17	-	-	ND	ND	ND	
Thcoz	18.7 - 31.1 (28.3 ± 3.2); n=40	11.3 - 29.7 (19.8 ± 6.9); n=17	variable	variable	ND	ND	ND	
Thror	194 - 318 (258 ± 32); n=30	237 - 324 (293 ± 27); n=12	-	-	99.5 - 291 (191 ± 25); n=51	<b>84 - 200 (145 ± 25); n=112</b>	93 - 136 (112 ± 13); n=13	
P <sub>bulk</sub> (GPa)	0.84 - 1.00; n=37	0.72 - 0.89; n=9	-	-	1.00 - 1.08; n=9	<b>0.90 - 1.08; n=110</b>	1.08 - 1.16; n=12	
X <sub>coz</sub>	0.076 ± 0.026; n=38	0.52 ± 0.14; n=12	1	1	0.041 ± 0.009; n=9	<b>trace</b>	0	

Note: All temperature data reported in °C. The % vapor, or all carbonic phases present (e.g., Type 1 inclusions containing L<sub>coz</sub>+V<sub>mci</sub>); the remaining volume % is aqueous liquid. No type 2b inclusions were measured. Dashes represent the absence of data. CO<sub>2</sub> in inclusions is shaded grey; Tm<sub>coz</sub> temperatures > -56.6°C reflect cumulative measurement uncertainty. Salinity of the aqueous phase was determined via final ice melting temperature or calibrate melting temperature. X<sub>mci</sub> and X<sub>coz</sub> are bulk fluid inclusion values; bulk density values were calculated by applying the equations of state outlined by Bowers and Helgeson (1983) and Bakker (1999). The X<sub>coz</sub> of inclusions were calculated using the program BULK (Bakker, 2003). Data in brackets represent averages ± 1σ standard deviation. The presence of CO<sub>2</sub> in type 3b inclusions was confirmed via Raman spectroscopy but X<sub>coz</sub> could not be quantified (i.e., spectral peaks could not be integrated). Abbreviations: aq - aqueous; FIA - fluid inclusion assemblage; GBS - grain boundaries; ND - not determined; P - primary; PS - pseudosecondary; S - secondary; Tm<sub>ice</sub> - final ice melting; Tm<sub>cla</sub> - final calcite dissociation; Tm<sub>coz</sub> - final melting of CO<sub>2</sub>; Th<sub>coz</sub> - CO<sub>2</sub> homogenization; Th<sub>ror</sub> - total homogenization temperatures; qtz - quartz

## Chapter 3

### **Fluid inclusion and microtextural evidence for efficient gold precipitation from Au-undersaturated fluids through coupled redox-pH change, Meguma terrane, Nova Scotia, Canada.**

#### **3.1 Abstract**

The flysch-hosted ~380 Ma Dufferin Au deposit in the Meguma terrane (Nova Scotia, Canada) comprises mineralized saddle reef-type quartz veins localized along lithological contacts between metasandstones and black slates in a tightly folded anticline. Ubiquitous to the saddle veins is the occurrence of carbonaceous material (CM), as immature amorphous organic matter (i.e., pyrobitumen), within cavities and along mineral grain boundaries adjacent to, and in contact with, vein laminations and margins. The occurrence of Au inclusions ( $\leq 1 \mu\text{m}$ ; 88 – 92 at. % Au; balance Ag) in CM-filled cavities indicates the gold mineralization is genetically related to CM. Through a combination of microanalytical methods (SEM, confocal Raman microspectroscopy, microthermometry, fluid inclusion LA-ICP-MS, cathodoluminescence), we show that Au precipitated through coupled fluid  $f\text{O}_2$  reduction (via interaction with CM) and pH increase. This destabilized gold bisulfide complexes leading to efficient Au precipitation from an aqueous-carbonic fluid ( $\text{H}_2\text{O}$ -NaCl- $\text{CO}_2$ ,  $\text{N}_2$ ,  $\text{CH}_4$ ) that was gold-undersaturated ( $0.045 \pm 0.024$  ppm Au). The proposed mineralization mechanism is supported by: (i) a decrease in Au content of the fluid along with redox-sensitive semimetals (As, Sb), and an increase in the concentration of elements inherited from metasedimentary rocks (i.e., Mg, K, Ca, Sr, Fe) from early, Au-bearing to later, Au-depleted fluids; (ii) a decrease in the  $X_{\text{CO}_2}$  from Au-bearing to Au-depleted fluids, consistent with  $\text{CO}_2$  removal via reduction/respeciation and late carbonate precipitation; and (iii) Au in contact with CM inside mineralized cavities and fractures.

Despite mineralizing fluids only transporting low concentrations of Au, they may still produce Meguma-type (metasedimentary rock-hosted) deposits provided the efficiency of Au precipitation from these fluids is high, a process that can be greatly facilitated by the presence of CM. This work revises the genetic model for Au precipitation in the Meguma terrane along with similar orogenic metasedimentary settings globally (e.g., Bendigo, Ballarat, Carlin, Kupferschiefer) and emphasizes the importance of CM as a prerequisite for gold mineralization.

### **3.2 Introduction**

Formation of orogenic gold deposits has long been known to require the critical combination of a gold reservoir and a highly efficient precipitation mechanism(s), as recently reviewed by Gaboury (2019). The gold-transporting potential of aqueous-carbonic fluids, such as those associated with metamorphic terranes (Roedder, 1984; Ridley and Diamond, 2000, and references therein), is not necessarily limited by their transport of gold at concentrations well below saturation levels (Williams-Jones et al., 2009; Wagner et al., 2016), but rather the availability of labile Au in source rocks (Rauchenstein-Martinek et al., 2014, 2016). However, even if a Au-rich reservoir is available (e.g., Large et al., 2007, 2009; Pitcairn et al., 2006, 2014), efficient mechanisms are prerequisites for Au liberation from source rocks, its transportation and subsequent precipitation for deposit formation. It is noted that very low concentrations of Au in geothermal and metamorphic fluids (e.g., 1 – 3 ppb; Roedder, 1984; Brown, 1986) can still yield Au-rich deposits if the volume of a channelized fluid and duration of hydrothermal activity are sufficiently high (e.g.,  $\sim 10^6$  kg/hr over  $\sim 1500$  years at 1.5 ppb Au; Brown, 1986). However, in systems affected by lower volumes of auriferous fluid, precipitation mechanisms must be sufficiently efficient to produce significant concentrations of Au, and hence deposit.

Suggested mechanisms for gold precipitation include: (i) fluid unmixing due to rapid pressure fluctuations (Smith et al, 1984; Craw et al. 1993; Loucks and Mavrogenes, 1999); (ii) fluid dilution via mixing (Groves and Foster, 1991; Groves et al., 2003); (iii) desulfidation from fluid/rock interaction (e.g., Williams-Jones et al. 2009; Lafrance, 2015) or gold adsorption on earlier sulfides (Kusebauch et al., 2019); (iv) changes in fluid pH and/or  $fO_2$  due to fluid/rock reaction (Evans et al., 2006; Williams-Jones et al., 2009; Hu et al., 2017) or fluid mixing (Olivo and Williams-Jones, 2002; Dinel et al., 2008; Beaudoin and Chiaradia, 2016); v) fluid cooling (Mernagh et al., 2004); and (vi) interaction with carbonaceous matterl ‘CM’ (e.g., Witwatersrand: Parnell, 1996; Carlin gold deposits: Radtke and Scheiner, 1970; Hoyle Pond deposit: Dinel et al., 2008). However, in most cases gold precipitation results from the destabilization of soluble gold bisulfide complexes (e.g.,  $AuHS^0$ ,  $Au[HS]_2^-$ ) due to a variety of reactions (Seward, 1973; Stefansson and Seward, 2004).

Recently, the relative importance of traditional high-grade vein-type mineralization has been re-evaluated in light of lower-grade, high-tonnage gold systems; examples include the world class Archean Detour Lake (15.6 Moz; Dubosq et al., 2018) and Malartic (10.7 Moz; De Souza et al., 2017) deposits, Canada. Another example of this, albeit smaller but relevant to the present study, is disseminated style gold mineralization in metasedimentary rocks of the Meguma terrane of Nova Scotia, Canada (Ryan and Smith, 1998; Bierlein and Smith, 2003; Bierlein et al., 2004) which contrasts with the historically mined high-grade (15-20 g/t Au), low-tonnage (< 200,000 t) quartz veins (Ryan and Smith, 1998; Sangster and Smith, 2007). This disseminated-type mineralization, such as the currently mined Touquoy deposit (445,000 oz Au at 1.23 g/t; Staples et al., 2018), occurs in carbonaceous flysch and reflects infiltration of gold-bearing fluids into metasedimentary country rocks and precipitation of gold in favorable lithologies. In the Meguma terrane, these

favorable lithologies are mudstones and slates containing carbonaceous material (CM; ~1% organic C; Bierlein and Smith, 2003).

The textural association of variably metamorphosed, or thermally degraded, carbonaceous material (e.g., pyrobitumen, bitumen, graphite) and gold in metasedimentary rock-hosted gold deposits is not uncommon (e.g., Bierlein and Maher, 2001). However, the physicochemical mechanisms through which aqueous gold bisulfide complexes are destabilized by CM remains equivocal. The spatial association of gold mineralization and CM has been known for over a century (e.g., Brooks, 1912), with seminal work on the Carlin gold deposit identifying the intimate relationship between gold and CM (Joralemon, 1951), in addition to the subsequent work of Radtke and Scheine (1970) who demonstrated that Au grade correlates with the abundance of organic carbon in the host rocks. Additionally, the relationship between gold and CM has been recognized historically in the mineral processing industry (Breerwood, 1938; Scheiner, 1971) since flotation and separation of gold from carbonaceous matter can be problematic due in part to the phenomenon of “preg-robbing” (Vaughan, 2004; Miller et al., 2005).

The occurrence of CM in other sediment-hosted gold systems has been observed elsewhere with similarities to those in the Meguma terrane (e.g., Witwatersrand, South Africa: Parnell, 1996; the Kupferschiefer, Poland: Oszczepalski et al., 2011; Cosmopolitan Howley gold deposit, Northern Australia: Matthäi et al., 1995; Western Lachlan Orogen, Victoria, Australia: Bierlein et al., 2001; Macraes Gold Mine, Otago Schist, New Zealand: Craw, 2002; Pitcairn et al., 2006; Hoyle Pond deposit, Abitibi greenstone belt, Canada: Dinel et al., 2008; Ashanti gold belt, Ghana: Berge, 2011), in which CM is spatially associated with gold and sulfides, and may have been chemically

involved in ore genesis as a fluid reductant, redox buffer and/or Au adsorbent (Vilor, 1983; Tan et al., 2005; Williams-Jones et al., 2009; Oszczepalski et al., 2011).

The intermittent mining (to 2018) of Dufferin deposit of Nova Scotia, Canada (Horne and Jodrey, 2001) for the past 15 years has provided an extensive assay database in addition to excellent underground vein exposures. The latter provided rare but exceptional examples of quartz crystals lining cavities that preserve unusually large and unmodified fluid inclusions that are broadly coeval with gold deposition. As with other deposits in the Meguma terrane (Horne and Culshaw, 2001; Sangster and Smith, 2007; Kontak and Horne, 2010), the auriferous saddle reef veins at Dufferin are associated with anticlinal fold crests where CM-bearing black slates are in contact with overlying metasandstone rocks and greywackes. Thus, the setting provides an excellent opportunity to elucidate the chemical mechanisms responsible for efficient fluid reduction and the generation of auriferous vein systems from gold-undersaturated hydrothermal fluids. In this regard, this study presents one of the few examples of measured gold concentrations in aqueous-carbonic fluids in an economic “orogenic” gold deposit globally and reports direct evidence for the genetic relationship between gold and CM in a flysch-hosted gold system.

### **3.3 Geologic setting of the Dufferin gold deposit**

The Lower Paleozoic metasedimentary rock-hosted Dufferin deposit, located ~100 km east of Halifax, lies in the Meguma terrane of southern Nova Scotia, Canada (Fig. 1A inset), which is one of several exotic terranes that make up the Appalachian collage (Williams, 1979). This terrane was dextrally docked to the adjacent Avalon terrane along the east-west trending Cobequid-Chedabucto Fault Zone (CCFZ in Fig. 1A) as part of the Neocadian Orogeny (van Staal, 2007; Murphy et al., 2011). The terrane is dominated by a thick sequence (12 km) of Early Cambrian to

Ordovician turbiditic metasedimentary rocks of the Goldenville and Halifax groups that disconformably overlie Silurian to Early Devonian metasedimentary and metavolcanic rocks of the Rockville Notch Group (White et al., 2012). This sequence was metamorphosed (greenschist and locally amphibolite facies) and deformed (northeast trending open- to closed, upright folds) at ~410 to 380 Ma (Kontak et al., 1998; Hicks et al., 1999; Morelli et al., 2005) and subsequently intruded at ~370-380 Ma by meta- to peraluminous granitoids and minor mafic bodies (Clarke et al., 1997) constrained to emplacement between 2.5 – 3.0 kbars (Kontak et al., 2011; Hilchie and Jamieson, 2015)

The Meguma terrane is well known for its numerous slate-belt type gold deposits characterized by massive- to laminated, bedding concordant quartz ± carbonate ± Fe sulfide veins (Malcolm, 1929; Kontak et al., 1990; Ryan and Smith, 1998; Sangster and Smith, 2007; Kontak and Horne, 2010). These deposits are mainly hosted in the metasandstone Goldenville Group, although some extend into the overlying slate dominant Halifax Group, and are preferentially localized to anticlinal hinges across the Meguma terrane (Kontak et al., 1990; Sangster and Smith, 2007; Kontak and Horne, 2010). Previous work indicates they generally conform to features of orogenic type deposits in regards to vein types and fluid chemistry (Kontak and Horne, 2010). Importantly, both field relationships and direct dating ( $^{40}\text{Ar}/^{39}\text{Ar}$ , Re-Os) suggests most deposits formed at ~380 Ma and thus overlap the emplacement of the large granitoid batholiths (see Kontak and Horne (2010) for review). This timing is consistent with the structural model of Horne and Culshaw (2001) whereby vein formation is related to late-stage fold tightening, as expected during batholith emplacement and related horizontal shortening (Benn et al., 1997).

The Dufferin deposit is hosted in a sandy flysch sequence of the Goldenville Group that is characterized by medium- to thickly-bedded metasandstones with lesser metasilstone and black slate comprising Bouma sequences (Harris and Schenk, 1975). A typical sedimentary cycle is characterized by graded metasandstone (~1 m) fining-upwards to metasilstone (5-10 cm) and capped by black carbonaceous slate (1-5 cm; Horne and Jodrey, 2002); importantly the auriferous bedding-concordant veins are localized to the latter unit. The deposit is associated with a fault-bound portion of the Crown Reserve Anticline that consists of a tight, plunging chevron fold which, from diamond drilling, is known to host 17 stacked saddle reefs with  $\leq 7000$  m of strike continuity (Fig. 1A; Hannon et al., 2017). Veining includes bedding-concordant saddle reefs (Fig. 1B) and their contiguous down-limb extensions (i.e., “leg” veins), with lesser discordant and en echelon vein types. All veins types are auriferous and can be related to flexural slip and hinge zone dilation (Horne and Culshaw, 2001; Horne and Jodrey, 2002; Hannon et al., 2017). The down-limb leg veins are commonly laminated (i.e., ribbon or crack-seal) and relate to incremental vein opening along bedding-parallel flexural slip movement horizons.

The hinge-hosted saddle-reef veins are composed of both laminated and massive quartz vein generations (Fig. 1C) with local quartz crystal-lined cavities/vugs (Fig. 1D). Thus, saddle veins are the product of repeated intervals of dilation, fluid ingress, vein formation and mineralization. Carbonate (primarily ferroan dolomite) and sulfides (arsenopyrite, minor pyrite) are common accessory phases coating euhedral quartz crystals (Fig.1E). Sulfides occur as arsenopyrite-rich aggregates disseminated in the wall rock or in vein laminations (Horne et al., 2002). Gold occurs along the margins of CM-bearing wall rock selvages (commonly along the footwall of saddle reef veins; Fig. 1B) and vein laminations, and as coarse-grained aggregates in massive quartz (Hannon et al., 2017).

The deposit is low-tonnage with a current indicated resource of 151,500 tonnes yielding 58,000 oz of Au at 11.9 g/t, and an inferred resource of 703,000 tonnes yielding 150,000 oz of Au at 6.6 g/t (Hannon et al., 2017). Gold grade varies considerably among the saddle environments due to the nugget effect. Routinely assayed material within individual saddles may contain between 0.02 (l.o.d.) and >280 g/t Au. Assays of combined saddle and leg vein material from saddles 3 and 6 (focus of this study) average  $4.6 \pm 4.0$  g/t (n=20; 44549 total tonnes assayed) and  $12.4 \pm 10.6$  g/t (n=16; 77331 total tonnes assayed), respectively (Hannon et al., 2017).

### **3.4 Methods**

#### **3.4.1 Sampling**

Euhedral quartz crystals hosting abundant fluid inclusions were collected from vugs at dilational sites in the thickest part of saddle reef veins 3 and 6 near the apex of the anticline. Care was taken to select translucent quartz crystals that showed limited signs of recrystallization (e.g., milky white with saccharoidal texture). This quartz variety was identified as being a particularly good host for exceptional fluid inclusions with respect to size and preservation, and were thus sampled for this study. Quartz crystals cut sub-parallel to the c-axis were made into 200  $\mu$ m thick fluid inclusion plates for clear identification of growth zones, if present. Samples were also collected from a laminated down-limb leg vein from saddle vein 5 to investigate the mineralogy of carbonaceous vein laminations and associated gold occurrence.

#### **3.4.2 Analytical techniques**

Vein and vein lamination mineralogy was determined using a TESCAN MIRA 3 LMU VPS Field Emission Scanning Electron Microscope (SEM) at Saint Mary's University (Halifax, Canada)

equipped with a back-scattered electron detector coupled with EDS functionality. The instrument was operated at an accelerating voltage of 20 kV and an approximate working distance of 17 mm was used.

Fluid inclusion microthermometry was performed at Saint Mary's University using a Linkham FTIR600 heating-freezing stage mounted to an Olympus BX51 microscope. Temperature calibration was performed using synthetic fluid inclusion standards of pure H<sub>2</sub>O (melting at 0°C and homogenization at the critical point of 374.1°C) and pure CO<sub>2</sub> (melting at -56.6°C; T<sub>mCO<sub>2</sub></sub>). Uncertainties associated with microthermometric measurements range from ±2 to 3°C for temperatures recorded near the extremes of working conditions (i.e., -190 and 560°C) to ±0.1°C for temperatures near 0°C. For type 1a inclusions (LH<sub>2</sub>O + LCO<sub>2</sub> + VCO<sub>2</sub>) salinity was determined based on clathrate melting temperatures (T<sub>mCLA</sub>; Darling, 1991; Diamond, 1992). Type 1b and type 2 inclusions (LH<sub>2</sub>O + LCO<sub>2</sub>) lacked clathrate nucleation, thus salinity was determined through final ice melting temperatures (T<sub>mICE</sub>; Bodnar and Vityk, 1994). The software packages BULK and ISOC (Bakker, 2003) were used to determine bulk fluid inclusion compositions (informed from Raman spectroscopic analysis), molar volumes (cm<sup>3</sup>/mol) and isochores, utilizing temperatures and modes of total homogenization (Th<sub>TOT</sub>), the homogenization of the CO<sub>2</sub> phase in type 1a inclusions (Th<sub>CO<sub>2</sub></sub>), and the estimated volumetric proportion of the CO<sub>2</sub> phase at Th<sub>CO<sub>2</sub></sub>.

Laser Raman microspectroscopy (LRM) was performed at Saint Mary's University using a Horiba Jobin-Yvon LabRam HR confocal instrument equipped with a 100 mW (~2-3 mW at sample surface) 532 nm Nd-YAG diode laser (Toptica Photonics) and Synapse charge-coupled device detector. Pure silicon was used as a frequency calibration standard. A 600 grooves/mm grating (spectral resolution of approximately ± 2 cm<sup>-1</sup>) was used for identification and mapping of fluid

inclusion-hosted volatile species whereas a 1800 grooves/mm grating (spectral resolution of approximately  $\pm 0.5 \text{ cm}^{-1}$ ) was used to accurately determine the Fermi diad spacing between the  $\nu_1$  and  $\nu_2$  Raman peaks of  $\text{CO}_2$  (for  $\rho\text{CO}_2$  determination; Rosso and Bodnar, 1995). Semi-quantitative determination of the relative molar abundances of fluid inclusion-hosted volatile species followed the methodology of Beeskow et al. (2005, and references therein).

Fluid inclusion analysis by laser ablation inductively-coupled plasma mass spectrometry (LA-ICP-MS) was done using a NWR 193 UC laser ablation system mounted to an Agilent 7900 quadrupole MS at the University of Toronto (Toronto, Canada). Gas flow rates of 1.0 L/min (He – carrier) and 0.85 L/min (Ar – make-up) were used, and tuning of the ICP-MS was done by monitoring mass-21/mass-42, ThO/Th, and U/Th ratios in order to achieve a ThO production rate of  $<0.3\%$  and U/Th  $\sim 1$ . Dwell times were set to 10 ms, except for Au (100 ms), Ag (30 ms), As (20 ms), B (20 ms), S (40 ms), and Bi (20 ms). To avoid spalling, ablation was performed via stepwise expansion of the laser diameter to a final diameter  $\sim 5\text{-}10 \mu\text{m}$  larger than the inclusion being ablated. All analyte sensitivities, except for S, were calibrated using the reference standard SRM610 from NIST. Sulfur was calibrated using the Sca17 reference standard (Seo et al., 2011). Trace-element concentrations in bulk fluid inclusions were quantified using the software platform SILLS (Guillong et al. 2008), which involved deconvoluting the mixed inclusion + host signal from the host-only signal after calculation of background corrected count rates for each isotope. The salinity of the inclusions (wt.% equiv. NaCl), as determined by microthermometry, was used for internal standardization.

Carbon ( $^{13}\text{C}/^{12}\text{C}$ ) isotope ratios of dolomite crystals coating the surface of a euhedral quartz crystal from saddle 6 were determined. Using a 0.4 mm tungsten carbide microdrill, approximately 30-60

µg of carbonate powder was removed from the dolomite. Carbon isotope ratios of dolomite were measured using a Nu Perspective dual-inlet isotope ratio mass spectrometer connected to a NuCarb carbonate preparation system at McGill University Stable Isotope Laboratory (Montréal, Canada). Samples were calibrated to VPDB standards. Uncertainties are  $\pm 0.5\text{‰}$  ( $1\sigma$ ) for  $\delta^{13}\text{C}$ .

## **3.5 Results**

### **3.5.1 Vein mineralogy, nature of CM and C isotopic compositions**

The saddle reef veins at Dufferin consist of: (i) laminated quartz veins present in the down-limb legs and often near vein margins and interiors of the saddles, and (ii) massive quartz cross-cutting the laminated veins and volumetrically dominating saddle veins (Fig. 1C). In the laminated veins, the wallrock sourced septae contain the assemblage sericite + quartz + ferroan dolomite + apatite + rutile + monazite + CM (Fig. 2A). Large vugs (~5-30 cm diameter) occur in the massive quartz of saddle veins at fold hinges and are frequently lined with cm-size euhedral quartz crystals (Fig. 1D). The surfaces of quartz crystals are commonly coated with euhedral carbonate (ferroan dolomite) ± pyrite and display dissolution features, including striate- and triangularly-etched surface morphologies (Fig. 1E).

In vein laminations and along vein margins, CM is locally abundant and occurs as massive, spheroidal or blade-like masses in fractures and coating cavities, and along quartz grain boundaries adjacent to septae margins (Fig. 2B, C, D). The presence C, S, N, Cl and Na in the CM was confirmed by SEM-EDS elemental maps (Fig. EA 3-1 in Electronic Appendix) which show strong carbon enrichment compared to the associated dolomite. Raman spectroscopy confirmed that the CM is not crystalline graphite, but instead shares similar spectral characteristics (e.g., broad D and

G spectral bands) to bitumen or pyrobitumen (Fig. 2E; Jehlicka et al., 2003; Liu et al., 2013). Intimately associated with the CM are arsenopyrite and gold (88 – 92 at. % Au; Ag balance). Whereas the former is seen to be in textural equilibrium with the CM in late fractures (Fig. 2C), micron-scale gold grains (< 2 - 3  $\mu\text{m}$ ) are noted to occur coating CM-filled cavities (Fig. 2D). Micron-scale grains of quartz and rutile are also common in the CM.

The carbonate (ferroan dolomite) growing on euhedral quartz crystals yielded  $\delta^{13}\text{C}_{\text{VPDB}}$  values of -21.3 and -21.1‰ (average of -21.2‰; n = 2).

### **3.5.2 Fluid inclusion systematics**

#### *3.5.2.1 Fluid inclusion petrography and microthermometry*

In the euhedral quartz crystals from cavities in saddles 3 and 6, three distinct fluid inclusion types are recognized based on petrographic, microthermometric and Raman spectroscopic characteristics. Their petrographic and compositional features are summarized in Table 1 and the complete microthermometric data set is listed in Table EA 3-1 (Electronic Appendix).

Fluid inclusions are classified in the context of fluid inclusion assemblages (FIA) by establishing the relative timing of entrapment for groups of texturally coeval inclusions (cf., Goldstein and Reynolds, 1994). Fluid inclusion types are mainly distinguished by differences in composition and phases present during room-temperature (i.e., 20°C) observations supplemented with thermometric measurements and Raman analysis, as noted below.

*Type 1* inclusions contain an aqueous-carbonic fluid and show several variants based on morphology, composition and phase proportion. *Type 1a* inclusions (n = 36; Fig. 3A), commonly

having negative shapes, are three-phase ( $L_{\text{aq}} + L_{\text{car}} + V_{\text{car}}$ ) at 20°C, with an aqueous phase proportion of  $63 \pm 5$  vol.%, an aqueous phase salinity of  $1.3 \pm 0.4$  wt.% equiv. NaCl based on  $T_{\text{MCLA}}$  values between 9.1 and 10°C (cf., Darling, 1991; Diamond, 1992), and show  $T_{\text{H}_{\text{TOT}}}$  to liquid at  $287 \pm 8$ °C. Note that the carbonic phase may compositionally complex, containing variable concentrations of CO<sub>2</sub>, CH<sub>4</sub>, N<sub>2</sub>, H<sub>2</sub>S and hydrocarbons (Table EA 3-2, Fig. 4). These inclusions show  $T_{\text{mCO}_2}$  and  $T_{\text{hCO}_2}$  at  $-57.2 \pm 0.4$ °C and  $25.9 \pm 1.4$ °C, respectively. The mode of  $T_{\text{hCO}_2}$  (carbonic phase homogenization) varies between liquid and vapor, and likely reflects variable  $\rho_{\text{CO}_2}$  and/or CH<sub>4</sub> and N<sub>2</sub> abundances in the carbonic phase.

*Type 1b* inclusions (n = 52; Fig. 3B) are two-phase ( $L_{\text{aq}} + V_{\text{car}}$ ) at 20°C. Due to the lower abundance of CO<sub>2</sub> in these inclusions, a thin film of  $L_{\text{CO}_2}$  may surround the vapor phase but is optically obscured by the high relief of the inclusion margin; therefore,  $T_{\text{mCO}_2}$  and  $T_{\text{hCO}_2}$  could not be accurately measured. These inclusions have an aqueous phase proportion of  $79 \pm 5$  vol.%, an aqueous phase salinity of  $4.6 \pm 0.5$  wt.% equiv. NaCl based on  $T_{\text{MICE}}$ , and a  $T_{\text{H}_{\text{TOT}}}$  to liquid at  $241 \pm 21$ °C. As clathrate melting was not observed, the reported salinity values may slightly overestimate aqueous phase salinity.

*Type 2* fluid inclusions (n = 37; Fig. 3C) appear petrographically to be similar to type 1b inclusions, i.e., they are also two-phase ( $L_{\text{aq}} + V_{\text{car}}$ ) at 20°C and have an aqueous phase proportion of  $86 \pm 3$  vol.%. These inclusions may often show a higher aqueous phase volume percentage than type 1b inclusions, but are differentiated based on their microthermometric, Raman spectroscopic properties and bulk compositions (Table 2). They have a salinity of  $3.2 \pm 1$  wt.% equiv. NaCl and show  $T_{\text{H}_{\text{TOT}}}$  to liquid at  $210 \pm 9$ °C.

No evidence for a primary origin of any of the fluid inclusions (i.e., no fluid inclusions trapped along primary growth zones) was observed during petrographic study, which was confirmed by cathodoluminescence (CL) imaging of several euhedral quartz crystals. The CL imaging revealed that all the fluid inclusion types are confined to secondary planes around which quartz displays lower luminescence intensity than in regions absent of fluid inclusions (Fig. 3D). Where type 1a FIA are crosscut by type 2 FIA, some type 1a fluid inclusions appear to have been emptied and refilled through exchange with the later type 2 fluid (Fig. 3E; e.g., Goldstein, 1986).

#### *3.5.2.2 Fluid inclusion chemistry: LRM and LA-ICP-MS*

Analyses of fluid inclusion vapor phases by LRM show that, whereas the bulk compositions of types 1a and 1b inclusions are different, their volatile chemistries are similar (Fig. 4A; Table EA 3-2). An LRM map of a large (~100  $\mu\text{m}$  diameter) type 1a fluid inclusion (Fig. 4B-I) shows significant features of the fluid chemistry of these gold-bearing (see below) aqueous-carbonic fluids. In contrast, type 2 fluid inclusion vapor phases are characteristically richer in  $\text{CH}_4$  and  $\text{N}_2$  (i.e., by about an order of magnitude) relative to types 1a and 1b fluid inclusions (Fig. 4J), and consequently have lower vapor phase  $\text{CO}_2/(\text{CH}_4+\text{N}_2)$  ratios ( $18 \pm 1$ ,  $11 \pm 1$ , and  $1.3 \pm 1$  for type 1a, 1b and 2 inclusions, respectively; Table EA 3-2). Analyses of the aqueous phases show that both type 1a and 1b inclusions contain boron as boric acid, not detected in type 2 inclusions (Fig. 4K). All fluid inclusion types contain the aqueous carbonic species  $\text{CO}_{2(\text{aq})}$  and  $\text{HCO}_3^-_{(\text{aq})}$ . The main Raman shift for  $\text{CO}_3^{2-}_{(\text{aq})}$  (~1064  $\text{cm}^{-1}$ ) overlaps with a quartz host shift at ~1066  $\text{cm}^{-1}$  of variable intensity depending on crystallographic orientation (Frezzotti et al., 2012), thus  $\text{CO}_3^{2-}_{(\text{aq})}$  could not be accurately identified. Although only qualitative, type 2 inclusions show a more intense signal for  $\text{HCO}_3^-_{(\text{aq})}$  relative to  $\text{CO}_{2(\text{aq})}$ , compared to type 1a and type 1b inclusions (Fig.

4K). The average densities of CO<sub>2</sub> in type 1a, 1b, and 2 fluid inclusion vapor phases, determined based on the Fermi diad spacing between  $\nu_1$  and  $\nu_2$  CO<sub>2</sub> Raman shifts (cf., Rosso and Bodnar, 1995), were  $0.4 \pm 0.2$ ,  $0.23 \pm 0.1$ , and  $0.1 \pm 0.05$  g/cm<sup>3</sup>, respectively. Despite the compositional and density differences among the fluid inclusion vapor phases (Table 1), types 1a, 1b and 2 inclusions have identical bulk densities ( $0.89 \pm 0.04$ ,  $0.9 \pm 0.04$ , and  $0.9 \pm 0.03$  g/cm<sup>3</sup>, respectively; see Table 1), thus all isochores overlap in P-T space (Fig. 5).

The results of LA-ICP-MS analysis of type 1a (n = 84) and type 2 fluid inclusions (n = 32) are presented in Figure 6A and Table EA 3-3, whereas a representative LA-ICP-MS signal (cps) versus time (s) plot of a type 1a inclusion with corresponding calculated elemental concentrations is shown in Figure 6B. Limits of detection (LOD) are inclusion specific, and element concentrations below routine LOD are excluded from calculated averages and standard deviations. Elemental concentrations remained consistent with increasing fluid inclusions size, and concentrations did not increase systematically with cross sectional area (proxy for inclusion volume) of the inclusions. Type 2 fluids are relatively enriched in Mg ( $915 \pm 771$  ppm;  $1\sigma$  standard deviation) and Ca ( $2600 \pm 1620$  ppm) compared to type 1a fluid inclusions (Mg =  $175 \pm 177$  ppm and Ca =  $949 \pm 568$  ppm), whereas K is similar in both ( $202 \pm 121$  ppm and  $157 \pm 202$  ppm, respectively). Type 2 fluids are also relatively enriched, on average, in Sr ( $4.23 \pm 2.12$  ppm) and Fe ( $150 \pm 173$  ppm) compared to type 1a fluids ( $1.48 \pm 3.33$  ppm and  $60.4 \pm 74.4$ , respectively). The higher absolute concentrations of aqueous chloride-complexed cations (i.e., Mg, K, Ca, Rb, Sr, Fe, Cu, Zn, and Pb) in type 2 inclusions is a result of the bulk salinity difference between inclusion types, as relative concentrations of these species in type 1a and 2 fluids are similar (e.g., Mg-K-Ca ternary; Fig. 6C). As for other elements, type 1a and type 2 fluids share similar concentrations of B ( $353 \pm 137$  and  $326 \pm 156$  ppm, respectively) and S ( $333 \pm 296$  and  $250 \pm 202$  ppm, respectively). In regards to

sulfur, in both fluid inclusion populations it was often below routine LOD such that only 19% of type 1a inclusions and 13% of type 2 inclusions contained concentrations above the LOD. Notably, the average concentrations of As and Sb are significantly higher in type 1a inclusions ( $67.1 \pm 50.1$  and  $31.6 \pm 20.4$  ppm, respectively) than in type 2 inclusions ( $9.24 \pm 8.28$  and  $5.66 \pm 5.64$  ppm, respectively). Gold was detected in 70% of analyzed type 1a inclusions, averaging  $44.7 \pm 24.5$  ppb for values above the LOD. Conversely, Au was detected in 22% of analyzed type 2 inclusions, averaging  $24.7 \pm 12.3$  ppb. Importantly, we note that for individual FIA the metal contents, such as As, Sb and Au, can be very consistent. For example, in a single type 1a FIA (see Table EA 3-3) constituting eight fluid inclusions, gold concentration varied between 36.7 and 63.5 ppb (average of  $55.4 \pm 9.7$  ppb).

### **3.6 Discussion**

#### **3.6.1 A fluid chemical model for gold precipitation at the Dufferin deposit**

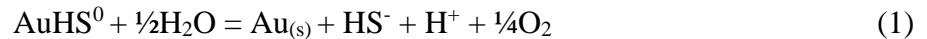
Efficient Au precipitation from an auriferous aqueous-carbonic fluid can occur in response to a variety of physicochemical changes, including a decrease in fluid pressure (which may initiate boiling or unmixing), fluid desulfidation, cooling, and/or a change in fluid  $fO_2$  or pH (e.g., Goldfarb et al., 2005; Williams-Jones et al., 2009 and references therein). At Dufferin, fluid inclusion isochoric fields span a range in pressure of approximately 2 kbar (Fig. 5), which may indicate significant pressure cycling during vein formation. However, the close spatial relationship of Au with CM-bearing units does not support changes in pressure as a significant factor for gold formation. Alternatively, fluid unmixing and subsequent Au precipitation from an aqueous-carbonic fluid can be achieved via cooling to temperatures below 300° to 350°C (Loucks and Mavrogenes, 1999; Mernagh et al., 2004), or by the addition of volatile components (e.g., CH<sub>4</sub> and

N<sub>2</sub>) which expand the P-T region of the 2-phase field at isobaric and/or isothermal conditions (Fig. 5). However, these processes are unlikely to have promoted Au precipitation as the necessary supporting petrographic evidence for either fluid immiscibility or fluid mixing is absent. Gold precipitation resulting from fluid desulfidation can also be dismissed, as the Meguma country rocks were already enriched in S at the time of mineralization, consistent with sulfur isotopic studies suggesting that the Meguma gold deposits have inherited S via fluid/rock interaction (Kontak and Smith, 1989; Sangster, 1992). Furthermore, Au and S concentrations show a positive correlation in type 1 and type 2 fluids, and these fluids are not S-undersaturated according to available thermodynamic models that investigated similar gold-bearing fluids (Rauchenstein-Martinek et al., 2014). We postulate instead that the Au mineralization at Dufferin occurred via coupled fluid  $fO_2$  reduction and pH change that induced Au precipitation from an initially Au-undersaturated hydrothermal solution, as represented by types 1a and 1b fluid inclusions.

The interaction of auriferous fluid with CM hosted in the in wallrock and/or fragments of earlier laminated parts of the quartz veins (i.e., Fig. 1C) provides the auriferous fluid the means to access the organic material necessary for efficient *in situ* fluid reduction and subsequent destabilization of solubilized gold bisulfide complexes. The occurrence of  $\mu\text{m}$ -sized Au particles in CM-filled cavities (Fig. 3D) provides direct evidence that Au precipitation and CM were intimately related, as observed in other gold settings (e.g., the Carbon Leader Reef, Witwatersrand; Fuchs et al., 2017). Concomitant with direct fluid reduction, precipitation of colloidal gold onto the surfaces of CM likely occurred via adsorption/chemisorption, analogous to the preg-robbing mechanism in which dissolved Au in cyanide leachates is adsorbed onto CM, which leads to decreased gold recovery during ore processing (cf., Vaughan, 2004; Miller et al., 2005). Additionally, flocculation

and precipitation of colloidal Au may occur due to changes in fluid chemistry related to increasing pH or salinity (Williams-Jones et al., 2009).

The solubility of Au as a bisulfide species at temperatures  $\leq 350^\circ\text{C}$  is described by reaction 1 and predicts that a decrease in fluid  $f\text{O}_2$  and/or an increase in pH cause(s) Au precipitation (Williams-Jones et al., 2009).



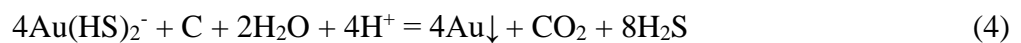
An aqueous-carbonic fluid formed through magmatic devolatilization and/or country rock dehydration and decarbonation reactions within the thermal aureole of an intrusion would have initially possessed favorable physicochemical conditions for Au mobilization by bisulfide (i.e., near-neutral to slightly acidic pH of ~4 to 6, mildly oxidizing to reducing  $f\text{O}_2$ , and  $T < 350^\circ\text{C}$ ; Wood and Samson, 1998 and references therein; Williams-Jones et al., 2009). As Au-bearing fluids interacted with CM-bearing lithologies during fluid migration through permeable lithologies and/or discrete fluid conduits, and during pooling in anticlinal hinge structures, the fluids would become strongly reduced via the graphite-COH buffer (Rns. 2 and 3). Furthermore, during fluid



ascent to higher crustal levels fluid cooling likely occurred. In open systems, a decrease in  $\text{XCO}_2/(\text{XCH}_4+\text{XCO}_2)$  is observed with decreasing temperatures (Fig. 7A; Huizenga and Touret, 1999), with oxygen fugacity buffered at lower  $\log f\text{O}_2$  values during cooling (Ulmer and Luth,

1991; Huizenga and Touret, 1999; Huizenga, 2001) and is negligibly influenced by the desulfidation of wall rocks at low- to medium metamorphic grades (Connolly and Cesare, 1993).

Additional evidence for fluid reduction with time at Dufferin is provided by the significant concentration differences of the redox-sensitive semi-metal elements, As and Sb, between type 1a and type 2 fluids (Fig. 6A). Arsenic and Sb are mobilized in hydrothermal fluids as bisulfide and hydroxide complexes rather than chlorides (Wood and Samson, 1998) and thus their differences in concentration are not a function of bulk fluid salinity (i.e., chlorinity). Notably, during fluid reduction from a log  $fO_2$  of -37 to -41 in the Fe-As-S-O-H system at 250°C, aqueous  $H_3AsO_3$  decomposes and precipitates arsenopyrite (Heinrich and Eadington, 1986; Fig. 8), as is observed in late fractures associated with CM (Fig. 2C). Furthermore, As and Sb have been noted as being potentially important gold-transporting ligands, however, their importance relative to bisulfide ligands is still unclear (Wood and Samson, 1998). During the crustal migration of fluid with subsequent cooling and interaction with CM-bearing lithologies, gold precipitation can proceed via reaction 4 (Hu et al., 2017):



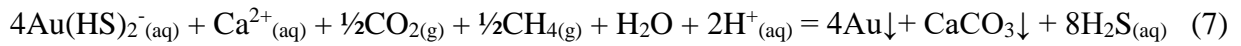
The oxidation of CM in country rocks at depth will produce  $^{13}C$ -depleted  $CO_2$  (i.e., Rn.4) that, once in solution, can combine with  $Ca^{2+}_{(aq)}$  ( $\pm Mg^{2+}_{(aq)}$ ) to produce carbonate (calcite, dolomite) during cooling (i.e., Rn.5; Newton and Manning, 2002) with predictably very low  $\delta^{13}C_{VPDB}$  values. The vein carbonates at Dufferin and other Meguma deposits record very low  $\delta^{13}C_{VPDB}$  values (avg.  $\delta^{13}C_{VPDB} = -21.2\%$ ; n = 2; this study and Kontak and Kerrich, 1997), and strongly suggests that C is sourced from the decomposition of sedimentary organic matter (Lizarralde et al., 2011).



Disassociating  $\text{CaCl}_2$  into its component aqueous ions, reactions 3, 4 and 5 can be combined to yield:



which induces the precipitation of Au and calcite. Alternatively, C can be expressed as  $\text{CH}_4$  and  $\text{CO}_2$  generated through the reaction of C with  $\text{H}_2\text{O}$  (i.e., Rn.3):



Reactions 6 and 7 consume  $\text{H}^+$  leading to pH increase and the precipitation of carbonate. An increase in pH also destabilizes Au bisulfide complexes and promotes Au precipitation (Williams-Jones et al., 2009). The increase in fluid pH at Dufferin is suggested by the presence of dissolution features on quartz surfaces and carbonate (dolomite) precipitation on euhedral quartz crystals lining vugs in the saddles (Fig. 1E). The dissolution of  $\text{SiO}_2$  at a fixed temperature is pH-independent up to pH~6, beyond which the rate of  $\text{SiO}_2$  dissolution increases with increasing pH (Crundwell, 2017). Furthermore, it has been shown that  $\text{SiO}_2$  solubility increases with the addition of dissolved organic compounds such as aliphatic and aromatic carboxylic acids, including hydroxy-acids and keto-acids (near-surface PT conditions; Bennett and Siegel, 1987), which can be introduced into aqueous-carbonic hydrothermal fluids upon interaction with CM, such as those at Dufferin.

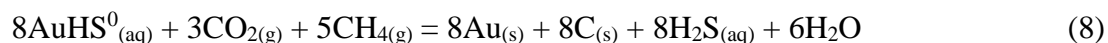
Carbonate precipitation, as is observed in the veins, can be modelled from a solution containing aqueous Ca, Mg and bicarbonate (i.e., type 1a fluid). The activity of  $\text{Ca}^{2+}$  ions in solution was

estimated to be  $\sim 0.00825$  based on an activity coefficient of  $\sim 0.33$  in a solution with an ionic strength of  $\sim 0.188$  (Garrels and Christ, 1965) and a Ca concentration of 0.025 molal (i.e., 1000 ppm Ca in type 1a fluid from LA-ICP-MS data). Similarly, using the measured chemistry of type 1a fluid inclusions discussed above, corresponding to estimated activities of  $\text{Mg}^{2+}$ ,  $\text{HCO}_3^-$ ,  $\text{Na}^+$ ,  $\text{Cl}^-$ , and S as 0.0001, 0.0005, 0.1, 0.1, and 0.01 respectively, Ca-Mg $\pm$ Fe-carbonates will begin to precipitate at a  $\text{pH} \geq 6 - 7$  at  $250^\circ\text{C}$  (Fig. 8). Carbonate precipitation will occur at lower pH values as  $\text{HCO}_3^-$  activity increases, but is independent of increasing  $\text{Mg}^{2+}$  activity. Raman spectroscopic analysis suggests that the relative abundance of  $\text{HCO}_3^-_{(\text{aq})}$  to  $\text{CO}_{2(\text{aq})}$  is higher in type 2 inclusions compared to type 1 inclusions (Fig. 4K). The persistence of appreciable concentrations of  $\text{HCO}_3^-_{(\text{aq})}$  and the decrease in  $\text{CO}_{2(\text{aq})}$  concentration (in equilibrium with carbonic acid) in the transition from type 1 to type 2 fluid inclusions is consistent with a decrease in  $\text{CO}_2$  partial pressure in the vapor phase (i.e., decreasing  $\rho\text{CO}_2$ ; Table 1) and a corresponding increase in pH (Andersen, 2002).

Considering reaction 6, an *a priori* equilibrium constant can be calculated by approximating relevant phase activities. The total measured Au in type 1a fluid inclusions ( $[\text{Au}]_{\text{avg}} = 0.045 \pm 0.025$  ppm;  $n = 84$ ), as determined by LA-ICP-MS, was likely present in the fluid as predominantly the gold bisulfide species  $\text{Au}(\text{HS})_2^-$ , which has been shown to be the dominant Au species in near-neutral,  $\text{CO}_2\text{-HCO}_3^- \text{-CO}_3^{2-}$  buffered solutions (Renders and Seward, 1989; Phillips and Evans, 2004; Tagirov et al., 2005). As already noted, the Ca content of the fluid is set at  $\sim 1000$  ppm. Hydrogen sulfide concentration in type 1a fluid could not be quantified via Raman spectroscopy due to its low concentrations and analytical limitations. Assuming that total S in the fluid is in the form of  $\text{H}_2\text{S}_{(\text{aq})}$  (or  $\text{HS}^-_{(\text{aq})}$ ), the average S concentration determined by fluid inclusion LA-ICP-MS ( $[\text{S}]_{\text{avg}} = 332$  ppm) was used. Assuming a pH of 6 (cf., Phillips and Evans, 2004), the equilibrium

constant for reaction 6 is very large (i.e.,  $K_5 > 1 \times 10^{10}$ ) favoring the precipitation Au and carbonate. However, kinetic factors influencing this reaction remain poorly understood.

Alternatively, CM can be deposited synchronous to Au precipitation through the consumption of  $\text{CO}_2$  and  $\text{CH}_4$  (Rn.8; Kendrick et al., 2011).



This mass action expression is driven to the right during cooling ( $\leq 350^\circ\text{C}$ ), during which time graphite precipitation is predicted for initially graphite-undersaturated fluids (Cesare, 1995; Huizenga, 2001). Late-stage CM is present in arsenopyrite-filled fractures and surrounding quartz grain boundaries adjacent to vein laminations (Fig. 3C), suggesting this reaction may also be locally controlling gold precipitation, providing evidence for a coupled Au-CM-precipitation model (Hu et al., 2017). Carbon dioxide plays a critical role in Au transportation by buffering the pH of the fluid in a range where Au bisulfide complexes remain soluble (Phillip and Evans, 2004). Therefore, removal of  $\text{CO}_2$  through the precipitation of CM (i.e., Rn.8; Hu et al., 2017) or through the precipitation of carbonates (i.e., Rn.7) would influence the pH of the fluid and destabilize soluble Au bisulfide complexes.

### 3.6.2 Fluid evolution during fluid/rock interaction

The presence of abundant secondary FIA along healed fractures indicates continued fluid flux after primary vein formation. The lower cathodoluminescence intensity that these secondary features display compared to the earlier host quartz (Fig. 2D) reflects coupled dissolution-reprecipitation features (e.g., Rusk et al., 2004a, b; Mao et al., 2017). This may result from pressure cycling (Sibson et al., 1988) encouraging the retrograde solubility of quartz in appropriate P-T-pH space

(Akinfiyev and Diamond, 2009; Steele-MacInnis et al., 2012; Monecke et al., 2018). Vapor (Fig. 4A, J) and aqueous phase compositions (Fig. 4K), and bulk fluid inclusion  $\text{CO}_2/(\text{CH}_4+\text{N}_2)$  ratios (Fig. 7B; Table EA 3-1) are similar in type 1a and 1b inclusions, suggesting they are genetically related. Variations in vapor phase  $\text{CO}_2/(\text{CH}_4+\text{N}_2)$  ratios (Table EA 3-2) and aqueous phase salinity (Fig. 7C) between type 1a and 1b inclusions indicate varying degrees of fluid/rock interaction (e.g.,  $\text{N}_2+\text{CH}_4$  from  $\text{NH}_4^+$ -bearing minerals or organic material, hydration reactions). Variation in the vapor phase density between types 1a and 1b inclusions likely reflects P fluctuation during fluid entrapment, a feature of this deposit setting in general. In addition, decreasing fluid  $X_{\text{CO}_2}$  (Fig. 7A) and increasing aqueous phase salinity (Fig. 7B) over the transition from type 1a to 1b fluids likely occurred through carbonate precipitation and fluid dehydration reactions, respectively.

The evolution of type 1 fluid through protracted fluid/rock interaction, fluid  $f\text{O}_2$  decrease, and  $\text{CO}_2$  removal through respeciation and/or carbonate precipitation would generate a fluid consistent with that observed in type 2 inclusions. This interpretation agrees with the temporal relationships inferred from fluid inclusion petrographic observations (Fig. 3E) and with fluid inclusion LA-ICP-MS data (Table EA 3-3), which show that type 2 inclusions are more enriched in wall rock-inherited elements (Mg, Ca, Sr, and possibly Fe) and have significantly lower concentrations of the redox-sensitive semimetals (As, Sb) relative to type 1a inclusions (cf., Heinrich and Eadington, 1986). Consistent bulk densities and consequently overlapping isochoric fields among all inclusion types suggest that the observed decrease in  $\text{Th}_{\text{TOT}}$  with decreasing bulk  $X_{\text{CO}_2}$  (Fig. 7A) reflects the contraction of the immiscibility (2-phase) field to lower T as the bulk  $\text{CO}_2(\pm\text{CH}_4+\text{N}_2)$  of the fluid decreases (Diamond, 2003). Therefore, carbonate (or CM) may have precipitated from a homogeneous fluid (e.g., type 1 fluid) at higher P-T conditions (~270 – 310°C, 2 to 3 kbar), reducing the (bulk) fluid  $\text{CO}_2$  and maintaining fluid homogeneity to lower P-T conditions (~190°

to 300°C, 1 to 2 kbar). Continued P-T decrease would eventually promote fluid unmixing yielding a fluid reminiscent of that observed in type 2 inclusions, along with a corresponding vapor-rich endmember. However, that this latter fluid was not identified in the fluid inclusion record at Dufferin precludes such a scenario. Furthermore, type 2 inclusions show distinct vapor phase volatile concentrations and bulk  $\text{CO}_2/(\text{CH}_4+\text{N}_2)$  ratios relative to type 1 inclusions. The high abundances of  $\text{CH}_4$  and  $\text{N}_2$  in type 2 fluid suggest it equilibrated with the organic-rich slates of the country rock (e.g., Glasmacher et al., 2003), as  $\text{N}_2$  and  $\text{CH}_4$  can be readily produced via the decomposition/devolatilization of organic matter present in the sedimentary protoliths (Beaumont and Robert, 1999), with additional  $\text{N}_2$  potentially from the decomposition of  $\text{NH}_4^+$ -bearing phyllosilicates (e.g., Papineau et al., 2005).

### **3.6.3 Potential origins of auriferous vein-forming fluids**

The origin of Au-mineralizing aqueous-carbonic fluids in metamorphic terranes continues to be enigmatic (Groves et al., 2003; Goldfarb et al., 2005; Goldfarb and Groves, 2015). Numerous studies have shown that aqueous-carbonic fluid compositions, including their volatile constituents (e.g.,  $\text{CO}_2$ ,  $\text{CH}_4$ ,  $\text{N}_2$ ) and fluid salinity, are similar in both intrusion-related (Thompson et al., 1999; Lang and Baker, 2001) and orogenic (McCuaig and Kerrich, 1998; Ridley and Diamond, 2000; Bodnar et al., 2014) gold settings. Furthermore, the timing of fluid entrapment is poorly constrained since unequivocal identification of primary quartz-hosted fluid inclusions (i.e., confined to growth zones) in orogenic Au deposits, and unmineralized metamorphic equivalents, are rarely reported (van den Kerkhof and Hein, 2001; Bons et al., 2012; Rauchenstein-Martinek et al., 2014; Zohier et al., 2019).

At Dufferin, the timing of saddle vein formation is constrained from two independent, but related parameters: absolute age dating and a robust structural model of vein emplacement. With respect to the former, Re-Os dating of vein-hosted arsenopyrite yielded coincident isochron and model ages of 380 Ma (Morelli et al., 2005), which supported earlier  $^{40}\text{Ar}/^{39}\text{Ar}$  age of ~380 Ma for wallrock ribbon material in the veins (Kontak et al., 1998). These dates are consistent with the proposed structural model of vein formation for Meguma Au veins (Horne and Culshaw, 2001), and Dufferin in particular (Horne and Jodrey, 2002), whereby fold tightening and development of flexural slip planes, and associated laminated and saddle-reef veins, relate to emplacement of the large granitoid intrusions at ~380 Ma (Horne and Jodrey, 2002). Thus, in this model, vein emplacement was late in the regional deformation history and overlapped with intrusion of the proximal (~10 km) Musquodoboit batholith dated at  $378 \pm 1$  Ma (concordant U-Pb zircon and monazite ages; Kontak et al., 2004). These constraints suggest the vein fluids are possibly: (i) derived from the exsolution of volatiles from cooling of an unexposed granitoid intrusion linked to the Musquodoboit batholith, and/or (ii) dehydration and decarbonation of Goldenville Group rocks in the contact aureole of the same putative cooling intrusion (e.g., Kempe et al., 2016).

Based on the metal contents of the Dufferin fluid inclusions, a distinction cannot be made with respect to the Au source. A review of the compositions of ore fluids from >19 deposits of magmatic-hydrothermal and metamorphic affinity (Fig. 6A) shows that, with respect to major-, minor- and trace-element concentrations, there are unfortunately no elemental discriminators. For example, enrichment in B-As-Sb-Au in type 1a fluid inclusions at Dufferin has been variably interpreted as evidence for a magmatic origin since they are preferentially enriched in magmatic vapors during boiling in magmatic-hydrothermal systems (Heinrich et al., 1999; Williams-Jones and Heinrich, 2005, and references therein). However, it remains equivocal whether such B-As-

Sb-Au-enriched fluids originate from deeply intruded S-type granitoids, such as the Musquodoboit Batholith, or from fluid interaction with metalliferous metasedimentary country rocks (e.g., Meguma terrane; White and Goodwin, 2011). Available data indicate that rocks of the Meguma stratigraphy are depleted in Sb but moderately enriched in As (e.g., Beaverbank Formation of the Goldenville Group: <0.1 – 0.4 ppm Sb vs. 5 – 75 ppm As in whole rock assays; White and Goodwin, 2011), which suggests a possible local contribution of As to the ore fluid through fluid/rock interaction. However, an increase in the presence of arsenopyrite (also chalcopyrite, galena, and sphalerite) in contact aureoles proximal to the granitic South Mountain Batholith that intrudes Meguma rocks (Clarke et al., 2009) suggests a possible magmatic metal input. Additionally, Au positively correlates with As+Sb in type 1a fluid inclusions and late-stage arsenopyrite mineralization is present in fractures (Fig. 2C) in auriferous quartz veins.

Regardless of the origin of Au, it is well documented that vein-forming fluids associated with Au deposits in the Meguma terrane interacted with their country rocks (Kontak and Kerrich, 1997, Kontak et al., 2011). For instance, vein carbonate  $\delta^{13}\text{C}_{\text{VPDB}}$  values overlap with those for diagenetic carbonate and graphite in Goldenville Group metasedimentary rocks (-13 to -22‰; Kontak and Kerrich, 1997). At Dufferin, late hydrothermal carbonate (ferroan dolomite) from saddle 6 (Fig. 1E) are similarly  $^{13}\text{C}$ -depleted (average  $\delta^{13}\text{C}_{\text{VPDB}}$  of -21.2‰; n=2). Given the inferred temperature of vein formation (350° to 400°C) and  $\text{CO}_2$ -rich nature of the fluids,  $\delta^{13}\text{C}_{\text{carbonate}} \approx \delta^{13}\text{C}_{\text{H}_2\text{CO}_3} \approx \delta^{13}\text{C}_{\text{fluid}}$  and the low  $\delta^{13}\text{C}$  signature is a primary feature of the fluid (cf., Kontak and Kerrich, 1997). Therefore, C in the ore fluid (as  $\text{CO}_2+\text{CH}_4$ ) at Dufferin was likely derived from organic-bearing country rocks. Furthermore, the gradual increase in  $\delta^{34}\text{S}_{\text{sulfide}}$  values for sulfides from the

Meguma Au deposits mimics the  $\delta^{34}\text{S}_{\text{sulfide}}$  trend for the Meguma Group stratigraphy in general (Sangster, 1992; Kontak et al., 2011), strongly suggesting S is wall rock derived.

The source of the Au in Meguma deposits is still a subject of debate, with both magmatic and country rock-derived sources debated (Kontak and Smith, 1989; Kontak et al., 1990, 1998, 2011; Kontak and Kerrich, 1997; Ryan and Smith, 1998; Morelli et al., 2005; Kontak and Kyser, 2011, Kontak et al., 2018). Additionally, Sangster (1992) theorized that Au may have been remobilized from the anoxic carbonaceous sedimentary rocks of the Goldenville Group which, in the context of the present study, suggests CM-bearing lithologies may act as both a Au source and Au sink. Regardless of the ultimate source of Au, we show that the late aqueous-carbonic fluids from mineralized Dufferin saddle veins are: (i) Au-undersaturated ( $[\text{Au}]_{\text{avg}} = 0.045$  ppm in type 1a fluid versus  $[\text{Au}]_{\text{calc.}} \approx 0.1 - 2$  ppm or  $[\text{Au}]_{\text{calc.}} \approx 5 \times 10^{-7} - 1 \times 10^{-5}$  mol/kg at 300°C); and (ii) S-saturated ( $[\text{S}]_{\text{avg}} = \sim 330$  ppm in type 1a inclusions versus  $[\text{S}]_{\text{calc.}} \approx 30 - 320$  ppm or  $[\text{S}]_{\text{calc.}} \approx 0.01 - 0.001$  mol/kg at 300°C) with respect to concentrations predicted in  $\text{H}_2\text{O}-\text{CO}_2-\text{H}_2\text{S}-\text{NaCl}$ -bearing hydrothermal fluids with similar compositions (Rauchenstein-Martinek et al., 2014). This suggests that the capacity of a fluid to mobilize Au is not necessarily a function of Au and S solubility, but rather labile nature of Au in the country rocks and/or causative magmatic intrusions (e.g., Rauchenstein-Martinek et al., 2014). The Au concentration in type 1a fluid is comparable to geochemically similar Alpine fluids of inferred metamorphic origin hosted in Au-barren veins (i.e.,  $[\text{Au}] \approx 0.03 - 0.11$  ppm; Rauchenstein-Martinek et al., 2014, 2016). Therefore, Au mineralization at Dufferin likely reflects a highly efficient precipitation mechanism(s) that is/are absent in barren orogenic systems involving similarly Au-enriched fluids.

### 3.7 Conclusions

This study presents the first reported Au concentrations in secondary aqueous-carbonic fluid inclusions in an actively mined orogenic Au deposit setting. Aqueous-carbonic fluids of similar composition and comparable Au content have been identified in unmineralized quartz vein systems elsewhere (Rauchenstein-Martinek et al., 2016), suggesting that Au-enriched fluids do not equate to Au-rich deposits. Instead, the nature of Au mineralization at the Dufferin deposit, and analogous bulk mineable metasedimentary rock-hosted deposits (e.g., Touquoy), indicates that a highly efficient precipitation mechanism is necessary to produce adequate gold from a relatively low volume of auriferous fluid (compared to high-tonnage gold systems with volumetrically-extensive veining; e.g., Abitibi-hosted deposits; Goldfarb et al., 2005; Gosselin and Dubé, 2005; Dubé and Gosselin, 2007). To accommodate the latter, a geological model is proposed based on the production of an auriferous, yet gold-undersaturated, fluid through a combined magmatic devolatilization, and/or country rock dehydration and decarbonation mechanism related to contact metamorphism (Fig. 9). Fluid ascent along lithological contacts and subsequent pooling in anticlinal hinge structures enhanced interaction of the fluid with reducing lithologies (e.g., CM-bearing black slate or argillite) that decreased fluid  $fO_2$  and increased pH which led to *in situ* precipitation of gold + carbonate + arsenopyrite  $\pm$  CM. Importantly, this process may also be responsible for gold mineralization in other CM-bearing, metasedimentary rock-hosted Au deposits throughout the Meguma terrane. It has been suggested that the disseminated- and vein-type Au deposits across the terrane represent mineralization style endmembers in the continuum of sediment-hosted orogenic deposits as these mineralization styles share similar characteristics, including alteration assemblages, fluid geochemistry and direct association with CM-bearing metasedimentary units (Bierlein and Smith, 2003).

The conclusions of this study provide the basis to better understand gold mineralization in settings spatially-associated with CM and/or in analogous geological settings worldwide, where a genetic association of Au with CM ( $\pm$  graphite) has been speculated, such as the western Lachlan orogeny, Otago schists, Carlin deposits, the Kupferschiefer, and Ashanti gold belt for example. Application of this model to the aforementioned areas, and elsewhere, may find that it better accommodates both the nature of gold mineralization and the fluid chemistry in such settings.

### **3.8 References**

- Akinfiyev, N.N., and Diamond, L.W. (2009). A simple predictive model of quartz solubility in water–salt–CO<sub>2</sub> systems at temperatures up to 1000 C and pressures up to 1000 MPa. *Geochimica et Cosmochimica Acta* 73(6), 1597-1608.
- Andersen, C.B. (2002). Understanding Carbonate Equilibria by Measuring Alkalinity in Experimental and Natural Systems. *Journal of Geoscience Education* 50(4), 389-403.
- Audétat, A., Günther, D., and Heinrich, C.A. (2000). Causes for Large-Scale Metal Zonation around Mineralized Plutons: Fluid Inclusion LA-ICP-MS Evidence from the Mole Granite, Australia. *Economic Geology* 95, 1563-1581.
- Bakker R.J. (1999). Adaption of Bowers and Helgeson (1983) equation of state to isochore and fugacity coefficient calculation in the H<sub>2</sub>O-CO<sub>2</sub>-CH<sub>4</sub>-N<sub>2</sub>-NaCl fluid system. *Chemical Geology* 154, 225–236.
- Bakker R.J. (2003). Package FLUIDS 1. Computer programs for analysis of fluid inclusion data and for modeling bulk fluid properties. *Chemical Geology* 194, 3–23.

- Beaudoin, G., and Chiaradia, M. (2016). Fluid mixing in orogenic gold deposits: Evidence from the HO-Sr isotope composition of the Val-d'Or vein field (Abitibi, Canada). *Chemical Geology* 437, 7-18.
- Beaumont, V., and Robert, F. (1999). Nitrogen isotope ratios of kerogens in Precambrian cherts: a record of the evolution of atmosphere chemistry?. *Precambrian Research* 96(1-2), 63-82.
- Beeskov B., Rankin A.H., Murphy P.J. and Treloar P.J. (2005). Mixed CH<sub>4</sub>-CO<sub>2</sub> fluid inclusions in quartz from the South Wales Coalfield as suitable natural calibration standards for microthermometry and Raman spectroscopy. *Chemical Geology* 223, 3–15.
- Benn, K., Horne, R.J., Kontak, D.J., Pignotta, G. and Evans, N.G. (1997). Syntectonic emplacement of the South Mountain Batholith, Meguma Terrane, Nova Scotia: magnetic fabric and structural analyses. *Bulletin Geological Society of America* 109, 1279-1293.
- Bennett, P. and Siegel, D.I. (1987). Increased solubility of quartz in water due to complexing by organic compounds. *Nature* 326, 684-686.
- Berge, J. (2011). Paleoproterozoic, turbidite-hosted, gold deposits of the Ashanti gold belt (Ghana, West Africa): Comparative analysis of turbidite-hosted gold deposits and an updated genetic model. *Ore Geology Reviews* 39, 91-100.
- Bierlein, F.P., Cartwright, I., McKnight, S., (2001). The role of carbonaceous “indicator” slates in the genesis of lode gold mineralization in the Western Lachlan orogen, Victoria, Southeastern Australia. *Economic Geology* 96, 431–451.
- Bierlein, F.P., and Maher, S. (2001). Orogenic disseminated gold in Phanerozoic fold belts – examples from Victoria, Australia, and elsewhere. *Ore Geology Reviews* 18: 113–148.

- Bierlein, F.P., and Smith, P.K., (2003). The Touquoy Zone deposit: an example of “unusual” orogenic gold mineralization in the Meguma Terrane, Nova Scotia, Canada. *Canadian Journal of Earth Science* 40, 447-466.
- Bierlein, F.P., Christie, A.B., and Smith, P.K. (2004). A comparison of orogenic gold mineralisation in central Victoria (AUS), western South Island (NZ) and Nova Scotia (CAN): implications for variations in the endowment of Palaeozoic metamorphic terrains. *Ore Geology Reviews* 25, 125-168.
- Bodnar R.J., Lecumberri-Sanchez P., Moncada D. and Steele-MacInnis M. (2014). Fluid inclusions in hydrothermal ore deposits. In *Reference Module in Earth Systems and Environmental Sciences Treatise on Geochemistry (Second Edition)*, pp. 119–142.
- Bodnar R.J. and Vityk M.O. (1994). Interpretation of microthermometric data for H<sub>2</sub>O-NaCl fluid inclusions. In *Fluid Inclusions in Minerals, Methods, and Applications* (eds. B. De Vivo and M. L. Frezzotti). Tech, Virginia, pp. 117–130.
- Bons, P.D, Elburg, M.A., and Gomez-Rivas, E. (2012). A review of the formation of tectonic veins and their microstructures. *Journal of Structural Geology* 43, 33-62.
- Bowers T.S. and Helgeson H. C. (1983). Calculation of the thermodynamic and geochemical consequences of nonideal mixing in the system H<sub>2</sub>O-CO<sub>2</sub>-NaCl on phase relations in geologic systems: Equation of state for H<sub>2</sub>O-CO<sub>2</sub>-NaCl fluids at high pressures and temperatures. *Geochimica et Cosmochimica Acta* 47(7), 1247–1275.
- Breerwood, C.H. (1938). US Patent No. 2130574. Flotation of Carbonaceous Ore.
- Brooks, A.H. (1912). Gold Deposits Near Valdez. U.S. Geology Survey Bulletin 520-D, pp. 108-130.

- Brown, K.L. (1986). Gold Deposition from Geothermal Discharges in New Zealand. *Economic Geology* 81, 979-983.
- Cesare, B. (1995). Graphite precipitation in C–O–H fluid inclusions: closed system compositional and density changes, and thermobarometric implications. *Contributions to Mineralogy and Petrology* 122, 25-33.
- Clarke, D.B., MacDonald, M.A., and Tate, M.C., (1997). Late Devonian mafic-felsic magmatism in the Meguma zone, Nova Scotia. In, Sinha, A.K., Whalen, J.F., and Hogan, J.P., eds., *The Nature of Magmatism in the Appalachian Orogen: Geological Society of America Memoir* 191, p. 107–127.
- Clarke, D.B., MacDonald, M.A., and Tate, M.C., (1997), Late Devonian mafic-felsic magmatism in the Meguma zone, Nova Scotia, *in* Sinha, A.K., Whalen, J.F., and Hogan, J.P., eds., *The Nature of Magmatism in the Appalachian Orogen: Geological Society of America Memoir* 191, p. 107–127.
- Clarke, D.B., Erdmann, S., Samson, H., and Jamieson, R.A. (2009). Contamination of the South Mountain Batholith by sulfides from the country rocks. *The Canadian Mineralogist* 47(5), 1159-1176.
- Connolly, J.A.D., and Cesare, B. (1993). C-O-H-S fluid composition and oxygen fugacity in graphitic metapelites. *Journal of Metamorphic Geology* 11, 379-388.
- Craw, D., (2002). Geochemistry of late metamorphic hydrothermal alteration and graphitization of host rock, Macraes gold mine, Otago Schist, New Zealand. *Chemical Geology* 191, 257–275.
- Craw, D., Teagle, D.A.H., and Belocky, R. (1993). Fluid immiscibility in late-Alpine gold-bearing veins, Eastern and Northwestern European Alps. *Mineralium Deposita* 28(1), 28-36.

- Crundwell, F.K. (2017). On the Mechanism of the Dissolution of Quartz and Silica in Aqueous Solutions. *ACS Omega* 2, 1116-1127.
- Darling R.S. (1991). An extended equation to calculate NaCl contents from final clathrate melting temperatures in H<sub>2</sub>O-CO<sub>2</sub>-NaCl fluid inclusions: Implications for P-T isochores location. *Geochimica et Cosmochimica Acta* 55, 3869–3871.
- De Souza, S., Dubé, B., McNicoll, V., Dupuis, C., Mercier-Langevin, P., Creaser, R.A., and Kjarsgaard, I. (2017). Geology and hydrothermal alteration of the world-class Canadian Malartic gold deposit: Genesis of an Archean stockwork-disseminated gold deposit in the Abitibi greenstone belt: *Reviews in Economic Geology* 19, 263–291.
- Diamond L. (1992). Stability of CO<sub>2</sub> clathrate hydrate + CO<sub>2</sub> liquid + CO<sub>2</sub> vapour + aqueous KCl-NaCl solutions: Experimental determination and application to salinity estimates of fluid inclusions. *Geochimica et Cosmochimica Acta* 56, 273–280.
- Diamond, L.W. (2003). Introduction to gas-bearing, aqueous fluid inclusions. In Samson, I., Anderson, A., and Marshall, M., eds. *Fluid Inclusions: Analysis and Interpretation: Mineralogical Association of Canada Short Course* 32, 101-158.
- Dinel, E., Fowler, A.D., Ayer, J., Still, A., Tylee, K., and Barr, E. (2008). Lithogeochemical and Stratigraphic Controls on Gold Mineralization within the Metavolcanic Rocks of the Hoyle Pond Mine, Timmins, Ontario. *Economic Geology* 103, 1341-1363.
- Duan, Z., Møller, N., Weare, J.H. (2003). Equations of State for the NaCl-H<sub>2</sub>O-CH<sub>4</sub> System and the NaCl-H<sub>2</sub>O-CO<sub>2</sub>-CH<sub>4</sub> System: Phase Equilibria and Volumetric Properties above 573 K. *Geochimica et Cosmochimica Acta* 67, 671-680.
- Dubé, B., and Gosselin, P. (2007). Greenstone-hosted quartz-carbonate vein deposits, in Goodfellow, W.D., ed., *Mineral Deposits of Canada: A Synthesis of Major Deposit-Types*,

- District Metallogeny, the Evolution of Geological Provinces, and Exploration Methods: Geological Association of Canada, Mineral Deposits Division, Special Publication No. 5, p. 49-73.
- Dubosq, R., Lawley, C.J.M., Rogowitz, A., Schneider, D. A., and Jackson, S. (2018). Pyrite deformation and connections to gold mobility: Insight from micro-structural analysis and trace element mapping. *Lithos* 310, 86-104.
- Evans, K.A., Phillips, G.N., and Powell, R. (2006). Rock-buffering of auriferous fluids in altered rocks associated with the Golden Mile-style mineralization, Kalgoorlie gold field, Western Australia. *Economic Geology* 101(4), 805-817.
- Frezzotti, M.L., Tecce, F., and Casagli, A. (2012). Raman spectroscopy for fluid inclusion analysis. *Journal of Geochemical Exploration* 112, 1-20.
- Fuchs, S.H.J., Schumann, D., Williams-Jones, A.E., Murray, A.J., Couillard, M., Lagarec, K., Phaneuf, M.W., and Vali, H. (2017). Gold and uranium concentration by interaction of immiscible fluids (hydrothermal and hydrocarbon) in the Carbon Leader Reef, Witwatersrand Supergroup, South Africa. *Precambrian Research* 293, 39-55.
- Fusswinkel T., Wagner T. and Sakellaris G. (2017). Fluid evolution of the Neoproterozoic Pampalo orogenic gold deposit (E Finland): Constraints from LA-ICPMS fluid inclusion microanalysis. *Chemical Geology* 450, 96–121.
- Gaboury, D. (2019). Parameters for the formation of orogenic gold deposits. *Applied Earth Science* 1-10.
- Garrels, R.M. and Christ, C.L. (1965). *Solutions, Minerals and Equilibria*. Ch. 2, Harper and Row, New York.

- Glasmacher, U.A., Zentilli, M., and Ryan, R. (2003). Nitrogen distribution in Lower Palaeozoic slates/phyllites of the Meguma Supergroup, Nova Scotia, Canada: implications for Au and Zn–Pb mineralisation and exploration. *Chemical Geology* 194, 297-329.
- Goldfarb R.J., Baker T., Dubé´ B., Groves D.I., Hart C.J.R. and Gosselin P. (2005). Distribution, character, and genesis of gold deposits in metamorphic terranes. In *Economic Geology 100<sup>th</sup> Anniversary Volume*, pp. 407–450.
- Goldfarb R.J. and Groves D.J. (2015). Orogenic gold: Common or evolving fluid and metal sources. *Lithos* 2, 2–26.
- Goldstein, R.H. (1986). Reequilibration of fluid inclusions in low-temperature calcium-carbonate cement. *Geology* 14(9), 792-795.
- Goldstein R.H. and Reynolds T.J. (1994). Fluid inclusion microthermometry 31. In *Systematics of Fluid Inclusions in Diagenetic Minerals* (eds. R. H. Goldstein and T. J. Reynolds). Soc. Sed. Geology Short Course, pp. 87–122.
- Gosselin, P., and Dubé´, B. (2005). Gold deposits of Canada: Distribution, geological parameters and gold content. Geological Survey of Canada, Open File 4896.
- Groves, D.I., and Foster, R.P. (1991). Archaean lode gold deposits, in Foster, R.P., ed., *Gold metallogeny and exploration*: London, Blackie, p. 63–103.
- Groves D.I., Goldfarb R.J., Robert F. and Hart C.J.R. (2003). Gold deposits in metamorphic belts: overview of current understanding, outstanding problems, future research, and exploration significance. *Economic Geology* 98, 1–29.
- Guillong M., Meier D.L., Allan M.M., Heinrich C.A., Yardley B.W.D. (2008). Appendix A6: SILLS: a Matlab-based program for the reduction of Laser Ablation ICP–MS data of

- homogeneous materials and inclusions. Short Course Ser., Mineralogical Association of Canada 40, 328–333. Vancouver B.C.
- Hannon, P., Roy, D., Mosher, G. (2017). Revised Preliminary Economic Assessment of the Dufferin Gold Deposit. Resource Capital Gold Corp. April 2017.
- Harris, I.M., and Schenk, P.E. (1975). The Meguma Group. *Atlantic Geology* 11(1), 25-46.
- Heinrich, C.A., and Eadington, P.J. (1986). Thermodynamic Predictions of the Hydrothermal Chemistry of Arsenic, and Their Significance for the Paragenetic Sequence of Some Cassiterite-Arsenopyrite-Base Metal Sulfide Deposits. *Economic Geology* 81, 511-529.
- Heinrich, C.A., Gunther, D., Audéat, A., Ulrich, T. and Frischknecht, R. (1999). Metal fractionation between magmatic brine and vapor, determined by microanalysis of fluid inclusions. *Geology* 27(8), 755–758.
- Hicks, R.J., Jamieson, R.A. and Reynolds, P.H. (1999). Detrital and metamorphic  $^{40}\text{Ar}/^{39}\text{Ar}$  ages from muscovite and whole-rock samples, Meguma Supergroup, southern Nova Scotia; *Canadian Journal of Earth Sciences* 36, 23-32.
- Hilchie, L.J., and Jamieson, R.A. (2014). Graphite thermometry in a low-pressure contact aureole, Halifax, Nova Scotia. *Lithos* 208, 21-33.
- Horne, R.J. and Culshaw, N. (2001). Flexural-slip folding in the Meguma Group, Nova Scotia, Canada. *Journal of Structural Geology* 23, 1631-1652.
- Horne, R.J., Jodrey, M. (2002). Geology of the Dufferin gold deposit (NTS 11D/16), Halifax County. In: MacDonald DR (ed) Mineral Res Branch, Rpt Act 2001, Nova Scotia Dept Nat Res, Rpt 2002-1, pp. 51–68.

- Horne, R.J., Jodrey, M., and Woodman, K. (2002). Geology of the Dufferin gold deposit, Port Dufferin, Nova Scotia. Atlantic Geoscience Society Colloquium and Annual General Meeting, February 2002. Abstracts.
- Hu, Si-Yu, Evans, K., Craw, D., Rempel, K., and Grice, K. (2017). Resolving the role of carbonaceous material in gold precipitation in metasediment-hosted orogenic gold deposits. *Geology* 45, 167-170.
- Huizenga, J.M. (2001). Thermodynamic modelling of C–O–H fluids. *Lithos* 55, 101-114.
- Huizenga, J.M., and Touret, J.L.R. (1999). Fluid inclusions in shear zones: The case of the Umwindsi shear zone in the Harare-Shamva-Bindura greenstone belt, NE Zimbabwe. *European Journal of Mineralogy* 11, 1079-1090.
- Jehlička, J., Urban, O., and Pokorný, J. (2003). Raman spectroscopy of carbon and solid bitumens in sedimentary and metamorphic rocks. *Spectrochimica Acta Part A*, 59, 2341-2352.
- Joralemon, P. (1951). The occurrence of gold at the Getchell Mine, Nevada. *Economic Geology* 46, 267-310.
- Kempe, U., Graupner, T., Seltmann, R., de Boorder, H., Dolgoplova, A., and van Emmichoven, M. Z. (2016). The Muruntau gold deposit (Uzbekistan)—a unique ancient hydrothermal system in the southern Tien Shan. *Geoscience Frontiers* 7(3), 495-528.
- Kendrick, M.A., Honda, M., Walshe, J., and Petersen, K. (2011). Fluid sources and the role of abiogenic-CH<sub>4</sub> in Archean gold mineralization: Constraints from noble gases and halogens. *Precambrian Research* 189, 313-327.
- Kontak, D.J., Archibald, D.A. (2002). <sup>40</sup>Ar/<sup>39</sup>Ar dating of hydrothermal biotite from high-grade gold mineralization, Tangier gold deposit, Nova Scotia, Canada: Further evidence ca. 370 Ma gold metallogeny in the Meguma Terrane. *Economic Geology* 97, 619–628.

- Kontak, D.J., Ham, L.J., and Dunning, G. (2004). U-Pb dating of the Musquodoboit Batholith, southern Nova Scotia: evidence for a protracted magmatic-hydrothermal event in a Devonian intrusion. *Atlantic Geology* 40, 207-216.
- Kontak, D.J., and Horne, R.J. (2010). A multi-stage origin for the Meguma lode gold deposits, Nova Scotia, Canada: a possible global model for slate belt-hosted gold mineralization. *Gold metallogeny: India and beyond*. Alpha Science International Ltd., Oxford, 58-82.
- Kontak, D.J., Horne, R.J., and Kyser, K., (2011). An oxygen isotope study of two contrasting orogenic vein gold systems in the Meguma Terrane, Nova Scotia, Canada, with implications for fluid sources and genetic models: *Mineralium Deposita* 46, 289-304.
- Kontak, D.J., Horne, R.J., Sandeman, H., Archibald, D.A. (1998).  $^{40}\text{Ar}/^{39}\text{Ar}$  dating of whole-rock slates from auriferous veins in the Meguma Group, Nova Scotia: Evidence for post metamorphic timing of vein formation. *Canadian Journal of Earth Science* 35, 746–761
- Kontak, D.J., Horne, R.J., and Smith, P. (2001). Meguma gold deposits, Nova Scotia: overview of past work with implications for future work. *The Gangué*, GAC Mineral Deposits Division, (71), 1-9.
- Kontak, D.J., Kerrich, R. (1997). An isotopic (C, O, Sr) study of vein quartz and carbonate from Meguma gold deposits, Nova Scotia, Canada. *Economic Geology* 92, 161–180.
- Kontak, D.J., and Kyser, K. (2011). A fluid inclusion and isotopic study of an intrusion-related gold deposit (IRGD) setting in the 380 Ma South Mountain Batholith, Nova Scotia, Canada: evidence for multiple fluid reservoirs. *Mineralium Deposita* 46, 337-363.
- Kontak, D.J., Smith, P.K. (1989). Preliminary results of a fluid inclusion study of the Stockwork Zone vein mineralization, Caribou deposit, Meguma Terrane, Nova Scotia. In: McDonald

- DR (ed) Mines and Minerals Branch Rpt Act for 1989, Part A. Nova Scotia Dept Mines and Energy, Rpt 89-3, pp. 65–70.
- Kontak, D.J., Smith, P.K., Kerrich, R., Williams, P.F. (1990). An integrated model for Meguma Group lode gold deposits, Nova Scotia, Canada. *Geology* 17, 238–242.
- Kontak, D.J., Ulrich, T., and Kyser, K.T. (2018). Mixing of magmatic and wall-rock derived fluids in a 380 Ma reduced intrusion-related gold setting, Nova Scotia, Canada: Evidence from LA ICP-MS analysis of fluid inclusions and stable isotopes. *Mineralium Deposita*, IN PRESS.
- Kusebauch, C., Gleeson, S.A., and Oelze, M. (2019). Coupled partitioning of Au and As into pyrite controls formation of giant Au deposits. *Science Advances* 5(5), eaav5891.
- Lafrance, B. (2015). Geology of the orogenic Cheminis gold deposit along the Larder Lake–Cadillac deformation zone, Ontario. *Canadian Journal of Earth Sciences* 52(12), 1093–1108.
- Lang, J.R. and Baker, T. (2001). Intrusion-related gold systems: the present level of understanding. *Mineralium Deposita* 36, 477–489.
- Large, R.R., Danyushevsky, L., Hollit, C., Maslennikov, V., Meffre, S., Gilbert, S.B., Scott, R., Emsbo, P., Thomas, H., Singh, B., and Foster, J. (2009). Gold and trace element zonation in pyrite using a laser imaging technique: Implications for the timing of gold in orogenic and Carlin-style sediment-hosted deposits. *Economic Geology* 104, 635–668.
- Large, R.R., Maslennikov, V.V., Robert, F., Danyushevsky, L.V., and Chang, Z. (2007). Multistage sedimentary and metamorphic origin of pyrite and gold in the giant Sukhoi Log deposit, Lena gold province, Russia. *Economic Geology* 102(7), 1233–1267.

- Liu, D., Xiao, X., Tian, H., Min, Y., Zhou, Q., Cheng, P., and Shen, J. (2013). Sample maturation calculated using Raman spectroscopic parameters for solid organics: Methodology and geological applications. *Chinese Science Bulletin* 58, 1285-1298.
- Lizzarralde, D., Soule, S.A, Seewald, J.S., and Proskurowski, G. (2010). Carbon release by off-axis magmatism in a young sedimented spreading centre. *Nature Geoscience* 4, 50-55.
- Malcolm, W., (1929). *Gold Fields of Nova Scotia*. Geological Survey of Canada, Memoir 156, 253 p.
- Mao, W., Rusk, B., Yang, F., and Zhang, M. (2017). Physical and chemical evolution of the Dabaoshan porphyry Mo deposit, South China: Insights from fluid inclusions, cathodoluminescence, and trace elements in quartz. *Economic Geology* 112(4), 889-918.
- Matthäi, S.K., Henley, R.W., and Heinrich, C.A. (1995). Gold precipitation by fluid mixing in bedding-parallel fractures near carbonaceous slates at the Cosmopolitan Howley gold deposit, northern Australia. *Economic Geology* 90(8), 2123-2142.
- Mavrogenes, J.A., and Loucks, R.R. (1999). Gold Solubility in Supercritical Hydrothermal Brines Measured in Synthetic Fluid Inclusions. *Science* 284, 2159-2163.
- McCuaig, T.C. and Kerrich, R. (1998). P-T-t-deformation-fluid characteristics of lode gold deposits: evidence from alteration systematics. *Ore Geology Reviews* 12, 381–453.
- Mernagh, T.P., Heinrich, C.A., and Mikucki, E.J. (2004). Temperature gradients recorded by fluid inclusions and hydrothermal alteration at the Mount Charlotte gold deposit, Kalgoorlie, Australia. *The Canadian Mineralogist* 42(5), 1383-1404.
- Miller, J.D., Wan, R.Y., and Diaz, X. (2005). Preg-robbing gold ores. *Developments in Mineral Processing* 15, 937-972.

- Monecke, T., Monecke, J., Reynolds, T.J., Tsuruoka, S., Bennett, M.M., Skewes, W.B., and Palin, R.M. (2018). Quartz solubility in the H<sub>2</sub>O-NaCl system: a framework for understanding vein formation in porphyry copper deposits. *Economic Geology* 113(5), 1007-1046.
- Morelli, R.M., Creaser, R., Selby, D., Kontak, D.J., Horne, R.J. (2005). Rhenium-Osmium geochronology of arsenopyrite in Meguma Group gold deposits, Meguma Terrane, Nova Scotia, Canada: evidence for multiple gold-mineralizing events. *Economic Geology* 100, 1229–1242.
- Murphy, J.B., Waldron, J.W., Kontak, D.J., Pe-Piper, G., and Piper, D.J. (2011). Minas Fault Zone: Late Paleozoic history of an intra-continental orogenic transform fault in the Canadian Appalachians. *Journal of Structural Geology* 33(3), 312-328.
- Newton, R.C., and Manning, C.E. (2002). Experimental determination of calcite solubility in H<sub>2</sub>O-NaCl solutions at deep crust/upper mantle pressures and temperatures: Implications for metasomatic processes in shear zones. *American Mineralogist* 87, 1401-1409.
- Olivo, G.R., and Williams-Jones, A.E. (2002). Genesis of the auriferous C quartz-tourmaline vein of the Siscoe mine, Val d'Or district, Abitibi subprovince, Canada: structural, mineralogical and fluid inclusion constraints. *Economic Geology* 97(5), 929-947.
- Oszczepalski, S., Speczik, S., and Wojciechowski, A. (2011). Gold mineralization in the Kupferschiefer oxidized series of the North Sudetic trough, SW Poland. *Gold in Poland*, AM Momograph No.2, 153-168.
- Padgham, W.A., (1986). Turbidite-Hosted Gold–Quartz Veins in the Slave structural Province, NWT. In: Keppie, J.D., Boyle, R.W., Haynes, S.J. (Eds.), *Turbidite-Hosted Gold Deposits: Geologic Association of Canada, Special Paper*, 32, 119–134.

- Papineau, D.M.S.J., Mojzsis, S.J., Karhu, J.A., and Marty, B. (2005). Nitrogen isotopic composition of ammoniated phyllosilicates: case studies from Precambrian metamorphosed sedimentary rocks. *Chemical Geology* 216(1-2), 37-58.
- Parnell, J. (1996). Phanerozoic analogues for carbonaceous matter in Witwatersrand ore deposits. *Economic Geology* 91(1), 55-62.
- Phillips, G.N., and Evans, K.A. (2004). Role of CO<sub>2</sub> in the formation of gold deposits: *Nature* 429, 860-863.
- Pitcairn, I.K., Craw, D., and Teagle, D.A. (2014). The gold conveyor belt: Large-scale gold mobility in an active orogen. *Ore Geology Reviews* 62, 129-142.
- Pitcairn, I.K., Teagle, D.A., Craw, D., Olivo, G.R., Kerrich, R., and Brewer, T.S. (2006). Sources of metals and fluids in orogenic gold deposits: insights from the Otago and Alpine Schists, New Zealand. *Economic Geology* 101(8), 1525-1546.
- Radtke, A.S., and Scheiner, B.J. (1970). Studies of Hydrothermal Gold Deposition (I). Carlin Gold Deposit, Nevada: The Role of Carbonaceous Materials in Gold Deposition. *Economic Geology* 65, 87-102.
- Ridley J.B. and Diamond L.W. (2000). Fluid chemistry of orogenic lode gold deposits and implications for genetic models. *Society of Economic Geology Reviews* 13, 141–162.
- Roedder, E. (1984). Fluid inclusions. *Reviews in Mineralogy* 12, 644.
- Rosso K.M. and Bodnar R.J. (1995). Microthermometric and Raman spectroscopic detection limits of CO<sub>2</sub> in fluid inclusions and the Raman spectroscopic characterization of CO<sub>2</sub>. *Geochimica et Cosmochimica Acta* 59, 3961–3975.

- Rauchenstein-Martinek, K., Wagner, T., Wälle, M., and Heinrich, C.A. (2014). Gold concentrations in metamorphic fluids: A LA-ICPMS study of fluid inclusions from the Alpine orogenic belt. *Chemical Geology* 385, 70-83.
- Rauchenstein-Martinek, K., Wagner, T., Wälle, M., Heinrich, C.A., and Arlt, T. (2016). Chemical evolution of metamorphic fluids in the Central Alps, Switzerland: insight from LA-ICPMS analysis of fluid inclusions. *Geofluids* 16, 877-908.
- Renders, P.J. and Seward, T.M. (1989). The stability of hydrosulphido- and sulphido-complexes of Au(I) and Ag(I) at 25°C. *Geochimica et Cosmochimica Acta* 53, 245–253.
- Ryan, R.J., and Smith, P.K. (1998). A review of the mesothermal gold deposits of the Meguma Group, Nova Scotia, Canada. *Ore Geology Reviews* 13, 153-183.
- Rusk, B.G., Reed, M.H., Dilles, J.H., Klemm, L.M. and Heinrich, C.A. (2004a). Compositions of magmatic hydrothermal fluids determined by LA-ICP-MS of fluid inclusions from the porphyry copper–molybdenum deposit at Butte, MT. *Chemical Geology* 210(1–4), 173–199.
- Rusk, B., Reed, M., Bignall, G., and Tsuchiya, N. (2004b). Natural and synthetic quartz growth and dissolution revealed by scanning electron microscope cathodoluminescence. 14th International Conference on the Properties of Water and Steam. Kyoto, Japan.
- Sangster, A.L. (1992). Light stable isotope evidence for a metamorphogenic origin for bedding-parallel, gold-bearing veins in the Cambrian flysch, Meguma Group, Nova Scotia. *Expl. Min. Geology* 1, 69–79.
- Sangster, A.L., and Smith, P.K. (2007). Metallogenic summary of the Meguma gold deposits, Nova Scotia, in Goodfellow, W.D., (Ed.), *Mineral Deposits of Canada: A Synthesis of Major Deposit-Types, District Metallogeny, the Evolution of Geological Provinces, and*

- Exploration Methods: Geological Association of Canada, Mineral Deposits Division, Special Publication No. 5, 723-732.
- Scheiner, B.J. (1971). Processing refractory carbonaceous ores for gold recovery. *The Journal of The Minerals, Metals & Materials Society* 23(3), 37-40.
- Seo, J.H., Guillong, M., Aerts, M., Zajacz, Z., and Heinrich, C.A. (2011). Microanalysis of S, Cl, and Br in fluid inclusions by LA-ICP-MS. *Chemical Geology* 284, 35-44.
- Seward, T.M. (1973). Thio complexes of gold and the transport of gold in hydrothermal ore solutions. *Geochimica et Cosmochimica Acta* 37(3), 379-399.
- Sibson, R. H., Robert, F., and Poulsen, K. H. (1988). High-angle reverse faults, fluid-pressure cycling, and mesothermal gold-quartz deposits. *Geology* 16(6), 551-555.
- Sillitoe, R.H. and Thompson, J.F. (1998). Intrusion-related vein gold deposits: types, tectonomagmatic settings and difficulties of distinction from orogenic gold deposits. *Resource Geology* 48(4), 237–250.
- Smith, T.J., Cloke, P.L., and Kesler, S.E. (1984). Geochemistry of fluid inclusions from the McIntyre-Hollinger gold deposit, Timmins, Ontario, Canada. *Economic Geology* 79(6), 1265-1285.
- Staples, L.P., Schofield, N., Schulte, M., Meintjes, T., Millard, J., Parks, J., and Fontaine, D. (2018). Moose River Consolidated Project, Nova Scotia, Canada. NI 43-101 Technical Report on Moose River Consolidated Phase 1 and Phase 2 Expansion.
- Steele-MacInnis, M., Han, L., Lowell, R.P., Rimstidt, J.D., and Bodnar, R.J. (2012). The role of fluid phase immiscibility in quartz dissolution and precipitation in sub-seafloor hydrothermal systems. *Earth and Planetary Science Letters* 321, 139-151.

- Stefánsson, A., and Seward, T. M. (2004). Gold (I) complexing in aqueous sulphide solutions to 500 C at 500 bar. *Geochimica et Cosmochimica Acta* 68(20), 4121-4143.
- Tagirov, B.R., Salvi, S., Schott, J., and Baranova, N.N. (2005). Experimental study of gold-hydrosulphide complexing in aqueous solutions at 350–500°C, 500 and 1000 bars using mineral buffers. *Geochimica et Cosmochimica Acta* 69(8), 2119-2132.
- Tan, H., Feng, D., van Deventer, J.S.J., and Lukey, G.C. (2005). Effect of contaminant carbonaceous matter on the sorption of gold by pyrite. *International Journal of Mineral Processing* 76, 244-259.
- Taylor, B.E. (2007). Epithermal gold deposits No. 5. In *Mineral deposits of Canada: a synthesis of major deposit-types, district metallogeny, the evolution of geological provinces, and exploration methods* (ed., W. D. Goodfellow). Geological Association of Canada, MDD Spec. Pub., pp. 113–139.
- Thompson, J.F.H., Sillitoe, R.H., Baker, T., Lang, J.R. and Mortensen, J.K. (1999). Intrusion-related gold deposits associated with tungsten-tin provinces. *Mineralium Deposita* 34(4), 323–334.
- Tödheide, K., and Franck, E.U. (1963). Das Zweiphasengebiet und die kritische Kurve im System Kohlendioxid–Wasser bis zu Drucken von 3500 bar. *Zeitschrift für Physikalische Chemie* 37, 387-401.
- Ulmer, P., and Luth, R.W. (1991). The graphite-COH fluid equilibrium in P, T,  $f_{O_2}$  space: An experimental determination to 30 kbar and 1600°C. *Contributions to Mineralogy and Petrology* 106, 265-272.
- Ulrich, T., Guenther, D. and Heinrich, C.A. (1999) Gold concentrations of magmatic brines and the metal budget of porphyry copper deposits. *Nature* 399(6737), 676.

- Van den Kerkhof, A.M., and Hein, U.F. (2001). Fluid inclusion petrography. *Lithos* 55, 27-47.
- Van Staal, C.R. (2007). Pre-Carboniferous tectonic evolution and metallogeny of the Canadian Appalachians. In Goodfellow, W.D. (Ed) *Mineral deposits of Canada: a synthesis of major deposit-types, district metallogeny, the evolution of geological provinces, and exploration methods*. Geological Association of Canada, Mineral Deposits Division, Special Publication 5, p. 793-818.
- Vaughan, J.P. (2004). The process mineralogy of gold: The classification of ore types. *Journal of Minerals, Metals and Materials Society* 56(7), 46-48.
- Vilor, N.V. (1983). Gold in black shales. *Geochemistry International* 20, 167–177.
- Wagner, T., Fusswinkel, T., Wälle, M., and Heinrich, C.A. (2016). Microanalysis of fluid inclusions in crustal hydrothermal systems using laser ablation methods. *Elements* 12(5), 323-328.
- White, C.E., and Goodwin, T.A. (2011). Litho-geochemistry, petrology, and the acid-generating potential of the Goldenville and Halifax groups and associated granitoid rocks in metropolitan Halifax Regional Municipality, Nova Scotia, Canada. *Atlantic Geology* 47, 158-184.
- White, C.E., Palacios, T., Jensen, S., and Barr, S.M. (2012). Cambrian–Ordovician acritarchs in the Meguma terrane, Nova Scotia, Canada: Resolution of early Paleozoic stratigraphy and implications for paleogeography. *GSA Bulletin* 124(11-12), 1773-1792.
- Williams, H. (1979). Appalachian orogen in Canada. *Canadian Journal of Earth Sciences* 16(3), 792-807.
- Williams-Jones, A.E., Powell, R.J., and Migdisov, A.A. (2009). Gold in Solution. *Elements* 5, 281-287.

- Williams-Jones, A.E., and Heinrich, C.A. (2005). 100th Anniversary special paper: vapor transport of metals and the formation of magmatic-hydrothermal ore deposits. *Economic Geology* 100(7), 1287-1312.
- Wood, S.A., and Samson, I.M. (1998). Solubility of ore minerals and complexation of ore metals in hydrothermal solutions. In *Reviews in Economic Geology*. Society of Economic Geologists, pp. 33-80.
- Zoheir, B., Akawy, A., and Hassan, I. (2008). Role of fluid mixing and wallrock sulfidation in gold mineralization at the Semna mine area, central Eastern Desert of Egypt: Evidence from hydrothermal alteration, fluid inclusions and stable isotope data. *Ore Geology Reviews* 34(4), 580-596.

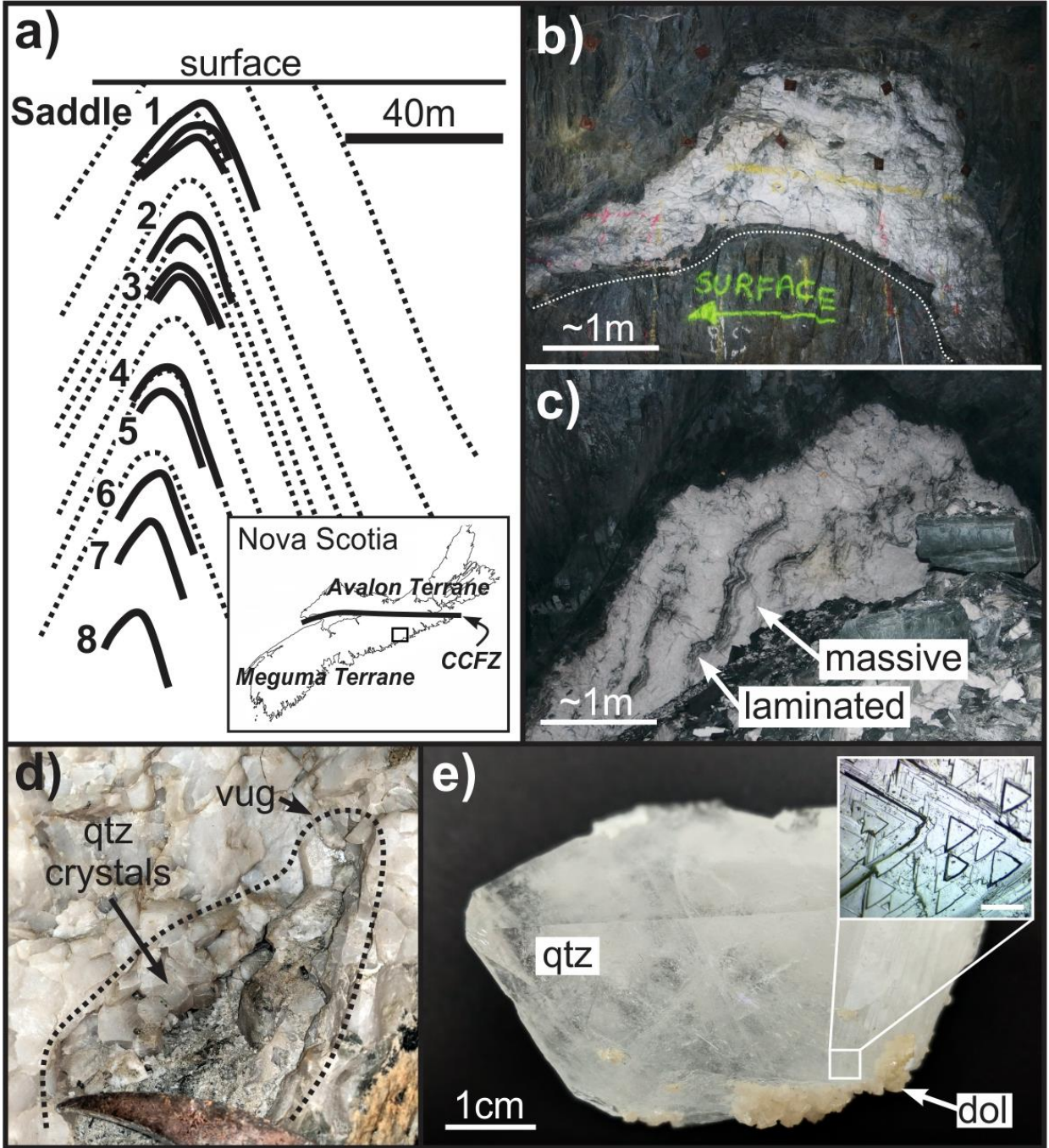


Figure 3-1: Macroscopic features of Dufferin saddle veins. **a)** Cross-sectional view of the Dufferin deposit and fold structure showing the drill indicated geology with saddle veins highlighted by the thick black lines and bedding as dotted lines. Note that veins are localized to the lithological contacts of black fissile slate and metasandstone. Inset map shows the location of the deposit in the Meguma terrane which is in contact with the Avalon terrane along the east-west trending Cobequid-Chedabucto Fault Zone (CCFZ). **b)** Underground exposure of saddles 3. Dotted white line outlines black slate. **c)** Saddle 5 quartz vein showing both laminated and massive vein morphologies. **d)** Translucent, free-standing quartz crystals lining a cavity in a saddle reef vein. **e)** A partially translucent euhedral quartz (qtz) crystal extracted from a cavity. The surface of the quartz, which shows dissolution features (e.g., striate and triangular etch pits), is coated with euhedral dolomite (dol) ± pyrite. Scale bar in inset is ~1 mm.

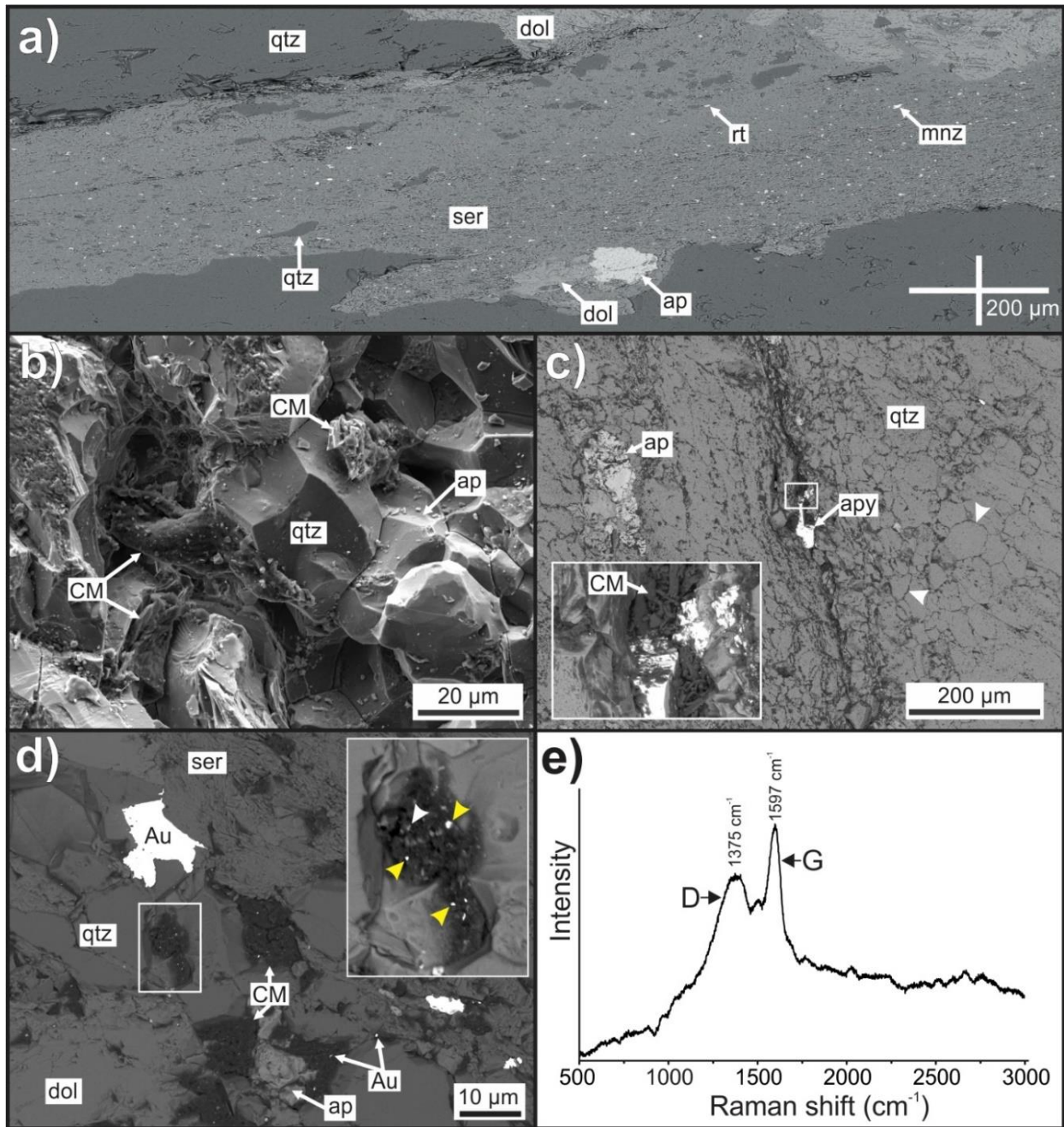


Figure 3-2: Microscopic and Raman spectroscopic features of Au-mineralized septa in vein laminations. **a)** Wallrock septa in laminated quartz vein dominated by sericite + quartz + ferroan dolomite + apatite with subordinate monazite + rutile  $\pm$  Au. **b)** A secondary electron image showing carbonaceous material (CM) in vein lamination. **c)** A back-scattered electron (BSE) SEM image of CM in an arsenopyrite-bearing fracture and along quartz grain boundaries (white arrows). **d)** A BSE-SEM image showing gold in an exposed quartz-sericite-dolomite-apatite lamination in saddle 5 leg vein. Note the CM hosts abundant submicron grains of Au (yellow arrows in inset) and pyrite (white arrow in inset). **e)** A representative Raman spectrum of the carbonaceous material (with D and G Raman bands shown) which is present in cavities and fractures associated with submicron diameter gold grains (in frame C). Abbreviations: ap – apatite; apy – arsenopyrite; CM – carbonaceous material; dol – dolomite; qtz – quartz; ser – sericite.

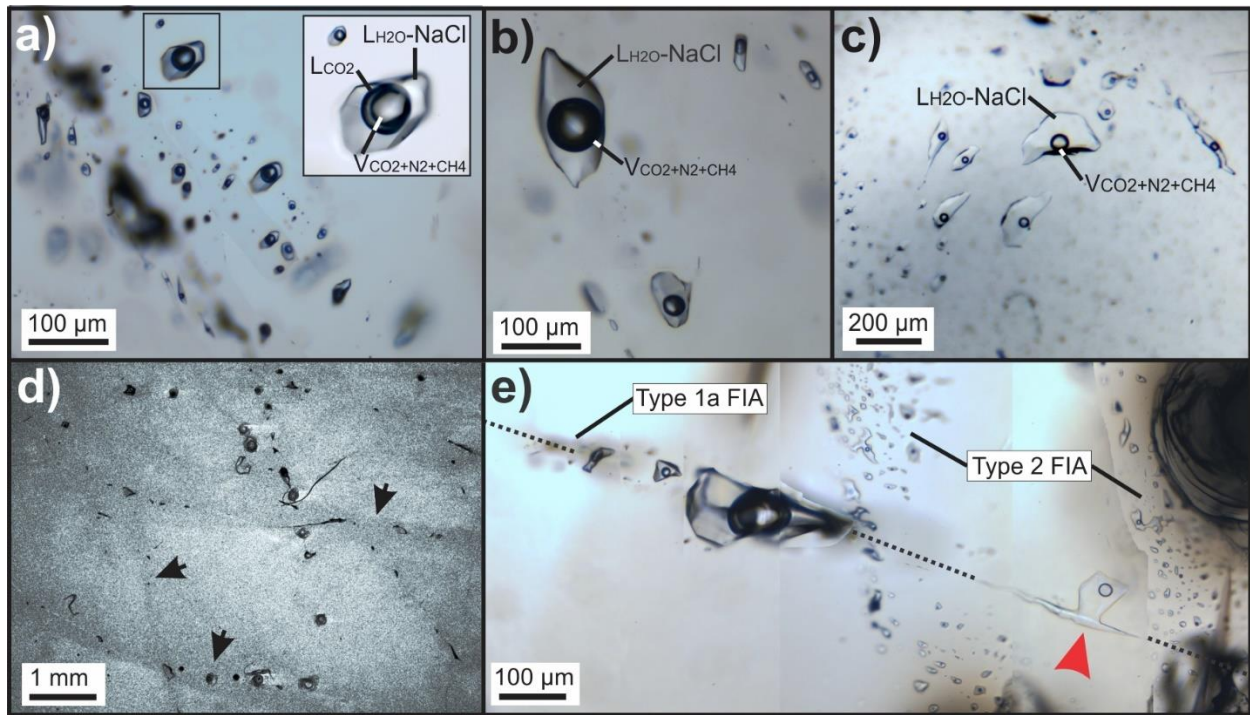


Figure 3-3: Petrographic characteristics of quartz-hosted fluid inclusions from veins in saddles 3 and 6. **a)** A fluid inclusion assemblage (FIA) of secondary type 1a, three-phase,  $\text{H}_2\text{O-NaCl-CO}_2$  (+  $\text{N}_2 + \text{CH}_4$ ) inclusions. **b)** A FIA of secondary type 1b, two-phase  $\text{H}_2\text{O-NaCl} + \text{CO}_2$  (+  $\text{N}_2 + \text{CH}_4$ ) inclusions. **c)** A FIA of secondary type 2, two-phase  $\text{H}_2\text{O-NaCl} + \text{CO}_2$  (+  $\text{N}_2 + \text{CH}_4$ ) inclusions displaying a low vapor to liquid ratio. **d)** An enhanced-contrast SEM cathodoluminescence (CL) image displaying darker CL intensity along secondary fluid inclusion trails. Note that no fluid inclusion trails along crystallographic features (e.g., growth zones) were observed. **e)** Trail of type 1a FIA crosscut by type 2 FIA. A type 1a inclusion has been emptied and refilled with type 2 fluid (red arrow).

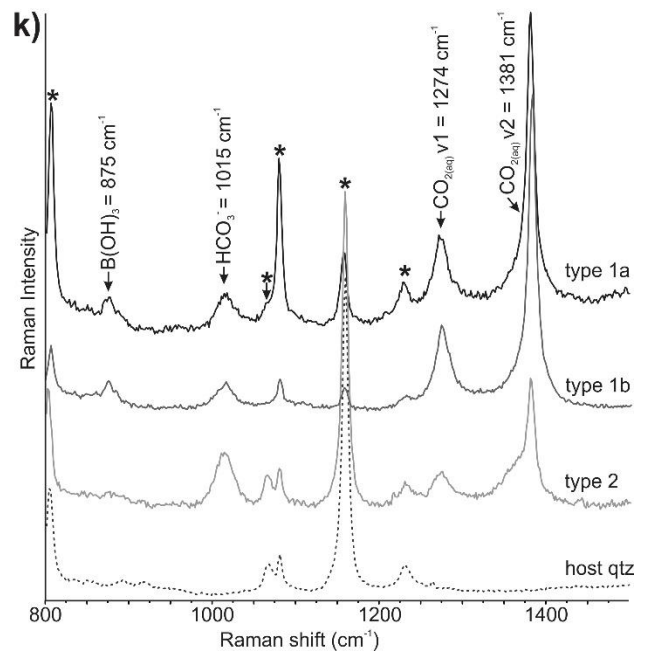
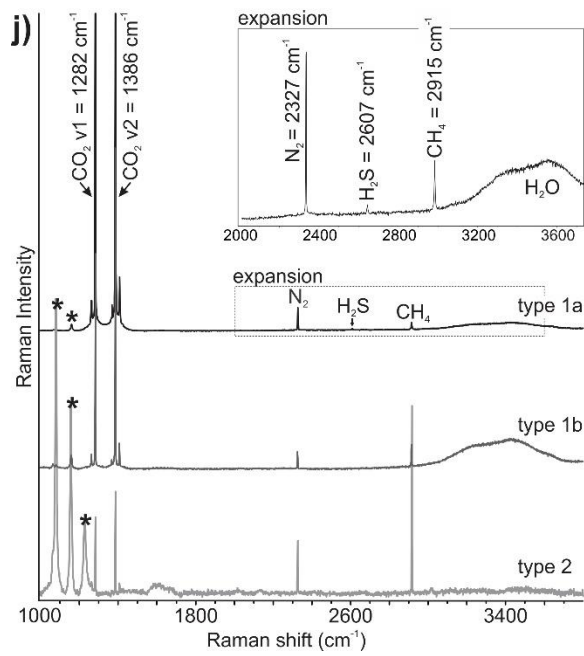
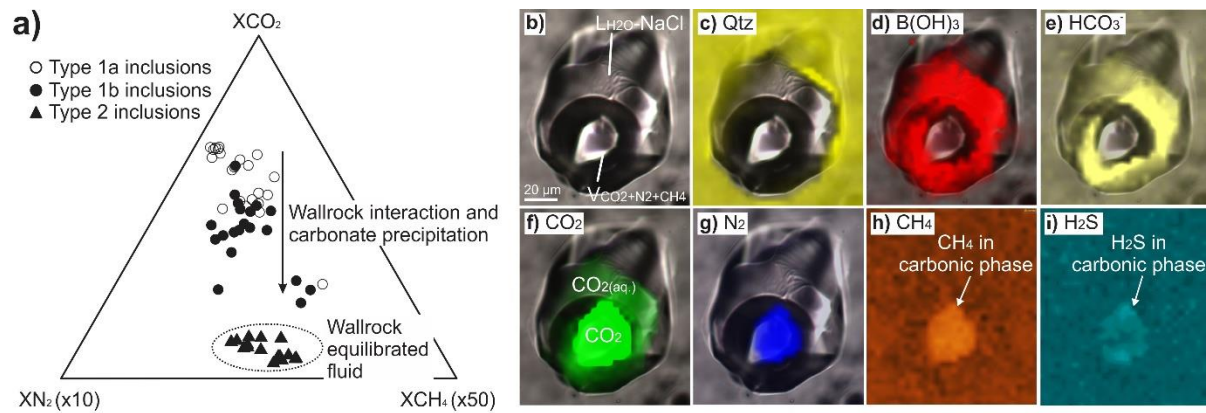


Figure 3-4: Raman spectra and molecular maps. **a)** Raman quantification of CO<sub>2</sub>, CH<sub>4</sub> and N<sub>2</sub> in fluid inclusion vapor phases. Note that types 1a and 1b inclusions display similar vapor phase gas compositions despite differences in their bulk compositions, whereas type 2 inclusions display enrichment in N<sub>2</sub> and CH<sub>4</sub> relative to type 1a and 1b inclusions. **b)** A Type 1a fluid inclusion that was mapped via laser Raman microspectroscopy. The carbonic phase (i.e., L<sub>CO2</sub>+V<sub>CO2</sub>) was homogenous during mapping. **c)** Quartz host map. **d)** Boric acid map. Boric acid was only detected in the aqueous phase. **e)** HCO<sub>3</sub><sup>-</sup> (bicarbonate) map. Bicarbonate was only detected in the aqueous phase. **f)** CO<sub>2</sub> map showing CO<sub>2(aq)</sub> and CO<sub>2</sub> in the carbonic phase. **g)** N<sub>2</sub> map. N<sub>2</sub> was detected only in carbonic phase. **h)** CH<sub>4</sub> map. CH<sub>4</sub> was detected only in the carbonic phase. The fluid inclusion was excluded for clarity. **i)** H<sub>2</sub>S map. Only very trace H<sub>2</sub>S was detected in the carbonic phase. The fluid inclusion was excluded for clarity. **j)** Raman spectra of the aqueous phases of types 1a, 1b and 2 fluid inclusions. Raman spectrum of quartz host is shown for reference. **k)** Raman spectra of the vapor phases of types 1a, 1b and 2 fluid inclusions. Note: Raman shifts of the quartz host are indicated with asterisks.

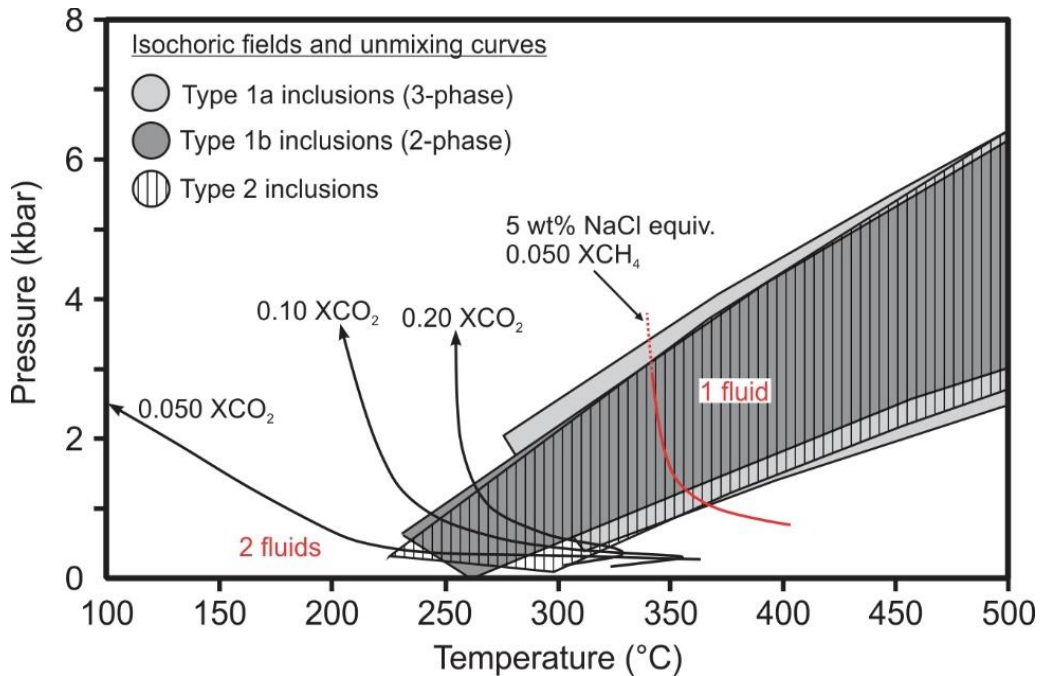


Figure 3-5: Isochoric fields for all inclusion types. All fluid inclusion types display nearly identical bulk densities and thus their isochores overlap in PT space. Lines representing the solvi (unmixing curves) are shown that separate 2-phase (i.e., unmixed aqueous-carbonic fluids) from 1-phase (i.e., homogeneous fluid) fields for three distinct fluid compositions (Tödheide and Franck, 1963; Duan et al., 2003; dashed line represents extrapolation of the curve to high pressure). Note how the addition of volatiles (e.g., CH<sub>4</sub>, N<sub>2</sub>), and/or solute species (e.g., NaCl) increases the P-T range of immiscibility.

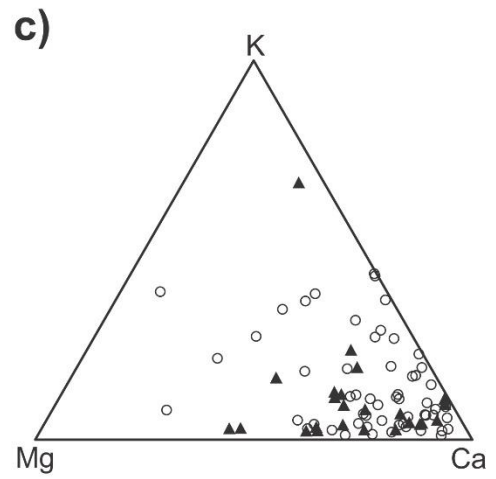
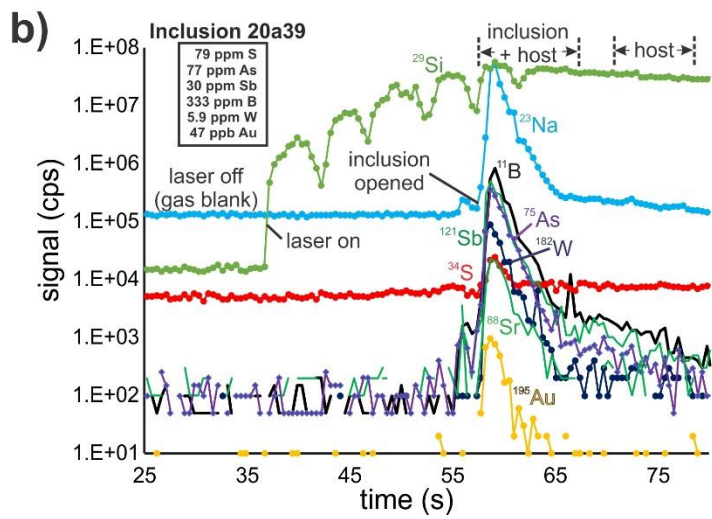
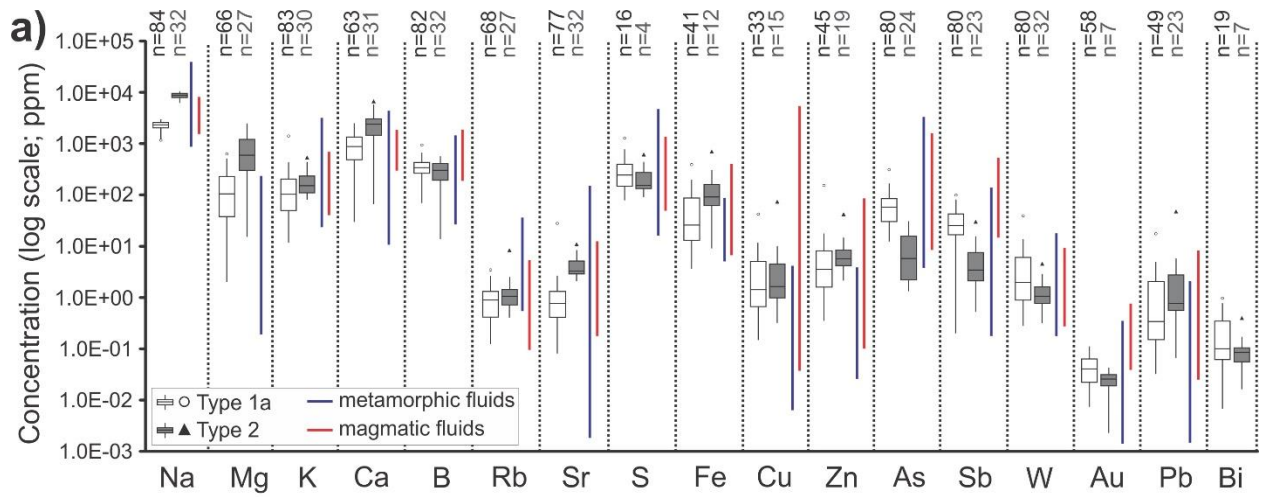


Figure 3-6: LA-ICP-MS quantified elemental concentrations and signal. **a)** LA-ICP-MS data for type 1a (n = 84) and type 2 (n = 32) fluid inclusions. Note that element concentrations below analytical limits of detection, which are element specific, are excluded from statistical treatment, thus the number of analyses is different depending on which fluid inclusion type and elements is considered (i.e., see ‘n’ values at top of plot). Ranges for unmixed metamorphic fluids (Rauchenstein-Martinek et al., 2014; Fusswinkel et al., 2017) and magmatic fluids (Williams-Jones and Heinrich; 2005 and references therein) are shown for comparison. The ends of the whiskers are set to 1.5 x IQR (interquartile range) above and below the third and first quartiles, respectively. Data points plotting outside of this range are shown as outliers. **b)** LA-ICP-MS signal (count rate versus time) from a type 1a inclusion. The complete LA-ICP-MS data set for all analyzed inclusions can be found in Table EA 3-3. **c)** Mg-K-Ca ternary for type 1a and type 2 fluid inclusions showing overlapping fluid compositions.

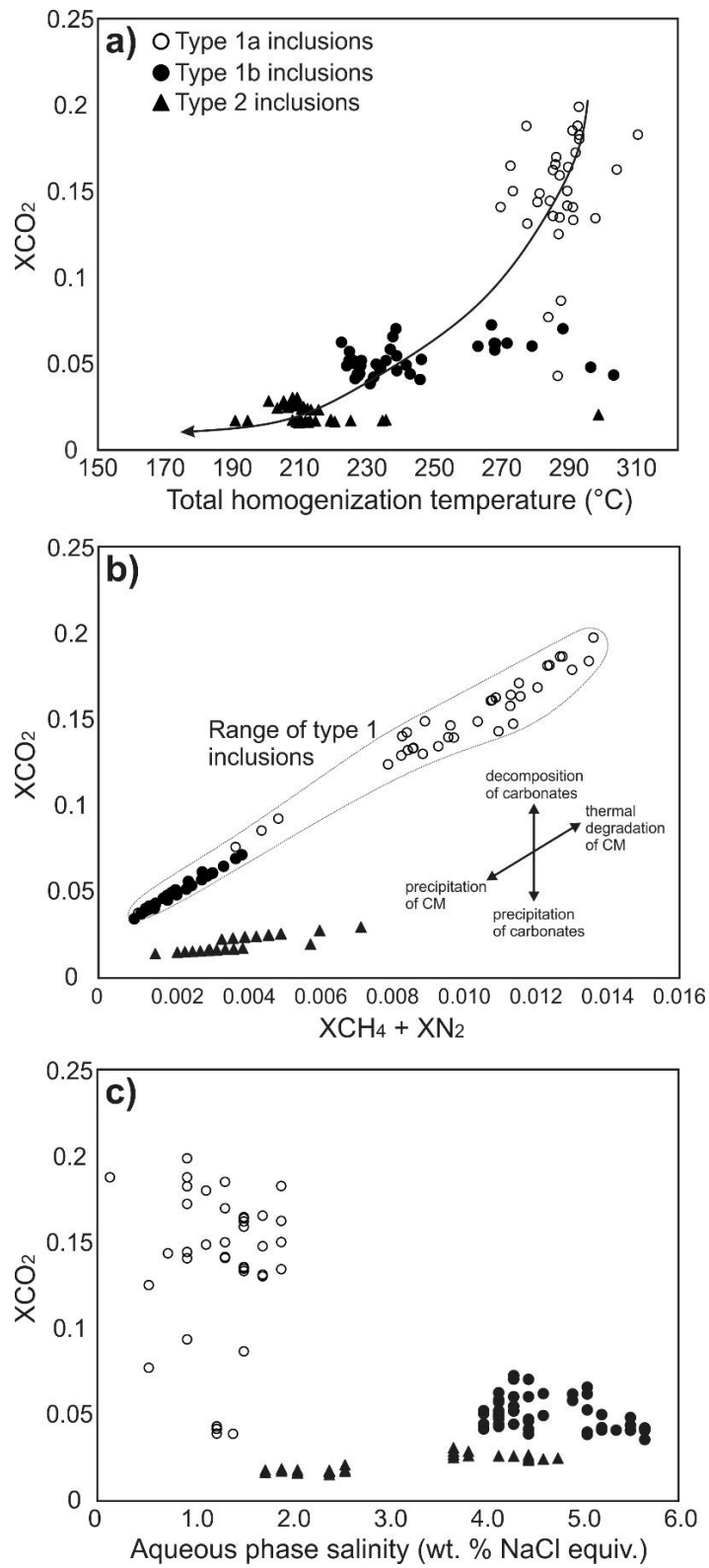


Figure 3-7: Microthermometric and bulk compositional data for all fluid inclusion types. **a)** Bulk  $[\text{CH}_4+\text{N}_2]$  abundance versus bulk  $\text{CO}_2$  abundance. Type 1a and 1b inclusions share a consistent  $\text{CO}_2/[\text{CH}_4+\text{N}_2]$  ratio. **b)** Bulk  $\text{CO}_2$  abundance versus aqueous phase salinity (wt% NaCl equiv.). **c)** Bulk  $\text{CO}_2$  abundance versus total homogenization temperature ( $T_{\text{TOT}}$ ). Abbreviations: CM – carbonaceous material.

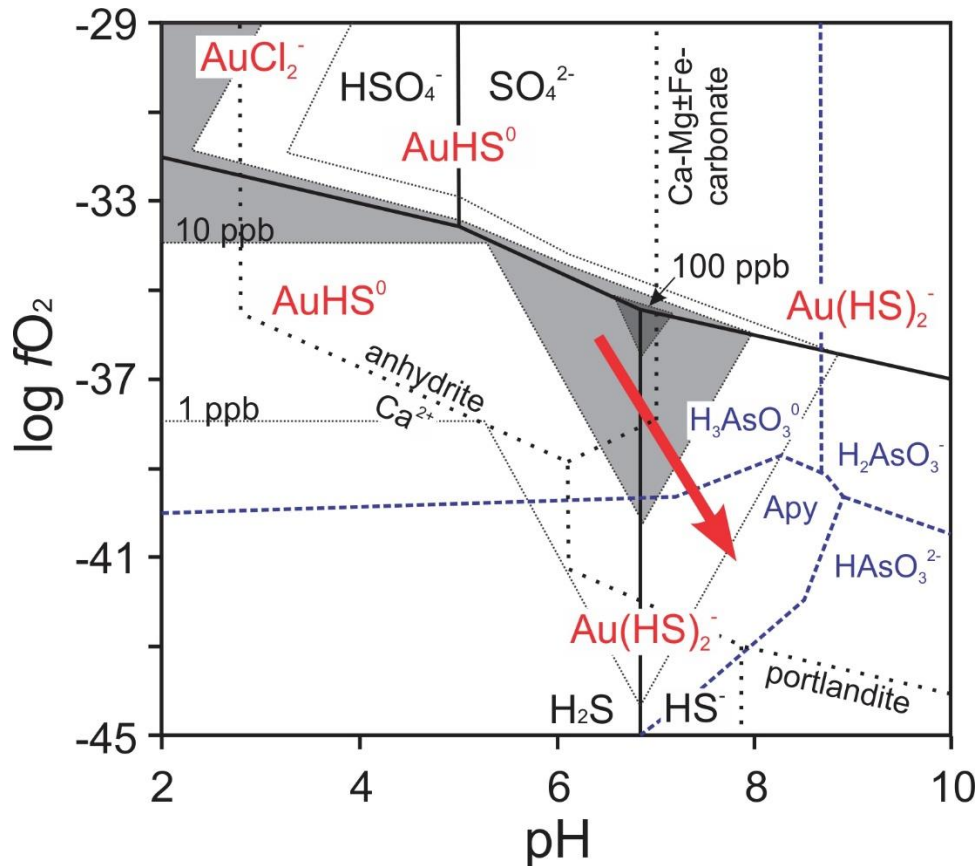


Figure 3-8: Log  $fO_2$  - pH diagram showing fluid evolution pathway during gold precipitation at Dufferin. The fluid evolution pathway (red arrow) is related to the precipitation of Au (cf., Williams-Jones et al., 2009: 0.5 kbar and 250°C in an aqueous solution of 1 m NaCl and 0.01 m  $\Sigma S$ ), arsenopyrite (cf., Heinrich and Eadington, 1986: 250°C in Fe-As-S-O-H-bearing aqueous fluid), and carbonates. Carbonate stability fields were modelled using Geochemist's Workbench (Aqueous Solutions LLC) Act2 platform: 1 kbar and 250°C in an aqueous solution with  $a_{H_2O} = 1$ ,  $a_{Ca^{2+}} = 0.00825$  (using activity coefficient of  $\sim 0.3$  based on a fluid ionic strength of 0.188; cf., Garrels and Christ, 1965),  $a_{S\ total} = 0.01$ ,  $a_{Cl^-} = 0.1$ ,  $a_{Na^+} = 0.1$ ,  $a_{Mg^{2+}}$  of 0.0001, and  $a_{HCO_3^-} = 0.0005$ . Aqueous sulfur species and carbonate species were allowed to speciate over the log  $fO_2$  and pH range specified.

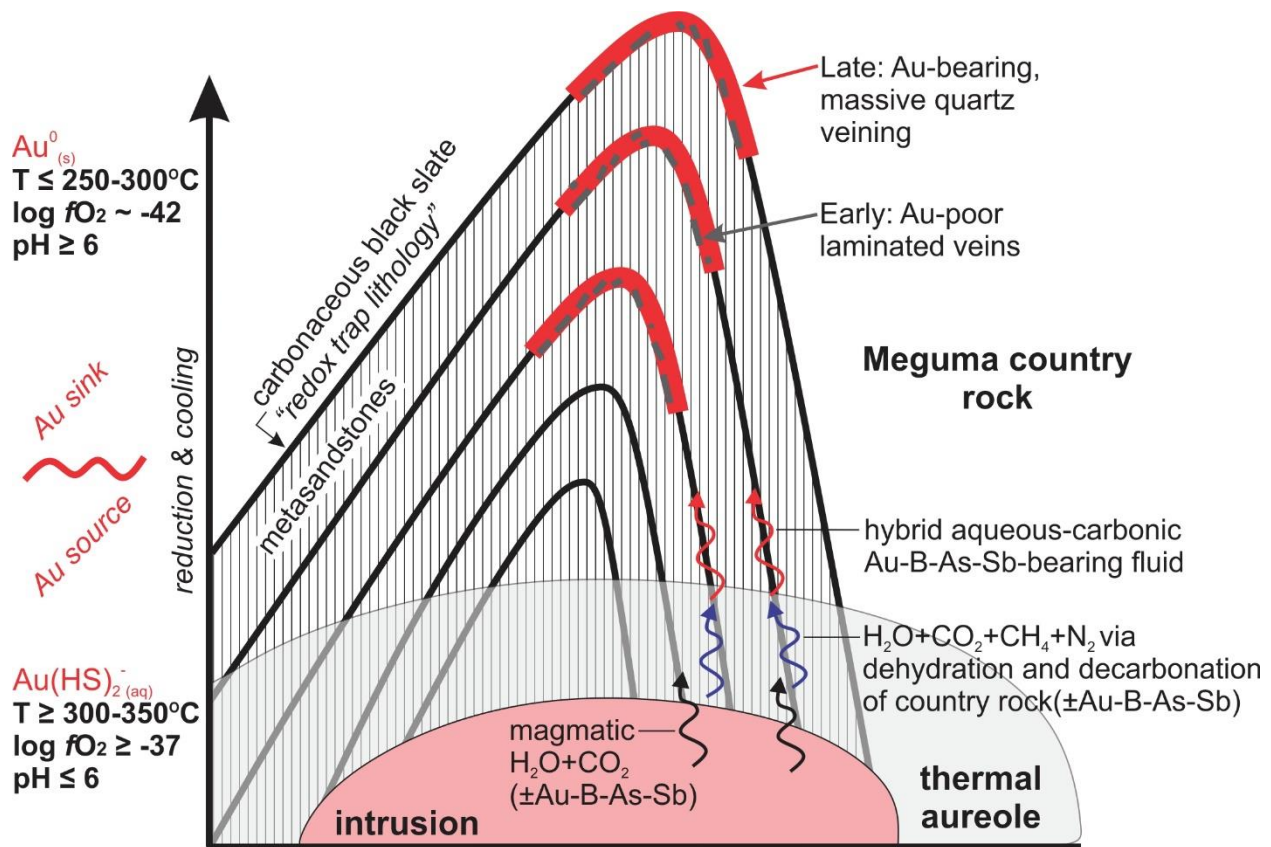


Figure 3-9: Geological model for gold precipitation at Dufferin. Schematic model (not to scale) which involves fluid generation by magmatic devolatilization and/or dehydration/decarbonation through thermal metamorphism. The fluid is endowed in Au from an underlying ~380 Ma magmatic intrusion and also possibly through leaching of adjacent country rocks. Soluble gold from the "Au source" region is mobilized to a higher crustal elevation. The auriferous fluid is subsequently cooled and reduced through interaction with organic-rich lithologies, precipitating gold in the "Au sink" region.

Table 3-1: Fluid inclusion types identified in the Dufferin quartz veins and corresponding compositional data.

Properties	FI Types			
	Type 1a (L <sub>aq</sub> + L <sub>car</sub> + V <sub>car</sub> )	Type 1b (L <sub>aq</sub> + V <sub>car</sub> )	Type 2 (L <sub>aq</sub> + V <sub>car</sub> )	
Phases present at 21°C	(H <sub>2</sub> O-NaCl) <sub>L</sub> + (CO <sub>2</sub> ) <sub>L</sub> + (CO <sub>2</sub> ± CH <sub>4</sub> ± N <sub>2</sub> ) <sub>V</sub>	(H <sub>2</sub> O-NaCl) <sub>L</sub> + (CO <sub>2</sub> ± CH <sub>4</sub> ± N <sub>2</sub> ) <sub>V</sub>	(H <sub>2</sub> O-NaCl) <sub>L</sub> + (CO <sub>2</sub> ± CH <sub>4</sub> ± N <sub>2</sub> ) <sub>V</sub>	
Total # of inclusions measured	41 (9 FIA)	52 (9 FIA)	37 (6 FIA)	
vol.% aqueous liquid phase at 21°C	53 - 79 (63±5); n=36	69 - 89 (79±5)	75 - 93 (86±3)	
T <sub>mICE</sub>	ND	-2.4 to -3.4; n=52	-1.0 to -2.9; n=37	
T <sub>mCLA</sub>	9.1 - 10; n=36	ND	ND	
Aq. phase salinity (wt. % NaCl equiv.)	0.1 - 1.9 (1.3±0.4); n=36	4.0 - 5.6 (4.6±0.6); n=52	1.7 - 4.7 (3.2±1.0); n=37	
T <sub>mCO2</sub>	-58.4 to -56.4 (-57.2±0.6); n=33	ND	ND	
Th <sub>CO2</sub>	19.8 - 27 (25.9±1.4); n=32	ND	ND	
Th <sub>TOT</sub>	269 - 310 (286±8); n=30	221 - 302 (241±21); n=40	190 - 235 (210±9); n=34	
BULK	ρ <sub>BULK</sub> (g/cm <sup>3</sup> )	0.76 - 0.94 (0.89±0.04); n=36	0.82 - 0.97 (0.90±0.04); n=52	0.79 - 0.96 (0.90±0.03); n=37
	X <sub>NaCl</sub>	0.007 ± 0.0026; n=33	0.027 ± 0.0034; n=52	0.019 ± 0.0066; n=37
	X <sub>CO2</sub>	0.151 ± 0.028; n=33	0.05 ± 0.009; n=52	0.022 ± 0.005; n=37
	X <sub>CH4</sub>	0.002 ± 0.001; n=33	0.0003 ± 0.0002; n=52	0.0007 ± 0.0002; n=37
	X <sub>N2</sub>	0.009 ± 0.002; n=33	0.002 ± 0.0001; n=52	0.003 ± 0.001; n=37
VAPOR PHASE	ρ <sub>CO2</sub> (g/cm <sup>3</sup> )	0.4 ± 0.2; n=17	0.23 ± 0.1; n=18	0.1 ± 0.05; n=16
	X <sub>CO2</sub>	0.951 ± 0.014; n=22	0.915 ± 0.031; n=20	0.598 ± 0.07; n=16
	X <sub>CH4</sub>	0.006 ± 0.007; n=22	0.013 ± 0.009; n=20	0.073 ± 0.023; n=16
	X <sub>N2</sub>	0.042 ± 0.01; n=22	0.072 ± 0.025; n=20	0.328 ± 0.051; n=16
	X <sub>H2S</sub>	-	-	-

Note: All temperature data reported in °C. T<sub>mCO2</sub> temperatures > -56.6°C reflect cumulative measurement uncertainty. Salinity of the aqueous phase was determined via final ice melting temperature or clathrate melting temperature. X<sub>NaCl</sub>, X<sub>CO2</sub>, X<sub>CH4</sub>, X<sub>N2</sub>, and X<sub>H2S</sub> represent bulk fluid inclusion values calculated using the program BULK (Bakker, 2003) or vapor phase compositions determined by Raman spectroscopic analysis. Bulk density values were calculated by applying the equations of state outlined by Bowers and Helgeson (1983) and Bakker (1999). CO<sub>2</sub> density was determined using the Fermi diad spacing between spectral peaks (after Rosso and Bodnar, 1995). Errors (including data in brackets) represent ± 1σ standard deviation. Abbreviations: aq. - aqueous; car - carbonic; FIA - fluid inclusion assemblage; ND - not determined/not observed; T<sub>mICE</sub> - final ice melting; T<sub>mCLA</sub> - final clathrate dissociation; T<sub>mCO2</sub> - final melting of CO<sub>2</sub>; Th<sub>CO2</sub> - CO<sub>2</sub> homogenization; Th<sub>TOT</sub> - total homogenization temperatures.

## Chapter 4

### **An initial study on the use of bulk fluid volatile chemistry for exploration of metasedimentary-hosted orogenic gold deposits: An example from the Meguma terrane, Nova Scotia, Canada.**

#### **4.1 Abstract**

Disseminated gold deposits hosted in metasedimentary rocks present unique exploration challenges as the gold is generally very fine-grained (micron-scale) or pyrite-hosted, and by definition not vein hosted. Therefore, it follows that exploration programs in such settings rely on detailed lithogeochemical and structural analysis in addition to extensive assaying of host rock with little emphasis on ore fluid geochemistry (i.e., volatile phases). The Moose River anticline (MRA) in the Lower Paleozoic Meguma terrane, Nova Scotia, Canada, is host to several high tonnage (~10 Mt), low grade (~1 – 2 g/t Au) disseminated gold deposits in Lower Paleozoic metamudstone host rocks, one of which is in production (e.g., Touquoy mine). This setting offers an excellent opportunity to apply and assess the efficacy of an underdeveloped gas chemistry-based exploration technique applying gas chromatography (GC) to analyze the bulk volatile content (i.e., compound identification and abundance) of crushed metasedimentary rocks (slates) to vector towards mineralized regions within the anticline.

Since GC is a bulk analytical technique (i.e., all volatiles from multiple generations of fluid inclusions are liberated from the crushed sample to yield a mixed analytical volume), the compositions of quartz-hosted fluid inclusions in porphyroblast pressure shadows, and in quartz veins crosscutting metamudstone units, were investigated using laser Raman microspectroscopy to reconcile bulk analyses with the composition and abundance of different inclusion types. Pressure-shadow quartz hosts inclusions displaying  $N_2 \pm CH_4$ -dominant vapor phases, and are

inferred to represent wall rock-equilibrated fluids. Conversely, in quartz veins, fluid inclusion vapor phases are more complex, displaying CO<sub>2</sub>-dominant or N<sub>2</sub>±CH<sub>4</sub>-dominant compositions; the former is interpreted as the likely the suspected fluid responsible for lode and disseminated Au mineralization in the Meguma terrane (e.g., H<sub>2</sub>O-CO<sub>2</sub>±CH<sub>4</sub>±N<sub>2</sub> fluids). Gas chromatography shows statistically significant differences (t-tests) between metamudstones from the Touquoy deposit (n = 21) and barren (n = 24) settings. Whereas the former commonly contain CO<sub>2</sub> (50% of samples) only ~4% of metamudstones from barren settings along the MRA contain CO<sub>2</sub>, which yields a t-test p-value of 0.0103. The presence of elevated CO<sub>2</sub> abundances in mineralized samples agrees with previous observations of carbonate alteration (i.e., CO<sub>2</sub> addition) spatially-related to disseminated gold mineralization. No correlation was observed between bulk CO<sub>2</sub> abundance and the Au grade of metamudstone intervals. Furthermore, statistically anomalous differences in C<sub>3</sub> (t-test p-value = 0.043) and C<sub>4</sub> (t-test p-value = 0.03) hydrocarbon (HC) abundances between the two populations are seen. Furthermore, metamudstones from the mineralized region have higher Σ(C<sub>3</sub> HCs)/CH<sub>4</sub> and Σ(C<sub>4</sub> HCs)/CH<sub>4</sub> ratios compared to analogous samples from barren settings. The compositional differences suggest that more aqueous-carbonic fluid infiltrated the metamudstone units of the MRA in areas where Au precipitated due to locally favourable physical (e.g., structural connectivity, permeability) and/or chemical (e.g., host rock reactivity) conditions.

Although the results may be considered preliminary, they suggest that bulk analysis of metamudstone-hosted volatiles may be useful in vectoring towards disseminated Au mineralization in Meguma-type gold systems and similar settings. With further refinement (e.g., sample preparation and throughput optimization) and more robust sampling via contemporary drilling programs, a GC-based technique may make an effective addition to exploration programs.

## 4.2 Introduction

Disseminated gold occurrences in Phanerozoic slate belts represent a significant global resource, including examples in the Lachlan Orogen, Australia, (Bierlein et al., 2002), the Otago Schist, New Zealand (Craw, 2002; Pitcairn et al., 2006), the Qinling Mountains, China (Liu et al., 2000), the Ashanti gold belt, Ghana (Berge et al., 2011), and El Toro, Peru (Montoya et al., 1995). Such gold deposits present significant challenges to exploration programs as gold in these settings is not hosted in easily recognizable quartz-carbonate veins but instead occurs as micron-size gold grains or dissolved in disseminated Fe-As-sulfides, and hence invisible during core logging, in the host rock sequences (Bierlein and Maher, 2001). One such district where this occurs is the Meguma terrane of eastern Canada where disseminated gold deposits mined currently (e.g., Touquoy) or awaiting mine development (e.g., Beaver Dam, Fifteen Mile Stream; see [www.atlanticgoldcorporation.com](http://www.atlanticgoldcorporation.com)) were previously exploited as more traditional high-grade (i.e., 15 – 20 g/t Au) auriferous vein lodes (Malcolm, 1929; Kontak et al., 1990; Ryan and Smith, 1998). Recently, there has been a shift away from remaining vein-lode gold resources to the evaluation and exploitation of more economically viable low-grade (~1 – 2 g/t Au), high-tonnage, disseminated gold resources in the Meguma terrane (Staples et al., 2018). However, at present only a few recent discoveries of disseminated gold (e.g., Steve's Road Au-Pb occurrence: Ryan and Smith, 1993, 1998) have been identified that are not coincident with areas historically mined for their vein-hosted lodes. In addition, the very cryptic nature of alteration associated with this mineralization both in the Meguma (Bierlien and Smith, 2003) and such deposits globally (Bierlein et al., 2000; Herron, 2018) makes their exploration challenging.

Current orogenic gold exploration programs rely heavily on detailed lithological, lithochemical, and structural analysis coupled with extensive assaying of host rocks and vein material to define mineralized zones. Consequently, the current deposit models (e.g., Goldfarb et al., 2005; Dubé and Gosselin, 2007; Robert et al., 2007) fail to address how ore-bearing fluids may have been modified at the ‘deposit-scale’ such that a fluid geochemical signature or footprint of the ore system is generated that is discernable away from mineralization. Exceptions include where SWIR is used to detect for example changes in mica chemistry related to fluid flow around an ore zone (e.g., Robert et al., 2017), the depletion of  $\delta^{18}\text{O}$  signature in carbonate around Carlin-type gold deposits (e.g., Barker et al. 2012; Herron, 2018), or where extensive alteration halos (>150m; K+CO<sub>2</sub> addition) outline mineralized domains (e.g., Malartic: De Souza et al., 2015). In carbonaceous- or carbon-rich metasedimentary rock-hosted disseminated gold deposits alteration is cryptic when: (i) the alteration is pervasive but spotty, and thus difficult to detect via petrographically, (ii) the host rock compositions vary in terms of geochemical parameters that are similar to parameters that vary in response to mineralization, or (iii) the differences between “barren” and “mineralized” hosts are very small. Consequently, a rock-crushing gas chromatographic (GC) technique for bulk analysis of fluid inclusions (cf., Bray and Spooner, 1992; Salvi and Williams-Jones, 1997a; Kerr et al., 2015), combined with laser Raman microspectroscopic (LRM) analysis of single inclusions, is being applied to evaluate the effectiveness of bulk-fluid signatures for vectoring towards mineralization in disseminated-gold deposits in metasedimentary rocks. To test and apply the approach, one particular Au-mineralized site in the Meguma terrane exposed along the Moose River anticline (Bierlein and Smith, 2003; Horne and Pelley, 2007; Staples et al., 2018) is investigated, in addition to four Au-barren sites within the same anticlinal structure. The abundance of disseminated gold in host rocks would

imply that auriferous ore fluids (e.g., Kontak et al., 1989a, 1996, 2001; Bierlein and Smith, 2003) were channelled along fracture/fault systems from depth and locally infiltrated permeable lithologies to form broadly stratabound disseminated gold deposits.

Gold precipitation in metasedimentary rock-hosted gold settings such as the Meguma may be a result of the following processes, all of which act to destabilize soluble gold complexes (i.e., gold bisulfides) and precipitate gold from ore fluid: (i) depressurization leading to fluid unmixing (Craw et al., 1993; Loucks and Mavrogenes, 1999), (ii) mixing of Au-bearing fluid with another fluid (e.g., Olivo and Williams-Jones, 2002; Dinel et al., 2008), or (iii) fluid  $fO_2$  and/or pH modification (e.g., Phillips and Evans, 2004; Williams-Jones et al., 2009; see Ch.3 of this thesis). Regardless of the mechanism involved, it has been proposed that mineralized metamudstones in the Meguma terrane may preserve evidence of ore fluid infiltration as a recognizable “halo” of volatile enrichment, analogous to carbonate alteration halos commonly associated with mineralized metasedimentary rocks in the same terrane (Smith and Kontak, 1987; Ryan and Smith, 1998; Bierlein et al., 2000; Bierlein and Smith, 2003; Staples, 2018).

In this initial study we evaluate the use of bulk volatile signatures (i.e., composition and abundances of volatile species) released from fluid inclusions and grain boundaries in crushed metamudstone host rocks in the context of application to gold exploration in the Meguma terrane. Specifically, the following questions are addressed: (i) can the bulk volatile chemistry of metamudstone-hosted fluids be used to determine proximity to mineralization, or to differentiate ore-bearing from barren domains of metasedimentary rocks at a strategic distance that is relevant to exploration; (ii) what are the likely fluid sources in these ore systems; and (iii) can the GC technique be integrated effectively into current exploration protocols? Through the improvement

of exploration criteria and addition of new data relevant to existing genetic models, this study aims to provide more effective geochemical tools can be used to vector towards mineralized units within the Meguma terrane and potentially analogous gold systems elsewhere.

### **4.3 Geological Setting**

#### **4.3.1 Regional geology of the Meguma terrane**

Two distinct geological and metallogenic terranes are defined in Nova Scotia; these are the Meguma and Avalon which are separated by the east-west trending Cobequid-Chebucto fault zone (Keppie and Dallmeyer, 1987; Murphy et al., 2011). This fault zone represents a paleo-suture where the Meguma terrane was dextrally emplaced against the Avalon terrane during widespread orogenesis in the mid- to late Devonian. The strongly folded Cambro-Ordovician sedimentary rocks of the Meguma terrane consist of a deep-water flysch package consisting of metasediments dominated by metasediments of the gold deposit hosting Goldenville Group (~8000 m; gold deposit host) overlain by metasediments dominated by metasediments of the Halifax Group (<5000 m); these groups are subdivided into stratigraphically- and petrographically-distinct formations (White 2010; Horne and Pelley, 2007; White et al., 2012). In the southwestern part of the Meguma terrane these rocks are overlain by Silurian-Early Devonian shallow-marine sedimentary and rift related volcanic rocks of the Rockville Notch Group (White et al., 2018). Following regional deformation and lower greenschist facies metamorphism of the Meguma terrane during the mid- to late Devonian Neocadian deformation (van Staal, 2007), widespread granitoid magmatism followed between ~375 and 360 Ma (Clarke et al., 1997; Kontak et al., 2013). Unconformably overlying the aforementioned units are Carboniferous to Permian terrestrial clastic

sequences and lastly, Jurassic volcanic rocks along the western margin of the Meguma terrane (i.e., North Mountain basalts).

#### **4.3.2 Stratigraphy of the Meguma metasedimentary rocks**

Whereas the thick metasedimentary rock sequence that dominates the Meguma terrane was originally divided into the Goldenville and Halifax formations of the former Meguma Group, as discussed by White et al. (2012), more recently these formations were elevated to Group status and an internal stratigraphy recognized (White, 2010 and references therein; Horne and Pelley, 2007). This is relevant to the gold metallogeny of the Meguma terrane (Ryan and Smith, 1998; Kontak and Horne, 2010) and aspects of the present study; thus, this nomenclature is summarized below.

The Goldenville Group hosts most of the known gold deposits in the Meguma terrane (Malcolm, 1929; Kontak et al., 1990; Ryan and Smith, 1998), in particular along the eastern shore of Nova Scotia where the present study is focused (Fig. 1). In this area the sequence of metaturbiditic units have been subdivided into (from stratigraphic lowest to top) the Moose River, Tangier and Taylors Head formations (Horne and Pelley, 2007). The Moose River Formation, which hosts the Touquoy, Beaver Dam, and Fifteen Mile Stream gold deposits in the core of the northeast-trending Moose River anticline (MRA; Fig. 1b; Horne and Pelley, 2007), is characterized by thick intervals of dark grey to green slate and metasilstone lacking significant intervals of metasandstone. Minor sulfides (e.g., pyrite, pyrrhotite) occur which correlate to elevated magnetic highs, and spotting is present due to carbonate alteration. The overlying Tangier and Taylors Head formations consist predominantly of thick metasandstone or metasilstone units that fine upwards with the former distinguished by the common presence of dark grey to black, finely laminated slate beds at the

tops of depositional cycles. As with the Goldenville Group, the Halifax Group has also been subdivided (Horne and Pelley, 2007) into three distinct mappable units which relies in part based on the lateral continuity of units to the west where earlier work was done (e.g. see Ryan and Smith, 1998); from bottom to top the units are Beaverbank, Cunard and Glen Brook formations. The Beaverbank Formation is dominated by thinly bedded to finely laminated, grey to green metasilstone and slate. The presence of brown laminations is attributed to manganese-rich carbonate layers and locally coticule layers (i.e., spessartine-garnet rich) occur. This unit equates in general to the earlier term of Goldenville-Halifax Transition Zone (GHT) used for this stratigraphic horizon (see Sangster, 1990 and references therein). The Cunard Formation is characterized by finely laminated black slate with variable amounts of interbedded cross-laminated metasilstone and metasandstone. It may contain abundant both pyrite and pyrrhotite, but this varies. Lastly, the Glen Brook Formation consist of green-grey, sulphide-poor and hence low-magnetic response, thinly-bedded slate and metasilstone that locally has small (cm scale) concretions.

#### **4.3.3 Summary of metasedimentary rock-hosted disseminated gold mineralization**

The presence of metasedimentary rock-hosted disseminated gold occurrences in Phanerozoic slate belts is not unique to the Meguma terrane. These have also been identified and developed in a variety of geologically similar systems elsewhere (e.g., Lachlan Orogen, Australia: Bierlein et al., 2001; Macraes gold mine, Otago Schist, New Zealand: Craw, 2002; Pitcairn et al., 2006; Yana-Kolyma fold belt, Russia: Bierlein and Maher, 2001). Similar characteristics between disseminated and vein-type mineralization styles (e.g., physicochemical characteristics, alteration assemblages, fluid geochemistry), and their coexistence within the same structural environments (e.g., MRA in

Meguma terrane) suggest they represent mineralization style “endmembers” of a broader continuum of sediment-hosted orogenic deposits (Bierlein and Smith, 2003). Whereas vein-hosted mineralization relates to channelized fluid flow and vein formation through repeating cycles of hydrofracturing and resealing (e.g., crack-seal and fault valve processes; Ramsay, 1980; Sibson et al., 1988), disseminated-style mineralization must reflect development of secondary porosity and structural permeability in the host rocks. It has been recognized that although porous, rocks of this nature inherently have a low primary permeability (Neuzil, 1994; Wood, 1996). Thus, the permeability needed to account for the ingress of mineralizing fluids may instead have been generated by the production of secondary porosity through hydrothermal alteration reactions (Schwartz, 1959) and formation of small-scale structural channelways (veinlets, stockworks) during post-folding hydrothermal activity. Intermittently active, deep-seated fault systems may have provided the Au-bearing fluids for both lode and disseminated gold deposits in the Meguma terrane (Kontak et al., 1990; Bierlein and Smith, 2003). However, the structure, geometry, rheology, porosity, permeability, and chemical reactivity of host rocks, as well as the hydrostatic versus lithostatic pressure conditions, influence the “style” of gold deposit generated (Bierlein and Maher, 2001; Bierlein and Smith, 2003). Despite a variety of previous studies on the occurrence of disseminated gold mineralization (e.g., see Bierlein and Maher, 2001), this style of mineralization remains understudied with regard to the lithostructural controls on, and precipitation mechanisms for, gold mineralization in these environments. We further explore some of these latter aspects below based on the current study.

#### **4.3.4 Nature and origin of Meguma gold deposits**

The majority of Meguma gold deposits occur primarily within the Goldenville Group, and can be broadly delineated into vein-rich (e.g., South Uniacke, Dufferin, The Ovens, Seal Harbour) and vein-poor (e.g., Touquoy zone, North Brookfield) deposit types. Meguma gold deposits are largely structurally controlled, occurring in association with anticlinal structures, domes and overturned fold limbs (Kontak et al., 2001). The historically mined Meguma gold deposits are variable in style (Keppie, 1976; Ryan and Smith, 1998; Horne and Culshaw, 2001; Kontak et al., 2001; Sangster and Smith, 2007; Kontak and Horne, 2010), but in general were dominated by bedding-parallel or concordant, laminated (i.e., ribbon textured) veins on fold limbs which thicken in fold hinges to form classic saddle-reef type veins. These veins consist of quartz  $\pm$  carbonate  $\pm$  Fe-As sulfide  $\pm$  silicate (e.g., chlorite, muscovite, tourmaline, biotite, feldspar; Newhouse, 1936; Kontak and Smith, 1993; Kontak and Horne, 2010) and have complementary haloes of disseminated sulfides and rare silicate alteration that extend from vein margins on a cm-scale. Variably developed wall rock alteration displaying secondary quartz, carbonate, Fe-sulfides, tourmaline, biotite and sericite are common to both vein-rich and vein-poor deposit types (Kontak et al., 2001).

The timing of auriferous vein emplacement has been inferred through structural relationships and dating of hydrothermal vein minerals (e.g.,  $^{40}\text{Ar}/^{39}\text{Ar}$  dating of muscovite) at Touquoy, Beaver Dam and Fifteen Mile Stream (Kontak et al., 1990, 1993, 1998), Tangier (Kontak et al., 2001), and the Dufferin deposit (Morelli et al., 2005), which determined that gold mineralization occurred between ~365 – 380 Ma and is therefore late in the orogenic episode (i.e., Neoacadian orogeny at ~410 to 380 Ma; Reynolds and Muecke, 1978; Muecke et al., 1988; Hicks et al., 1999; Kontak et al., 1998; Morelli et al., 2005). Also, it was demonstrated that bedding-concordant and discordant conjugate vein emplacement at The Ovens occurred late in the deformational history, resulting from flexural-slip during late-stage fold tightening as would be expected during granitic intrusion

and associated horizontal shortening in the vicinity (Benn et al., 1997; Horne and Culshaw, 2001). Additional summary of Meguma gold deposit models can be found in Kontak et al. (1990, 2001), Sangster and Smith (2007), and Kontak and Horne (2010).

In recent years there has been a recognition that the traditional high-grade vein-hosted ore (e.g., ~15 g/t Au) historically mined (Malcolm, 1929) may be displaced by a lower-grade or disseminated (e.g., 0.5 – 4 g/t) style of gold mineralization in the host rocks which can be mined by bulk tonnage methods. Importantly this style of mineralization was recognized over 30 years ago (see Ryan and Smith 1998 and references therein), but it is only recently that such ore has been mined at the Touquoy deposit. Furthermore, the disseminated nature of the gold mineralization means that was likely overlooked by past mining operations due to its low grade and cryptic nature. A common feature of this mineralization style is the general lack of quartz veining, with gold occurring as disseminations in sulfide bearing host rocks or associated with rare stockwork of quartz-carbonate veinlets (Bierlein and Smith, 2003). In the only detailed study of this mineralization undertaken for the Touquoy deposit, Bierlein and Smith (2003) noted that gold was associated with an increase in pyrrhotite and sericite, the latter reflecting addition of K.

#### **4.3.5 Geology of the Moose River anticline and Touquoy gold mineralization**

The study area for this project is focused on the Touquoy disseminated gold deposit (43-101 defined mineral resource estimate of ~450,000 oz Au [measured + indicated]; [www.atlanticgoldcorporation.com](http://www.atlanticgoldcorporation.com)) and other similar mineralized settings at Beaver Dam (resource of ~390,000 oz Au) and Fifteen Mile Stream (resource of ~675,000 oz Au) in addition to barren parcels of analogous host rocks. The latter sites are all associated with the Moose River anticline (MRA; Fig. 1b), a doubly-plunging structure that can be traced for at least 47 km (e.g.,

Staples et al., 2018). Significantly, three named deposits are hosted in the Mooser River Formation (Fig. 1), the lower most unit in the Goldenville Group, with disseminated gold mineralization occurring primarily in argillite host rocks and to a lesser extent metasandstone. Note that non-fissile (Fig. 2A) and fissile metamudstones (Fig. 2B) are commonly referred to as ‘argillites’ in the local literature related to for disseminated gold mineralization (e.g., Staples et al., 2018).

Gold was discovered and mined as vein-type ore at the Moose River (i.e., current site of Touquoy mine) and Beaver Dam deposits in the mid to late 19th century, however, mining was restricted to small underground and open pit operations that exploited narrow quartz vein lodes. Several small open pits in host rock were however developed in the early 1900s which might suggest that disseminated gold mineralization may have been actively mined (Bierlein and Smith, 2003). During the mid-1980’s, disseminated gold hosted in the metasandstones and mudstones of the MRA, and similar deposits elsewhere in the Meguma terrane (Ryan and Smith, 1998), were recognized and, because of their potential for open pit mining, became significant exploration targets. The recent (autumn of 2017) opening of the Touquoy deposit and delineation of significant reserves in other disseminated-style deposits (e.g., Fifteen Mile Stream, part of the Beaver Dam system) has further advanced the significance of these exploration targets (Staples et al., 2018).

In the Touquoy deposit, gold mineralization is confined to the “Touquoy argillite” unit of the Moose River anticline (Staples et al., 2018), which is a massive, homogeneous, green-grey argillite with minor interbedded black argillite (Hudgins, 1989; Bierlein and Smith, 2003). This unit can be as much as 180 m thick near the anticlinal hinge but thins with depth. In the northern limb of the MRA, the argillite is divided into upper and lower units separated by a thin horizon (“rip-up unit”) of sandstone clasts in a fine- to medium-grained greywacke (Staples et al., 2018). The MRA

and associated mineralization have been dislocated by steeply-dipping faults that post-date the regional folding event, with typical offsets ranging from <1 m to >80 m (Bierlein and Smith, 2003).

Mineralization in the Touquoy deposit is dominated by argillite-hosted disseminated gold and lacks conspicuous quartz veining in excess of 10 cm (Bierlein and Smith, 2003). Therefore, the metasedimentary rocks in the Touquoy deposit that carry grade are vein-free to vein-poor, however, the volumetric proportion of vein in this setting has not been studied in detail. The gold mineralization is best developed in the northern limb of the MRA and broadly conforms to bedding over a ~600 m strike length (Staples et al., 2018). The gold occurs as native grains (1  $\mu$ m to >1 mm) and has been observed in the following settings: (i) along cleavage; (ii) in hair-line fractures; (iii) in pressure shadows; (iv) as inclusions in or on the margins of sulfide grains (i.e., sphalerite, galena, pyrite, pyrrhotite, arsenopyrite); (v) in thin, bedding-parallel, often laminated quartz veins containing pyrite  $\pm$  pyrrhotite  $\pm$  chalcopyrite  $\pm$  galena; and (vi) on the margins of tightly folded quartz veins (Bierlein and Smith, 2003; Staples et al., 2018; and our own observations). Arsenopyrite, commonly multi-cm size porphyroblasts, and fine-grained disseminated and flattened pyrrhotite are the most abundant sulfide phases and show a spatial association with auriferous zones. Rarer chalcopyrite, sphalerite and galena are texturally-late and is inferred to post-date pyrrhotite (Bierlein and Smith, 2003).

As the focus of this study is on the Touquoy deposit and surrounding barren rocks, detailed descriptions of the structure, geology and mineralization of the other relevant deposit sites noted above, Beaver Dam and Fifteen Mile Stream, were not provided but are reviewed by Kontak et al. (1990, 1993) and Kontak and Smith (1993). In addition, summaries of the relevant geological

aspects in regards to exploration are available elsewhere (Beaver Dam: Mersereau, 1987; Webster, 1998; Staples et al., 2018; Fifteen Mile Stream: Graves et al., 2011; Staples et al., 2018).

## **4.4 Methods**

### **4.4.1 Sample selection and preparation**

As this work constitutes the initial study of this type in such a gold setting, a goal of this project was to develop a method that can exploit a minimalistic sampling approach in order to be attractive and easily integrated into an industry exploration program with regards to the quantity of samples required, since exploration and subsequent assay/analysis can be financially intensive. Thus, for gas chromatographic (GC) analysis, relatively small sample sets were used with a total of 21 samples from the mineralized Touquoy setting and 24 samples from barren settings (Wire Lake, Otter Lake, Como Lake, Beaver Dam East; Fig. 1B1; Table 1). Samples of fissile and non-fissile dark grey to black metamudstones (slates, argillites; Fig. 2A, B) were collected from a variety of historic diamond drill cores drilled between 1988 and 1997 which are currently archived and easily accessible at the Nova Scotia Department of Energy and Mines Core Library, Stellarton, Nova Scotia.

This study sampled archived core resulting from earlier exploration drilling throughout the 1980's and 1990's. Sampling targeted argillaceous metamudstones in both mineralized and barren settings, which is the host rock to the disseminated-type gold mineralization at the Touquoy and Beaver Dam, Fifteen Mile Stream deposits. Drill core samples were compared to drill core logs and assay data (Sangster, 1981; Hudgins, 1989, 1997; Miller et al., 1989; King and Webster, 1997;

Webster, 1998) to determine the gold grades of samples. Table 1 present a list of all samples selected for analysis via GC.

Samples collected from drill holes (Table 1) were chosen specifically so as to target gold-bearing (e.g.,  $0.01 \text{ g/t} \leq \text{Au} \leq 5 \text{ g/t}$ ) versus gold-deficient ( $\leq 0.01 \text{ g/t Au}$ ) metamudstone units in order to evaluate the influence of gold grade on the bulk volatile fluid chemistry. However, for the purpose of understanding the broad-scale differences in bulk fluid chemistry between mineralized and barren settings, metamudstone samples are considered to be from a mineralized setting if they were acquired from within the “mineralized zone” of the Touquoy deposit (Bierlein and Smith, 2003; Staples et al., 2018), regardless of the gold grade of the drill core interval from which the samples were collected. For instance, according to historic drill core logs (Hudgins, 1989, 1997), the metamudstone samples from the Touquoy deposit range in grade between 0.01 (i.e., gold deficient) and 4.83 g/t Au (i.e., gold bearing). In addition, a sample of a thin quartz vein (~2 cm) hosted along the lithological contact between mineralized metamudstone (Touquoy argillite) and metagreywacke from drill hole MR-88-174 (sample 88-174-67.97, 0.02 g/t Au; Table 1) was collected to characterize the composition of the mineralizing fluids preserved as fluid inclusions that presumably infiltrated the metamudstone sequences.

In order to evaluate the occurrence and composition of fluids that would constitute a “bulk fluid” upon crushing of whole rock material, a representative vein sample (88-174-67.97) and a Touquoy argillite metamudstone (88-228-89.5) were prepared as fluid inclusion sections. The samples collected were from historic drill holes that penetrated mineralized metamudstones that have since been mined via open pit (Touquoy/Moose River project – Atlantic Gold Corp.; Staples et al., 2018).

#### 4.4.2 Confocal laser Raman microspectroscopy (LRM)

Laser Raman microspectroscopy was performed to determine the volatile composition of the vapor phase of selected quartz-hosted fluid inclusions present in veins and pressure shadows about porphyroblasts. The LRM was used to identify and quantify trace amounts of gas phases (CO<sub>2</sub>, N<sub>2</sub>, CH<sub>4</sub>, etc.) that were otherwise unidentifiable using microthermometry. The LRM analysis was done using a Horiba Jobin-Yvon LabRam HR confocal instrument at Saint Mary's University, Halifax, Nova Scotia, Canada. It is equipped with a 100 mW 532 nm Nd-YAG diode laser (Toptica Photonics) and a Synapse charge-coupled device (CCD; Horiba Jobin-Yvon) detector. Pure silicon was used as a frequency calibration standard. Analyses were performed using a 20 – 30 µm confocal hole diameter to maximize resolution at depth in the host quartz. A 600 grooves/mm grating (spectral resolution of approximately  $\pm 2$  cm<sup>-1</sup>) was used for identification of the volatile phases. In contrast, a 1800 grooves/mm grating (spectral resolution of approximately  $\pm 0.5$  cm<sup>-1</sup>) was used to accurately determine the Fermi diad spacing between the  $\nu_1$  and  $\nu_2$  Raman peaks of CO<sub>2</sub>. The fermi diad spacing was used to determine the density of CO<sub>2</sub> in the vapor phase (e.g., Rosso and Bodnar, 1995; Yamamoto et al., 2002; Yamamoto and Kagi, 2006; Fall et al., 2011; Wang et al., 2011). Spectra were collected using an accumulation of three, 40-50 second acquisitions with a laser spot size of ~1-2 micron at 100% laser power (~2.15 mW at sample surface). Semi-quantitative determination of the relative abundance of inclusion-hosted gas species (in mol %) was performed using the methodology and empirical quantification parameters described by Wopenka and Pasteris (1986, 1987), Dubessy et al., (1989), Burke (2001), and Beeskow et al. (2005). The instrument efficiency factors ( $z$ ) for CO<sub>2</sub> and CH<sub>4</sub> were determined by comparing CO<sub>2</sub> and CH<sub>4</sub> contents determined by Raman spectroscopy to the results obtained via microthermometric analysis for quartz-hosted CO<sub>2</sub>-CH<sub>4</sub> standard inclusions from the South Wales

Coal Field (Beeskow et al., 2005). Instrument efficiencies for other gas species were assumed to be unity in the absence of standards, and results in a slight overestimation of the mole fraction (e.g., N<sub>2</sub>, H<sub>2</sub>S). Uncertainties in the mole fractions of dissolved species in the carbonic phase of the inclusions are estimated to be within 20% relative.

#### **4.4.3 On-line rock-crushing gas chromatography**

Samples of metamudstone collected from drill core (Table 1) were fragmented in jaw crushers to produce uniformly small fragments (Fig. 2C) suitable for use in the GC on-line crushers (Fig. 3). Sample aliquots were hand-picked for GC analysis ( $\leq 1 - 5$  mm in maximum dimension) and weighed. Samples were picked to avoid obvious signs of surface weathering. Aliquots were washed twice in deionized water and allowed to dry on a hot plate in sterile glass vials and weighed again prior to analysis.

Samples were analyzed using an Agilent 7890 series gas chromatograph (GC), also at Saint Mary's University, adapted with appropriate valve and injection systems by Wasson-ECE Instrumentation. For the analysis of trace hydrocarbon phases (Method 2), an alumina-PLOT capillary analytical column (50 m  $\times$  0.53 mm  $\times$  10  $\mu$ m) was used in series with a flame ionization detector (FID) capable of analyzing combustible compounds (e.g., alkanes, alkenes/alkynes, thiols). Ultrapure He carrier gas was employed at a flow rate of  $11.9 \pm 0.5$  ml/min for Method 2. For the analysis of non-combustible volatile species (e.g., H<sub>2</sub>O, CO<sub>2</sub>; Method 1) an alumina-PLOT analytical column (30 m  $\times$  0.53 mm  $\times$  10  $\mu$ m) in series with a thermal conductivity detector (TCD) and FID was used. Ultrapure He carrier gas was set to a flow rate of  $8.65 \pm 0.5$  ml/min for Method 1. Sample crushing was carried out at elevated temperature ( $\sim 105^\circ - 110^\circ\text{C}$ ) in order to ensure complete volatilization of all trapped volatile species upon crushing. Previous work by Kerr et al.

(2015) showed that, although sonication has no appreciable effect of GC reproducibility, crushes that are not performed at elevated temperature yield lower total hydrocarbon and unsaturated hydrocarbon abundances. Stainless steel, hydraulically driven rock crushers (Fig. 3), custom-made by the University of Toronto Machine Shop based on the designs of Bray and Spooner (1992) and Bray et al. (1991), were adapted from the designs of Andrawes and Gibson (1979) and Andrawes et al. (1984). Detailed descriptions of the analytical system are presented elsewhere (Bray et al., 1991; Salvi and Williams-Jones, 1997; Kerr, 2013; Kerr et al., 2015). Table EA 4-3 (Electronic Appendix) provides the full list of hydrocarbon species that are detectable and quantifiable using this technique.

Samples of inclusion-free, ultrasonically-cleaned synthetic quartz (n =20; 4 blanks per crusher for Method 1, and 1 blank per crusher for Method 2) were used to acquire a background to account for any volatiles generated as a result of the mechanical action of the crushers. Blank crushes yielded minor amounts of CH<sub>4</sub> and an unknown impurity peaks located at a retention time of approximately 15 and 32.2 minutes for Method 2. Blank crushes on Method 1 yielded minor water and trace CH<sub>4</sub> upon crushing. Methane and water abundances from the blank crushes were averaged and subtracted from all sample chromatograms. Identification and standardization of gas species (other than H<sub>2</sub>O) was performed using standard gas mixtures supplied by Matheson Tri-Gas and Scotty Specialty Gases. The last quantifiable hydrocarbons to elute from the column were hexanes, which elute between 25 to 28 min. Lower limits of quantification are approximately 10<sup>-12</sup> to 10<sup>-13</sup> mol/g of crushed material (Kerr et al., 2015). Calibration of water was performed by the injection of water-saturated air at known temperatures (headspace analysis).

In order to evaluate reproducibility between samples, preliminary gas chromatographic analysis was performed on samples of fragmented fluid inclusion-rich quartz extracted from across the widths of two separate quartz veins unrelated to this study area. Sample preparation was identical for all aliquots. Sample fragments were washed in deionized water and allowed to sit in 1 M HCl overnight (~8 hrs) to remove any carbonate. The samples were washed again and allowed to dry on a hotplate in a sterile glass vial prior to loading into the cleaned stainless-steel crushers.

## **4.5 Results**

### **4.5.1 Petrography of mineralized metamudstones from Touquoy**

Representative samples of mineralized metamudstone from the Moose River Formation at the Touquoy deposit, the gold-bearing Touquoy argillite unit (samples 88-90-112.4 [0.13 g/t], 88-158-13.85 [0.26 g/t], 88-174-67.97 [0.02 g/t], 88-221-53.64 [3.97 g/t], and 88-228-89.5 [0.37 g/t]), were investigated in order to evaluate their mineralogy and textural features, both of which presumably relate in part to interaction with mineralizing fluids. Two metamudstone samples from Au-barren settings (Wire Lake sample WL-229-04-27.1 [ $<0.01$  g/t]; Como Lake sample CL-97-06-16.9 [0.0025 g/t]) were investigated for comparison. The metamudstones from both mineralized and barren settings may be either non-fissile (Fig. 2A) or fissile (Fig. 2B) in nature and is characterized by a muscovite + quartz + chlorite  $\pm$  carbonate  $\pm$  sulfide (pyrrhotite, arsenopyrite) association. In coarser-grained units (i.e., metasiltsstones; samples 88-158-13.85 and 88-174-67.97), grains of plagioclase and K-feldspar are observed. In Touquoy metamudstone samples (i.e., mineralized setting), carbonate is common and occurs as sieve-textured porphyroblasts with quartz-rich pressure shadows (Fig. 4A, B). Importantly, similar carbonate porphyroblasts have been documented in alteration halos associated with lode gold mineralization

in the Meguma terrane (Smith and Kontak, 1987; Kontak and Horne, 2010), and pervasive carbonate (ankerite and calcite) alteration directly correlates with gold mineralization (Smith and Kontak, 1987; Ryan and Smith, 1998; Bierlein and Smith, 2003; Staples et al., 2018). Conversely, in metamudstones from barren settings, carbonate porphyroblasts were very rare, or not observed. In metamudstones from the Wire Lake region (sample WL-229-04-27.1), staurolite porphyroblasts are observed. Accessory phases in all investigated metamudstones from both mineralized and barren settings include pyrrhotite, ilmenite, rutile and arsenopyrite (Fig. 4). Pyrrhotite occurs primarily as bedding-concordant bands/lozenges (Fig. 4C, D), and its morphology and association with particular units suggests it likely formed from an earlier diagenetic Fe-sulfide phase (e.g., framboidal pyrite; see Horne and Pelley, 2007). Further relevant observations include the presence of porphyroblasts of euhedral arsenopyrite in all investigated metamudstone samples that are associated with fluid inclusion-bearing quartz-chlorite pressure shadows (Fig. 4E) and the presence of abundant pore space (Fig. 4F) in rocks which may be a reservoir for volatile fluids, although this cannot be observed directly.

#### **4.5.2 Fluid inclusion petrography**

Relevant to the present study (i.e., bulk compositional analysis of metamudstone-hosted volatiles), it is important to evaluate the occurrence and volatile composition of the fluid types that may contribute to and thus constitute a “bulk fluid”. To assess this aspect, samples from the Touquoy deposits were studied in detail to locate where fluids are present in the samples and to assess their volatile compositions (e.g., H<sub>2</sub>O, CO<sub>2</sub>, CH<sub>4</sub>, N<sub>2</sub>, etc.).

Examination of four samples from Touquoy drill core intervals (samples 88-158-13.85, 88-221-53.64, 88-228-69.5, and 88-174-67.97) reveal that fluids can be: (i) along mineral grain

boundaries, (ii) trapped in pore spaces (Fig. 4F), (iii) as fluid inclusions in detrital quartz (Fig. 5A) or porphyroblasts (Fig. 5B), (iv) as fluid inclusions in pressure-shadow minerals (quartz; Fig. 5C – F), and (v) as fluid inclusions in discrete quartz veins (Fig. 6). We note that fluids hosted in the pore spaces cannot be directly observed, but are inferred to be present. In addition, fluid inclusions along grain boundaries or in carbonate porphyroblasts, although observed, often cannot be accurately identified due to their size (i.e., inclusions <2-3  $\mu\text{m}$ ) and consequent limitations of optics and instrumentation.

In quartz-chlorite pressure shadows around arsenopyrite porphyroblasts in metamudstone (Fig. 4B – E) and quartz veins (Fig. 6A), two fluid inclusion types are identified using petrography and LRM analysis. However, the vapor phase compositions of these inclusions can vary dramatically depending on the setting. When possible, fluid inclusions are classified in the context of fluid inclusion assemblages (FIA) integrated with establishing the relative timing of entrapment (i.e., primary versus secondary) for small groups of texturally coeval inclusions (Goldstein and Reynolds, 1994; Bodnar, 2003). Fluid inclusion types identified follow:

(i) *Type 1*: Two-phase aqueous-carbonic ( $L_{\text{aq}} + V_{\text{car}}$ ;  $\text{H}_2\text{O} \pm \text{CO}_2 \pm \text{CH}_4 \pm \text{N}_2$ ) with the aqueous phase proportion estimated at between 50 and 90 vol. % (Fig. 6B). These inclusions may display a negative crystal shape or appear wormy to irregular. These latter shapes suggest post-entrapment modification. The inclusions occur on secondary planes (Fig. 6B, C) and as 3D arrays or clusters of indeterminate origin in vein quartz, in quartz pressure shadows around arsenopyrite (Fig. 5F), and rarely along grain boundaries.

(ii) *Type 2*: vapor-dominated, aqueous-carbonic ( $V_{\text{car-N}_2} \pm L_{\text{aq}}$ ) inclusions (Fig. 5E). The vapor phase compositions are highly variable with regard to  $\text{N}_2\text{-CH}_4\text{-CO}_2$  abundances (Table EA 4-1).

The aqueous phase wets the edges of the inclusions and may not be visible using the petrographic microscope, but its presence is confirmed via LRM. They occur in pressure-shadow quartz associated with arsenopyrite porphyroblasts (Fig. 5E), as secondary trails (Fig. 6C, D) and along grain boundaries (Fig. 6E) in vein quartz, and as clusters of indeterminate origin in grains of vein-hosted quartz. They also appear present in carbonate porphyroblasts (Fig. 5B), however, the inclusions are too small and potentially densities that are too low to characterize.

#### **4.5.3 Fluid inclusion laser Raman microspectroscopic (LRM) analysis**

Vapor phases of type 1 and 2 fluid inclusions hosted in vein and pressure shadow type quartz from the Touquoy deposit were analyzed via LRM in order to determine their chemistry (Table EA 4-1). Fluid inclusions hosted in carbonate porphyroblasts and along quartz grain boundaries (Fig. 5B) were not analyzed due to optical and/or analytical limitations. Fluid compositions in all settings investigated are highly variable. Type 1 fluid inclusions hosted in vein quartz (n = 21; Fig. 7A) show ranges of vapor phase  $X_{CO_2}$ ,  $X_{CH_4}$ , and  $X_{N_2}$  values between 0 – 0.95, 0.02 – 0.8, and 0 – 0.84 mol%, respectively. Evidence of ethane, and potentially higher order hydrocarbon species, is present particularly in  $CH_4$ -rich type 1 inclusions. In contrast, type 1 fluid inclusions hosted in pressure-shadow quartz (n = 8; Fig. 7B) are devoid of  $CO_2$ , and show ranges of vapor phase  $X_{CH_4}$  and  $X_{N_2}$  values between 0 – 0.82 and 0.19 – 1 mol%, respectively. Type 2 fluid inclusions hosted in vein quartz (n = 25; Fig. 7C) show ranges of vapor phase  $X_{CO_2}$ ,  $X_{CH_4}$ , and  $X_{N_2}$  values between 0 – 0.98, 0 – 0.78, and 0 – 0.91 mol%, respectively. The large ranges for volatile abundances in type 2 inclusions hosted in vein quartz reflects the high degree of variability in composition, as some inclusions are  $CO_2$ -,  $CH_4$ -, or  $N_2$ -dominated, depending on the FIA. In a similar fashion to type 1 inclusions, type 2 inclusions in pressure shadow quartz (n = 12; Fig. 7D) are devoid of  $CO_2$ ,

and show ranges of vapor phase  $X_{\text{CH}_4}$  and  $X_{\text{N}_2}$  values between 0 – 0.41 and 0.6 – 1 mol%, respectively, and average  $0.05 \pm 0.12$  and  $0.95 \pm 0.12$  mol%, respectively.

In summary, type 1 and 2 fluid inclusions hosted in quartz veins crosscutting metamudstone, or along lithological contacts between greywacke and metamudstones, contain variable  $\text{CO}_2$ ,  $\text{CH}_4$ , or  $\text{N}_2$  abundances (Fig. 8A), but are infrequently devoid of  $\text{CO}_2$  (i.e., 9 out of 46 type 1 and 2 inclusions analyzed lacked detectable  $\text{CO}_2$ ). Interestingly, the vein-hosted inclusions that are devoid of  $\text{CO}_2$  were hosted in secondary FIA extending away from metamudstone-vein contacts. In contrast, pressure-shadow quartz hosted type 1 and 2 fluid inclusions are characteristically devoid of  $\text{CO}_2$  (in *all* analyzed inclusions,  $n = 20$ ), while displaying significant variability in  $\text{CH}_4$  and  $\text{N}_2$  abundances (Fig. 8B).

#### **4.5.4 On-line rock-crushing gas chromatography of metamudstones**

##### *4.5.4.1 Evaluation of sample reproducibility*

Prior to the analysis of the metamudstone samples, trials were performed to evaluate the accuracy and reproducibility of the GC technique. Quartz samples collected from across two different laminated veins and assigned vein sequence numbers were selected for analysis (Fig. 9). These veins from the Madrid deposit of the Hope Bay Greenstone Belt, Nunavut, Canada, are unrelated to the study area, but instead were chosen based on the consistency of densely populated fluid inclusions in the quartz across the entire vein width. Quartz collected from each vein sequence was divided into two aliquots (original and duplicate = 2 aliquots per sample/vein sequence) and analyzed by GC at different times (~1 month apart). Considering the potential variability of fluid compositions in natural samples, the good bulk volatile ratio reproducibility is noted with respect

to both  $\text{CO}_2/(\text{CO}_2+\text{H}_2\text{O})$  (Fig. 9A, B) and  $\text{CO}_2/(\text{CO}_2+\text{HCs})$  (HCs – hydrocarbons; Fig. 9C, D) ratios across the vein sequences. With respect to discrete volatile species, reproducibility was good with standard deviations of 1.31 mol%, 0.007 mol%, and 1.32 mol% for  $\text{CO}_2$ ,  $\text{CH}_4$  and  $\text{H}_2\text{O}$ , respectively, between duplicate analyses.

#### *4.5.4.2 Gas chromatographic analysis of metamudstones*

Metamudstone-hosted volatile species were analyzed via on-line, rock-crushing gas chromatography (GC). A complete data table of all GC analyses from methods 1 and 2 have been compiled in Tables EA 4-2 and EA 4-3, respectively. For the purpose of comparison between gold-mineralized and gold-barren settings, bulk volatile ratios are used rather than absolute abundance (i.e., total moles of species) in order to avoid differences that may arise due to variability in crushing efficiency, and corresponding total volatile liberation, between samples.

All samples analyzed contained detectable amounts of water and hydrocarbon-bearing volatiles, such as methane (Fig. 10), but the abundances of these volatiles varied among samples. Methane and  $\text{H}_2\text{O}$  were observed in all samples using the GC method 1 (Fig. 10A, B). However, upon subtraction of background  $\text{H}_2\text{O}$  (determined through analysis of synthetic quartz blanks; see above),  $\text{H}_2\text{O}$  was often below limits of quantification (l.o.q) determined from inclusion-free quartz blanks ( $\sim 3.5 \times 10^{-6}$  mol/g); samples with water abundance above l.o.q was only observed in 5 out of 21 samples from the mineralized setting and in only 2 out of 24 samples from barren settings. Except for one sample from a barren setting (sample BDE-97-03-26.95),  $\text{CO}_2$  was only detected in samples from the mineralized setting (e.g., Fig. 10A). Approximately 50% (11 out of 21) of metamudstone samples collected from the Au-mineralized Touquoy deposit (Fig. 1B) show elevated  $\text{CO}_2$  abundances. T-test results demonstrate that there are statistically discernable

differences in the abundance of CO<sub>2</sub> from mineralized (n = 21) versus barren (n = 24) settings (Fig. 11A), yielding a one-tailed p-value of 0.0103 (95% confidence interval; assuming unequal variances). A one-tailed p-value is expressed here because it was correctly hypothesized that an increase in CO<sub>2</sub> abundance would be observed in metamudstone samples from gold-mineralized settings. Metamudstone CO<sub>2</sub> abundance and Au grade are not commensurate, and no correlation is present between the reported Au grade of the drill core intervals from which the analyzed samples were collected and the abundance of CO<sub>2</sub> in those samples.

Trace hydrocarbons, including ethane, propane and butane determined using GC method 2 (Fig. 10C) were observed in samples from both mineralized and barren settings. No statistically significant difference is observed in the ethane/methane (C<sub>2</sub>H<sub>6</sub>/CH<sub>4</sub>) ratios between populations (Fig. 11B; two-tailed p-value of 0.0957). Statistically anomalous differences are identified between populations when comparing the ratios of summed C<sub>3</sub> hydrocarbon [ $\Sigma$ (C<sub>3</sub> HCs); Fig. 11C] and summed C<sub>4</sub> hydrocarbon [ $\Sigma$ (C<sub>4</sub> HCs); Fig. 11D] species to CH<sub>4</sub>, with two-tailed p-values of 0.043 and 0.0303, respectively. No statistically significant distinction is observed in the comparison of propene/propane (C<sub>3</sub>H<sub>6</sub>/C<sub>3</sub>H<sub>8</sub>; Fig. 11E) and isobutane/butane (i-C<sub>4</sub>H<sub>10</sub>/n-C<sub>4</sub>H<sub>10</sub>; Fig. 11F) ratios between metamudstone populations from mineralized and barren settings, with two-tailed p-values of 0.5969 and 0.0776, respectively. No correlations were identified between the reported Au grades of the drill core intervals from which the analyzed samples were collected and the abundances of hydrocarbon species or ratios thereof. Unfortunately, due to analytical limitations the presence of N<sub>2</sub> could not be quantified by GC as it co-elutes with CH<sub>4</sub> using method 1 and cannot be detected using method 2.

## 4.6 Discussion

#### **4.6.1 Limitations and advantages of GC-based exploration methods**

Due to the inherent bulk nature of this GC technique, a single sample crush liberates all volatile species contained in the metamudstone. In theory, all volatiles trapped as fluid inclusions or in pore spaces are liberated to yield a bulk volatile signature, thus compositional information for specific fluid generations cannot be determined using this technique. The bulk volatile signatures of competent igneous rocks and quartz vein material has been shown elsewhere to be a potentially effective criteria to consider in exploration programs (e.g., footwall-style sulfide mineralization in Sudbury, Canada; Kerr et al., 2015); however, the analysis of metasedimentary rocks of variable fissility (i.e., this study) using this technique has not been investigated for its viability or efficacy to the best of our knowledge. For example, fissile clastic rocks may be prone to volatile loss via fluid migration along grain or lamination boundaries, or cleavage planes, especially during exposure to elevated temperatures in the GC crushers, thus lowering (or modifying) total volatile contents.

Despite the limitation noted above, the GC technique of this nature presents a variety of advantages. For instance, sample preparation is simple and can be done on site (e.g., core lab). Also, GC analyses are rather inexpensive compared to other potential exploration vectors (e.g., fire assays, isotopic analyses, lithogeochemistry). Although the GC system used in this study uses helium as a carrier gas, GC systems are available that exploit less expensive nitrogen (or air), making them potentially more attractive for rapid on-site sample analysis. Furthermore, by considering fluid signatures in addition to lithogeochemical and structural characteristics, more refined genetic models may emerge leading to more robust exploration programs.

#### **4.6.2 Origin of volatiles in metamudstones of the Moose River anticline**

Volatile fluids in mineralized metamudstones that are variably crosscut by quartz veins can be hosted in a variety of settings: (i) along mineral grain boundaries; (ii) in pore spaces in the metamudstone (Fig. 4F); (iii) as fluid inclusions in quartz clasts (Fig. 5A) or porphyroblast minerals (Fig. 5B); (iv) as fluid inclusions in pressure-shadow minerals (quartz ; Fig. 5B – E); and (v) as fluid inclusions in discrete quartz veins (Fig. 6). As fluids hosted in pore spaces could not be observed and fluid inclusions along grain boundaries or in carbonate porphyroblasts could not be accurately observed and/or analyzed directly due to optical and instrumental limitations, fluid inclusions preserved in metamudstone-hosted quartz veins and in pressure-shadow quartz were investigated in order to constitute a reasonable bulk-fluid proxy. As two distinct fluid chemistries have been defined that are spatially restricted in the samples, their origins are addressed separately below.

#### *4.6.2.1 Origin of the $N_2$ - $CH_4$ fluids*

Fluid inclusions hosted in pressure-shadow quartz are  $N_2$ - $CH_4$ -dominated and therefore contrast markedly with the  $H_2O$ - $CO_2$  ( $X_{CO_2}=0.1-0.2$ ) fluids typically found in quartz veins of the Meguma deposits (Kontak and Horne, 2010 and references therein) which are themselves typical of global orogenic gold deposit fluids (e.g., Ridley and Diamond, 2000; Hageman and Cassidy, 2000; Bodnar et al., 2014). These  $N_2$ - $CH_4$  inclusions occur as clusters of indeterminate origin, hence permissible with them being synchronous with quartz growth and suggests the inclusions represent fluids present in the mudstones broadly synchronous to, or post-dating, formation of arsenopyrite porphyroblasts. As the latter deflect deformation fabrics in the host mudstones and often display evidence of brittle deformation, they likely formed synchronous with or prior to deformation that accompanied regional metamorphism of the Meguma terrane during the Neocadian event at ~410

to 380 Ma (Reynolds and Muecke, 1978; Muecke et al., 1988; Hicks et al., 1999; Kontak et al., 1998; Morelli et al., 2005). This deformation event was also responsible for the production of slaty cleavage (Fig. 2B) and porphyroblast pressure shadows (Fig. 5B) observed in rocks associated with MRA (Graves and Zentilli, 1982; Horne and Pelley, 2007) and elsewhere across the Meguma terrane (Hicks et al., 1999). Also, the temperature of formation of arsenopyrite (~480°C) in metamudstones from the MRA has been shown to be higher than that for chlorite occurring with quartz and arsenopyrite (~390°C; Kontak et al., 1991; Kontak and Smith, 1993). Therefore, it is suggested that the fluids present in pressure-shadow quartz represent metamorphic fluids or highly modified meteoric-sourced fluids that have equilibrated with reducing country rocks (e.g., argillaceous and organic carbon-bearing [~1 wt.%] metamudstones; Bierlein and Smith, 2003) through fluid-rock interaction.

Methane in pressure-shadow quartz as type 1 and 2 inclusions may have originated from: (i) a magmatic contribution related to the intrusion of ~375 Ma granitic magmas in the vicinity (Kontak and Kyser, 2011); (ii) the reduction and respeciation of initially CO<sub>2</sub>-bearing fluids present in the metamudstones (e.g., Holloway, 1984); and/or (iii) the degradation of carbonaceous material in the mudstone host rocks during regional or thermal metamorphism (e.g., Ma and Li, 2018). A magmatic origin for methane in pressure shadow-hosted inclusions is unlikely based on the timing between the regional metamorphism responsible for deformation and pressure shadow formation, and the granitic intrusions in the area. Also, the absence of secondary fluid inclusion trails in pressure shadow minerals (i.e., only clusters) suggests these fluids were not introduced by late fluid circulation. However, a magmatic origin cannot be discounted to explain the presence of methane in vein-hosted inclusions.

Alternatively, methane may be from the respeciation of CO<sub>2</sub> under reducing conditions:



It has been documented that a CH<sub>4</sub>-rich fluid can evolve in equilibrium from an initially more oxidizing, CO<sub>2</sub>-bearing fluid, under geologically realistic reducing conditions (below 500°–600°C and *f*O<sub>2</sub> between QMF and QMF-3; Holloway, 1984; Huizenga, 2001). However, this mechanism fails to explain the occurrence of the higher order hydrocarbons (HCs) identified in metamudstones (Fig. 10C). Methane and higher order HC species (≥C<sub>2</sub>) may have an organogenic origin, originating from the thermal destruction of organic matter present in the metamudstone units of the MRA (e.g., Moose River Formation; Beirlein and Smith, 2003). These “thermogenic” HCs may have been leached from the country rocks by circulating hydrothermal fluids (e.g., Welhan and Lupton, 1987) or incorporated into magmatic intrusions through country rock assimilation (e.g., Gunter and Musgrave, 1971; Darling et al., 1995). Conversely, higher order HCs may have an abiogenic origin by which CO or CO<sub>2</sub> may be reduced to methane and higher order species through reactions with H<sub>2</sub> at temperatures of ~200 - 300°C (i.e., Fischer-Tropsch synthesis; rxns 2 and 3; Anderson, 1984; Sherwood-Lollar et al., 1993; Salvi and Williams-Jones, 1997a; Potter et al., 2004; Taran et al., 2007; Potter and Konnerup-Madsen, 2003; Kerr et al., 2015), which favor unbranched, shorter chain (e.g., C<sub>1</sub> – C<sub>4</sub>), saturated HC species, and is catalyzed by Fe-bearing silicates (e.g., chlorite).



In reality, the methane and higher order HC species present in metamudstones may originate from a combination of sources. Bulk volatile HC signatures from metamudstones do not show a consistently log-linear decrease in the proportion of HC species with increasing carbon number for saturated HCs (Fig. 12), consistent with a Schultz-Flory distribution characteristic to HCs generated abiogenically (Fig. 12; Salvi and Williams-Jones, 1997a; Sherwood Lollar et al., 2006, 2008). Rather, a log-linear decrease is observed between C<sub>1</sub> – C<sub>3</sub> HCs in metamudstones, after which point a flatter relationship is displayed. Hydrocarbons with an organogenic origin produced as a result of thermogenic processes such as pyrolysis (e.g., Ma and Li, 2018) generally display a flatter distribution (Fig. 12; Sakata et al., 1997; Chen et al., 2000; Potter and Konnerup-Madsen, 2003 and references therein). This suggests that thermogenic and abiogenic processes may have contributed to the HC budget present in metamudstones. However, in order to unravel HC origin, compound-specific stable isotope analysis (i.e.,  $\delta^{13}\text{C}$ ) of the HC species is suggested (cf., Schoell, 1983, 1988).

Nitrogen is intimately associated with methane in pressure shadow-hosted type 1 and 2 fluid inclusions (Fig. 7B, D, 8B). Nitrogen is a common volatile phase in sedimentary rocks, distributed amongst both organic (e.g., carbonaceous material) and inorganic (e.g., phyllosilicate) components (Glasmacher, et al., 2003). Nitrogen (and methane) can be released during the maturation of organic matter during diagenesis and metamorphism (Jurisch et al., 2012 and references therein), as well as from heating (>200°C) of phyllosilicate-bearing sedimentary rocks during metamorphism (Itihara and Honma, 1983; Everlien, 1990), such as those in the Meguma terrane. Glasmacher et al. (2003) observed elevated ratios between fixed nitrogen and K<sub>2</sub>O in hydrothermal sericite (i.e.,  $N_{\text{fix}}/K_2O_{\text{ms}}$ ) within alteration halos around Au-mineralized quartz veins at The Ovens

gold occurrence in southwestern Nova Scotia and concluded that the nitrogen in mineralized areas may be of secondary origin, presumably introduced by late-stage fluids. Therefore, although one cannot discount an exotic origin, it is inferred that the CH<sub>4</sub>+N<sub>2</sub>-rich fluids in pressure shadow-hosted fluid inclusions result from the low-grade regional metamorphism (i.e., low- to mid-greenschist facies around the Moose River district; Keppie and Muecke, 1979) of the phyllosilicate- and organic-bearing sedimentary rocks present throughout the Meguma Supergroup.

#### *4.6.2.2 Origin of the CO<sub>2</sub>-bearing fluids*

Carbon dioxide is a common volatile phase in type 1 and 2 fluid inclusions hosted in quartz veins from the Au-mineralized settings. Importantly the same fluid is well documented as the dominant fluid type in the Meguma auriferous quartz vein systems (i.e., H<sub>2</sub>O-CO<sub>2</sub> fluids with X<sub>CO<sub>2</sub></sub> = 0.1 – 0.2; Kontak et al., 1989a, b, 1990, 1996, 2001; Bierlein and Smith, 2003; Kontak and Horne, 2010; Kontak and Tuba, 2017). More recently, the same fluid has been directly implicated as a gold-mobilizing fluid at the Dufferin gold deposit approximately 40 km to the SE of the Touquoy mine (e.g., Ch.3 of this thesis).

Previous work on Meguma-hosted gold systems, including the Touquoy, Fifteen Mile Stream and Beaver Dam deposits that lie on the MRA structure (Kontak et al., 1991, 1993, 1998), has shown that vein-forming fluids must have originated from a structural level beneath the deposits and that the timing of veining is consistent with reactivation of fault and shear zones which temporally overlaps with emplacement of granitic intrusions at ~375 Ma. However, this does not imply a purely magmatic CO<sub>2</sub> source, as it has also been shown that ore-forming fluids have interacted significantly with Meguma country rocks (Sangster, 1992; Kontak and Kerrich, 1997; Kontak et

al., 2011, 2018), or have been contaminated by country rock-equilibrated fluids (Kontak and Kyser, 2011). In addition, CO<sub>2</sub> is not identified in the pressure-shadow hosted fluid inclusions and is only present in vein-hosted fluids, providing evidence that CO<sub>2</sub> relates to the vein-forming fluids. That secondary trails of type 1 and 2 inclusions in vein quartz adjacent the contact with metamudstone (e.g., Fig. 6) show highly variable CO<sub>2</sub>, CH<sub>4</sub> and N<sub>2</sub> abundances among FIA (Table EA 4-1), and often among individual inclusions within clusters of indeterminate origin suggest that both CO<sub>2</sub>-rich vein-forming fluids and CH<sub>4</sub>+N<sub>2</sub>-dominated wall rock-equilibrated fluids coexisted, and potentially mixing (e.g., Matthai et al., 1995), in these settings. The presence of disseminated gold mineralization in the metamudstones indicates therefore that an auriferous H<sub>2</sub>O-CO<sub>2</sub>-bearing fluid must have directly infiltrated these units.

During hydrofracturing of wall rocks and subsequent vein formation, the fluid pressure within the vein ( $P_{vf}$ ) must have exceeded the cumulative normal stress and tensile strength of the host rock (i.e.,  $P_{lithostatic}$ ). However, in order to drive fluids into the surrounding host rocks from discrete fluid pathways, the fluid pressure in the wall rock ( $P_{wr}$ ) must have been lower than that of the incoming fluid (Matthai et al., 1995) and sufficient permeability must have been present to accommodate fluid influx. During periods when  $P_{lithostatic} \geq P_{vf}$ , circulating fluids may have utilized anisotropy, such as rock cleavage and foliation, as fluid channelways (Mawer, 1987; Kontak and Smith, 1993).

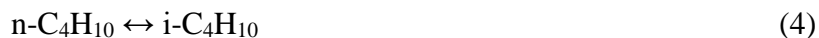
#### **4.6.3 Bulk volatile systematics – Comparison between mineralized and barren metamudstones**

Sporadic disseminated gold occurrences in metasedimentary rocks associated with anticlinal structures such as the MRA may result from two potential scenarios: (1) heterogeneous infiltration of an aqueous-carbonic ore fluid into the metamudstone units along the MRA that resulted in

localized gold mineralization; or (2) homogenous infiltration of a similar fluid with the caveat that gold only formed economic concentrations where favorable physical (e.g., structural connectivity, increased permeability, localized unmixing) and/or chemical (e.g., host rock reactivity) conditions prevailed. It is expected that, if gold mineralization resulted from the former scenario, evidence of localized ore fluid infiltration and associated host rock alteration would be confined primarily to ore zones and alteration halos (e.g., Touquoy zone; Bierlein and Smith, 2003). Conversely, if metamudstone units were collectively infiltrated in the second scenario by the same aqueous-carbonic fluids, the bulk volatile signatures (and alteration) would be similar between barren and mineralized regions.

Approximately 50% (11 out of 21) of metamudstone samples collected from the Au-mineralized Touquoy deposit (Fig. 1B) show elevated CO<sub>2</sub> abundances (Fig. 13A, B), whereas only 1 out of 24 samples from Au-barren settings along the MRA contained detectable CO<sub>2</sub>. Furthermore, it has been noted that pervasive carbonate (ankerite and calcite) alteration directly correlates with disseminated gold mineralization in the MRA (Ryan and Smith, 1998; Bierlein and Smith, 2003; Staples et al., 2018). This observation strongly suggests that mineralizing fluids did not permeate metamudstones uniformly on a regional scale based on the sampling density. Mineralization at the Touquoy deposit is apparently associated with a network of complex faulting and commonly sub-millimeter quartz-carbonate stockwork (although cm- to m-scale are present in places), which are collectively inferred to have provided the conduit system necessary for deeper sourced fluids to ascend to higher crustal levels (Bierlein and Smith, 2003). Similar complex faulting and veining is also observed in the other gold deposits across the Meguma terrane (Malcolm, 1929; Kontak et al., 1990a, b; Ryan and Smith, 1998; Sangster and Smith 2007; Kontak and Horne, 2010).

No effective distinctions using HC signatures could be determined between mineralized and barren settings, instead they display largely overlapping compositional fields in ternary plots (Fig. 13C, D). Minor, statistically anomalous (i.e.,  $0.03 \leq p\text{-value} \leq 0.05$ ; Fig. 11C, D) differences are present between C<sub>3</sub> and C<sub>4</sub> HC ratios (Fig. 11C, D) that may reflect a modest increase in volatile HC productivity through the interaction of hydrothermal fluids with carbonaceous matter present in the host rocks (e.g., Kawka and Simoneit, 1994). Despite a  $p\text{-value} > 0.05$ , differences in the isobutane/butane ratio between settings (Fig. 11F) also warrant further investigation. The thermodynamic and kinetic properties of butane isomerization in geological systems has not been investigated. In the chemical literature (e.g., Chen et al., 1975), the  $\Delta G^\circ$  for the isomerization of butane to isobutane (rxn. 4) becomes more negative with decreasing temperature, thus favoring the i-C<sub>4</sub>H<sub>10</sub> isomer at lower equilibrium temperatures.



Higher isobutane/butane ratios are present in metamudstones from the mineralized setting (Fig. 11F), which would suggest that, if the isobutane/butane ratios in the metamudstones preserve equilibria compositions, C<sub>4</sub> HCs in the mineralized setting equilibrated at lower temperatures than in barren settings. This is counterintuitive based on a model that suggests mineralized metamudstones experienced an increased hydrothermal fluid flux relative to barren counterparts (i.e., heterogeneous infiltration). Therefore, we might assume that the C<sub>4</sub> HC signatures preserved in metamudstones do not reflect equilibrium compositions as a result of yet unidentified catalytic or kinetic influences. However, since GC is an inherently bulk fluid analysis, multiple inputs of HC from separate reservoirs (e.g., abiogenic HCs of magmatic origin versus thermogenic HCs

from pyrolysis of carbonaceous matter) may be present and thus broader interpretations are circumstantial without supporting lines of evidence (e.g., compound-specific isotopic analysis).

#### **4.6.4 Implications for disseminated gold mineralization and exploration**

The absence of conspicuous quartz veining and the presence of carbonate alteration halos associated with the disseminated gold mineralization at the Touquoy deposit implies that the ore fluids precipitated Au and carbonate in vein-poor rocks rather than silica during gold deposition (Smith and Kontak, 1986; Ryan and Smith, 1998; Bierlein and Smith, 2003; Bierlein et al., 2004; Staples et al., 2018). Also, evidence for the late precipitation of carbonate and the retrograde solubility of quartz was suggested at the nearby Dufferin gold deposit (Ch.3 of this thesis). Thus, during the ingress of the H<sub>2</sub>O-CO<sub>2</sub> ore fluid, appreciable CO<sub>2</sub> may have been lost through interaction with reducing lithologies and subsequent reduction/respeciation (see reaction 1 above), and/or through carbonate precipitation. These processes affect fluid CO<sub>2</sub> concentrations, in particular fluid pH and bisulfide solubility leading to the destabilization gold bisulfide complexes and Au precipitation (Naden and Shepard, 1989; Phillips and Evans, 2004; Williams-Jones et al., 2009). However, the detection of CO<sub>2</sub> via GC in metamudstones from the mineralized setting suggests that some CO<sub>2</sub> was trapped as a volatile phase within host rocks as fluid inclusions in clasts, porphyroblasts, along grain boundaries, or in pore spaces in metamudstones. The abundance of CO<sub>2</sub>-bearing (e.g., Fig. 6A) and CH<sub>4</sub>+N<sub>2</sub>-bearing (e.g., Fig. 6D) type 1 and 2 secondary fluid inclusions with variable volatile compositions (Fig. 8; Table EA 4-1) in quartz veinlets adjacent to metamudstone contacts may suggest fluid mixing. Auriferous fluids from deeper crustal levels may have migrated along mechanical anisotropies including bedding and foliation, or through fault planes, pooling beneath less permeable lithologies (e.g., Touquoy argillite) in anticlinal structures

such as the MRA (e.g., North Brookfield gold district: Smith et al., 1994). Subsequent fluid infiltration into reactive host rocks proximal to fluid conduits (e.g., stockworks) is likely facilitated by the generation of secondary permeability via hydrothermal alteration reactions (Schwartz, 1959). In these settings, the mixing of CO<sub>2</sub>-rich (i.e., oxidized) ore fluids with reducing fluids or reducing wall rocks themselves has been suggested as a viable gold precipitating mechanism (Matthäi et al., 1995; Walshe et al., 2003; Neumayr et al., 2007; Kendrick et al., 2011; Kontak et al., 2018). However, this conclusion requires additional study to confirm.

Gold concentration in the metamudstone does not directly correlate with bulk CO<sub>2</sub> abundance. Rather, elevated CO<sub>2</sub> abundances broadly correspond to the economically mineralized Touquoy zone (i.e., ~0.5 – 5 g/t) and its carbonate alteration halo. The variability of CO<sub>2</sub> abundance within mineralized zones may result from lower volumes of trapped volatiles (i.e., <LOD) in the rock resulting from natural variability in pore space volume, porphyroblast abundance and/or fluid inclusions preservation along grain boundaries. Alternatively, this variability may reflect the heterogeneity of ore fluid infiltration into host rocks adjacent to fluid conduits (e.g., veins). However, the sampling resolution of this study is insufficient to conclusively determine the origin of bulk CO<sub>2</sub> variability in mineralized zones and will require additional study. The fact that elevated CO<sub>2</sub> concentrations are present in some lower grade samples (<0.5 g/t; n = 7) and absent in certain higher-grade samples (~1.75 – 4 g/t; n = 2) suggests that a GC technique may have the potential to identify significantly mineralization zones of metamudstone despite modest Au concentrations determined by whole rock assay.

#### **4.6.5 Methodological refinements and future work**

Preliminary evaluation of a bulk fluid GC-based technique for disseminated gold exploration in the Meguma terrane of Nova Scotia suggests it may be potentially informative and applied to exploration programs as a supplement to other vectoring tools. However, several follow-up studies are suggested in order to refine the technique and better address issues regarding the generation and origin of fluids present, which include:

- 1) Further analyses of material from ongoing reverse circulation (RC) and diamond drilling operations at the Touquoy deposit and other gold mineralized sites in the MRA (e.g., Beaver Dam, Fifteen Mile Stream) to improve the current data base;
- 2) Access to strategic, spatially-resolved drill core samples within single deposits. For example, drill holes intersecting high-grade versus low-grade metamudstone intervals spatially related to significant structures at the Touquoy and Fifteen Mile Stream deposits (Staples et al., 2018) may help clarify fluid flux systematics that may have mineralized high-grade disseminated gold intercepts in certain metamudstone sequences over others in singular deposit settings;
- 3) Minor differences between C<sub>3</sub> and C<sub>4</sub> HC ratios (Fig. 11C, D) that are statistically anomalous (i.e.,  $0.03 \leq p\text{-value} \leq 0.05$ ) warrant additional investigation into HC systematics in hydrothermal systems;
- 4) Compound-specific isotopic analysis of CO<sub>2</sub> and CH<sub>4</sub>, along with microthermometric analysis, may help clarify the source(s) of vein-hosted and pressure-shadow hosted fluids. These findings may confirm (or refute) fluid mixing as a causative factor for gold mineralization within the MRA.

Additionally, for an analytical method such as that discussed herein to be attractive to industry as a viable exploration criterion several instrumental/methodological modifications are suggested.

Ideally, an inexpensive carrier gas such as N<sub>2</sub> (or air) would be used rather than He. Analytical capillary columns specifically selected to provide maximum resolution between CH<sub>4</sub> and CO<sub>2</sub> peaks, and more sensitive detection capabilities (e.g., photoionization detector [PID] over FID for conjugated and aromatic HC species) are recommended. Also, to allow more rapid throughput of samples, a high-leverage, hand-driven rock-crusher would be less cumbersome and easier to clean compared to traditional, hydraulically-driven rock crushing systems (i.e., this study).

#### **4.7 Conclusions**

This initial study represents the only reported bulk volatile signatures in metamudstone-hosted disseminated gold systems, to the best of our knowledge, in the Meguma terrane of Nova Scotia or globally. This study makes use of an underutilized gas chromatographic technique that boasts low limits of detection (e.g., 10<sup>-12</sup> to 10<sup>-13</sup> mol/g crushed) and good reproducibility. Furthermore, this technique has been shown to be a potentially effective exploration tool in ore systems elsewhere (e.g., massive sulfide deposits; Kerr et al., 2015). In order to determine if a bulk volatile GC technique can make an effective supplement to current exploration programs, attention was focussed on an appropriate sampling strategy and minimal sample preparation (i.e., see Methodology section).

Although additional work is needed to test some of the conclusions and further evaluate the method, some important conclusions are identified:

- CO<sub>2</sub>-bearing fluid inclusions were only identified in vein quartz. CO<sub>2</sub> is entirely absent in fluid inclusions in pressure-shadow quartz, which are instead dominated by N<sub>2</sub>±CH<sub>4</sub>. The latter

fluids are interpreted to represent metamorphic or highly-modified meteoric fluids that have equilibrated with reducing wall rocks.

- $\text{N}_2\pm\text{CH}_4$ -bearing and  $\text{CO}_2$ -bearing fluids with variable volatile compositions are present in secondary inclusion trails in quartz veinlets crosscutting metamudstones and may suggest fluid mixing between aqueous-carbonic ore fluids and reducing wall rock-equilibrated fluids.
- $\text{CO}_2$  was detected in ~50% of analyzed (i.e., crushed) metamudstones from the Au-mineralized Touquoy deposit compared to ~4% of metamudstones from surrounding Au-barren regions and results in a statistically significant p-value of 0.0103 between populations. This suggests that auriferous hydrothermal fluids did not equally permeate all regions of the study area (i.e., the MRA) equally and thus economic concentrations of Au are localized to regions where favorable structural characteristics (e.g., fault systems, stockworking) resulting in increased fluid fluxes allowed fluids to infiltrate and react with appropriate rocks.
- Volatile hydrocarbon compositional fields display significant overlap between populations. However, statistically anomalous differences in  $\text{C}_3$  and  $\text{C}_4$  hydrocarbon compositions between metamudstone populations warrants further investigation.

Although preliminary in nature, these results may help to elucidate details related to fluid flux and ore genesis in metasedimentary-hosted disseminated gold deposits. Future refinement may yield a viable geochemical tool for vectoring toward mineralized units within the Meguma terrane, and potentially analogous systems elsewhere.

#### **4.8 References**

Anderson, R.B., (1984). The Fischer-Tropsch synthesis: Orlando, Academic Press, Inc., 620 p.

- Barker, S. L., Dipple, G. M., Hickey, K. A., Lepore, W. A., and Vaughan, J. R. (2013). Applying stable isotopes to mineral exploration: Teaching an old dog new tricks. *Economic Geology* 108(1), 1-9.
- Beeskow, B., Rankin, A.H., Murphy, P.J., and Treloar, P. J. (2005). Mixed CH<sub>4</sub>-CO<sub>2</sub> fluid inclusions in quartz from the South Wales Coalfield as suitable natural calibration standards for microthermometry and Raman spectroscopy. *Chemical Geology* 223, 3-15.
- Benn, K., Horne, R.J., Kontak, D.J., Pignotta, G. and Evans, N.G. (1997). Syntectonic emplacement of the South Mountain Batholith, Meguma Terrane, Nova Scotia: magnetic fabric and structural analyses. *Bulletin Geological Society of America* 109, 1279-1293.
- Bierlein, F.P., Arne, D.C., McKnight, S., Lu, J., Reeves, S., Besanko, J., Marek, J. and Cooke, D. (2000). Wall-rock petrology and geochemistry in alteration halos associated with mesothermal gold mineralization, central Victoria, Australia. *Economic Geology* 95(2), 283-311.
- Bierlein, F.P., Gray, D.R., and Foster, D.A. (2002). Metallogenic relationships to tectonic evolution—the Lachlan Orogen, Australia. *Earth and Planetary Science Letters* 202(1), 1-13.
- Bierlein, F.P., and Maher, S. (2001). Orogenic disseminated gold in Phanerozoic fold belts — examples from Victoria, Australia, and elsewhere. *Ore Geology Reviews* 18: 113–148.
- Bierlein, F.P., and Smith, P.K. (2003). The Touquoy Zone deposit: an example of “unusual” orogenic gold mineralisation in the Meguma Terrane, Nova Scotia, Canada. *Canadian Journal of Earth Sciences* 40(3), 447-466.

- Bodnar, R.J., Lecumberri-Sanchez, P., Moncada, D. and Steele-MacInnis, M. (2014). Fluid inclusions in hydrothermal ore deposits. In, Reference Module in Earth Systems and Environmental Sciences Treatise on Geochemistry (Second Edition), pp. 119–142.
- Burke, E.A. (2001). Raman microspectrometry of fluid inclusions. *Lithos* 55, 139–158.
- Chen, S.S., Wilhoit, R.C., and Zwolinski, B.J. (1975). Ideals gas thermodynamic properties and isomerization of n-butane and isobutane. *Journal of Physical and Chemical Reference Data* 4(4), 859-870.
- Chen, J., Xu, Y., and Huang, D., (2000). Geochemical characteristics and origin of natural gas in Tarim Basin, China: *American Association of Petroleum Geologists Bulletin* 84, 591–606.
- Clarke, D.B., MacDonald, M.A., and Tate, M.C., (1997). Late Devonian mafic-felsic magmatism in the Meguma zone, Nova Scotia, *in* Sinha, A.K., Whalen, J.F., and Hogan, J.P., eds., *The Nature of Magmatism in the Appalachian Orogen: Geological Society of America Memoir* 191, p. 107–127.
- Craw, D. (2002). Geochemistry of late metamorphic hydrothermal alteration and graphitization of host rock, Macraes gold mine, Otago Schist, New Zealand. *Chemical Geology* 191, 257–275.
- Craw, D., Teagle, D. A. H., and Belocky, R. (1993). Fluid immiscibility in late-Alpine gold-bearing veins, Eastern and Northwestern European Alps. *Mineralium Deposita* 28(1), 28–36.
- Darling, W.G., Greisshaber, E., Andrews, J.N., Armannson, H., and O’Nions, R.K. (1995). The origin of hydrothermal and other gases in the Kenyan Rift Valley. *Geochimica et Cosmochimica Acta* 59(12), 2501-2512.

- De Souza, S., Dubé, B., McNicoll, V., Dupuis, C., Mercier-Langevin, P., Creaser, R.A., and Kjarsgaard, I. (2017). Geology and hydrothermal alteration of the world-class Canadian Malartic gold deposit: Genesis of an Archean stockwork-disseminated gold deposit in the Abitibi greenstone belt: *Reviews in Economic Geology* 19, 263–291.
- Dinel, E., Fowler, A.D., Ayer, J., Still, A., Tylee, K., and Barr, E. (2008). Lithogeochemical and stratigraphic controls on gold mineralization within the metavolcanic rocks of the Hoyle Pond Mine, Timmins, Ontario. *Economic Geology* 103(6), 1341-1363.
- Dubé, B., and Gosselin, P. (2007). Greenstone-hosted quartz-carbonate vein deposits, In, Goodfellow, W.D. (ed.), *Mineral Deposits of Canada: A Synthesis of Major Deposit-Types, District Metallogeny, the Evolution of Geological Provinces, and Exploration Methods*: Geological Association of Canada, Mineral Deposits Division, Special Publication No. 5, 49-73.
- Dubessy, J., Poty, B., and Ramboz, C. (1989). Advances in C-O-H-N-S fluid geochemistry based on micro-Raman spectrometric analysis of fluid inclusions. *European Journal of Mineralogy* 1, 517 - 534.
- Everlien, G. (1990). Das Verhalten des in Mineralen enthaltenen Stickstoffs während der Diagenese und Metamorphose von Sedimenten. Doktorarbeit TUBraunschweig. 154 pp., Braunschweig.
- Fall, A., Tattitch, B., and Bodnar, R. J. (2011). Combined microthermometric and Raman spectroscopic technique to determine the salinity of H<sub>2</sub>O–CO<sub>2</sub>–NaCl fluid inclusions based on clathrate melting. *Geochimica et Cosmochimica Acta* 75(4), 951-964.

- Glasmacher, U.A., Zentilli, M., and Ryan, R. (2003). Nitrogen distribution in Lower Palaeozoic slates/phyllites of the Meguma Supergroup, Nova Scotia, Canada: implications for Au and Zn Pb mineralisation and exploration. *Chemical Geology* 194(4), 297-329.
- Goldfarb, R.J., Baker, T., Dubé, B., Groves, D.I., Hart, C.J.R., and Gosselin, P. (2005). Distribution, character, and genesis of gold deposits in metamorphic terranes. *Economic Geology* 100th Anniversary Volume, p. 407-450.
- Graves, M., Horne, R., Banks, C., Pelley, D., and Sherry, A. (2011). Assessment Report: Exploration Licenses SL11/90 & 06134 Report on Diamond Drilling, Fifteen Mile Stream Property, Halifax County, Nova Scotia. Acadian Mining Corporation. File AR2012-004.
- Gunter, B.D., and Musgrave, B.C. (1971) New evidence on the origin of methane in hydrothermal gases. *Geochim. Cosmochim. Acta* 35, 113-118.
- Hagemann, S.G. and Cassidy, K.F. (2000). Archean orogenic lode gold deposits. *Society of Economic Geology Review* 13, 9-68.
- Herron, C.S. (2014). Mapping the carbonate alteration footprint of the Cortez Hills Carlin-type gold deposit, Nevada using carbon-oxygen isotopes, and geochemistry as a vectoring tool. Unpublished M.Sc. thesis, Vancouver, British Columbia, University of British Columbia, 514 p.
- Hicks, R.J., Jamieson, R.A. and Reynolds, P.H. (1999): Detrital and metamorphic  $^{40}\text{Ar}/^{39}\text{Ar}$  ages from muscovite and whole-rock samples, Meguma Supergroup, southern Nova Scotia; *Canadian Journal of Earth Sciences* 36, 23-32.
- Holloway, J.R. (1984). Graphite- $\text{CH}_4$ - $\text{H}_2\text{O}$ - $\text{CO}_2$  equilibria at low grade metamorphic conditions. *Geology* 12, 455-458.

- Horne, R.J. and Culshaw, N. (2001). Flexural-slip folding in the Meguma Group, Nova Scotia, Canada. *Journal of Structural Geology* 23, 1631-1652.
- Horne, R.J. and Pelley, D.E. (2007). Geological Transect of the Meguma Terrane from Centre Musquodoboit to Tangier. *In* Mineral Resources Branch, Report of Activities 2006. Nova Scotia Department of Natural Resources Report ME 2007-01, p. 71-89.
- Hudgins, A.B. (1989). Report on Geological Resource Estimates and Bulk Sample Results, Touquoy Project, Moose River, Halifax County, Nova Scotia. Seabright Explorations Inc. NTS: 11D15C. December 1989.
- Hudgins, A.B. (1997). Report on Work Performed, License 00313, Moose River Project. Moose River Resources Inc. AR97-087. August 1997.
- Huizenga, J.M. (2001). Thermodynamic modelling of C-O-H fluids. *Lithos* 55, 101-114.
- Itihara, Y., Honma, H., (1983). Content and origin of ammonium in biotites of granitic and metamorphic rocks. *In*, Augustithis, S.S. (ed.), *The Significance of Trace Elements in solving petrogenetic problems and controversies*. Theophrastus Publications, Athens, pp. 431– 444.
- Jurisch, S.A., Heim, S., Krooss, B.M., and Littke, R. (2012). Systematics of pyrolytic gas (N<sub>2</sub>, CH<sub>4</sub>) liberation from sedimentary rocks: Contribution of organic and inorganic rock constituents. *International Journal of Coal Geology* 89, 95-107.
- Kawka, O. E., and Simoneit, B. R. (1994). Hydrothermal pyrolysis of organic matter in Guaymas Basin: I. Comparison of hydrocarbon distributions in subsurface sediments and seabed petroleum. *Organic Geochemistry* 22(6), 947-978.

- Kendrick, M.A., Honda, M., Walshe, J., Petersen, K., (2011). Fluid sources and the role of abiogenic-CH<sub>4</sub> in Archean gold mineralization: constraints from noble gases and halogens. *Precambrian Research* 189, 313–327.
- Keppie, J.D., and Dallmeyer, R.D. (1987). Dating transcurrent terrane accretion: an example from the Meguma and Avalon composite terranes in the northern Appalachians. *Tectonics* 6(6), 831-847.
- Keppie, J.D., and Muecke, G.K. (Compilers). (1979). *Metamorphic map of Nova Scotia*. Scale 1:500 000. Nova Scotia Department of Mines and Energy.
- Kerr, M.J. (2013). *The application of gas chromatography in characterizing bulk fluid inclusion hydrocarbons in the footwall of the Sudbury Igneous Complex and other magmatic, hydrothermal and surficial ore-forming environments: Unpublished M.Sc. thesis*, Halifax, Canada, Saint Mary's University, 241 p.
- Kerr, M.J, Hanley, J.J, Morrison, G., Everest, J., and Bray, C.J. (2015). Preliminary Evaluation of Trace Hydrocarbon Speciation and Abundance as an Exploration Tool for Footwall-Style Sulfide Ores Associated with the Sudbury Igneous Complex, Ontario, Canada. *Economic Geology* 110(2), 531-556.
- King, M.S. and Webster, P.C. (1997). Report of Work, First Year Assessment, RJZ Mining Inc., Meguma Gold Project, Eastern Shore Claim Group. Mercator Geological Services Limited. AR97-118. November 1997.
- Konnerup-Madsen, J., Larsen, E., and Rose-Hansen, J. (1979). Hydrocarbon rich inclusions in minerals from the alkaline Ilimaussaq intrusion, South Greenland: *Bulletin de Minéralogie*, v. 102, p. 642–653.

- Kontak, D.J., and Horne, R.J. (2010). A multi-stage origin for the Meguma lode gold deposits, Nova Scotia, Canada: a possible global model for slate belt-hosted gold mineralization. *Gold metallogeny: India and beyond*. Alpha Science International Ltd., Oxford, 58-82.
- Kontak, D.J., Horne, R.J., Creaser, R.A., Petrus, J.A., and Archibald, D. (2013). A petrological and geochronological study of a 360 Ma metallogenic event in Maritime Canada with implications for lithophile-metal mineralization in the Canadian Appalachians. *Canadian Journal of Earth Sciences* 50(11), 1147-1163.
- Kontak, D.J., Horne, R.J., Sandeman, H., Archibald, D., and Lee, J.K. (1998).  $^{40}\text{Ar}/^{39}\text{Ar}$  dating of ribbon-textured veins and wall-rock material from Meguma lode gold deposits, Nova Scotia: implications for timing and duration of vein formation in slate-belt hosted vein gold deposits. *Canadian Journal of Earth Sciences* 35(7), 746-761.
- Kontak, D.J., Horne, R.J., Smith, P.K., & Archibald, D.A. (2001).  $^{40}\text{Ar}/^{39}\text{Ar}$  dating of hydrothermal biotite associated with high-grade gold mineralization in the Whin Vein, Tangier gold deposit (NTS 11D/15), southern Nova Scotia. Report of Activities for 2000, Nova Scotia Department of Natural Resources, Report 2001-1, Edited by D.R. MacDonald, p. 29-36.
- Kontak, D.J., and Kerrich, R. (1995). Geological and geochemical studies of a metaturbidite-hosted lode gold deposit; the Beaver Dam Deposit, Nova Scotia; II, Isotopic studies. *Economic Geology* 90(4), 885-901.
- Kontak, D.J., and Smith, P.K. (1989a). Fluid inclusion study of quartz vein polytypes in the Beaver Dam gold deposit, Meguma Terrane, Nova Scotia, Canada, in PACROFIII: Biennial Pan-American Conference on Research on Fluid Inclusions, 2nd, Blacksburg, Virginia, Program and Abstracts, p. 38.

- Kontak, D.J., and Smith, P.K. (1989b). Fluid inclusion studies of quartz vein polytypes from the Beaver Dam and Caribou gold deposits, Meguma Zone, Nova Scotia: Evidence for a single vein-forming event: Atlantic Geoscience Society Colloquium '89, Amherst, Nova Scotia, Abstracts with Program.
- Kontak, D.J., and Smith, P.K. (1993). A metaturbidite-hosted lode gold deposit; the Beaver Dam Deposit, Nova Scotia; I, Vein paragenesis and mineral chemistry. *The Canadian Mineralogist* 31(2), 471-522.
- Kontak, D.J., Smith, P.K., Kerrich, R., and Williams, P.F. (1990). Integrated model for Meguma Group lode gold deposits, Nova Scotia, Canada. *Geology* 18(3), 238-242.
- Kontak, D.J., Smith, P.K., and Kerrich, R. (1991). A mineralogic, isotopic and fluid inclusion study of the Beaver Dam gold deposit, southern Nova Scotia: A metaturbidite-hosted lode gold deposit of 370 Ma age. *Geologic Association of Canada-Mineralogical Association of Canada Program with Abstracts*, 16, A67.
- Kontak, D.J., Smith, P.K., and Reynolds, P.H. (1993). *Geology and  $^{40}\text{Ar}/^{39}\text{Ar}$  geochronology of the Beaver Dam gold deposit, Meguma Terrane, Nova Scotia, Canada; evidence for mineralization at 370 Ma.* *Economic Geology* 88(1), 139-170.
- Kontak, D.J., and Tuba, G. (2017). How can fluid inclusion studies better constrain orogenic gold deposit models: case studies from the Superior Province and Meguma terrane, Canada. In, Mercier-Langevin, P., et al. (eds.), *Proceedings of the 14<sup>th</sup> Biennial SGA Meeting, Quebec, Canada, Volume 1.*
- Liu, J., Zheng, M., Liu, J.M., Su, W. (2000). Geochemistry of the La'erma and Qiongmo Au–Se deposits in the western Qinling Mountains, China. *Ore Geology Reviews* 17, 91–111.

- Loucks, R.R. and Mavrogenes, J.A. (1999). Gold Solubility in Supercritical Hydrothermal Brines Measured in Synthetic Fluid Inclusions. *Science* 284(5423), 2159-2163.
- Ma, Y., and Li, S. (2018). The mechanism and kinetics of oil shale pyrolysis in the presence of water. *Carbon Resources Conversion* 1(2), 160-164.
- Malcolm, W. (1929). *Gold Fields of Nova Scotia*. Geological Survey of Canada, Memoir 156, 253 p.
- Matthäi, S.K., Henley, R.W., and Heinrich, C.A. (1995). Gold precipitation by fluid mixing in bedding-parallel fractures near carbonaceous slates at the Cosmopolitan Howley gold deposit, northern Australia. *Economic Geology* 90(8), 2123-2142.
- Mawer, C.K. (1987). Mechanics of formation of gold-bearing quartz veins, Nova Scotia, Canada. *Tectonophysics* 135(1-3), 99-119.
- Mersereau, T.G. (1987). Report on a Diamond Drilling Programme Beaverdam Property, Portions of Tracts 60, 61, 62, 83, 84, Beaverdam Area, Nova Scotia. File 87 275.
- Miller, C., Reeves, J. and Conrod, D. (1989). An Assessment Report of Work Performed Within Exploration License 14740 [Otter Lake]. Scotia Prime Resources Inc. AR89-084. March 1989.
- Montoya, D.E., Noble, D.C., Eyzaguirre, V.R., DesRosiers, D.F. (1995). Sandstone-hosted gold deposits—a new exploration target is recognized in Peru. *Exploration and Mining Journal* 110, 41–43.
- Muecke, G.K., Elias, P., and Reynolds, P.H. (1988). Hercynian/Alleghanian overprinting of an acadian terrane:  $^{40}\text{Ar}/^{39}\text{Ar}$  studies in the Meguma zone, Nova Scotia, Canada. *Chemical Geology: Isotope Geoscience Section* 73(2), 153–167.

- Murphy, J. B., Waldron, J. W., Kontak, D. J., Pe-Piper, G., and Piper, D. J. (2011). Minas Fault Zone: Late Paleozoic history of an intra-continental orogenic transform fault in the Canadian Appalachians. *Journal of Structural Geology* 33(3), 312-328.
- Naden, J., and Shephard, T.J. (1989). Role of methane and carbon dioxide in gold deposition: *Nature* 342, 793–795.
- Neumayr, P., Walshe, J., Hagemann, S., Petersen, K., Roache, A., Frikken, P., Horn, L., Halley, S. (2007). Oxidized and reduced mineral assemblages in greenstone belt rocks of the St. Ives gold camp, Western Australia—vectors to high-grade ore bodies in Archean gold deposits. *Mineralium Deposita* 43, 363–371.
- Neuzil, C.E. (1994). How permeable are clays and shales? *Water Resources Research* 30(2), 145-150.
- Olivo, G.R., and Williams-Jones, A.E. (2002). Genesis of the auriferous C quartz-tourmaline vein of the Siscoe mine, Val d’Or district, Abitibi subprovince, Canada: structural, mineralogical and fluid inclusion constraints. *Economic Geology* 97(5), 929-947.
- Petersilie, I.A., and Sørensen, H., (1970). Hydrocarbon gases and bituminous substances in rocks from the Illimaussaq alkaline intrusion, South Greenland: *Lithos* 3, 59–76.
- Phillips, G.N., and Evans, K.A. (2004). Role of CO<sub>2</sub> in the formation of gold deposits. *Nature*, 429(6994), 860.
- Pitcairn I.K., Teagle D.A., Craw D., Olivo G. R., Kerrich R. and Brewer T.S. (2006). Sources of metals and fluids in orogenic gold deposits: insights from the Otago and Alpine Schists, New Zealand. *Economic Geology* 101(8), 1525–1546.

- Potter, J., Rankin, A.H. and Treloar, P.J. (2004). Abiogenic Fischer-Tropsch synthesis of hydrocarbons in alkaline igneous rocks; fluid inclusion, textural and isotopic evidence from the Lovozero Complex, N.W. Russia: *Lithos* 75, 311–330.
- Potter, J. and Konnerup-Madsen, J. (2003) A review of the occurrence and origin of abiogenic hydrocarbons in igneous rocks: Geological Society of London, Special Publications 214, p.151–173.
- Radtke, A.S., and Scheiner, B.J. (1970). Studies of Hydrothermal Gold Deposition (I). Carlin Gold Deposit, Nevada: The Role of Carbonaceous Materials in Gold Deposition. *Economic Geology* 65, 87-102.
- Ramsay, J.G. (1980), The crack-seal mechanism of rock deformation. *Nature* 284, 135-139.
- Reynolds, P.H., and Muecke, G.K. (1978). Age studies on slates: Applicability of the  $^{40}\text{Ar}/^{39}\text{Ar}$  stepwise outgassing method. *Earth and Planetary Science Letters* 40(1), 111-118.
- Ridley, J.B., and Diamond, L.W. (2000). Fluid chemistry of orogenic lode gold deposits and implications for genetic models. *Society of Economic Geologists Review* 13, 141-162.
- Robert, F., Brommecker, R., Bourne, B.T., Dobak, P.J., McEwan, C.J., Rowe, R.R., and Zhou, X. (2007). Models and Exploration Methods for Major Gold Deposit Types, in Milkereit, B., ed., *Ore Deposits and Exploration Technology: Proceedings of Exploration 07, Fifth Decennial International Conference on Mineral Exploration*, p.691-711.
- Rosso, K.M. and Bodnar, R.J. (1995). Microthermometric and Raman spectroscopic detection limits of  $\text{CO}_2$  in fluid inclusions and the Raman spectroscopic characterization of  $\text{CO}_2$ . *Geochimica et Cosmochimica Acta* 59, 3961–3975.
- Ryan, R.J., and Smith, P.K. (1998). A review of the mesothermal gold deposits of the Meguma Group, Nova Scotia, Canada. *Ore Geology Reviews* 13, 153-183.

- Salvi, S., and Williams-Jones, A.E. (1997a). Fluid-inclusion volatile analysis by gas chromatography: Application of a wide-bore porous-polymer capillary column to the separation of organic and inorganic compounds. *Canadian Mineralogist* 35, 1391–1414.
- Salvi, S., and Williams-Jones, A.E. (1997b). Fischer-Tropsch synthesis of hydrocarbons during sub-solidus alteration of the Strange Lake peralkaline granite, Quebec/Labrador, Canada. *Geochimica et Cosmochimica Acta* 61, 83–99.
- Sakata, S., Sano, Y., Maekawa, T., and Igari, S.I. (1997). Hydrogen and carbon isotopic composition of methane as evidence for biogenic origin of natural gases from the Green Tuff Basin, Japan. *Organic Geochemistry* 26, 399–407.
- Sangster, A.L. (1981). Report on 1981 Drilling Wire Lake, N.S, Project 1229 – Licenses 3628, 4979. Sulpetro Minerals Ltd. 434429. October 1981.
- Sangster, A.L. (1990). Metallogeny of the Meguma Terrane, Nova Scotia. In, Sangster, A.L. (ed.), *Mineral Deposits Studies in Nova Scotia*, vol. 1. Geological Survey of Canada, Paper 90-8, 115–162.
- Sangster, A.L. (1992). Light stable isotope evidence for a metamorphogenic origin for bedding-parallel, gold-bearing veins in the Cambrian flysch, Meguma Group, Nova Scotia. *Exploration and Mining Geology* 1, 69–79.
- Sangster, A.L., and Smith, P.K. (2007). Metallogenic summary of the Meguma gold deposits, Nova Scotia, in Goodfellow, W.D., (ed.), *Mineral Deposits of Canada: A Synthesis of Major Deposit-Types, District Metallogeny, the Evolution of Geological Provinces, and Exploration Methods*: Geological Association of Canada, Mineral Deposits Division, Special Publication No. 5, 723-732.
- Schoell, M. (1983). Genetic characterization of natural gases. *AAPG bulletin* 67(12), 2225-2238.

- Schoell, M. (1988). Multiple origins of methane in the Earth. *Chemical Geology* 71(1-3), 1-10.
- Schwartz, G.M. (1959). Hydrothermal alteration. *Economic Geology* 54(2), 161-183.
- Sherwood Lollar, B., Frapre, S.K., Weise, S.M., Fritz, P., Macko, S.A., and Welhan, J.A. (1993).  
Abiogenic methanogenesis in crystalline rocks. *Geochimica et Cosmochimica Acta* 57,  
5087–5097.
- Sherwood Lollar, B., Lacrampe-Couloume, G., Slater, G.F., Ward, J., Moser, D.P., Gihring,  
T.M., Lin, L.-H., and Onstott, T.C. (2006). Unravelling abiogenic and biogenic sources  
of methane in the Earth's deep subsurface. *Chemical Geology* 226, 328–339.
- Sherwood Lollar, B., Lacrampe-Couloume, G., Voglesonger, K., Onstott, T.C., Pratt, L.M., and  
Slater, G.F. (2008) Isotopic signatures of CH<sub>4</sub> and higher hydrocarbons gases from  
Precambrian Shield sites: A model for abiogenic polymerization of hydrocarbons.  
*Geochimica et Cosmochimica Acta* 72, 4778–4795.
- Sibson, R., Robert, F., and Poulsen, K.H. (1988). High-angle reverse faults, fluid-pressure  
cycling, and mesothermal gold-quartz deposits. *Geology* 16(6), 551-555.
- Schoell, M. (1983). Genetic characterization of natural gases. *AAPG Bulletin* 67(12), 2225-  
2238.
- Schoell, M. (1988). Multiple origins of methane in the earth. *Chemical Geology* 71(1-3), 1-10.
- Smith, P.K. and Kontak, D.J. (1987). Alteration haloes and their implications for gold  
mineralization in the Meguma Group of Nova Scotia, In, *Gold Potential of Nova Scotia,*  
*Selected Papers, Open File Report 95-007.*
- Smith, P.K, Chatterjee, A.K., and Rogers, P.J. (1994). Electrum and intermetallic compounds: A  
new style of stratabound Meguma gold and its implications for bulk mining in Nova

- Scotia, Canada. In, Nova Scotia Department of Natural Resources, Minerals and Energy Branch. Gold Potential of Nova Scotia, Selected Papers 1995.
- Staples, L.P., Schofield, N., Schulte, M., Meintjes, T., Millard, J., Parks, J., and Fontaine, D. (2018) Moose River Consolidated Project, Nova Scotia, Canada. NI 43-101 Technical Report on Moose River Consolidated Phase 1 and Phase 2 Expansion.
- Taran, Y.A., Kliger, G.A., and Sevastianov, V.S. (2007). Carbon isotope effects in the open-system Fischer-Tropsch synthesis. *Geochimica et Cosmochimica Acta* 71, 4474–4487.
- Van Staal, C.R. (2007). Pre-Carboniferous tectonic evolution and metallogeny of the Canadian Appalachians. In Goodfellow, W.D. (ed) *Mineral deposits of Canada: a synthesis of major deposit-types, district metallogeny, the evolution of geological provinces, and exploration methods*. Geological Association of Canada, Mineral Deposits Division, Special Publication 5, p. 793-818.
- Voytov, G.I. (1992). Chemical and carbon-isotope fluctuations in free gases (gas jets) in the Khibiny. *Geochemistry International* 29(1-3), 14.
- Waldron, J.W.F. and Jensen, L.R. (1985). *Sedimentology of the Goldenville Formation, Eastern Shore, Nova Scotia*; Geological Survey of Canada, Paper 85-15.
- Walshe, J.L., Halley, S.W., Hall, G.A., Kitto, P. (2003). Contrasting fluid systems, chemical gradients and controls on large-tonnage, high-grade Au deposits, Eastern Goldfields Province, Yilgarn Craton, Western Australia. In, *Mineral Exploration and Sustainable Development*. 7th Biennial SGA Meeting, Athens, pp. 827–830.
- Wang, X., Chou, I. M., Hu, W., Burruss, R. C., Sun, Q., and Song, Y. (2011). Raman spectroscopic measurements of CO<sub>2</sub> density: Experimental calibration with high-pressure

- optical cell (HPOC) and fused silica capillary capsule (FSCC) with application to fluid inclusion observations. *Geochimica et Cosmochimica Acta* 75(14), 4080-4093.
- Webster, P.C. (1998). Second Year Assessment Report, Exploration License 02512. Report for RJZ Mining Inc by Mercator Geological Services Limited. File AR98-104. September 1998.
- Welhan, J.A., and Lupton, J.E. (1987). Light hydrocarbon gases in Guaymas Basin hydrothermal fluids: Thermogenic versus abiogenic origin. *AAPG Bulletin* 71(2), 215-223.
- White, C.E., and Barr, S.M. (2012). Meguma Terrane Revisited: Stratigraphy, Metamorphism, Paleontology, and Provenance: *Journal of the Geological Society of Canada*, Volume 39, Number 1 (2012); GAC-MAC 2012 St. John's post-meeting field trip
- White, C.E., Barr, S.M., and Linnemann, U. (2018). U–Pb (zircon) ages and provenance of the White Rock Formation of the Rockville Notch Group, Meguma terrane, Nova Scotia, Canada: evidence for the “Sardian gap” and West African origin. *Canadian Journal of Earth Sciences* 55(6), 589-603.
- White, C.E., Horne, R.J., and Barr, S.M. (2007). The Meguma Group of southern Nova Scotia: new insights on the stratigraphy, tectonic setting, and provenance. In, *Programs and abstracts: Atlantic Geoscience Society Colloquium and Annual General Meeting*.
- White, C.E., Palacios, T., Jensen, S., and Barr, S.M. (2012). Cambrian–Ordovician acritarchs in the Meguma terrane, Nova Scotia, Canada: Resolution of early Paleozoic stratigraphy and implications for paleogeography. *GSA Bulletin* 124(11-12), 1773-1792.
- Williams-Jones, A.E., Howell, R.J., and Migdisov, A.A. (2009). Gold in Solution. *Elements* 5, 281-287.

- Wood, C.P. (1996). Basement geology and structure of TVZ geothermal fields, New Zealand. In Proceedings of the 18th New Zealand Geothermal Workshop. Edited by S.F. Simmons, M.M. Rahman, and A. Watson. Geothermal Institute, The University of Auckland, Auckland, New Zealand, pp. 157–162.
- Wopenka, B., and Pasteris, J. D. (1986). Limitations to quantitative analysis of fluid inclusions in geological samples by laser Raman microprobe spectroscopy. *Applied Spectroscopy* 24, 144–151.
- Wopenka, B., and Pasteris, J.D. (1987). Raman intensities and detection limits of geochemically relevant gas mixtures for a laser Raman microprobe. *Analytical Chemistry* 59, 2165-2170.
- Yamamoto, J., and Kagi, H. (2006). Extended micro-Raman densimeter for CO<sub>2</sub> applicable to mantle-originated fluid inclusions. *Chemistry Letters* 35(6), 610-611
- Yamamoto, J., Kagi, H., Kaneoka, I., Lai, Y., Prikhod'ko, V. S., and Arai, S. (2002). Fossil pressures of fluid inclusions in mantle xenoliths exhibiting rheology of mantle minerals: implications for the geobarometry of mantle minerals using micro-Raman spectroscopy. *Earth and Planetary Science Letters* 198(3-4), 511-519.

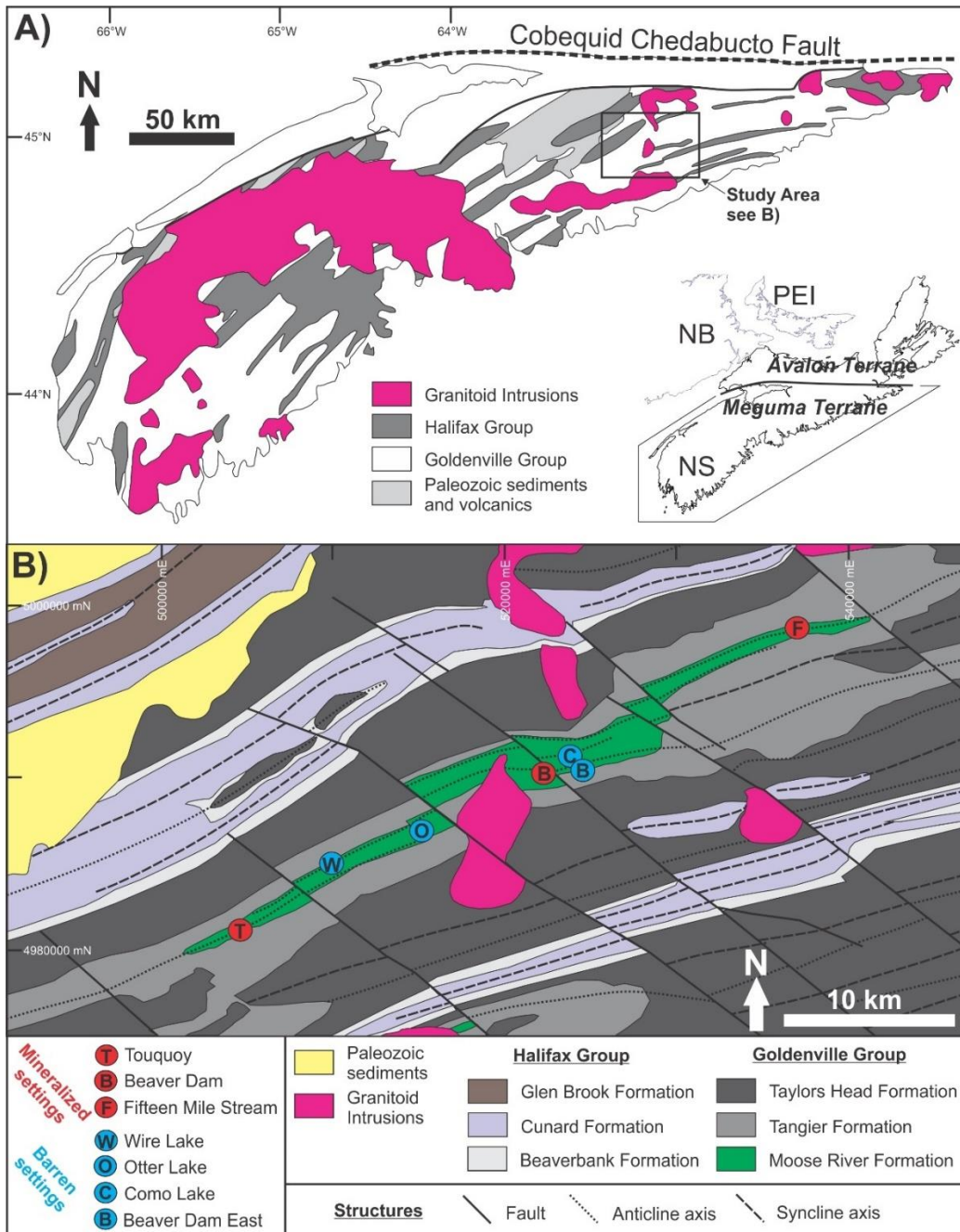


Figure 4-1: **A)** Simplified regional geology of the Meguma terrane in southern Nova Scotia. The study area is outlined in the black box. **B)** The geology of the area hosting the Moose River anticline with mineralized settings (i.e. gold deposits) shown in red circles. Barren settings from which samples have been collected from drill core are shown in blue circles. Maps have been adapted from the compiled work of Hudgins (1989) and Staples et al. (2018).

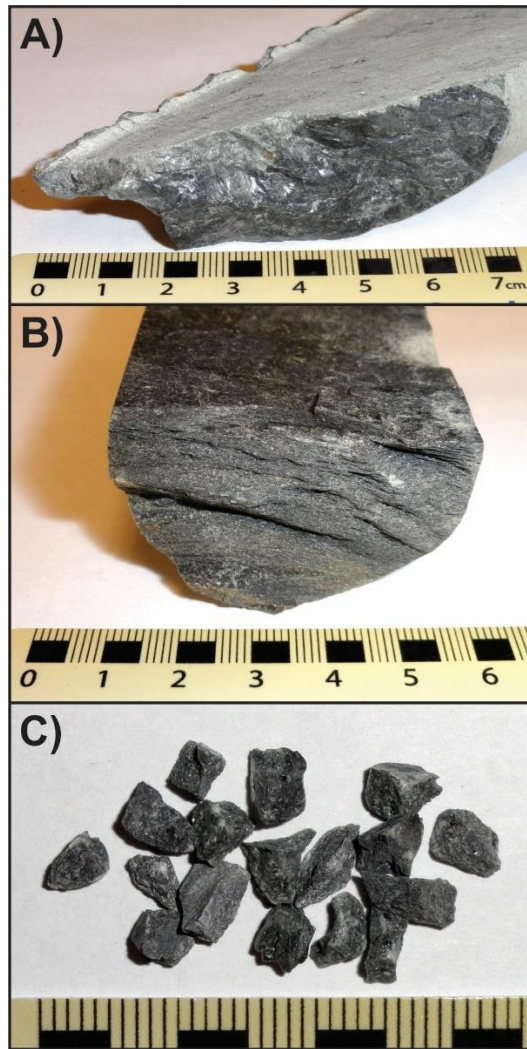


Figure 4-2: **A)** Sample (87-90-112.4) of non-fissile metamudstone from drill core MR-87-90 at 112.4 m. **B)** Sample (88-221-29.9) of fissile metamudstone from drill core MR-88-221 at 29.9 m. **C)** Fractured and cleaned sample fragments for use in the online rock-crushing gas chromatograph (GC). In all cases the sample fragments were  $\leq 0.5$  cm in order to ensure effective crushing.

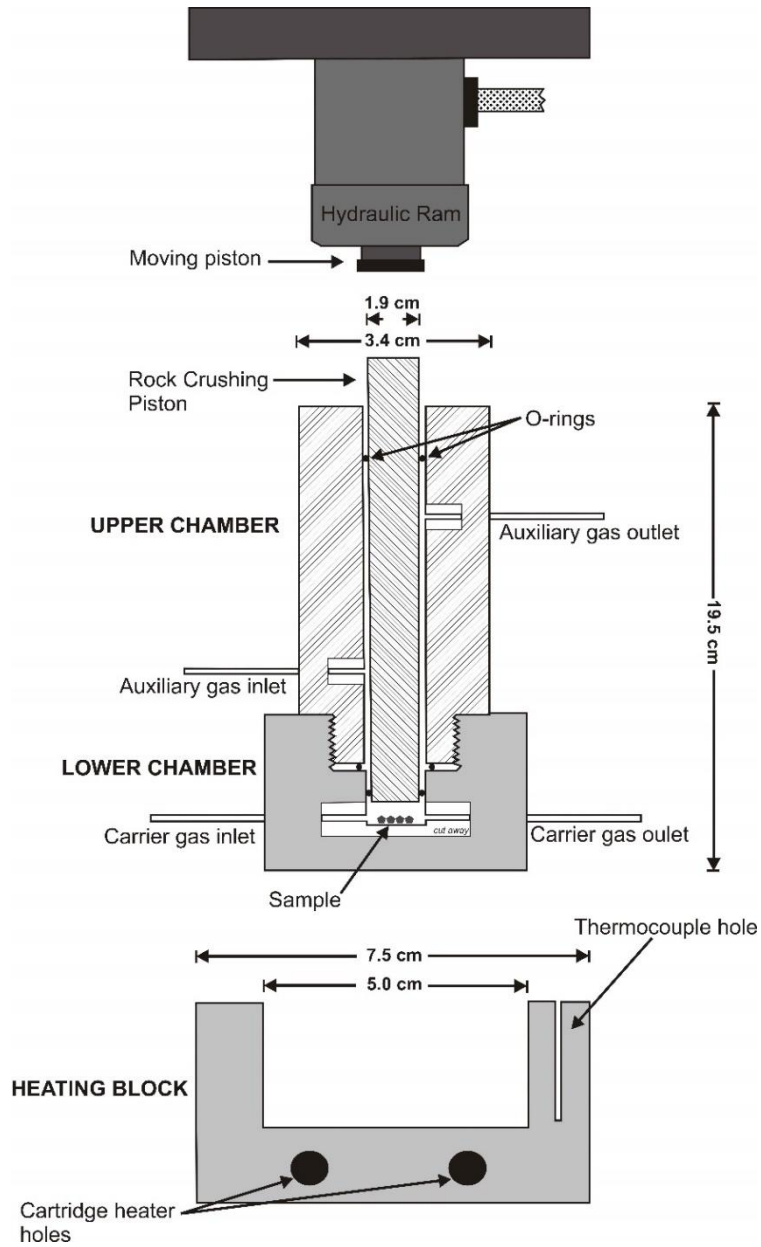


Figure 4-3: Schematic of the online rock-crushing apparatus used for gas chromatographic analysis of liberated bulk volatiles. Adapted from Kerr et al. (2015).

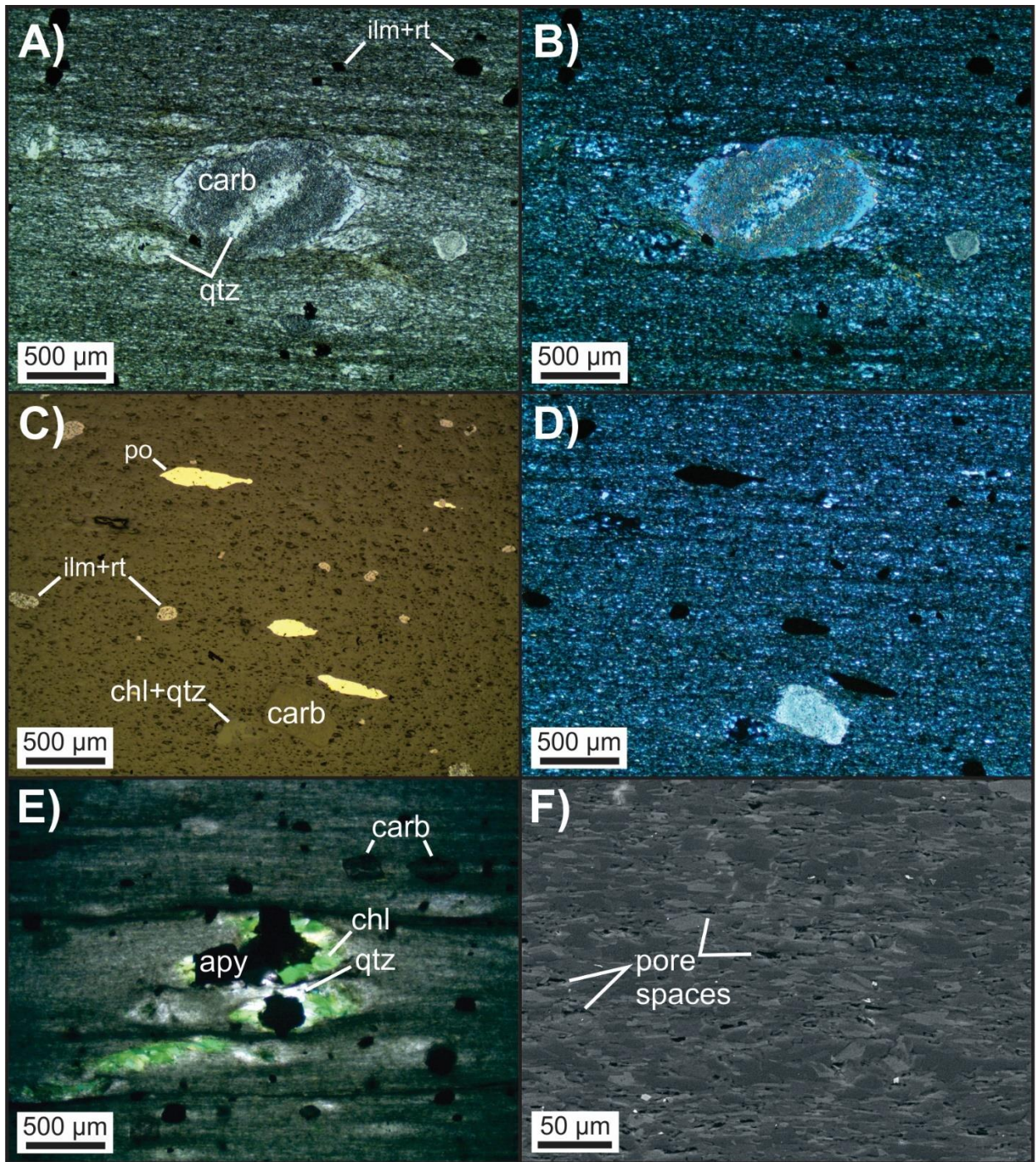


Figure 4-4: Petrography of Touquoy metamudstones. **A+B**) Plane-polarized (A) and cross-polarized (B) photomicrographs of representative fine-grained metamudstone (sample 88-221-53.64) displaying carbonate and ilmenite-rutile porphyroblasts. Carbonate grains often have quartz pressure shadows. Metamudstone matrix consist of muscovite + quartz + chlorite + carbonate  $\pm$  albitic plagioclase  $\pm$  K-feldspar. **C+D**) Reflected light (C) and cross-polarized (D) photomicrographs of representative metamudstone (sample 88-221-53.64) showing lozenge-shaped pyrrhotite concordant with bedding/laminations. **E**) Plane polarized photomicrograph of a metamudstone (sample 88-228-89.5) prepared as a fluid inclusion section ( $\sim 150 \mu\text{m}$  thick); note the presence of the arsenopyrite porphyroblasts with chlorite-quartz pressure shadows. **F**) SEM secondary electron image of a representative metamudstone (sample 88-228-89.5) showing abundant pore spaces.

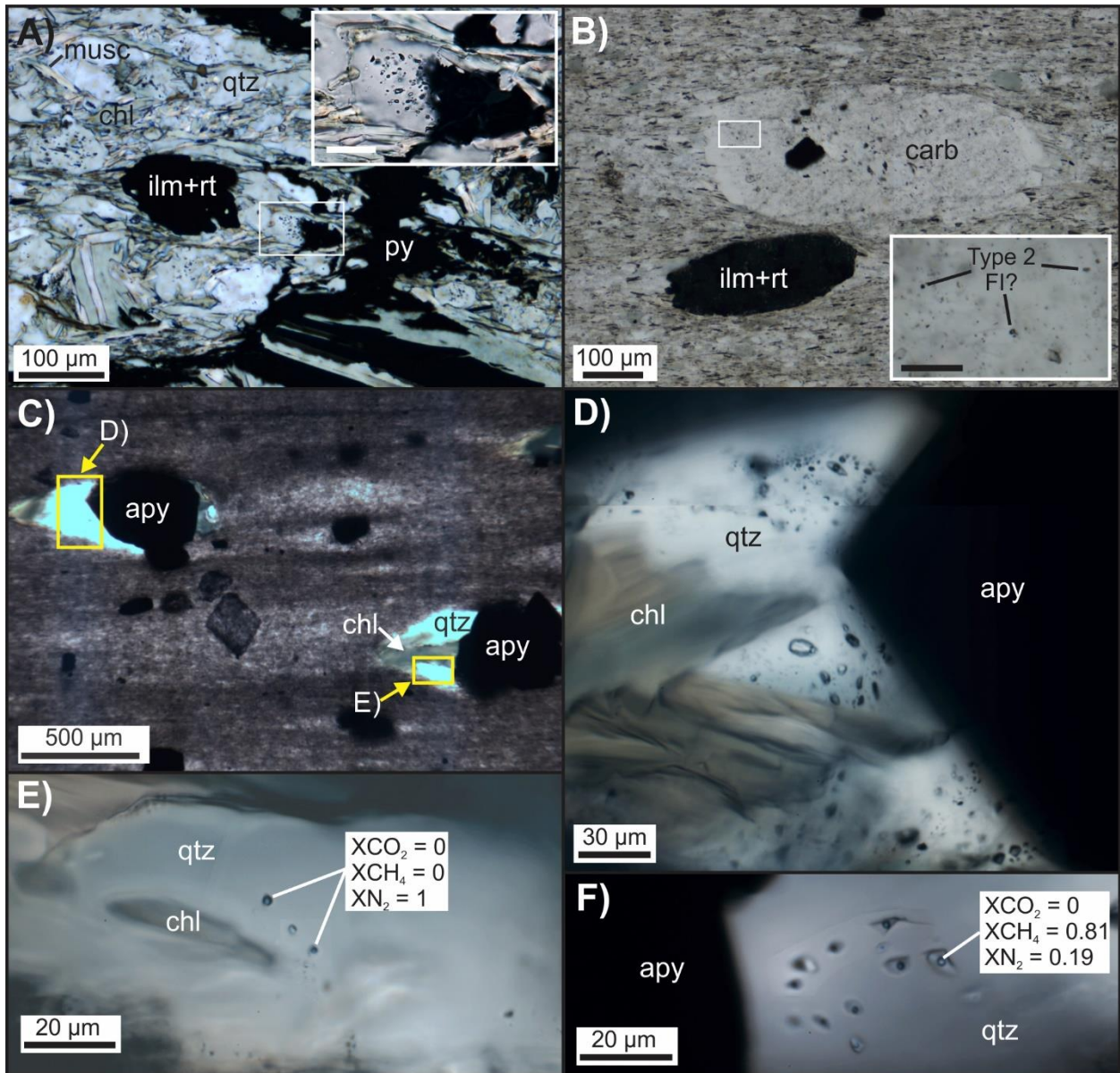


Figure 4-5: Fluid inclusions hosted in non-vein quartz samples from the Touquoy metamudstone.

**A)** Plane-polarized light (PPL) photomicrograph of a cluster of type 1 and 2 fluid inclusions in detrital quartz in metamudstone 88-158-13.85. Inset shows enlargement of white box. Scale bar in inset is 20  $\mu\text{m}$ . **B)** PPL photomicrograph of very small ( $\leq 2 - 3 \mu\text{m}$ ) type 2 fluid inclusions in carbonate porphyroblast in metamudstone 88-221-53.64. Inset shows enlargement of white box. Scale bar in inset is 20  $\mu\text{m}$ . **C)** PPL photomicrograph of arsenopyrite porphyroblasts with quartz-chlorite pressure shadows in Touquoy argillite (sample 88-228-69.5). Refer to frames C and D for higher magnification images of areas outlined by yellow dashed boxes. **D)** PPL photomicrograph of quartz pressure shadow (yellow box in C) hosting abundant type 1 and 2 fluid inclusions. **E)** PPL photomicrograph of quartz pressure shadow (yellow box in frame C) showing type 2 inclusions; the fluid composition shown was determined by LRM. **F)** PPL photomicrograph of a quartz pressure shadow showing type 1 inclusions; the fluid composition shown was determined by LRM.

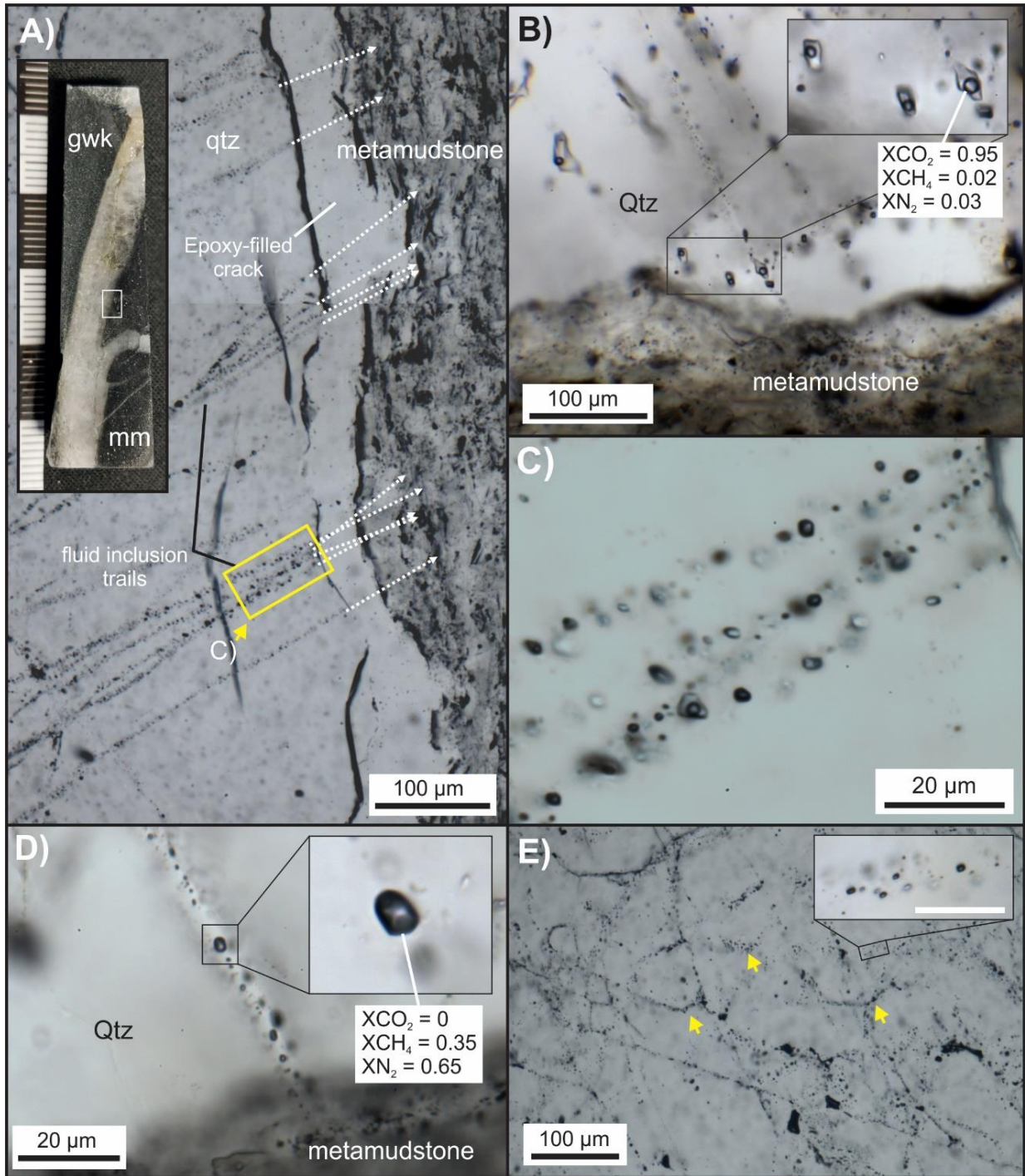


Figure 4-6: Quartz vein-hosted fluid inclusions. **A)** Plane polarized light (PPL) photomicrograph showing secondary fluid inclusion assemblages (FIA) in quartz vein (~1 cm; inset) extending into (or out of) adjacent metamudstone. The quartz vein is hosted along the lithological contact between greywacke (gwk) and black argillaceous metamudstone (mm) from sample 88-174-67.97. The dashed white lines refer to the inferred continuation of secondary fluid inclusion trails into the adjacent metamudstone unit. **B)** Secondary type 1 FIA in quartz at the contact of metamudstone; the fluid composition shown was determined by LRM. **C)** Enlargement of yellow box in frame A showing array of secondary type 1 and 2 fluid inclusion trails normal to the vein-metamudstone margin. **D)** FIA of secondary type 2 inclusions at the contact of metamudstone; the fluid composition shown was determined by LRM. **E)** Type 2 fluid inclusions decorating quartz grain boundaries (yellow arrows) in sample 88-174-67.97. Scale bar in inset is 20  $\mu\text{m}$ .

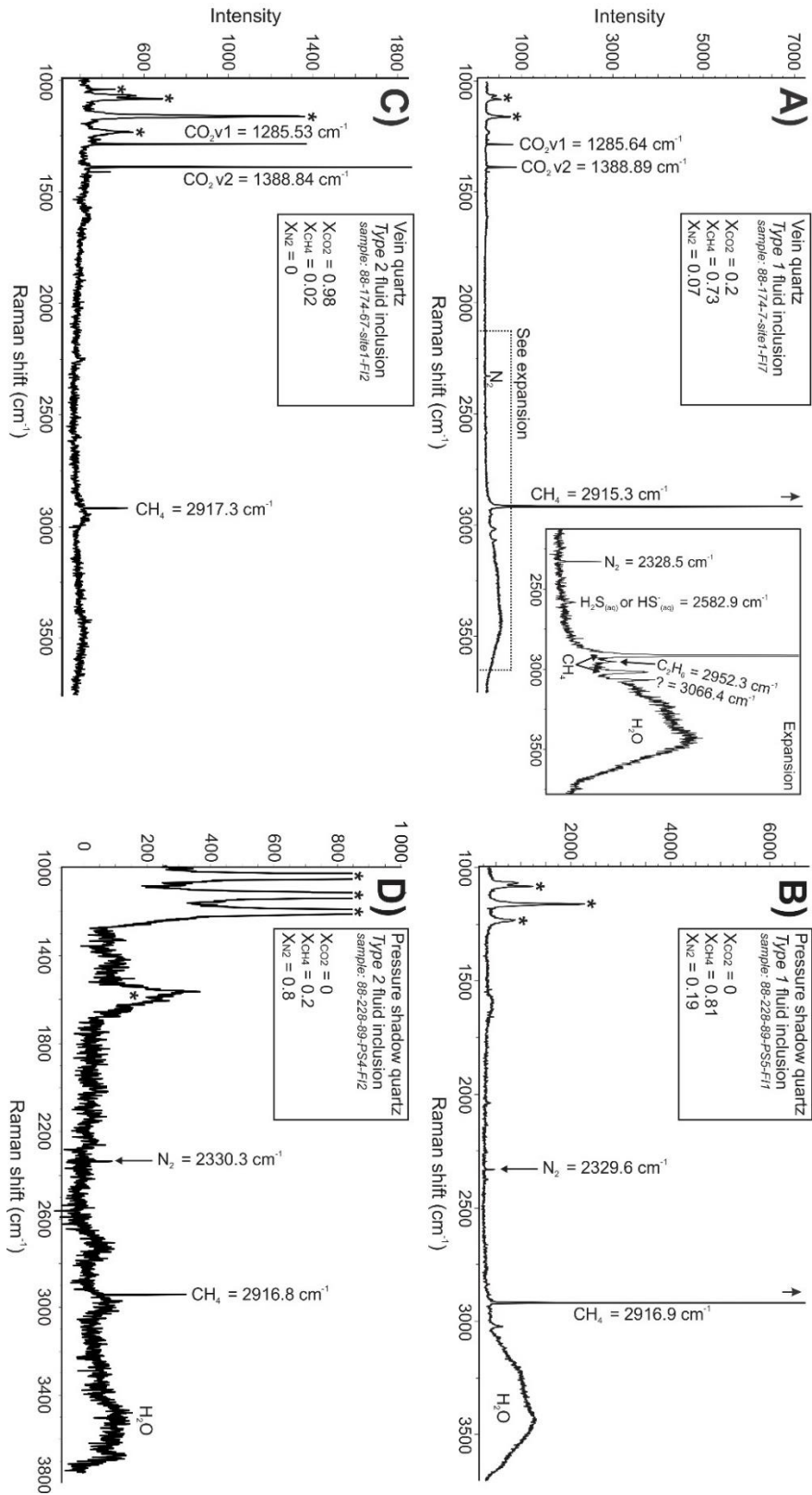


Figure 4-7: Representative LRM spectra of fluid inclusion vapour-phase analysis. **A)** Vapor-phase composition of a type 1 inclusion from a FIA trapped in vein quartz from sample 88-174-7.1. This particular inclusion is very CH<sub>4</sub>-rich and shows evidence for trace H<sub>2</sub>S and ethane (inset). **B)** Vapor-phase composition of a type 1 inclusion from a FIA trapped in pressure shadow quartz from sample 88-228-89.5. This inclusion is CH<sub>4</sub>+N<sub>2</sub>-dominated; no evidence of CO<sub>2</sub> is present. **C)** Composition of vapor-dominated type 2 inclusion from an FIA in vein quartz from sample 88-174-67.97. This inclusion is CO<sub>2</sub>-dominated with minor CH<sub>4</sub> and H<sub>2</sub>O. **D)** Composition of vapor-dominated type 2 inclusion from a cluster of indeterminate origin in pressure shadow quartz from sample 88-228-89.5. This inclusion shows only the presence of N<sub>2</sub> and CH<sub>4</sub>, and no evidence of CO<sub>2</sub>; however, the intensity of the Raman shifts is very weak on account of the low density of the inclusion. Note: asterisks indicate Raman signals from quartz host. Please see Table 4-1 and Table EA 4-1 for a complete sample log and LRM analyses, respectively.

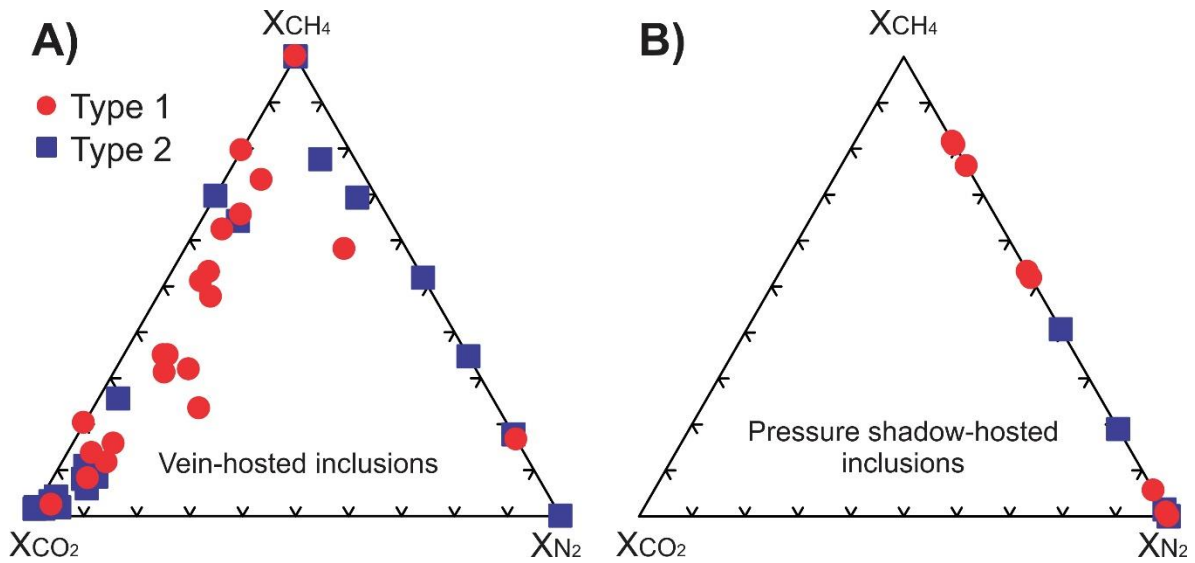


Figure 4-8: Fluid inclusion vapor phase compositions determined via LRM. **A)** Type 1 and type 2 fluid inclusion vapor phase compositions ( $n = 46$ ) from inclusions hosted in bedding concordant type vein quartz at metamudstone and greywacke lithological contacts. **B)** Type 1 and type 2 fluid inclusion vapor phase compositions ( $n = 20$ ) from inclusions in pressure-shadow quartz. Note that inclusions in this setting are  $N_2$ -rich/dominated and thus cluster at the  $N_2$  apex. Fluid inclusions are characteristically  $CO_2$ -depleted in this setting.

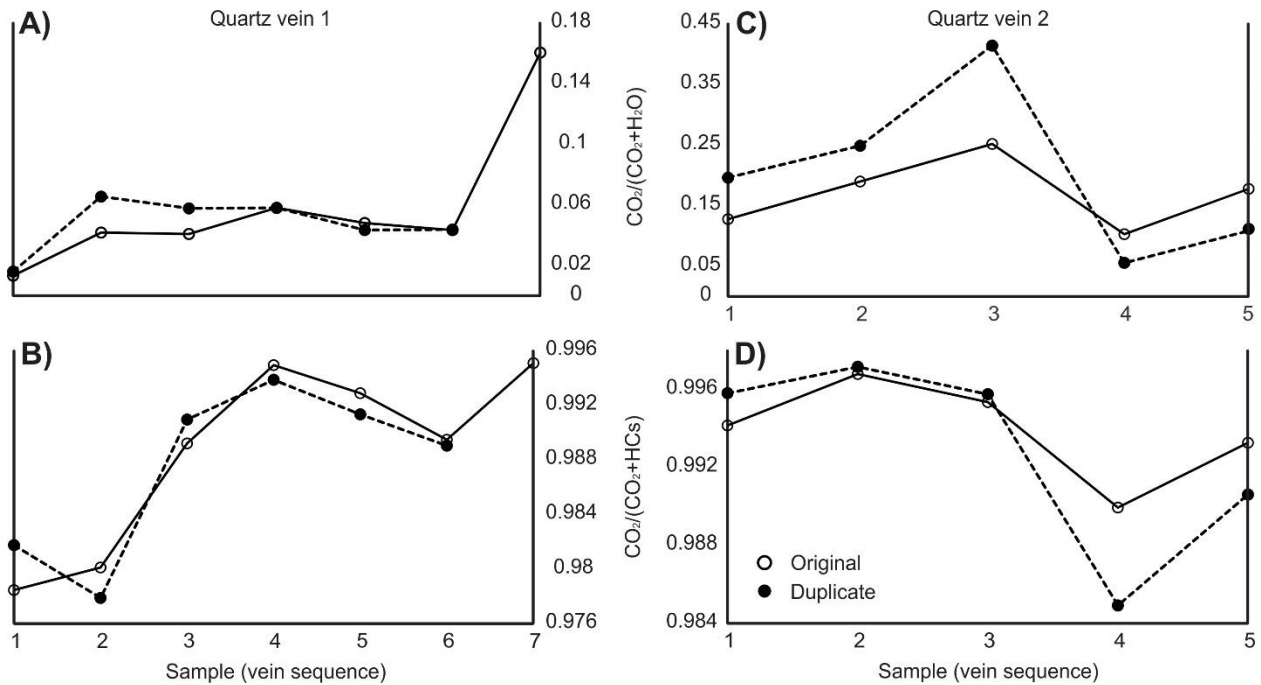


Figure 4-9: Evaluation of the reproducibility of gas chromatographic analysis. Summary of GC analysis for fluid inclusion rich veins quartz samples from two traverses across laminated quartz veins from the Madrid deposit in the Hope Bay Greenstone Belt, Nunavut, Canada. Note that the quartz samples were divided into two separate aliquots (original and duplicate = 2 aliquots per sample). The volatile ratio relationships can be seen to be consistent and reproducible. **A)** CO<sub>2</sub> / (CO<sub>2</sub> + H<sub>2</sub>O) ratios across vein 1. **B)** CO<sub>2</sub> / (CO<sub>2</sub> + HCs) ratios across vein 1. **C)** CO<sub>2</sub> / (CO<sub>2</sub> + H<sub>2</sub>O) ratios across vein 2. **D)** CO<sub>2</sub> / (CO<sub>2</sub> + HCs) ratios across vein 2. Abbreviations: HCs – hydrocarbons

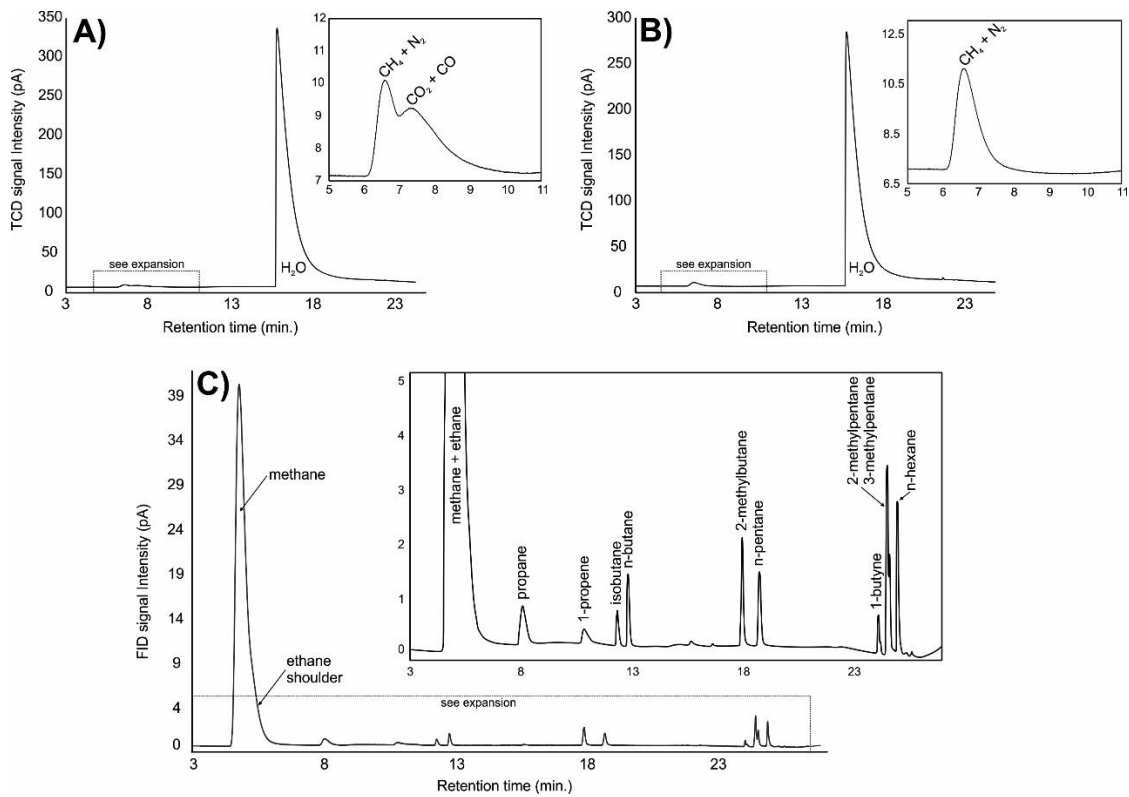


Figure 4-10: Representative chromatograms of crushed metamudstones. **A)** The method 1 TCD signal from crushed metamudstone (muddy argillite) sample 88-174-53 in proximity to a ~5 mm strataform quartz veinlet. The chromatogram shows the presence of CH<sub>4</sub>+N<sub>2</sub> and CO<sub>2</sub>+CO as volatile species trapped in the metamudstone. This sample was collected from a diamond drillcore drilled at the Touquoy mine and assay data reports a gold grade of 4.2 g/t over 1.1 m (Hudgins, 1989). **B)** The method 1 TCD signal from crushed metamudstone sample 88-228-104). This sample was collected from a diamond drillcore drilled at the Touquoy mine and assay date reports a gold grade of 0.2 g/t over 1.04 m (Hudgins, 1989). No CO<sub>2</sub>+CO was detected in this sample. **C)** The method 2 FID signal from crushed metamudstone sample 88-174-10. Although methane is the dominate hydrocarbon species, trace hydrocarbons detectable up to n-hexane are present. This sample was collected from a diamond drillcore drilled at the Touquoy mine and assay date reports a gold grade of 0.35 g/t over 0.65 m (Hudgins, 1989).

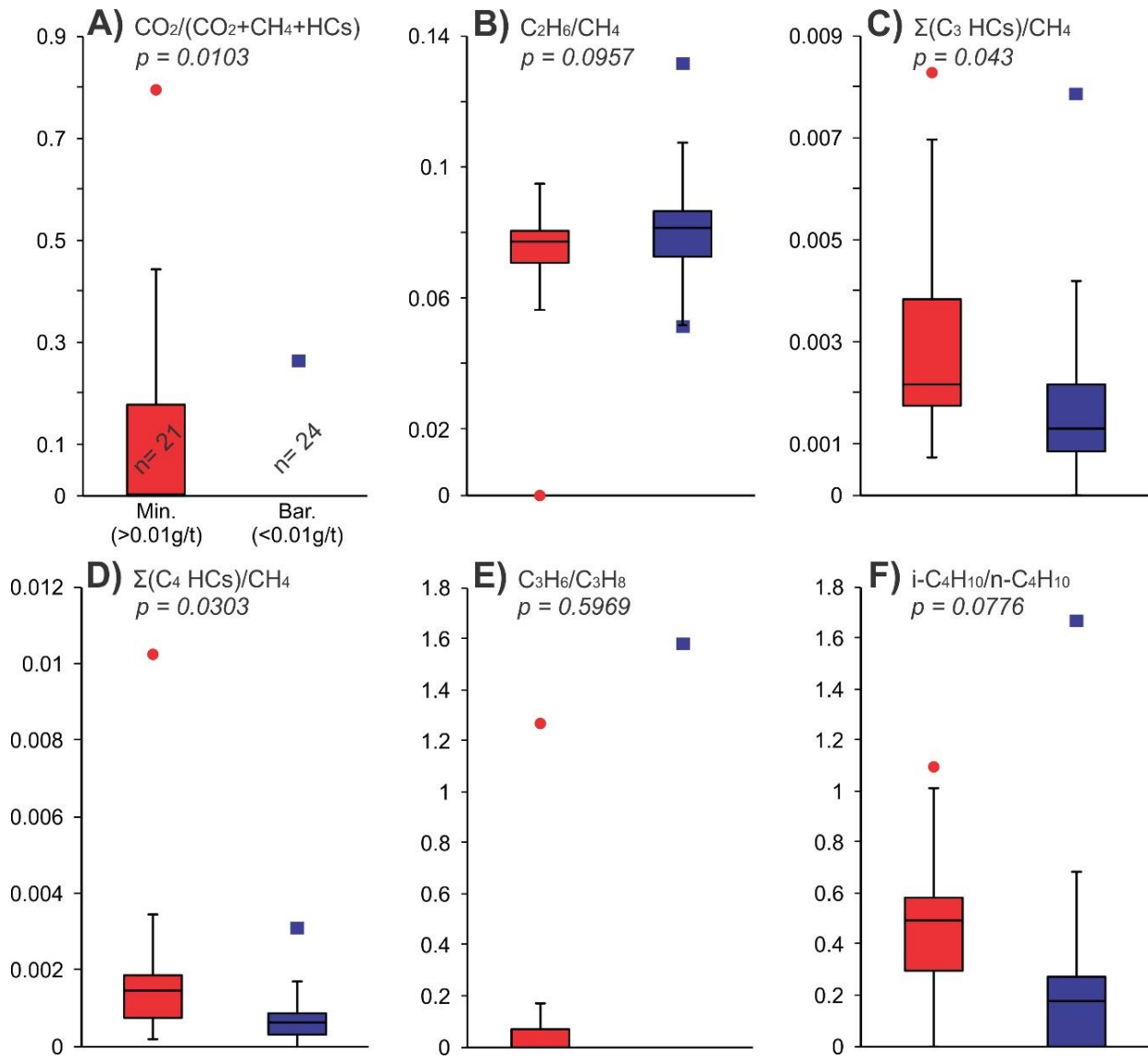


Figure 4-11: Box-and-whisker plots, with associated p-values, of bulk volatile ratios in metamudstones from Au-mineralized ( $0.01 \text{ g/t} \leq \text{Au} \leq 5 \text{ g/t}$ ) and gold-barren ( $<0.01 \text{ g/t}$ ) settings along the Moose River anticline. P-values were calculated using a Welch's t-test. Two-tailed p-values were used for all populations except for the  $\text{CO}_2/(\text{CO}_2+\text{CH}_4+\text{HCs})$  ratio as mineralized samples were hypothesized to have elevated  $\text{CO}_2$  ratios. **A)**  $\text{CO}_2/(\text{CO}_2+\text{CH}_4+\text{HCs})$  ratio. Ratio of  $\text{CO}_2$  to all additional carbonic phases, including hydrocarbons (HCs). **B)** Ethane to methane ratio. **C)** Ratio of all  $\text{C}_3$  hydrocarbons to methane. **D)** Ratio of all  $\text{C}_4$  hydrocarbons to methane. **E)** Propene to propane ratio. **F)** Isobutane to n-butane ratio.

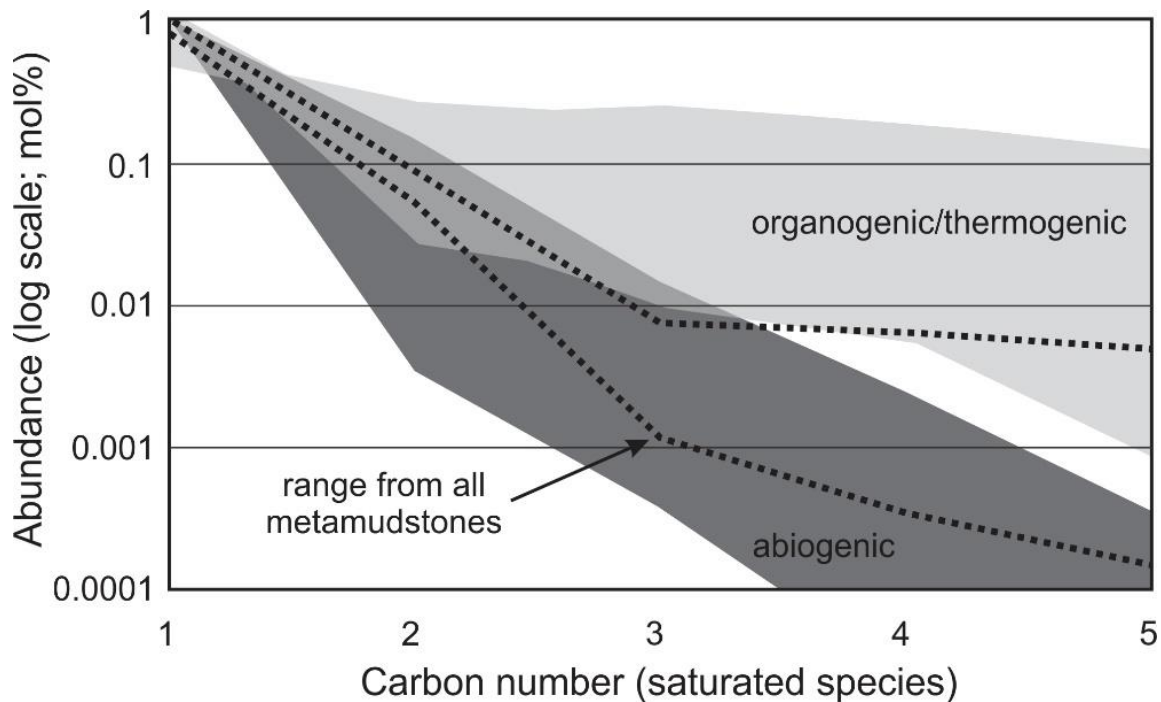


Figure 4-12: Saturated hydrocarbon abundances versus carbon number. Hydrocarbon abundances (log scale; mole %) follow a log linear (e.g., Schultz-Flory) distribution between C<sub>1</sub> and C<sub>3</sub>, at which point a flatter distribution is observed. The organogenic/thermogenic and abiogenic HC fields are adapted from Potter and Konnerup-Madsen (2003). Organogenic/thermogenic field shows data from China oil fields (Chen et al., 2000), the Ula Formation in Norway (Potter and Konnerup-Madsen, 2003 and references therein), and the Green Tuff Basin in Japan (Sakata et al., 1997). Abiogenic field shows data from Khibina and Lovozero, Russia (Petersilie and Sørensen, 1970; Voytov, 1992), Illimaussaq, Greenland (Petersilie and Sørensen, 1970; Konnerup-Madsen et al., 1979), Strange Lake, Canada (Salvi and Williams-Jones, 1997), and Sudbury, Timmins and Red Lake, Canada (Sherwood-Lollar et al., 1993; Kerr et al., 2015).

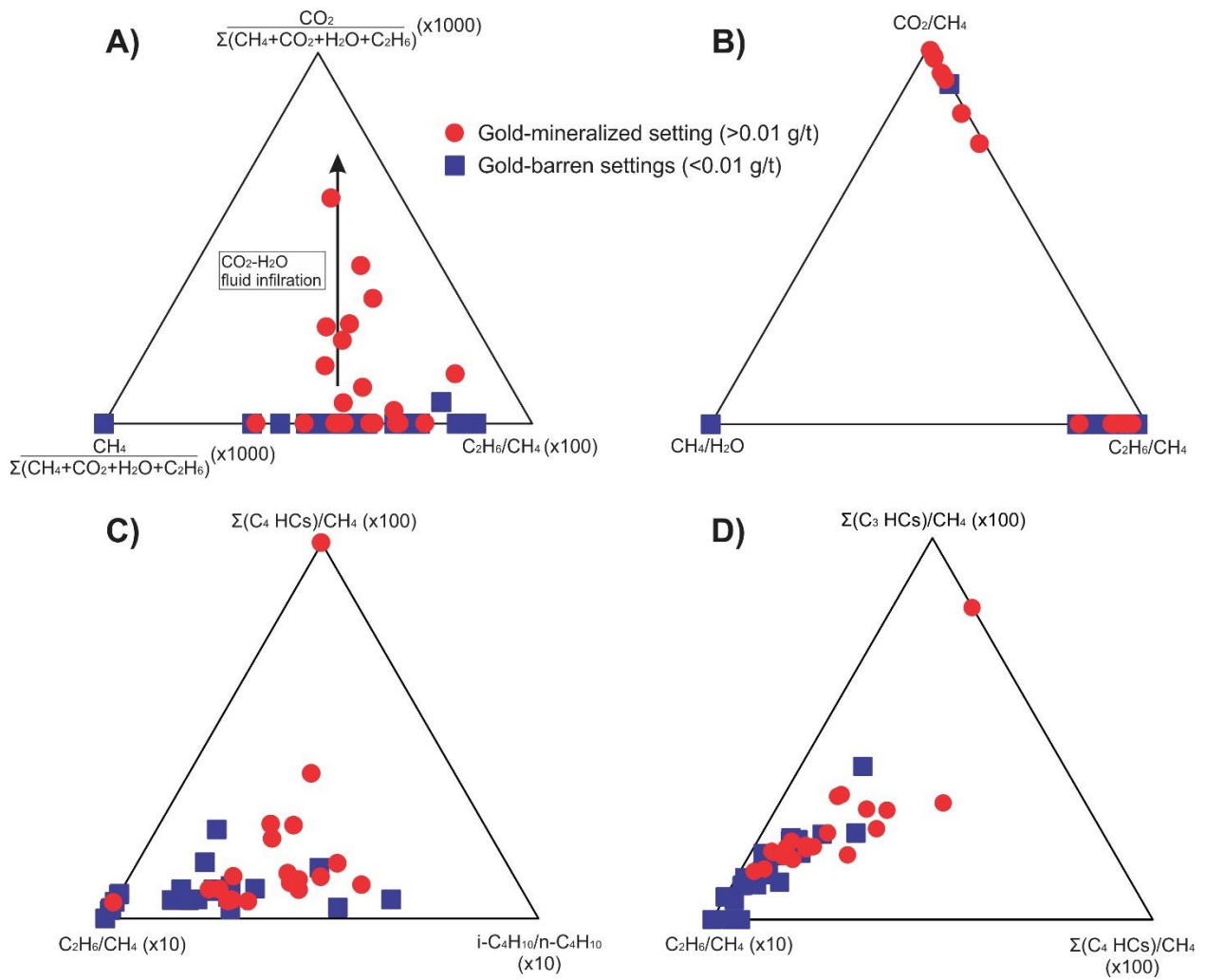


Figure 4-13: Ternary plots of bulk volatile ratios in metamudstones from Au-mineralized ( $0.01 \text{ g/t} \leq \text{Au} \leq 5 \text{ g/t}$ ;  $n = 21$ ) and gold-barren ( $<0.01 \text{ g/t}$ ;  $n = 24$ ) settings in the Moose River anticline. **A)** Ternary plot comparing ratios of  $\text{CO}_2$  and  $\text{CH}_4$  to  $\Sigma\text{CO}_2 + \text{CH}_4 + \text{H}_2\text{O} + \text{C}_2\text{H}_6$ , and  $\text{C}_2\text{H}_6/\text{CH}_4$  ratios. Note that there is an increase of  $\text{CO}_2$  abundance in samples from Au-mineralized settings that does not correspond with gold grades in sampled metamudstone intervals. **B)** Ternary plot comparing  $\text{CH}_4/\text{H}_2\text{O}$ ,  $\text{CO}_2/\text{CH}_4$ , and  $\text{C}_2\text{H}_6/\text{CH}_4$  ratios. **C)** Ternary plot comparing ethane/methane, sum of all  $\text{C}_4$  hydrocarbons to methane, and isobutane to n-butane ratios. **D)** Ternary plot comparing ethane/methane, sum of all  $\text{C}_3$  hydrocarbons to methane, and sum of all  $\text{C}_4$  hydrocarbons to methane ratios. Note there is no significant distinction between clusters from mineralized versus barren settings is observed.

Table 4-1: Sampled metamudstones from Au-mineralized and -barren settings. All listed samples were analyzed via GC. Select samples were examined petrographically and analyzed via Raman spectroscopy.

Drillhole	Sample ID (year-hole-depth [m])	Sample Description	Reported gold grade (g/t)	Assay length (m)	
Touquoy deposit (Au-mineralized)	MR-87-090				
	87-90-102.8	silty argillite; <1% po, <1% apy	0.01	0.4	
		87-90-112.4	muddy argillite; non-fissile; <1% po, <1% apy	0.13	0.24
	MR-88-158				
		88-158-13.85	silty argillite that grades into greywacke; <1% po, <1% apy	0.26	0.41
	MR-88-174				
		88-174-10.26	black muddy argillite with strong pressure shadows; <1% po, <1% apy. @ 10.23 m a 0.1 cm qtz-carb vein is present.	0.35	0.65
		88-174-42.4	muddy argillite; <1% po, <1% apy	0.2	0.92
		88-174-53.9	muddy argillite in proximity to 0.3cm strataform qtz vein. Carbonate veinlets displaing parasitic folding. VG present in intersection; 1% po, <1% apy	4.2	1.1
		88-174-67.97	thin quartz vein (~0.5 cm) along boundary between laminated silty argillite/greywacke and muddy black argillite	0.02	1.2
	MR-88-221				
		88-221-29.9	silty argillite; 1% po, <1% apy	0.36	1
		88-221-53.64	muddy argillite; <1% po, <1% apy	3.97	1
	MR-88-224				
		88-224-65.9	muddy argillite; <1% po, <1% apy	0.04	1.2
		88-224-71.8	muddy argillite; <1% po, <1% apy	0.09	1.11
	MR-88-225				
		88-225-123.2	muddy argillite; <1% po, <1% apy	0.77	1.03
	MR-88-228				
		88-228-89.5	muddy argillite; <1% po, <1% apy	0.37	1.12
		88-228-95	muddy argillite; <1% po, <1% apy	0.05	1.13
		88-228-104	muddy argillite, carbonate vein (<1cm), minor py; <1% po, <1% apy	0.2	1.04
		88-228-131	muddy argillite; <1% po, <1% apy	0.1	1
	88-228-159.3	muddy argillite; <1% po, <1% apy	0.01	1.36	
TOUQ-95-1					
	TOUQ-95-1-72	black, fissile, argillite (flame assay results DDV)	4.83	1	
TOUQ-95-2					
	TOUQ-95-2-37.1	black, fissile, argillite	1.76	3.2	
	TOUQ-95-2-67	black, mod-fissile, in region of 2.9 g/t over 92.71m (commonly VG in area)	1.65	1.5	
	TOUQ-95-2-82.5	black, mod-fissile, in region of 6.03 g/t over 14.5m (Commonly VG in area)	4.03	1.5	
Otter Lake (Au-barren)	OL-88-01				
		OL-88-01-9.45	muddy argillite/slate; fissile (called 'metawacke' by original logs)	<0.01	-
		OL-88-01-26.9	argillite/slate; fissile	<0.01	-
		OL-88-01-65.4	argillite/slate; fissile; sampled by DDV Gold in 2009	<0.01	-
	OL-88-04				
		OL-88-04-32.1	black muddy argillite/slate; fissile	<0.01	-
		OL-88-04-68.79	black/grey argillite/slate; fissile; sampled by DDV Gold in 2009	<0.01	-
		OL-88-04-71.25	black argillite with parasitic folded laminations (good sed structures for thin section); sampled by DDV Gold in 2009	<0.01	-
		OL-88-04-87.5	black, muddy argillite; fissile	<0.01	-
Wire Lake (Au-barren)	WL-229-02				
		WL-229-02-20.42	argillite; moderate fissility	<0.01	-
		WL-229-02-36.1	argillite; fissile	<0.01	-
	WL-229-04				
		WL-229-04-9.4	argillite; between two quartz veins	trace oz/ton (?)	-
	WL-229-04-27.1	argillite near quartz veining	trace oz/ton (?)	-	

Table 4-1 Continued

Como Lake (Au-barren)	CL-97-07			-
	CL-97-07-14	argillite/slate; black/grey; fissile	0.0025	-
	CL-97-07-26	argillite/slate; black/grey; fissile	0.0025	-
	CL-97-07-69.5	argillite/slate near qtz veinlets; black/grey; fissile	0.0025	-
Como Lake (Au-barren)	CL-97-06			-
	CL-97-06-16.9	argillite/slate; black/grey; fissile	0.0025	-
	CL-97-06-54.7	argillite/slate; black/grey; fissile	0.0025	-
	CL-97-06-92	argillite/slate; black/grey; fissile; carbonate stockwork near	0.0025	-
Beaver Dam East (Au-barren)	BDE-97-01			-
	BDE-97-01-7	argillite; black; fissile (RJZ assay 2111)	0.005	2
	BDE-97-01-114.8	argillite; black (RJZ assay 2155)	0.105	3
	BDE-97-02			
	BDE-97-02-8.6	argillite/slate; black; fissile (RJZ assay 2183)	0.015	3
	BDE-97-02-20.6	argillite/slate; black; moderate fissile (RJZ assay 2163)	0.015	3
	BDE-97-03			-
BDE-97-03-26.95	black argillite adjacent to ~20cm qtz vein with grey clear and white bull qtz with calcite veinlets. (RJZ assay 2230)	0.0025	0.3	
BDE-97-03-104.8	black argillite interbedded with greywacke (RJZ assay 2218)	0.0025	3	

Note: Sample descriptions are based off direct observation and historic drill core logs. Abbreviations: apy - arsenopyrite; po - pyrrhotite; qtz - quartz; VG - visible gold

## Chapter 5

### 5.1 Conclusions

This thesis documents and characterizes important concepts related to gold mineralization in greenstone-hosted and metasedimentary-hosted orogenic gold deposits, with an ultimate aim to better refine genetic models and inform exploration practices. This thesis provides the following:

- Chapter 2 presents the first integrated textural, mineralogical and fluid inclusion examination of the giant Hope Bay Greenstone Belt (HBGB) orogenic gold system (Nunavut, Canada) using a protocol of in situ microanalytical techniques. This work provides direct evidence for gold upgrading via the introduction of late-stage hydrothermal fluids sourced from protracted magmatic-hydrothermal activity. Although volumetrically minor, the potential magnitude of secondary gold enrichment makes overprinted and upgraded veins important exploration targets to consider. This work provides insights into a generally unrecognized process of gold enrichment in orogenic systems, and illustrates that late-stage magmatic-hydrothermal overprinting and local upgrading of pre-existing vein systems is likely more common than previously thought.
- Chapter 3 presents detailed mechanistic interpretations for gold mineralization in the Dufferin gold deposit (Nova Scotia, Canada) as a result of coupled ore fluid reduction and pH change due to the interaction with reducing (i.e., organic carbon-bearing) host rock lithologies. These conclusions are supported by a variety of mineralogical, isotopic and fluid geochemical evidences. For instance, submicron gold grains are texturally-associated with carbonaceous material (e.g., pyrobitumen) within cavities in vein lamination or along vein margins. Also, this study presents the first quantified gold concentrations in secondary fluid inclusions from an economic, Phanerozoic slate belt-hosted gold deposit. Gold concentrations in these aqueous-

carbonic ore fluids is appreciable (~45 ppb), yet undersaturated, and similar fluids have been documented in unmineralized vein systems elsewhere. This suggests that gold-bearing fluids do not necessitate gold-rich deposit, underscoring the importance of highly efficient precipitation mechanisms from relatively low volumes of auriferous fluids (compared to high-tonnage gold systems with extensive veining).

- Chapter 3 presents a pilot project that employed an unconventional rock-crushing gas chromatographic (GC) technique as a potential exploration vector for country rock-hosted disseminated gold deposits of the Moose River Anticline (MRA) in the Meguma terrane (Nova Scotia, Canada). The bulk volatile signatures (e.g., volatile speciation and abundances) of crushed metamudstones from the gold mineralized Touquoy deposit and several analogous barren units along the MRA were compared. Fluid inclusion petrography complimented by laser Raman microspectroscopy determined that host rocks broadly contain two distinct fluids: (i)  $N_2 \pm CH_4$ -dominated fluids interpreted to be formational fluids that have equilibrated with organic-bearing metamudstone host rocks; and (ii)  $CO_2-H_2O \pm CH_4 \pm N_2$ -bearing vein-forming fluids implicated as the main Au-mobilizing ore fluid responsible for Au mineralization in the MRA and elsewhere in the Meguma terrane. Preliminary GC analysis has demonstrated that metamudstones associated with mineralized regions of the MRA contain more bulk  $CO_2$  than analogous samples from barren settings (p-value of 0.0103 between populations). Furthermore, GC work identified differences in the abundances of high-order hydrocarbon abundances between populations that warrants additional investigation. These findings suggest that auriferous hydrothermal fluids did not equally permeate all regions of the MRA, and thus economic concentrations of Au are localized to regions with favorable structural characteristics (e.g., fault systems, stockworking) resulting in increased fluid fluxes. Future refinement of this technique may yield a viable geochemical tool for vectoring

toward mineralized units within the Meguma terrane, and potentially analogous systems elsewhere.

## **5.2 Future Work**

Chapter 2 presented evidence for vein overprinting and secondary gold upgrading via protracted magmatic-hydrothermal activity in the HBGB. This study was constrained to the southern region of the Madrid deposit in the HBGB. Therefore, future work should be aimed at systematically exploring additional veins associated with the Madrid deposit to validate these conclusions. We have provided important insights into the role of late magmatic-hydrothermal processes in gold enrichment in the HBGB, however, the extent to which these processes have affected the Madrid deposit and other deposits in the HBGB (e.g., Doris, Boston) is yet unknown.

The study of gold mineralization in the Dufferin deposit presented in Chapter 3 was largely a mechanistic investigation of gold bisulfide destabilization and precipitation. Work was largely constrained to a few representative samples from saddle veins and their extensions down fold limbs (i.e., leg veins). However, a comprehensive investigation of the stable isotope and fluid geochemical (e.g., microthermometric properties, and volatile and solute compositions) characteristics between saddles (at least 13) has not yet been performed. There have been few focused studies of this nature due in part to the challenges of sampling active working faces. A more detailed investigation is required to synthesize a robust genetic model of the Dufferin deposit, which presents evidence of repeated intervals of saddle vein dilation, fluid ingress and veining, and multiple periods of mineralization. The Dufferin deposit shares a variety of similarities with other gold systems in the Meguma terrane, and thus would help inform gold deposit models in Nova Scotia and analogous systems elsewhere.

The preliminary investigation of bulk volatile systematics presented in Chapter 4 has determined differences in CO<sub>2</sub> and hydrocarbon abundances between mineralized and barren settings that warrant further investigation. Firstly, a follow-up study should be performed with an intra-deposit focus. For instance, a sampling approach focused on metamudstones from drill core intervals that intersect significant structures (e.g., faults), and Au-bearing and Au-barren regions within a single deposit. In certain MRA-hosted deposits (e.g., Touquoy) mineralization in metamudstone and metasandstone intervals is fault-bounded, with mineralized units juxtaposed to barren ones on the opposite side of the fault plane. This study has demonstrated that bulk fluid differences are recognizable between mineralized and barren parcels, however, recommended additional work may elucidate the spatial characteristics of fluid ingress and the role of structure in these systems. Furthermore, in order to take advantage of material from contemporary drilling operations along the MRA, a strategic partnership with an exploration and/or mining company (e.g., Atlantic Gold Corp., MegumaGold Corp.) would facilitate ease of access to important samples.